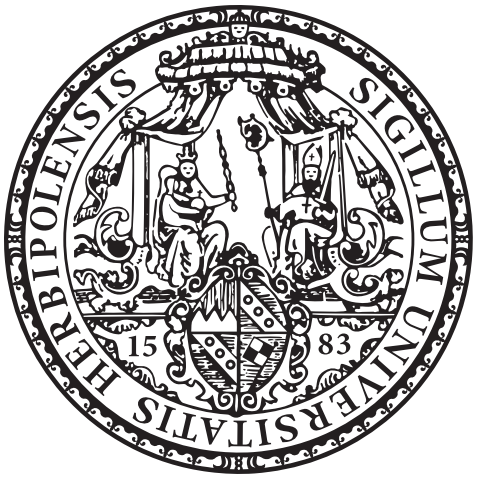

Electronic Correlations in Two-dimensional Triangular Adatom Lattices

Dissertation zur Erlangung des
naturwissenschaftlichen Doktorgrades
der Julius-Maximilians-Universität Würzburg

vorgelegt von
Florian Rudolf Adler
aus Würzburg

Würzburg 2020

Eingereicht am: 22.09.2020

bei der Fakultät für Physik und Astronomie

1. Gutachter: Prof. Dr. Ralph Claessen

2. Gutachter: Prof. Dr. Matthias Bode

3. Gutachter:

der Dissertation

Vorsitzender: Prof. Dr. Werner Porod

1. Prüfer: Prof. Dr. Ralph Claessen

2. Prüfer: Prof. Dr. Matthias Bode

3. Prüfer: Prof. Dr. Giorgio Sangiovanni

im Promotionskolloquium

Tag des Promotionskolloquiums: 07.05.2021

Doktorurkunde ausgehändigt am:

Abstract

Two-dimensional triangular lattices of group IV adatoms on semiconductor substrates provide a rich playground for the investigation of Mott-Hubbard physics. The possibility to combine various types of adatoms and substrates makes members of this material class versatile model systems to study the influence of correlation strength, band filling and spin-orbit coupling on the electronic structure – both experimentally and with dedicated many-body calculation techniques. The latter predict exotic ground states such as chiral superconductivity or spin liquid behavior for these frustrated lattices, however, experimental confirmation is still lacking. In this work, three different systems, namely the α-phases of Sn/SiC(0001), Pb/Si(111), and potassium-doped Sn/Si(111) are investigated with scanning tunneling microscopy and photoemission spectroscopy in this regard. The results are potentially relevant for spintronic applications or quantum computing.

For the novel group IV triangular lattice Sn/SiC(0001), a combined experimental and theoretical study reveals that the system features surprisingly strong electronic correlations because they are boosted by the substrate through its partly ionic character and weak screening capabilities. Interestingly, the spectral function, measured for the first time via angle-resolved photoemission, does not show any additional superstructure beyond the intrinsic $\sqrt{3} \times \sqrt{3}R30°$ reconstruction, thereby raising curiosity regarding the ground-state spin pattern.

For Pb/Si(111), preceding studies have noted a phase transition of the surface reconstruction from $\sqrt{3} \times \sqrt{3}R30°$ to 3×3 at 86 K. In this thesis, investigations of the low-temperature phase with high-resolution scanning tunneling microscopy and spectroscopy unveil the formation of a charge-ordered ground state. It is disentangled from a concomitant structural rearrangement which is found to be 2-up/1-down, in contrast to previous predictions. Applying an extended variational cluster approach, a phase diagram of local and nonlocal Coulomb interactions is mapped out. Based on a comparison of theoretical spectral functions with scattering vectors found via quasiparticle interference, Pb/Si(111) is placed in said phase diagram and electronic correlations are found to be the driving force of the charge-ordered state.

In order to realize a doped Mott insulator in a frustrated geometry, potassium was evaporated onto the well-known correlated Sn/Si(111) system. Instead of the expected insulator-to-metal transition, scanning tunneling spectroscopy data indicates that the electronic structure of Sn/Si(111) is only affected locally around potassium atoms while a metallization is suppressed. The potassium atoms were found to be adsorbed on empty T_4 sites of the substrate which eventually leads to the formation of two types of K-Sn alloys with a relative potassium content of 1/3 and 1/2, respectively. Complementary measurements of the spectral function via angle-resolved photoemission reveal that the lower Hubbard band of Sn/Si(111) gradually changes its shape upon potassium deposition. Once the tin and potassium portion on the surface are equal, this evolution is complete and the system can be described as a band insulator without the need to include Coulomb interactions.

Zusammenfassung

Zweidimensionale Dreiecksgitter aus Adatomen der vierten Hauptgruppe auf Halbleitersubstraten bieten eine reichhaltige Spielwiese für die Untersuchung von Mott-Hubbard-Physik. Die Möglichkeit, verschiedene Adatomsorten und Substrate zu kombinieren, macht die Mitglieder dieser Materialklasse zu vielseitigen Modellsystemen, um den Einfluss von Korrelationsstärke, Bandfüllung und Spin-Bahn-Kopplung auf die elektronische Struktur zu untersuchen – sowohl im Experiment als auch mit Vielkörper-Rechnungen. Letztere prognostizieren exotische Grundzustände, wie z. B. chirale Supraleitung oder eine Spin-Flüssigkeit, wobei eine experimentelle Bestätigung jeweils noch aussteht. In dieser Dissertation werden drei derartige Systeme, nämlich die α-Phasen von Sn/SiC(0001), Pb/Si(111) und kaliumdotiertem Sn/Si(111) mittels Rastertunnelmikroskopie und Photoemissionsspektroskopie diesbezüglich untersucht. Die Resultate sind potentiell relevant für Anwendungen im Bereich der Spintronik oder Quantencomputer.

Für das erst kürzlich realisierte Gruppe-IV-Dreiecksgitter Sn/SiC(0001) zeigt diese Studie, bei der experimentelle und theoretische Methoden kombiniert werden, dass das System unerwartet starke Korrelationen aufweist, weil sie durch den teilweise ionischen Charakter und das geringe Abschirmungsvermögen des Substrats verstärkt werden. Die Spektralfunktion, die erstmals mit winkelaufgelöster Photoemission gemessen wird, zeigt keine Überstruktur außer der intrinsischen $\sqrt{3} \times \sqrt{3}R30°$ Rekonstruktion des Gitters, was die Frage nach der Anordnung der Spins im Grundzustand aufwirft.

Bei Pb/Si(111) haben bereits frühere Veröffentlichungen einen Phasenübergang bei der Oberflächenrekonstruktion von $\sqrt{3} \times \sqrt{3}R30°$ auf 3×3 bei 86 K festgestellt. In dieser Arbeit zeigen Untersuchungen der Niedrigtemperaturphase mit hochaufgelöster Rastertunnelmikroskopie und -spektroskopie die Entstehung eines ladungsgeordneten Zustands. Dieser wird von der begleitend auftretenden strukturellen Neuordnung getrennt, welche entgegen bisheriger Voraussagen eine 2-hoch/1-tief-Anordnung aufweist. Mit Hilfe einer neu entwickelten Cluster-Rechenmethode wird ein Phasendiagramm erstellt, in dem die lokale und nichtlokale Coulomb-Wechselwirkung gegeneinander aufgetragen sind. Durch einen Vergleich zwischen theoretischen Spektralfunktionen mit Streuvektoren, die mittels Quasiteilchen-Interferenz bestimmt werden, kann Pb/Si(111) in besagtem Phasendiagramm platziert werden. Dadurch stellt sich heraus, dass elektronische Korrelationen die treibende Kraft für den ladungsgeordneten Zustand in Pb/Si(111) sind.

Um einen dotierten Mott-Isolator in einem frustrierten System zu verwirklichen, wird Kalium auf das bekannte, korrelierte System Sn/Si(111) aufgebracht. Statt des erwarteten Isolator-Metall Übergangs zeigen Messungen mit Rastertunnelspektroskopie, dass die elektronische Struktur von Sn/Si(111) nur lokal in der unmittelbaren Umgebung der Kaliumatome beeinflusst wird, ohne dass das System metallisch wird. Die Kaliumatome werden auf freien T_4-Plätzen des Substrats adsorbiert, was letztendlich zur Ausbildung von zwei unterschiedlichen Kalium-Zinn-Legierungen mit einem Kaliumanteil von 1/3 bzw. 1/2 führt. Komplementäre Messungen der Spektralfunktion mit winkelaufgelöster Photoemission zei-

gen, dass das untere Hubbardband von Sn/Si(111) durch die Kalium-Deposition allmählich seine Form verändert. Sobald Zinn und Kalium zu gleichen Teilen auf der Oberfläche vorliegen, ist diese Transformation beendet und das System kann als einfacher Bandisolator ohne die Notwendigkeit, elektronische Korrelationen zu berücksichtigen, beschrieben werden.

Contents

List of abbreviations

2D two-dimensional

2DES two-dimensional electron system

ARPES angle-resolved photoemission spectroscopy

BZ Brillouin zone

CDW charge density wave

CITS current imaging tunneling spectroscopy

CO charge order

DFT density functional theory

DMFT dynamical mean-field theory

DOS density of states

DS devil's staircase

EDC energy distribution curve

FFT fast Fourier transform

GGA generalized gradient approximation

IMT insulator-metal transition

LDA local density approximation

LDOS local density of states

LEED low-energy electron diffraction

LHB lower Hubbard band

LT low temperature

ML monolayer

PES photoemission spectroscopy

QPI quasiparticle interference

QPP quasiparticle peak

RT room temperature

SIP substrate-induced peak

SOC spin-orbit coupling

STM scanning tunneling microscopy

STS scanning tunneling spectroscopy

UHB upper Hubbard band

UHV ultra-high vacuum

VCA variational cluster approach

WS Wigner-Seitz

XPS X-ray photoemission spectroscopy

XVCA extended variational cluster approach

1. Introduction

Strongly correlated electron systems in a frustrated geometry are one of the most fruitful research areas in contemporary condensed matter physics. Through the interplay of different low-energy degrees of freedom, exciting phenomena such as unconventional superconductivity, spin-liquid physics or unusual magnetism have been observed [1–3]. A profound understanding of the underlying physics is a crucial part for the development of future devices, e.g., in the field of spintronics or quantum computation.

In this thesis, a class of such correlated materials, namely group IV triangular adatom lattices, is investigated. They consist of 1/3 monolayer (ML) of group IV adatoms on a semiconductor substrate such as Si(111), Ge(111), or SiC(0001) and form a $\sqrt{3} \times \sqrt{3}R30°$ reconstruction with respect to the substrate at room temperature (RT) as seen in Fig. 1.1(a). In literature, they are also called α-phases and therefore will be referred to as $\sqrt{3}_\alpha$-systems in this thesis, e.g., $\sqrt{3}_\alpha$-Sn/Si(111). Due to the reduced coordination in two dimensions and the dilute coverage of adatoms, electronic correlations naturally account for an integer part of the low-energy physics in these material systems. At lower temperature, a transition to a 3×3 reconstruction was observed for some representatives. While it was originally thought to be caused by a phonon-driven charge density wave (CDW) [4], newer studies hold charge order (CO) driven by electronic correlations responsible for the observed behavior [5, A1], e.g., in the charge-ordered phase of $\sqrt{3}_\alpha$-Pb/Si(111) illustrated in Fig. 1.1(b).

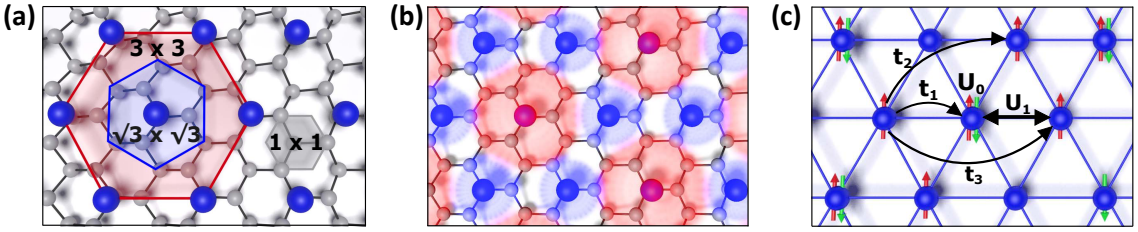

Fig. 1.1.: **(a)** Structure model of group IV triangular lattices with adatoms (blue) and substrate atoms (grey). The WS unit cells of typical reconstructions is depicted. **(b)** Model illustration of a 3×3 charge-ordered state as found, e.g., in $\sqrt{3}_\alpha$-Pb/Si(111). **(c)** Important parameters for the theoretical treatment of correlated triangular lattices: hopping parameters t_1, t_2, t_3, local Coulomb repulsion U_0, and nearest-neighbor Coulomb repulsion U_1. Image adapted from Ref. [A1].

The attractiveness of group IV triangular lattices lies in their simple structure and tunability. While three of the adatoms' valence electrons are saturated in covalent sp^3-type back-

bonds with the substrate, the correlated state consists of only a p_z-type orbital occupied by a single electron with an uncompensated spin. This renders these artificial lattices convenient model systems to investigate the versatile physics of frustrated and correlated materials in an easily accessible environment, thereby potentially providing insights that might be hidden in complex setups that are closer to technical applications. The simple structure is also beneficial for theoretical studies since the principally limited computer resources can thus be better focused on the solution of the many-body problem. This is oftentimes done within the Hubbard model that captures the interplay of Coulomb correlations and electron hopping between different sites as illustrated in Fig. 1.1(c). By combining different substrates and adatoms, many relevant parameters such as spin-orbit coupling (SOC), lattice constant, or dieletric screening can be varied which leads to a plenitude of possible ground states [6–8].

An essential ingredient for the rich physics found in these systems is the frustrated geometry induced by the triangular coordination of adatom sites. On a bipartite lattice, antiferromagnetism or CO can be easily realized. However, triangular lattices are frustrated, i.e., the energy between all lattice sites cannot be minimized simultaneously as depicted in Fig. 1.2(a) using the example of antiferromagnetism. In order to deal with the frustration, different kinds of magnetic patterns may arise, e.g., a 120° Néel order as in Fig. 1.2(b). For group IV triangular lattices, it turned out that a row-wise antiferromagnetic order, see Fig. 1.2(c), is favored when longer-range hopping is included into the calculations [9, 10]. However, tracing the boundary between these two realizations is a delicate task since it can depend on the theoretical method used, or certain parameters therein [8]. Including the nearest-neighbor Coulomb interaction U_1 into theoretical considerations makes the phase diagram even more complex and results in a multitude of possible charge- or spin-ordered ground states [11]. Frustration can also lead to a situation where the spins form a resonant valence bond state or do not order at all [2]. Such spin-liquid or quantum-paramagnetic phases are rarely observed in actual materials. It is a coveted state of matter since it is associated with exotic phenomena such as fractional excitations [12]. Indications for such behavior have been found in layered crystals with a triangular lattice [13, 14] but the group IV systems studied within this thesis are in principle candidate materials as well [6].

Another possible route towards exotic states of matter is the usage of heavy atoms to boost the effects of SOC. For oxide materials it was shown that the interplay of electronic correlations and strong SOC can result in the appearance of uncommon ground states [15]. A general effect of SOC on the electronic properties of group IV triangular lattices has already been verified experimentally by the detection of two spin-polarized bands in $\sqrt{3}_\alpha$-Sn/Si(111) via spin-resolved angle-resolved photoemission spectroscopy (ARPES) [16]. SOC is also predicted to trigger unusual magnetic states such as the formation of skyrmions in the presence of a magnetic field [17, 18] but a comprehensive study regarding the effects of SOC such as the review in Ref. [15] is missing so far.

The set of possible ground states in pristine group IV triangular lattices is limited by the available material systems and their respective correlation parameters shown in Fig. 1.1(c).

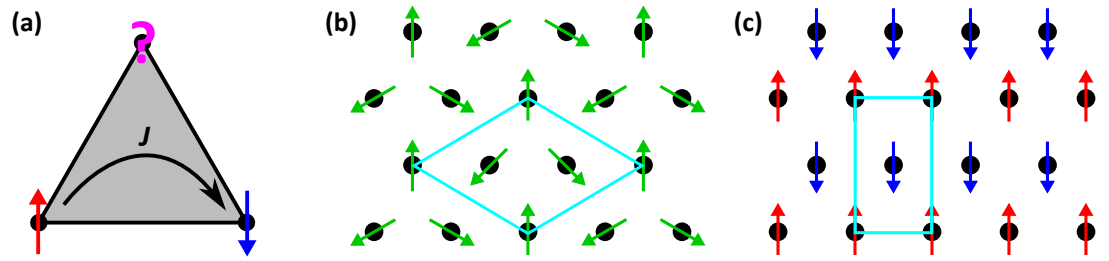

Fig. 1.2.: **(a)** Sketch to illustrate the concept of frustration. In a triangular lattice antiferromagnetic order cannot be satisfied for all sites at once. **(b)** Possible antiferromagnetic ground state in a triangular lattice: The 120° Néel order. It features a $\sqrt{3} \times \sqrt{3}R30°$ reconstruction (unit cell with teal lines) with respect to the lattice hosting the spins. **(c)** Another antiferromagnetic ground state that is supposedly realized in some group IV triangular lattice: The row-wise antiferromagnetic order. It comes in three possible rotational domains, each featuring a $1 \times \sqrt{3}$ reconstruction (unit cell again in teal lines).

However, it can be significantly extended by investigating systems also away from half filling. This renders the whole problem more challenging both experimentally and theoretically since it requires a suitable doping mechanism and the possible ground states are then distributed on a multi-dimensional phase diagram. Depending on the band filling, different types of magnetic order including antiferro-, para-, and ferromagnetic phases are expected [19]. Their formation might suppress an insulator-metal transition (IMT) as predicted in a simple Hubbard model, see Sect. 3.1.

On the other hand, if metallization can be achieved at low temperatures, superconductivity can emerge [6]. In this regard, it might also be worthwhile to start from a charge-ordered state since it was found that a frustrated CO allows for a wide range of the strength of electron-phonon coupling leading to the formation of superconductivity [20]. A correlated system that becomes superconducting at low temperatures immediately provokes associations with the well-known CuO_2-based high-temperature superconductors. However, triangular lattices might be even more interesting to study because they can potentially host chiral superconductivity with $d + id$ symmetry due to their lattice geometry [21]. Already very small doping concentrations below 5 %[1] might be sufficient to drive a triangular lattice into such a topologically non-trivial state [22]. Since it features characteristic edge states within the superconducting gap [23], a detailed knowledge of those boundaries is required for an experimental verification. So far, candidate materials for superconductivity are mostly limited to complex layered systems such as $Na_xCoO_2yH_2O$ or organic compounds like κ-(BEDT-TTF)$_2$X [1, 24, 25]. Group IV triangular lattices might therefore help to solve basic questions regarding this topic. Since they have a very simple structure, tracking the essential ingredients for an unconventionally superconducting state is facilitated. Calcula-

[1] In the context of this thesis doping concentrations are often given in percent, where 1 % doping means that there are 0.01 additional electrons or holes in the respective state compared to the half-filled case.

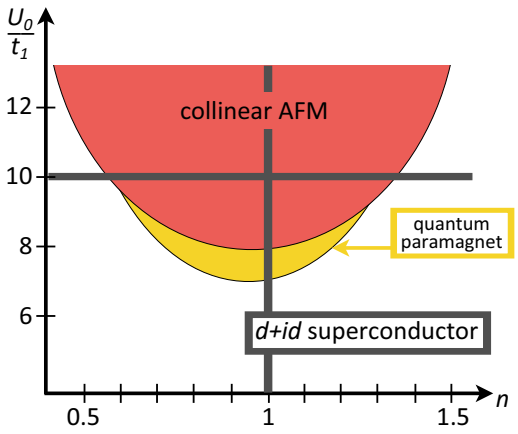

Fig. 1.3: Phase diagram of a triangular lattice in the plane of band filling n vs. on-site correlation strength U_0/t_1 using the hopping parameters t_1, t_2 and t_3 of $\sqrt{3}_\alpha$-Sn/Si(111) and $U_1 = 0$. The calculations are based on the variational cluster approach. So far, results are only available for the shaded cross while the rest of the diagram is based on the knowledge of related phase diagrams. It shows that doping might be a suitable method to drive a group IV triangular lattice into a superconducting or quantum-paramagnetic state. Taken from Ref. [26]

tions within our collaboration with the group of S. Rachel also showed the possibility of a superconducting or quantum-paramagnetic state specifically for $\sqrt{3}_\alpha$-Sn/Si(111), see Fig. 1.3. In this case, doping is required to drive the system out of the collinear antiferromagnetic state.

Finally, first promising experimental results were already achieved by doping the $\sqrt{3}_\alpha$-Sn/Si(111) system via charge transfer mediated by a strongly doped substrate [27]. The authors found typical hallmarks of superconductivity in scanning tunneling spectroscopy (STS) experiments at 0.5 K, namely a gap at the Fermi level that can be fitted using the Dynes formula [28] and closes both with increasing temperature or an increasing magnetic field. Furthermore, a spatial modulation within differential conductivity maps that could be associated with the appearance of flux quanta was detected. In this approach, the maximum doping concentration is limited by the substrate. For optimal doping, which potentially requires alternative doping approaches, a critical temperature for superconductivity as high as 65 K has been predicted [29]. Very recent calculations suggest that the superconductivity could be f-wave or chiral p-wave, depending on the doping level [30].

The goal of this thesis is to fabricate different group IV triangular lattices via molecular-beam epitaxy and to analyze them with regard to their structural and electronic properties. Supported by theoretical calculations conducted in various collaborations, results are classified and put into relation with the findings of peer researchers. To gain novel insights, three approaches were pursued:

- Extending the family of group IV triangular lattices by realizing new systems as done for $\sqrt{3}_\alpha$-Sn/SiC(0001) [A6].
- Investigating the ground states of known materials in great detail to extract information that was previously overlooked, see Ref. [A1].
- Investigating doped group IV triangular lattices via ARPES and scanning tunneling microscopy (STM), two techniques that have hardly been applied in this regard.

Outline of this thesis

In Chap. 2 the crystallography and preparation of substrates as well as the crystallography of group IV triangular lattices is presented. In Chap. 3 the Hubbard model which is a standard framework for the theoretical treatment of correlated electron systems, and the extended variational cluster approach (XVCA), a numerical technique for its approximate solution, are introduced. Chap. 4 gives an overview of STM, photoemission spectroscopy (PES), and low-energy electron diffraction (LEED) which are the experimental methods used to analyze the properties of the group IV traingular lattices. Chap. 5 deals with the substrate-boosted electronic correlations in $\sqrt{3}_\alpha$-Sn/SiC(0001). In Chap. 6 evidence for correlation-driven CO in $\sqrt{3}_\alpha$-Pb/Si(111) is provided. Furthermore, a comparison with the mosaic $\sqrt{3}_\gamma$-Pb/Si(111) is made. In Chap. 7 the results of potassium-doping of $\sqrt{3}_\alpha$-Sn/Si(111) are presented.

2. Group IV adatom systems on semiconductor substrates

A basic requirement for the growth of two-dimensional triangular lattices is a suitable substrate with 120° rotational symmetry on one of its surfaces. Furthermore, it should be semiconducting with a sufficiently large bandgap since any states in close vicinity of the Fermi level will obscure the low energy properties of the adatom system to be investigated. Group IV semiconductors fulfill both of these requirements and have been successfully used as templates for decades [31–33]. In the context of this thesis, Si(111) and SiC(0001) are utilized. They differ in their lattice constant and dielectric constant which allows us to study systems with different effective correlation strength as the electron hopping and the electronic screening are modified, respectively. However, other substrate surfaces, especially Ge(111), have proven to be a suitable choice as well [4, 5].

2.1. The (111) surface of silicon

Silicon crystallizes in the cubic diamond structure and has a bulk band gap of 1.12 eV at RT [34]. When truncated perpendicular to the [111] direction one usually ends up with a bilayer of Si atoms terminating the cleavage plane which offers one dangling bond per surface unit cell, see Fig. 2.1(a). Note that a separation of the silicon bilayer leads to an energetically unfavorable surface termination due to the higher amount of dangling bonds and will therefore not be treated any further here. The bilayer terminated 1×1 surface of Si(111) is, however, also not stable. Instead, a truncated wafer would form π-bonded chains of dangling bonds leading to a 2×1 reconstruction at RT [35, 36]. At elevated temperatures this surface undergoes an irreversible transition to a 7×7 reconstruction [37] which is the desired surface for the epitaxy of the adatom systems described in this thesis. Upon adsorption of atoms the substrate surface is again reorganized meaning that an adatom system is ultimately residing on an effective 1×1 surface of Si(111).

Si(111) has a surface lattice constant of 3.84 Å and offers three threefold symmetric adsorption sites, see Fig. 2.1(b): directly above a Si atom of the top layer (T_1), directly above a Si atom of the second layer (T_4), and on a hollow site in between the Si atoms of the bilayer (H_3). The index in these nomenclatures accounts for the number of nearest neighbors an adatom has got when its position has relaxed vertically. Although this is usually not fulfilled exactly for the T_4 position since bond distances may vary in different surface systems, the notation has still prevailed [38]. Two-dimensional adatom systems

present on the substrate surface can be categorized by their coverage in fractions of MLs. In this work, we adapt the common definition from literature on systems of this kind where one ML is defined as one adatom per 1×1 unit cell of the substrate surface which amounts to 7.84 atoms/nm^2 in the case of Si(111). This also means that some dense adatom systems can have a coverage slightly above one ML and still have all atoms at a similar height.

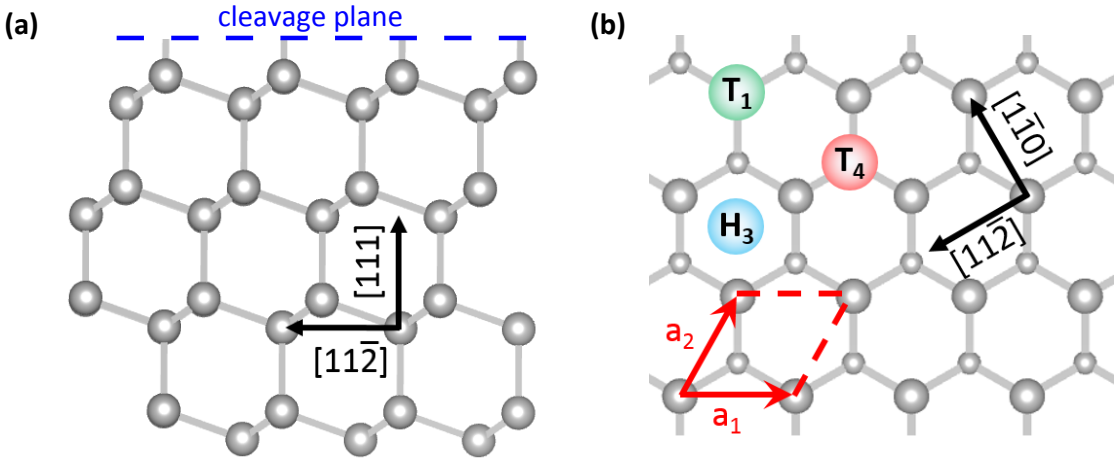

Fig. 2.1.: **(a)** Ball-and-stick model of Si illustrating the stacking in bilayers. The bilayer terminated surface offers one dangling bond per surface unit cell. **(b)** Ball-and-stick model of the 1×1 Si(111) surface. Atoms in the top layer are depicted bigger than atoms in the second layer, all other atoms are not drawn here. The most important adsorption sites T_1, T_4 and H_3 are indicated. Red arrows mark a surface unit cell with its primitive lattice vectors in the (111) plane. Model created using VESTA [39].

The electronic properties measured on such a (sub-)monolayer system can be altered by the doping of the substrate [40, 41]. In order to study these effects, different charges of Si(111) wafers were used. Details on dopant type, resistivity and nominal physical dimensions of all substrate charges are summarized in Tab. 2.1. However, researchers found that electron acceptors are accumulated in the topmost layers of Si(111) during high-temperature anneals [42–44] which are an inevitable part of the substrate preparation. The relevant mechanisms are incorporation of p-dopants that are naturally present in most ultra-high vacuum (UHV) chambers or the diffusion of doping atoms already preexisting in the substrate. Consequently, n-doped substrates feature an inversion layer at the surface region that is essentially undoped or even slightly p-doped. This can lead to small differences between results from various groups because the effective doping in the topmost layers of the substrate therefore also depends on the annealing history and contamination of the respective UHV chambers with potential hole dopants.

Description	Dopant	ρ [Ωcm]	c [$10^{16}\,\mathrm{cm}^{-3}$]	Size [mm^3]
lowly p-doped	Boron	$0.1 - 1$	$3 - 20$	$10 \times 2.5 \times 0.380$
highly p-doped	Boron	< 0.02	> 300	$10 \times 2.5 \times 0.525$
highly n-doped	Phosphorus	< 0.01	> 400	$10 \times 2.5 \times 0.500$

Tab. 2.1.: Overview of the different Si(111) substrates used within this thesis. The resistivity ρ at RT is provided by the supplier. The dopant concentration c is calculated according to Ref. [45].

Surface termination procedure

Before a substrate is introduced into the UHV system, there is a sequence of preparative steps that has to be performed ex situ, i.e., in a clean environment at ambient conditions. Most of the substrates are covered with a protective photoresist which is removed by two successive treatments with acetone in an ultrasonic bath for two minutes each. For wafer charges without the cover this step may be omitted. Subsequently, contaminants like hydrocarbons are removed by another sequence of rinsing with highly pure organic solvents in an ultrasonic bath, namely acetone, 2-propanole and methanol for two minutes each. Remnants of methanol are finally blown off using dry nitrogen.

After this treatment, the substrate is still covered with a persistent oxide layer which is removed in situ, i.e., in the UHV system. The process starts off with a thorough degas at $T = 600°\mathrm{C}$ for several hours by driving a current through the substrate (direct current heating) until the base pressure in the UHV system has almost recovered. The temperature is monitored through a quartz glass window via a Keller CellaTemp PA20 pyrometer set to an emissivity of 40 %. This method is tailored to offer an easily accessible and reproducible temperature reading, even though it might not capture the true temperature of the examined specimen. Within this thesis, all temperatures during an anneal are monitored this way. After the degas is finished, the substrate is flashed to temperatures close to the melting point of silicon, i.e., $T \approx 1400°\mathrm{C}$. This removes the oxide layer and supplies enough thermal energy to facilitate the formation of the desired 7×7 reconstruction during the cool-down to RT [37]. For substrates with high dopant concentration, a slow cool-down from $T = 950°\mathrm{C}$ to RT over a period of 20 min turned out to be necessary for decent results. Once cooled back to RT, the substrate is ready for epitaxy. Direct current heating often does not result in a spatially uniform temperature distribution on the sample. In this case, the pyrometer is focused on the hottest section of the substrate. This yields well prepared areas big enough for PES and therefore a fortiori big enough for STM experiments. This is not only true for Si(111), but for all substrates and adatom systems examined within the scope of this thesis.

2.2. The (0001) surface of silicon carbide

Silicon carbide can be found in diverse modifications, so-called polytypes, which differ in the way bilayers are aligned with respect to each other resulting in different bandgaps. Polytypes are labeled by the number of bilayers within a unit cell and their crystal symmetry (H – hexagonal, C – cubic). Here, silicon-terminated 4H-SiC was used, see Fig. 2.2(a), where a unit cell contains four bilayers along the [0001] direction[2] resulting in a bandgap of 3.26 eV at RT [47]. Although the actual crystal structures of various substrates can be different, e.g., a diamond cubic lattice for Si and a hexagonal lattice for 4H-SiC, the respective surfaces hosting the triangular adatom lattice are almost identical as can be seen by comparing the (0001) surface of 4H-SiC in Fig. 2.2(b) with the Si(111) surface shown before in Fig. 2.1(b). The SiC(0001) wafers used here are Si-terminated, i.e., the Si atoms offer one dangling bond each while the C atoms below are completely saturated. This results in the same adsorption sites T_1, T_4 and H_3 already known from the Si(111) surface, but with a surface lattice constant of $a = 3.08\,\text{Å}$, i.e., about 20 % smaller than for Si(111). The wafers are cut in pieces of $10\,\text{mm} \times 2.5\,\text{mm} \times 0.330\,\text{mm}$ and doped with nitrogen leading to a nominal resistivity of $0.1 - 0.3\,\Omega\text{cm}$ at RT which corresponds to a dopant concentration of roughly $10^{17}\,\text{cm}^{-3}$ [48].

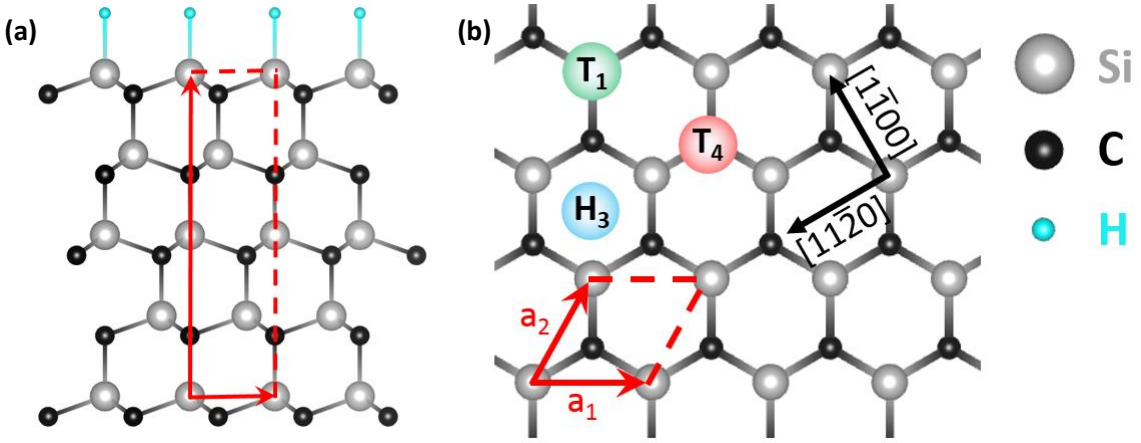

Fig. 2.2.: Ball-and-stick models of 4H-SiC. **(a)** View on the $(1\bar{1}00)$ plane. The projected unit cell illustrates that the stacking order is repeated only after four bilayers. One bilayer contains a layer of Si atoms and C atoms, respectively. The crystal is H-terminated at the [0001] surface which is achieved by a hydrogen etching procedure described in the main text. **(b)** View on the 1×1 reconstructed (0001) plane. Without the H-termination one finds a situation very similar to Si(111) in terms of the surface unit cell and the most important adsorption sites T_1, T_4 and H_3. For clarity, only the topmost bilayer is depicted here, other atoms are not drawn. All models created using VESTA [39].

[2]For hexagonal crystals the notation of the Miller-Bravais indices which contains four entries is employed [46].

Surface termination procedure

Experiments in the past suffered from the poor electrical contact between the substrate and the molybdenum clamps of the sample holder. Roughening this contact area on the substrate using a diamond stud and wrapping it with rhodium foil was found to minimize these problems as the Schottky barrier is reduced [49]. Subsequently, the ex situ cleaning process based on organic solvents and already described in section 2.1 for Si(111) is applied to the SiC substrates, too. Just as Si(111), the SiC(0001) substrates are still covered with an oxide layer after this process.

Simple flashing of SiC(0001) at elevated temperatures of about 950°C does indeed remove the oxide layer, but unfortunately goes along with a $\sqrt{3} \times \sqrt{3}$ reconstruction that prohibits the epitaxial growth of the adatom lattices of interest here [50]. The reconstruction forms when Si atoms from Si-rich islands diffuse on the surface and occupy T_4 positions [51]. In principle, this yields a triangular lattice $\sqrt{3}_\alpha$-Si/SiC(0001) which would make a proper candidate system for this study but so far results with a low defect rate were only achieved if additional Si atoms have been offered during the heating cycle, e.g., using a Si evaporation source [52, 53]. This reconstruction cannot be turned into the desired 1×1 reconstructed surface with a temperature or sputtering treatment, so a more elaborate approach is necessary.

To recover the 1×1 reconstruction we developed a hydrogen etching procedure as outlined in Ref. [A5] where the hot SiC substrate is exposed to a hydrogen atmosphere. Hydrogen molecules in close proximity to the hot sample can be cracked thermally allowing the atomic hydrogen to bond to any available dangling bond. Substrate atoms at the edge of a bilayer terrace or at its apex offer more dangling bonds making the described hydrogenation more likely. If a sufficient amount of hydrogen is offered, gaseous CH_4 and SiH_4 will form and remove the respective atom from the substrate. During the development of this procedure, it turned out that etching products which are redeposited and decomposed in the presence of the hot substrate are a significant source of defects, necessitating the two-step cycle described in the following.

Once a clean substrate is introduced into the dedicated etching chamber, it is degassed at 950°C for about an hour. Thereby, the $\sqrt{3}\times\sqrt{3}$ reconstruction described above is generated on the surface. Afterwards the hydrogen etching process is initiated. Therefor the chamber is filled with hydrogen and helium (7.0 purity) in equal parts until a total pressure of 950 mbar is reached. During the etching process the atmosphere in the chamber is continuously exchanged with a steady inflow of 2 standard liters per minute for both gases to effectively remove the etching products CH_4 and SiH_4 from the chamber. A control valve linked to a scroll pump is keeping the pressure in the etching chamber constant at the previously set value. By adding He to the process atmosphere, the total etching rate is lowered while etching products are still removed effectively, thereby reducing their redeposition rate onto the sample surface. The etching process itself consists of a subtly tuned temperature cycle shown in Fig. 2.2(a). The temperature is again monitored via a Keller CellaTemp PA20

pyrometer, for SiC the emissivity is set to 85 %. The first etching step at 1250°C is aimed to have a high etching rate to quickly reduce the roughness of the SiC surface. In the second etching step at 1180°C, the etching rate is a lot lower, decreasing the amount of etching products present for redeposition. Finally the sample is cooled down to about 1000°C over a time span of five minutes, thereby gradually reducing the etching rate to zero. After the power supply is turned off, the chamber is evacuated again. This whole process is also described in more detail in Ref. [A5].

The procedure results in the formation of ample terraces with clear edges which is the preferred morphology for the growth and examination of two-dimensional (2D) lattice systems, see Fig. 2.3(b). On the surface, the dangling bond of each Si atom is saturated by hydrogen, see Fig. 2.2(a). An STM image of the sample therefore shows a 1×1 reconstructed surface as seen in Fig. 2.3(c). Just like the oxide cover, this hydrogen layer could not be removed thermally without a surface reconstruction. The gain of the etching process is a decreased surface roughness and the fact that merely a well-defined single layer of hydrogen covers the SiC surface. Only very recent experiments indicate that a thermal removal without any reconstruction might be possible after all [54].

2.3. Triangular adatom systems on group IV semiconductor substrates

When evaporating a group IV element on a substrate of the kind described above with a coverage in the (sub-)monolayer regime, there are oftentimes multiple phases and reconstructions possible, and their appearance delicately depends on the thermodynamical conditions during the growth process. The phase which is aimed for in this thesis is a triangular lattice with a coverage of 1/3 ML with respect to the underlying substrate, forming a $\sqrt{3} \times \sqrt{3}\,R30°$ reconstruction on its surface. In a triangular lattice with a coverage of 1/3 ML, only one third of the T_4 positions is occupied with an adatom leading to three different rotational domains. A structure model of such a $\sqrt{3}_\alpha$-system was already shown in Fig. 1.1(a). Note that the phases described by those terms in literature can sometimes be poorly defined or even interchanged, see, e.g., Refs. [55] and [56].

In principle, all three high-symmetry sites (and technically any other site, too) shown in Figs. 2.1(b) and 2.2(b) are available for adsorption. However, it turned out that the T_4 site is preferred in all group IV triangular lattices investigated so far regarding this matter. For some representatives, e.g., $\sqrt{3}_\alpha$-Sn/Ge(111) or $\sqrt{3}_\alpha$-Sn/Si(111), which can be grown on scales big enough to allow for spatially averaging techniques, this has been verified experimentally using surface X-ray diffraction or X-ray standing waves [57–59]. For other systems like $\sqrt{3}_\alpha$-Pb/Si(111) or $\sqrt{3}_\alpha$-Si/SiC(0001) the T_4 position has been found to be energetically more favorable than other relevant positions based on density functional theory (DFT) calculations [55, 60]. If a group IV adatom resides on a T_4 site, three of its four valence electrons are saturated in backbonds with the substrate while the remaining

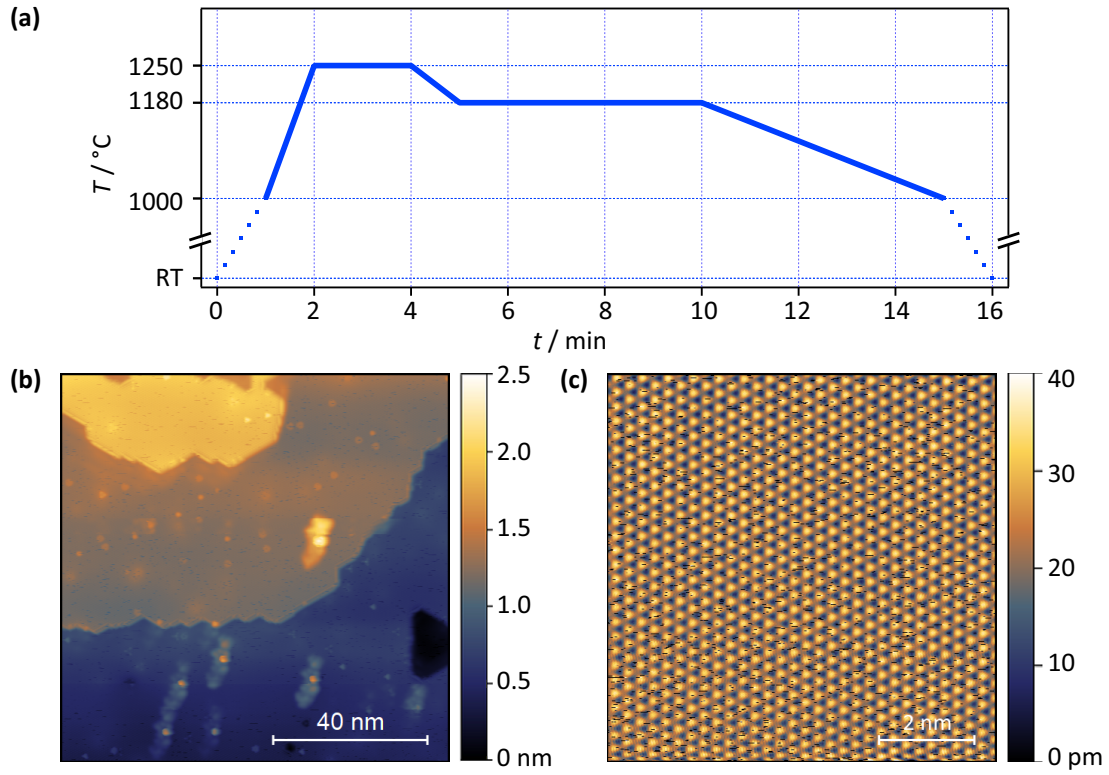

Fig. 2.3.: **(a)** Temperature profile driven during the Hydrogen etching of a SiC substrate. **(b)** Large scale STM image of hydrogen terminated 1×1 SiC(0001) image featuring four terraces separated by steps with a height of 4.93 Å, which – within the margin of error – corresponds to half the height of a unit cell which nominally amounts to 5.02 Å. **(c)** Close-up STM image of a defect-free area where the hydrogen atoms are atomically resolved. The black scars are related to occasional tip instabilities. Both STM images are measured at $V = 3\,\mathrm{V}$, $I = 50\,\mathrm{pA}$ and $T = 77.5\,\mathrm{K}$.

one forms a dangling bond pointing perpendicularly away from the substrate surface. These dangling bonds have mainly p_z character [61] and form a two-dimensional electron system (2DES) which is prone to electronic correlations due to the large distance between adatoms. This thesis is centered around the investigation of said state.

With a well-established structure model, a simple atomic configuration, and a correlated state that only originates from a single orbital, the various $\sqrt{3}_\alpha$ phases are ideal benchmark systems for theoretical simulations with different kinds of many-body calculation techniques. On the experimental side, the choice of different combinations of adatoms and substrates can be used realize a plenitude of related material systems in order to examine the effects correlation strength, SOC, or doping in an otherwise well-defined environment.

3. Theoretical concepts and calculation techniques

In this chapter the Hubbard model which is widely used to describe the physics of correlated electron systems is introduced. Although it cannot be solved exactly for an arbitrary system, many approximate calculation techniques have been developed. One of them is the XVCA, a many-body calculation technique applied in Chap. 6. The key concepts thereof are outlined, too.

3.1. Electronic correlations and the Hubbard model

In conventional band theory the classification of a material as a metal or an insulator is tied to the density of states at the Fermi level at zero temperature. If the topmost occupied band is only partly filled, it provides states at the Fermi level making the material a metal. Otherwise the Fermi level is located in a band gap and the material must be an insulator where all bands are either empty or completely filled. For the simplest case without any orbital degeneracy, filling a band requires two electrons. However, in the 1930s researchers realized that band theory fails for some materials, especially for some transition-metal oxides that have a partly-filled $3d$ shell and nevertheless behave as strong insulators [62]. Mott and Peierls pointed out that the electrostatic interaction between electrons might be responsible for the observed behavior [63]. These materials are nowadays known as Mott insulators.

In the following years Mott extended his arguments by considering a model system which consists of a regular array of hydrogen atoms with electrons in the $1s$ orbital [64]. Band theory predicts a half-filled metallic Bloch state independent of the interatomic distance a. An increasingly large distance between atoms would only affect the associated bandwidth as depicted in Fig. 3.1(a). This is against common sense and eventually leads to absurdity if a gets much bigger than typical interatomic distances. In his paper, Mott already noted important parameters that determine the occurrence of a metal-insulator transition: the aforementioned bandwidth, electronic screening, and doping of the system with additional carriers. All these aspects will be relevant for the 2D triangular lattices described in this thesis.

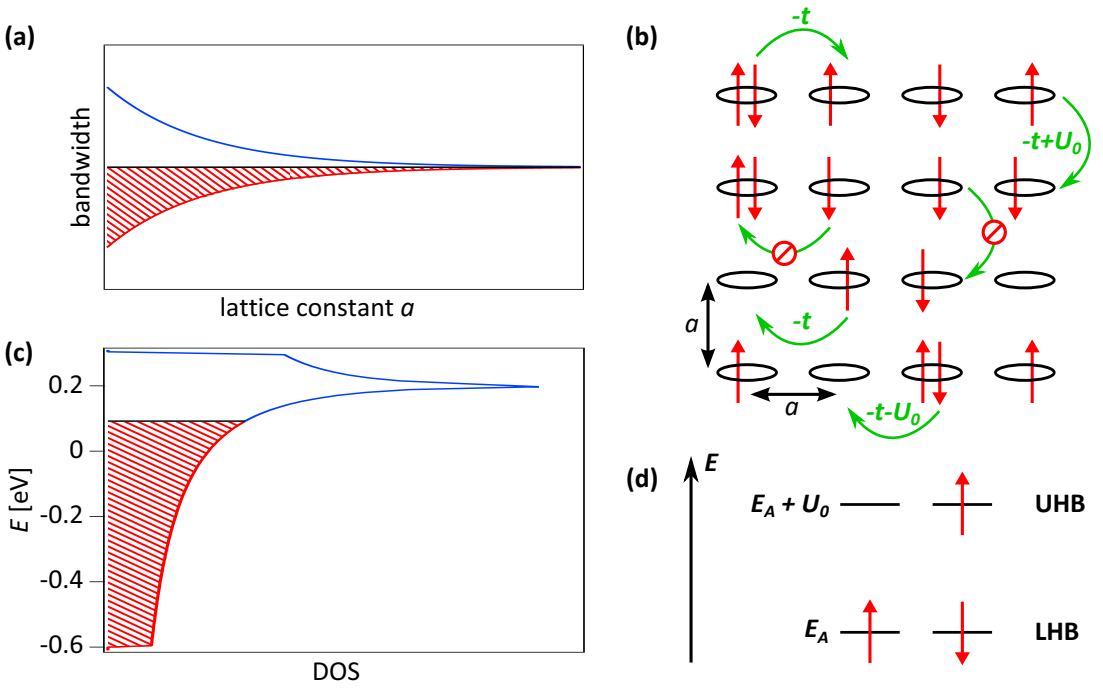

Fig. 3.1.: **(a)** Bandwidth of an array of monovalent atoms as a function of the lattice constant a. According to band theory the system can always be described as a metal with half filling. Picture adapted from Ref. [64]. **(b)** Sketch to illustrate the energetics of the Hubbard Hamiltonian in Eq. 3.1. Hopping to a neighboring site releases an energy t, while double occupancy requires an energy U_0. The Pauli principle forbids two electrons with the same spin to reside on a single site. **(c)** DOS of the Hubbard model for a 2D triangular lattice in the band limit, i.e., $U_0 = 0$. For the hopping matrix element $t = 0.1\,\text{eV}$ was chosen for simplicity. The shaded area indicates half filling. **(d)** Electronic structure of the Hubbard model for any lattice in the atomic limit, i.e., $t = 0$. The UHB is separated from the LHB by the Coulomb interaction U_0. Each "band" can host a maximum of one electron per site.

The Hubbard model

Mott's preliminary studies eventually lead to the development of the Hubbard model that ever since provides a theoretical framework for the description of correlated materials. It was named after J. Hubbard who introduced it in 1963 [65] but similar concepts were simultaneously published by other researchers, too [66, 67]. Accordingly, a correlated electron system is governed by two opposing terms: firstly, a kinetic term that favors a delocalization of electrons into itinerant Bloch waves, thereby decreasing the total energy of the system. Secondly, a Coulomb term that captures the effects of electron-electron interactions. If two electrons reside – in accordance with the Pauli principle – in the same orbital, they experience the mutual Coulomb repulsion which increases the total energy of the system. This term favors a single occupation of sites and therefore a localization of electrons in a

half-filled system. The two terms are captured in the Hubbard Hamiltonian:

$$H = H_{\text{band}} + H_{\text{Coulomb}} = -t \sum_{<i,j>\sigma} (c_{i\sigma}^{\dagger} c_{j\sigma} + c_{j\sigma}^{\dagger} c_{i\sigma}) + U_0 \sum_i \hat{n}_{i\uparrow} \hat{n}_{i\downarrow}. \tag{3.1}$$

Here, t denotes the tight-binding hopping matrix element and U_0 the effective Coulomb repulsion[3] between two electrons located at the same site. Only hopping events of electrons with spin σ between nearest neighbor sites $<i,j>$ are included in the summation. The operator $c_{i\sigma}$ ($c_{i\sigma}^{\dagger}$) annihilates (creates) an electron at lattice site i with spin $\sigma = \uparrow, \downarrow$, and the occupation number of a site i by electrons with spin σ is given by $\hat{n}_{i\sigma}$. Possible and forbidden hopping events and their respective energetic balance are summarized in a sketch of the aforementioned model system in Fig. 3.1(b).

Despite its simple form, the Hubbard model cannot be solved exactly for an arbitrary system [68]. In order to get some preliminary insight, we will investigate two limiting cases as outlined in Ref. [69].

- The band limit: $H = -t \sum_{<i,j>\sigma} (c_{i\sigma}^{\dagger} c_{j\sigma} + c_{j\sigma}^{\dagger} c_{i\sigma})$.
  For $U_0 = 0$, we are just left with a tight-binding Hamiltonian in second quantization. For a 2D triangular lattice, this results in a metallic Bloch band with a density of states (DOS) as depicted in Fig. 3.1(c). The shaded area indicates the occupied states for half filling.

- The atomic limit: $H = \sum_i \left(E_A \sum_\sigma \hat{n}_{i\sigma} + U_0 \hat{n}_{i\uparrow} \hat{n}_{i\downarrow} \right)$.
  In the case of no hopping, it is convenient to add the energy of the atomic level E_A to the Hamiltonian. In Eq. 3.1 it is set to zero without loss of generality. The resulting energy spectrum consist of two levels separated by U_0 as depicted in Fig. 3.1(d). A single electron on any site has the energy E_A. If another electron of opposite spin is added to the same site, it is assigned the energy $E_A + U_0$ since the mutual Coulomb repulsion has to be compensated for. The two energy levels are usually referred to as lower Hubbard band (LHB) and upper Hubbard band (UHB), respectively. Each band can only host a maximum of one electron per site, thus they are not bands in the sense of a Bloch picture. Instead, the existence of the UHB is tied to the occupation of the LHB. As hopping between sites is suppressed, the system is an insulator.

The simple Hubbard model discussed above only contains on-site Coulomb interactions U_0 and nearest-neighbor hopping t. In realistic systems, however, electrons can also be significantly affected by the Coulomb repulsion U_1 mediated by electrons on neighboring sites. Furthermore, the kinetic term can be modeled more accurately by including hopping events beyond the nearest neighbors. This can be accommodated by additional terms in the Hubbard Hamiltonian, resulting in an extended Hubbard model:

[3] In a solid, the bare Coulomb interaction is affected by electronic screening which yields a lower, effective Coulomb repulsion.

$$H = \sum_{<i,j>\sigma} t_{ij}(c^{\dagger}_{i\sigma}c_{j\sigma} + c^{\dagger}_{j\sigma}c_{i\sigma}) + U_0 \sum_i \hat{n}_{i,\uparrow}\hat{n}_{i,\downarrow} + U_1 \sum_{<i,j>} \hat{n}_i\hat{n}_j. \tag{3.2}$$

Here, $t_{ij} \equiv t_{|i-j|} \equiv t_n$ is the hopping to an nth neighboring atom. The parameters t_n are usually determined by other band structure calculation techniques such as DFT.

The Hubbard model in infinite dimensions

Although the limiting cases discussed previously provide a basic understanding of the effects of electron correlations, a more elaborate approach is required to investigate actual materials where both t and U_0 have a finite value. In this case, the system has to be described within Landau's Fermi liquid theory [70, 71]. Accordingly, correlated electrons are regarded as well-defined *quasiparticles*, i.e., electrons dressed in a cloud of virtual excitations. The low-energy spectrum consists of a coherent quasiparticle peak (QPP) and an incoherent part that is identified as the LHB and UHB, respectively. An important progress in the modeling of correlated systems was made when researchers found that the Hubbard model can be mapped onto a single-impurity Anderson model that can be solved exactly for infinite dimensions within the dynamical mean-field theory (DMFT) [72, 73]. This opened the possibility to study Mott IMTs within the Hubbard model since both the QPP and the Hubbard bands are equally well described within DMFT [74].

Accordingly, there are two possible mechanisms to drive the transition from a Mott insulator to a metallic state. By decreasing the ratio U_0/t, delocalization of electrons is favored leading to a bandwidth-induced IMT. In a phase diagram of filling vs correlation strength such as Fig. 3.2(a) this corresponds to a transition along a vertical arrow. Alternatively, adding or removing electrons from a half-filled band also results in a metallic state. In Fig. 3.2(a), this phase transition is described by a horizontal arrow. For an ideal system, the shaded area represents a metallic phase but carriers can be easily localized through interactions with the lattice [75]. The evolution of the spectral function for filling- and bandwidth-controlled Mott IMTs is depicted in Fig. 3.2(b). Metallization is always associated with the formation of a QPP, i.e., a coherent state at the Fermi level that can be described by Fermi liquid theory. Quasiparticles have been observed in correlated 2D triangular lattices both by ARPES [77] and STS [40].

The existence of local moments is an essential feature of the Mott-insulating state [68]. At low temperatures, these moments usually establish some kind of order to minimize the total energy of the system. For $U_0 \gg t$ the Hubbard model can even be mapped on a Heisenberg model [69]:

$$H = -J \sum_{<i,j>} S_i S_j = -4t^2/U_0 \sum_{<i,j>} S_i S_j \,, \tag{3.3}$$

where J is the exchange coupling constant and S_i are the quantum-mechanical spin operators. This is relevant for many group IV triangular lattices because the distances between

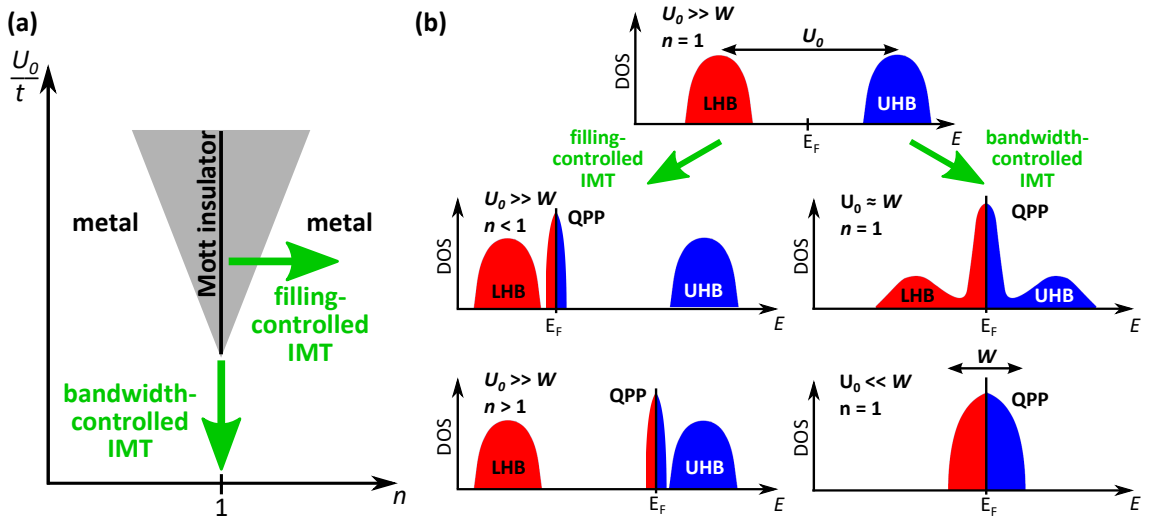

Fig. 3.2.: **(a)** Phase diagram for Mott insulator-metal transitions. The axes are the number of electrons per site n and the effective correlation strength U_0/t. In an ideal system the shaded area represents a metallic phase but carriers are easily localized due to interactions with the lattice. Image adapted from Ref. [75]. **(b)** Spectral functions of a correlated electron system for different values of n and U_0/t simulated within DMFT. Relevant features are the LHB, the UHB, and the QPP. In the case of weak correlations (bottom right spectrum) the bandwidth W is directly linked to the hopping matrix element t via the lattice geometry. For strong correlations (top center spectrum) the separation of the Hubbard bands is given by U_0. Images adapted from Refs. [74, 76].

adatoms are bigger than typical atomic spacings in crystals due to the dilute grid defined by the substrate. As a consequence the associated hopping integrals are relatively small placing many representatives into the regime of strong or intermediate correlations [7] which can lead to the emergence of a magnetic state as described in Eq. 3.3. Under consideration of the nearest neighbor Coulomb interaction U_1, however, CO is a possible ground state of 2D triangular lattices as well.

3.2. Extended variational cluster approach

As the 2D Hubbard model cannot be solved exactly for an arbitrary system, a plethora of many-body calculation techniques has been developed in recent years to find approximate solutions numerically, see, e.g., Ref. [78]. In the context of this thesis, an extension to the variational cluster approach (VCA) [79, 80] was used to calculate ground states and spectral functions of group IV triangular lattices. This XVCA has been designed and exerted by S. Rachel and M. Laubach. It extends the conventional VCA by including the nearest-neighbor Coulomb interaction which is necessary to be sensitive to charge-ordered ground states. In the following the key concepts of the XVCA will be briefly presented.

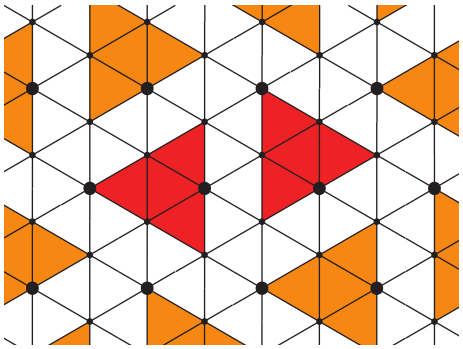

Fig. 3.3: Lattice tiling for a triangular lattice with a 6-site cluster and its mirror cluster (both in red) used in the XVCA to calculate ground states and spectral functions of $\sqrt{3}_\alpha$-Pb/Si(111) and $\sqrt{3}_\alpha$-Sn/Si(111) in Sect. 6.2.5. The remaining lattice is captured by replicas (orange) of the two original clusters. Adapted from Ref. [A1].

In order to cope with the many-body problem, the infinite lattice is constructed from a series of clusters with a defined size and shape. The concept of the VCA is to solve the Hubbard model exactly within a reference system and use these results to calculate the grand potential Ω of the full system. Usually the reference system is chosen to be an array of these clusters without any mutual coupling. Here, a supercluster consisting of two 6-site clusters with a different orientation as seen in red color in Fig. 3.3 is selected. It is sufficiently big to capture the most important possible ground states of group IV triangular lattices which were already described in Chap. 1, e.g., spiral or row-wise antiferromagnetism or CO. The whole triangular lattice can be tiled by replicas (orange color) of the original supercluster. A detailed compilation of challenges for this specific problem can be found in the supplementary material of Ref. [A1].

In the reference system the grand potential Ω', the self-energy Σ' and the Green's function G' are calculated exactly. Different symmetry-breaking ground states can be introduced as a Weiss field, see, e.g., Ref. [81], and consequently examined regarding their energy balance in a variational approach. The grand potential of the full system can then be calculated as [79]:

$$\Omega[\Sigma'] \quad = \Omega' + \mathrm{Tr}\ln\left(G_0^{-1} - \Sigma'\right)^{-1} - \mathrm{Tr}\ln(G')\,, \tag{3.4}$$

where G_0 is the Green's function of the system without any electronic correlations. The functional $\Omega[\Sigma']$ is only approximated in the sense that the parameter space of possible self-energies is restricted to the self-energies of the reference system. By using different correlation parameters and different Weiss fields, a phase diagram of the investigated system can be established based on energy considerations. Once the ground state is known, the Green's function G_{XVCA} which is indispensable for the calculation of the spectral function can be calculated [79]:

$$G_{\mathrm{XVCA}}^{-1} = G'^{-1} - V. \tag{3.5}$$

Here V is a matrix that describes the inter-cluster hopping. The VCA has been successfully applied to various correlated systems [82, 83] and has proven to be well suited to capture the complex physics in 2D triangular lattices [8, 84].

4. Experimental methods

In group IV triangular lattices, a p_z orbital sticks out of the surface and – given the band gap of the substrate is big enough – is energetically separated from other states. This makes PES and STM ideal probes for the analysis of this state. They will therefore be the two main analysis techniques used in the framework of this thesis. In the following, the underlying theoretical framework and a short description of the instrumentation of the two respective methods is presented. In addition, a brief review of LEED will be given.

4.1. Photoemission spectroscopy

Photoemission spectroscopy is a generic term comprising a variety of techniques based on the photoelectric effect which was discovered in 1887 by H. Hertz [85]. Accordingly, electrons are emitted from a material that is irradiated with electromagnetic radiation of sufficient energy. It was later explained by A. Einstein in 1905 under consideration of the quantum nature of light [86]. With the pioneering work done by K. Siegbahn in the development of electron spectrometers [87], PES became an integral method to analyze the chemical composition of a specimen. Nowadays, the availability of elaborate detectors and light sources with tunable energy has made PES one of the most versatile techniques to examine the electronic properties of crystalline solids.

4.1.1. Basic principle and instrumentation

In order to generate a free photoelectron, the energy $\hbar\omega$ of an incoming photon must be sufficiently high to overcome both the binding energy E_B of an electron in its initial state and the barrier between the Fermi energy and the vacuum level which is the work function Φ. Any remaining energy is transformed into kinetic energy E_{kin} of the photoelectron, which results in the following energy balance:

$$E_{kin} = \hbar\omega - \Phi - E_B. \tag{4.1}$$

This relation is also illustrated in the energy diagram in Fig. 4.1(a). In the spectrum of photoelectrons the sample states are subject to different broadening effects. While the finite lifetime of the core hole and the limited experimental resolution lead to a Lorentzian and Gaussian broadening, respectively, screening or electronic correlations can give rise to more complex lineshapes. If a metallic sample is investigated, the spectrum is cut off at the Fermi

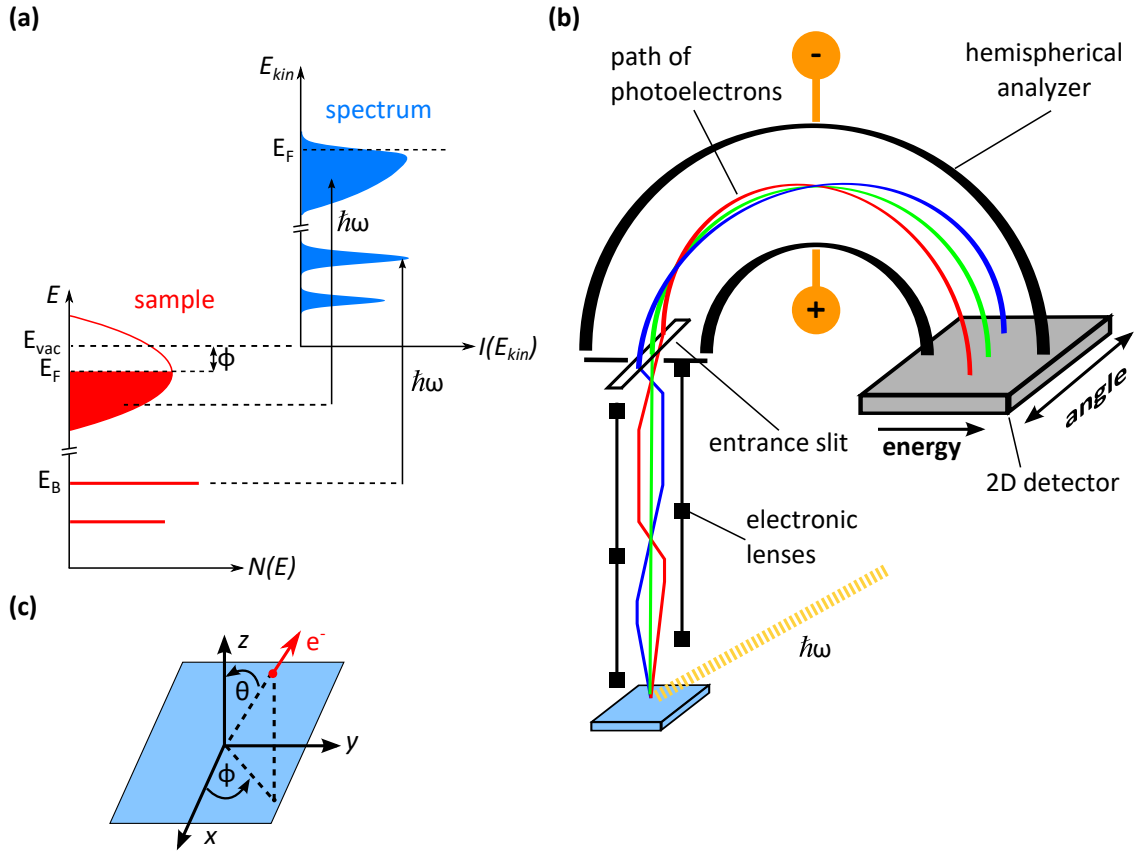

Fig. 4.1.: **(a)** Energetics of a PES experiment. Photons translate the electronic structure of a sample into a spectrum of photoelectrons. Image adapted from Ref. [88]. **(b)** Sketch of the key components of a hemispherical analyzer to detect energy and emission angle of the photoelectrons coming from a sample. **(c)** Sample geometry for the calculation of the photoelectron momentum.

level by the Fermi-Dirac distribution which determines the occupation of states based on the temperature.

In order to perform a successful PES experiment, three essential components have to be provided. Firstly, a light source with photons in a narrow energy range is required. In this thesis, the examination of the valence band is conducted using a gas discharge lamp operated with helium which provides the intense HeI emission line at 21.2 eV. For the examination of core levels, an x-ray tube with an aluminum anode which provides an intense emission line at an energy of 1486.6 eV is used. Both these lines are accompanied by several satellites with smaller intensity. While some PES setups use a monochromator to suppress these additional lines, they are not removed in the light sources used in the context of this thesis, thereby granting a higher photon flux in return. The second requirement is an energy analyzer to measure the kinetic energy of the photoelectrons. Nowadays a hemispherical analyzer as shown in Fig. 4.1(b) is part of most PES setups. On their way

to the entrance slit of the analyzer photoelectrons pass a series of electronic lenses that act as a tunable retardation field and arrange electrons according to their emission angle. The electric field inside the hemisphere is tailored to only let electrons with a kinetic energy in a certain range around a previously set pass energy go through the analyzer. By sweeping the retardation field, a spectrum over the whole available energy range can be recorded. In this thesis, the photoelectrons are counted via a 2D detector consisting of a microchannel plate, a fluorescent screen and a CCD camera. While the axis perpendicular to the entrance slit is reserved for the detection of photoelectrons with different kinetic energy, the parallel axis contains information about their emission angle. This way a complete set of variables $\{E_{kin}, K_x, K_y, K_z\}$ is recorded for each detected electron. The components of the photoelectron momentum K in vacuum can be calculated as follows:

$$K_x = \frac{1}{\hbar}\sqrt{2mE_{kin}}\sin\theta\cos\phi. \tag{4.2}$$

$$K_y = \frac{1}{\hbar}\sqrt{2mE_{kin}}\sin\theta\sin\phi. \tag{4.3}$$

$$K_z = \frac{1}{\hbar}\sqrt{2mE_{kin}}\cos\theta. \tag{4.4}$$

The definition of directions and angles is found in Fig. 4.1(c) and m is the mass of the electron. Photoelectrons from different angles can also be accessed by rotating or tilting the sample. Finally, the two previously mentioned components, namely, a light source and the analyzer, have to be integrated into an UHV system. Only a low ambient pressure ensures a clean sample surface during experiments and an unhindered travel of photoelectrons from the sample to the detector.

4.1.2. Theoretical description of photoemission

Photoemission is a quantum-mechanical one-step process converting an electronic state within a solid into a state with one electron less and a photoelectron outside the sample. Theoretically, it can be modeled as an inverted LEED experiment [89]. Since this is both challenging and not very illustrative, said one-step process is conveniently split up into three independent parts to form the three-step model of photoemission. The three steps are:

A) excitation of an electron into a bulk final state

B) transport of the photoelectron to the surface

C) transition of the photoelectron into vacuum.

In the following some important aspects of each individual step will be presented based on Refs. [88–90].

A) Excitation of an electron into a bulk final state

The photo-excitation of an initial N-particle state $|\Psi_i^N\rangle$ into a final N-particle state $|\Psi_f^N\rangle$ can be described within time-dependent perturbation theory. The transition rate $w_{i\to f}$ due to the interaction with a photon is given by Fermi's golden rule:

$$w_{i\to f} = \frac{2\pi}{\hbar}|\langle\Psi_f^N|\hat{H}_{int}|\Psi_i^N\rangle|^2\delta(E_f^N - E_i^N - \hbar\omega). \tag{4.5}$$

The delta function ensures the conservation of energy between E_f^N, E_i^N, and $\hbar\omega$ which are the energies of the final state, the initial state and the photon, respectively. The interaction operator $\hat{H}_{int}$ describing the perturbation through the photon field is given by

$$\hat{H}_{int} = -\frac{e}{2m}(\vec{A}\hat{\vec{p}} + \hat{\vec{p}}\vec{A}) + \frac{e^2}{2m}\vec{A}^2 = -\frac{e}{m}\vec{A}\hat{\vec{p}}. \tag{4.6}$$

Here, $\vec{A}$ is the vector potential of the electromagnetic field, $\hat{\vec{p}}$ the momentum operator and e the elementary charge of the electron. The second equality sign of this equation requires several approximations to be made. As typical light intensities in lab-based experiments are not high enough to trigger a significant contribution of non-linear processes, they can be neglected by dropping the summand proportional to $\vec{A}^2$. For PES experiments with vacuum-ultraviolet light, $\vec{A}$ is constant on the scale of atomic dimensions in which case $[\hat{\vec{p}}, \vec{A}] = i\hbar\nabla\vec{A} \approx 0$ holds. However, this approximation might not be justified at the surface where the electromagnetic field might vary more abruptly. Effects of this surface photoemission, however, have only been observed in very specific scenarios where they lead to an asymmetric line shape of bulk transitions [91, 92]. Therefore, it can be neglected here although this thesis deals with the examination of surface systems. In second quantization the interaction operator can be expressed as

$$\hat{H}_{int} = -\frac{e}{m}\sum_{k,n}\langle k|\vec{A}\hat{\vec{p}}|n\rangle c_k^\dagger c_n = \sum_{k,n} M_{k,n}c_k^\dagger c_n \tag{4.7}$$

where c_n annihilates an electron in a Bloch state $|n\rangle$, $c_k^\dagger$ creates a photoelectron with wave vector $\vec{k}$ and $M_{k,n} = \langle k|\vec{A}\hat{\vec{p}}|n\rangle$ is the transition matrix element. For the further considerations, it is convenient to add the photoelectron subspace to the initial and final state, respectively. Before the excitation, the photoelectron state is empty and reads $|0_{PE}\rangle$. The final state is factorized into a photoelectron state $|E_k\rangle$ and a remaining state $|\Psi_{f,s}^{N-1}\rangle$ which is the s^{th} eigenstate of the $N-1$ electron system.

$$|\Psi_i^N\rangle = |0_{PE}\rangle|\Psi_i^N\rangle. \tag{4.8}$$

$$|\Psi_f^N\rangle = |E_k\rangle|\Psi_{f,s}^{N-1}\rangle. \tag{4.9}$$

Here it is assumed that the photoelectron is instantly removed from the ionization site and does not interact with the remaining system. This is known as the *sudden approximation* which is valid if the energy of the photoelectron is bigger than 10 eV [93], i.e., for all PES

experiments within this thesis. By putting Eqs. 4.7 – 4.9 into Eq. 4.5 and summing over all possible final states s the total photocurrent $I(\vec{k},\omega)$ can be calculated.

$$\begin{aligned} I(\vec{k},\omega) &= \frac{2\pi}{\hbar}\sum_s |\langle\Psi_{f,s}^{N-1}|\langle E_k|\sum_{k',n} M_{k',n}c_{k'}^\dagger c_n|0_{PE}\rangle|\Psi_i^N\rangle|^2\delta(E_{f,s}^{N-1}-E_i^N+E_k-\hbar\omega) \\ &= \frac{2\pi}{\hbar}\sum_s |\sum_n M_{k,n}\langle\Psi_{f,s}^{N-1}|c_n|\Psi_i^N\rangle|^2\delta(E_{f,s}^{N-1}-E_i^N+E_k-\hbar\omega) \\ &= \frac{2\pi}{\hbar}\sum_n |M_{k,n}|^2 A^-(\vec{k},E_k-\hbar\omega). \end{aligned} \tag{4.10}$$

Here

$$A^-(\vec{k},E_k-\hbar\omega) = \sum_s |\langle\Psi_{f,s}^{N-1}|c_n|\Psi_i^N\rangle|^2\delta(E_{f,s}^{N-1}-E_i^N+E_k-\hbar\omega) \tag{4.11}$$

is the electron-removal part of the spectral function that is probed in ARPES. It describes the probability to remove an electron with momentum $\vec{k}$ and binding energy $E_k-\hbar\omega$ from the system. In experiment, the spectral function is weighted with the dipole matrix element $|M_{k,n}|$ that captures effects of the measurement geometry, photon frequency and polarization.

In case of an uncorrelated electron system, photoionization will create a final state $|\Psi_{f,s_0}^{N-1}\rangle$ that is an eigenstate of the remaining system so that $|\langle\Psi_{f,s}^{N-1}|c_n|\Psi_i^N\rangle|^2=\delta_{ss_0}$. Consequently, the spectral function collapses to a delta function and the PES signal only consists of a series of delta peaks at the single-particle energies $E^0(\vec{k})$:

$$A^0(\vec{k},E) = \frac{1}{\pi}\delta(E-E^0(\vec{k})). \tag{4.12}$$

For a correlated electron system, the possible final states are not an eigenstate of $|\Psi_i^{N-1}\rangle$. The system must then be described as a Fermi liquid, see Sect. 3.1. Using a Green's-function method it can be shown that the spectral function then reads:

$$A(\vec{k},E) = \frac{1}{\pi}\frac{\mathrm{Im}\Sigma(\vec{k},E)}{[E-E^0(k)-\mathrm{Re}\Sigma(\vec{k},E)]^2+[\mathrm{Im}\Sigma(\vec{k},E)]^2}\,. \tag{4.13}$$

Differences between a non-interacting electron system and a Fermi liquid are captured within the complex self energy $\Sigma(\vec{k},E)$. This has several consequences for the one-electron removal spectra[4] measured in ARPES:

- The PES signal cannot be described by a series of delta functions anymore but by a coherent main line, the QPP, and an incoherent part forming a smooth background. The distribution of spectral weight for a given $\vec{k}$ depends on the overlap $|\langle\Psi_{f,s}^{N-1}|\Psi_i^{N-1}\rangle|^2$.
- The quasiparticle energy is renormalized from $E^0(\vec{k})$ to $E^0(\vec{k})+\mathrm{Re}\Sigma(\vec{k},E)$. This also implies a renormalization of the effective mass.

[4] Equivalent arguments are valid for the one-electron addition spectra that would be the result of an inverse PES experiment.

- The lifetime of the quasiparticle is finite and determined by $\mathrm{Im}\Sigma(\vec{k}, E) \propto E^2$.
- Spectral weight can also be found beyond the Fermi vector, depending on the relative weight Z_k of the QPP.

As the total spectral weight is conserved, the spectral function can be separated into a coherent pole part representing the QPP and the incoherent smooth part A_{inc} without any poles:

$$A(\vec{k}, E) = \frac{1}{\pi} \frac{Z_k \mathrm{Im}\Sigma(\vec{k}, E)}{[E - E^0(k) - \mathrm{Re}\Sigma(\vec{k}, E)]^2 + [\mathrm{Im}\Sigma(\vec{k}, E)]^2} + (1 - Z_k) A_{inc}. \tag{4.14}$$

For strongly correlated electron systems the quasiparticle may be suppressed completely and the spectrum just consists of a smooth incoherent part.

B) Transport of the photoelectron to the surface

During their propagation to the surface, the photoelectrons interact with the crystal mostly through inelastic scattering, e.g., through the excitation of plasmons or interband transitions. As the former is almost independent of the examined material, the inelastic mean free path of photoelectrons can be compiled into a universal curve over a wide energy range [94]. Some of the scattered electrons might still reach the detector but their angle and energy can no longer be connected to their initial state. Instead, they form a continuous background in the resulting spectrum. Since detailed information about the scattering rates of electrons associated with certain lines are often not available, a pragmatic approach introduced by Shirley is widely used [95]. By assuming that the background intensity I_{bg} is proportional to the intrinsic signal I_0 at higher kinetic energies, a background from any given spectrum can be calculated in an iterative manner. The electronic states in the focus of this thesis are originating from a 2DES located at the surface of semiconductor samples. Therefore, this second step of the model is expected to have only a small influence on the respective photoelectrons because they are already close to the surface once they are created. However, spectra also include the electronic structure of the hosting substrate in which the considerations above are fully applicable.

C) Transition of the photoelectron into vacuum

When the photoelectron crosses the boundary of the crystal and escapes into the vacuum, the translational symmetry in the sample plane is not disturbed, i.e., the respective component of the photoelectron momentum inside the sample $\overrightarrow{k_{||}}$ is conserved and identical to the corresponding component in vacuum $\overrightarrow{K_{||}}$. This is important for ARPES of 2D materials since $\overrightarrow{k_{||}}$ can be directly calculated from a measurement and the full dispersion of a 2D system can be retrieved (see Fig. 4.1(c) for definition of directions and angles):

$$k_{||} = K_{||} = |\overrightarrow{K_x} + \overrightarrow{K_y}| = \frac{1}{\hbar}\sqrt{2mE_{kin}}\sin\theta. \tag{4.15}$$

On the other hand, $\overrightarrow{k_\perp}$ is not conserved due to the energy barrier at the sample surface and there are no easy ways for its determination. However, this thesis deals with the examination of the electronic structure of sub-monolayer adatom systems which do not have a dispersion along $k_\perp$ due to their dimensionality. Therefore, knowledge of $k_\perp$ is not necessary to understand the measured PES data. Bulk bands from the substrate which are subject to a dispersion along $k_\perp$ are naturally part of ARPES spectra but not analyzed in this regard since they originate from common semiconductors whose dispersion is well known and not relevant for the interpretation.

4.2. Scanning tunneling microscopy and spectroscopy

In 1982, G. Binnig and H. Rohrer demonstrated the capabilities of their newly developed scanning tunneling microscope by presenting topographic images of surfaces on an atomic scale [96]. Thereby, they greatly extended the possibilities of sample characterization down to single atoms that was previously restricted to field emission microscopy with its very limited choice of samples. Their breakthrough, which was awarded with the Nobel prize in 1986, opened a new pathway for the exploration of surfaces on a local level that is now used in laboratories all over the world.

4.2.1. Basic principal and instrumentation

The basic principle of STM is to bring a metallic tip close to the surface of a sample and apply a bias voltage between the two so that electrons can tunnel through the vacuum barrier. For a one-dimensional potential barrier of width s and effective height Φ, the transmission coefficient T for particles with mass m is given by [97]

$$T \propto \exp(-2\chi \cdot s) = \exp\Big(-2 \cdot \frac{\sqrt{2m\Phi}}{\hbar} \cdot s \Big). \tag{4.16}$$

Due to the exponential dependence of the transmission coefficient – and therefore the tunneling current – from the barrier width, even small variations of the distance between two separated electrodes can be monitored with great accuracy, granting STM a very high resolution perpendicular to the sample plane. If absorption of mechanical vibrations and shielding from electrical noise are done properly, it can be as high as one picometer. In order to visualize individual atoms, a high lateral resolution is required as well. In an ideal scenario the tip used as an electrode only has a single atom at its apex. This way the majority of the tunneling current is mediated by this atom or even by one of its orbitals. Effectively, only the sample area directly below the apex atom is probed resulting in atomic resolution.

In order to put such a resolution into effect, the tip must be controlled with likewise high precision. This is achieved with a set of calibrated piezo-electric crystals that allow to position the tip along the sample coordinates. Fig. 4.2 shows a simplified circuit diagram

for a STM setup capable of performing such an experiment. The potential between tip and sample is offset from equality by a voltage V. The resulting tunneling current is measured using a current amplifier (AMP) that is connected to a feedback control unit which controls the movement of the tip via the voltages applied to the piezo-electric crystals. The control unit is also linked to a computer where all data is processed and visualized.

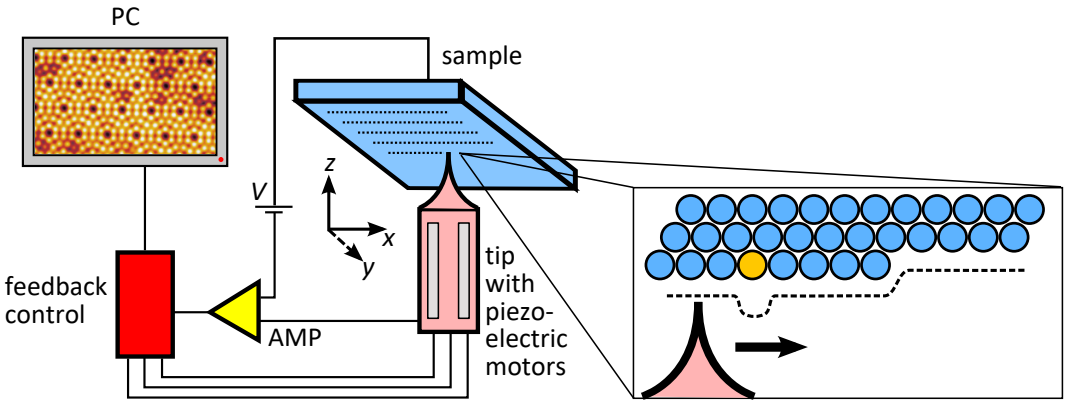

Fig. 4.2.: Key components of a STM setup. By applying a voltage V between sample and tip, electrons can tunnel across the vacuum barrier. The tunneling current is measured using an amplifier (AMP). In constant-current mode the tunneling current acts as a control variable to readjust the position of the tip via a feedback control unit. The data is then processed and visualized on a computer. The enlargement on the right side shows a step in the atomic stacking and an atom with different electronic properties (green) which both influence the tunneling current and therefore the path of the tip.

Most commonly, STM is performed in the constant-current mode. To start such a measurement a combination of tunneling voltage V and current I, the setpoint, is chosen. Then the tip is gradually moved towards the sample surface until the previously specified tunneling current is reached. Once the approach was successful, the sample surface is scanned in a pixel-wise manner. During the measurement the distance between tip and sample is constantly readjusted by a control loop to keep the tunneling current at the predefined value. As depicted in the enlargement on the right side of Fig. 4.2, the constant current contour $z(x, y)$ recorded by the tip contains information about both the surface corrugation and the electronic properties of individual atoms. Therefore, the interpretation of a pertinent tunneling map is not trivial.

4.2.2. Theoretical description of the tunneling current

The theoretical description of the tunneling current in this section will provide a deeper insight into how electronic properties of the tunneling electrodes affect the STM experiment. The derivation closely follows the one given in Ref. [98]. Using time-dependent perturbation

theory the tunneling current I between two electrodes can be calculated as[5]

$$I = \frac{2\pi e}{\hbar} \sum_{\mu,\nu} \Big\{ \underbrace{f(E_\mu)[1 - f(E_\nu + eV)]}_{\text{A}} - \underbrace{f(E_\nu + eV)[1 - f(E_\mu)]}_{\text{B}} \Big\} |M_{\mu,\nu}|^2 \delta(E_\nu - E_\mu). \quad (4.17)$$

Here, V is the applied tunneling voltage, $f(E)$ is the Fermi distribution and $|M_{\mu,\nu}|$ is the tunneling matrix element between unperturbed electronic states Ψ_μ of the tip and Ψ_ν of the sample with energies E_μ and E_ν, respectively. The delta function ensures the conservation of energy, thereby restricting the considerations to elastic tunneling. The formula includes both tunneling from the tip to the sample (term A) and vice versa (term B). Assuming small bias voltages ($V \lesssim 10\,\text{meV}$) and low temperatures, Eq. 4.17 collapses to [99]

$$I = \frac{2\pi e^2 V}{\hbar} \sum_{\mu,\nu} |M_{\mu,\nu}|^2 \delta(E_\mu - E_F) \delta(E_\nu - E_F). \quad (4.18)$$

The tunneling matrix element is given by [100]

$$M_{\mu,\nu} = \frac{-\hbar^2}{2m} \int d\vec{S} (\Psi_\mu^* \nabla \Psi_\nu - \Psi_\nu \nabla \Psi_\mu^*) \quad (4.19)$$

where the integral has to be evaluated for an arbitrary surface that lies entirely inside the vacuum barrier. Since it is in general not known, further approximations are required. Tersoff and Hamann [99, 101] modeled a tip with a spherical apex with a local curvature of radius R centered at r_0 as depicted in Fig. 4.3. Assuming the tip wave function does not have an angular dependence, they calculated the tunneling current to be

$$I \propto V n_t(E_F) e^{2\chi R} \sum_\nu |\Psi_\nu(\vec{r_0})|^2 \delta(E_\nu - E_F). \quad (4.20)$$

Here, $n_t(E)$ is the DOS of the tip at energy E, and χ is the decay rate for an effective local potential barrier height Φ as already introduced in Eq. 4.16. The expression

$$n_s(E_F, \vec{r_0}) = \sum_\nu |\Psi_\nu(\vec{r_0})|^2 \delta(E_\nu - E_F) \quad (4.21)$$

is the local density of states (LDOS) of the sample at the Fermi level. For low bias voltage and in the s-wave approximation, a constant current measurement thus represents a landscape of constant LDOS at the Fermi level.

However, real STM experiments are usually performed at different bias voltages and with a tip that is not guaranteed to satisfy the s-wave approximation introduced by Tersoff and Hamann. Thus, the simple picture derived above must be extended. If it is assumed that

[5] Strictly speaking, the calculation of the total tunneling current using discrete states requires a Kronecker delta instead of the Delta function shown here. For formal consistency with Refs. [98, 99], we will stick to their formulation in the following derivation.

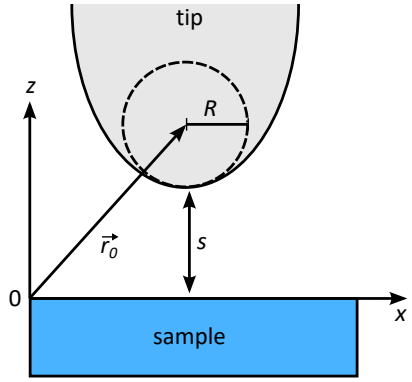

Fig. 4.3: Tersoff-Hamann model of a tip with a spherical apex with radius R centered at r_0. The minimum distance between tip and sample is s. Adapted from Ref. [99].

the wave functions $\Psi_{\mu,\nu}$ and their energy eigenvalues $E_{\mu,\nu}$ are not distorted due to the presence of an electric field at finite bias, the tunneling current can be written as

$$I \propto \int_0^{eV} n_t(\pm eV \pm \epsilon) n_s(\epsilon, \vec{r_0}) d\epsilon. \tag{4.22}$$

The LDOS of the sample can be further simplified since the wave functions decay exponentially in the direction perpendicular to the sample plane leading to

$$I \propto \int_0^{eV} n_t(\pm eV \mp \epsilon) n_s(\epsilon) T(\epsilon, eV) d\epsilon. \tag{4.23}$$

In a Wenzel-Kramers-Brillouin approximation the transmission coefficient $T(\epsilon, eV)$ can be written as

$$T(\epsilon, eV) = exp\left\{-2(s+R)\left[\frac{2m}{\hbar^2}\left(\frac{\Phi_t + \Phi_s}{2} + \frac{eV}{2} - \epsilon\right)\right]^{1/2}\right\} \tag{4.24}$$

where Φ_s (Φ_t) denotes the sample (tip) work function. In this form, the exponential dependence of the transmission coefficient from the width and the height of the barrier as expected from basic quantum mechanics, see Eq. 4.16, can be verified.

The consequences of Eq. 4.23 and 4.24 for an actual STM experiment are depicted in Fig. 4.4 for the investigation of (a) unoccupied and (b) occupied sample states. The DOS of the tip is assumed to be constant. An inspection of Eq. 4.24 reveals that the transmission coefficient is biggest for the electrons with the highest energy ϵ. For $V > 0$ electrons tunneling from the Fermi level of the tip to sample states which are $\epsilon = eV_1$ above the Fermi level are contributing most to the tunneling current. Therefore, variations in the sample DOS can effectively influence the tunneling current upon changes of the bias voltage. On the other hand, the transmission coefficient is always biggest for electrons tunneling from the Fermi level of the sample for $V < 0$. Additional sample states contributing to tunneling when increasing the absolute value of the bias voltage thus only make a small contribution to the overall tunneling current. This is called the *leading edge effect*.

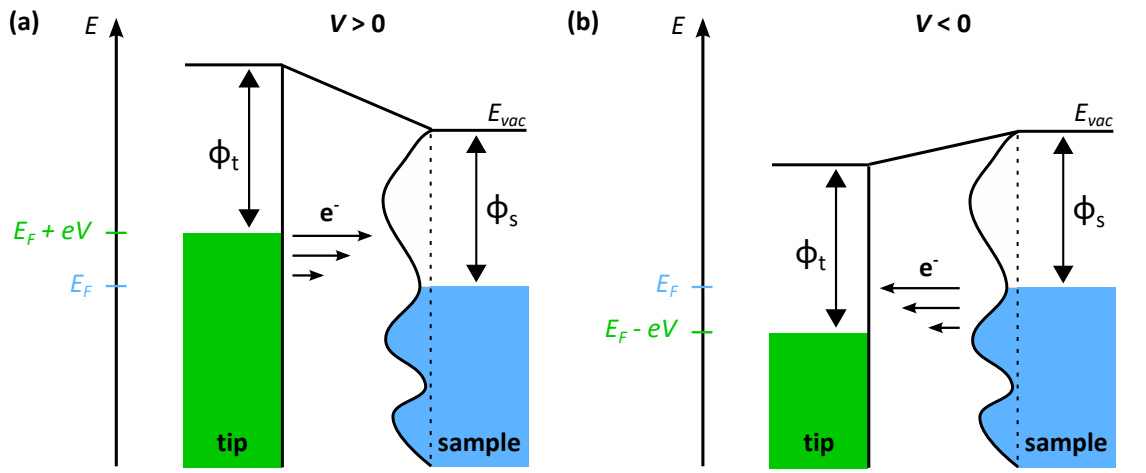

Fig. 4.4.: **(a)** Schematic for electrons tunneling from the tip to the sample, i.e., $V > 0$. The transmission coefficient is largest for electrons tunneling from the Fermi level of the tip and decreases for smaller energies as indicated by the length of the respective arrows. Φ_s (Φ_t) denotes the sample (tip) work function. **(b)** Same schematic for the situation $V < 0$ where electrons tunnel from the occupied states of the sample into empty tip states. As indicated by the arrows, electrons from the Fermi level of the sample make the largest contribution to the tunneling current.

4.2.3. Scanning tunneling spectroscopy

As delineated in the previous section, the tunneling current is sensitive to both the DOS of the electrodes and the sample corrugation. While this makes the interpretation of topographic STM images more challenging, it can be exploited to collect spectroscopic information. Differentiating Eq. 4.23 leads to

$$\frac{dI}{dV} \propto e n_t(0) n_s(eV) T(eV, eV) + \int_0^{eV} n_t(\pm eV \mp \epsilon) n_s(\epsilon) \frac{dT(\epsilon, eV)}{dV} d\epsilon. \tag{4.25}$$

As the transmission coefficient $T(\epsilon, eV)$ is smooth and monotonic, any structure found in the derivative of the tunneling current can usually be attributed to a variation of the DOS of one of the tunneling electrodes. If one can also verify that n_t is constant due to a careful tip preparation[6] with regard to a lack of eminent electronic states in the voltage region of interest, the derivative of the tunneling current is only proportional to the DOS of the sample:

$$\frac{dI}{dV} \propto n_s(eV). \tag{4.26}$$

It should be noted that the LDOS measured with STS does not directly correspond to the spectral function measured in PES. If the electrons can be assumed to tunnel between

[6] In the framework of this thesis, the electronic properties of the tip were tested on a clean Ag(111) crystal before any spectroscopic measurements.

the tip and the sample one by one, STS in principle measures the spectral function [102], i.e., both techniques are sensitive to electronic correlations. Pertinent effects have been found, e.g., in twisted-bilayer graphene where tunneling spectra can be heavily distorted compared to the non-interacting case for partial band filling [103]. However, a principle difference arises from band structure effects through a k-dependent apparent tunneling barrier:

$$\Phi(k) = \Phi(0) + \frac{\hbar^2}{2m} k_{||}^2 \tag{4.27}$$

where $\Phi(k)$ is the effective tunneling barrier height for electrons with momentum $\hbar k$. This means that electrons are preferably tunneling from the Γ point of the 2D Brillouin zone (BZ). Especially the group IV triangular lattices are a good example that the comparability of STS and PES is still not universally understood, see, e.g., Refs. [104, 105]. In order to perform a STS experiment, there are two different techniques available which will be introduced in the following.

Current imaging tunneling spectroscopy (CITS)

In a CITS measurement the tip is stabilized at a chosen setpoint and the feedback loop is turned off, i.e., the tip–sample separation remains constant. By sweeping the bias voltage, a spectrum $I(V)$ is measured. This can be repeated at different positions of the sample to produce a dI/dV map that shows the electronic properties of the sample spatially and energetically resolved. The derivative can either be calculated numerically or using a Lock-in technique as illustrated in Fig. 4.5(a). A small sinusoidal voltage with amplitude V_{mod} is added to the bias voltage. The frequency ω is chosen to be far away from typical noise frequencies and their higher orders, and above the cutoff frequency of the feedback loop. A Taylor expansion of the tunneling current up to the first order leads to:

$$I(V(t)) = I(V_0 + V_{mod}\sin(\omega t)) \approx I(V_0) + \underbrace{\frac{dI(V_0)}{dV} \cdot V_{mod}}_{\Delta I} \cos(\omega t). \tag{4.28}$$

The Lock-in amplifier is set to detect only signals with frequency ω which is almost exclusively ΔI. Its magnitude is proportional to the slope of $I(V)$ and therefore acts as a measure of the LDOS. The advantage of the Lock-in technique is that the resulting signal has a lower noise level than numerical derivation because other frequencies can be filtered effectively. The downside is that it can be associated with a static offset making the identification of band gaps more challenging. Thus, dI/dV curves in this thesis are generated by numerical differentiation. To reduce spikes in the resulting LDOS spectrum, a five-point average is usually applied to $I(V)$ and dI/dV.

LDOS mapping

Alternatively, the LDOS can be recorded simultaneously with a topographic map using the Lock-in technique described above. At the chosen setpoint the modulating voltage is added

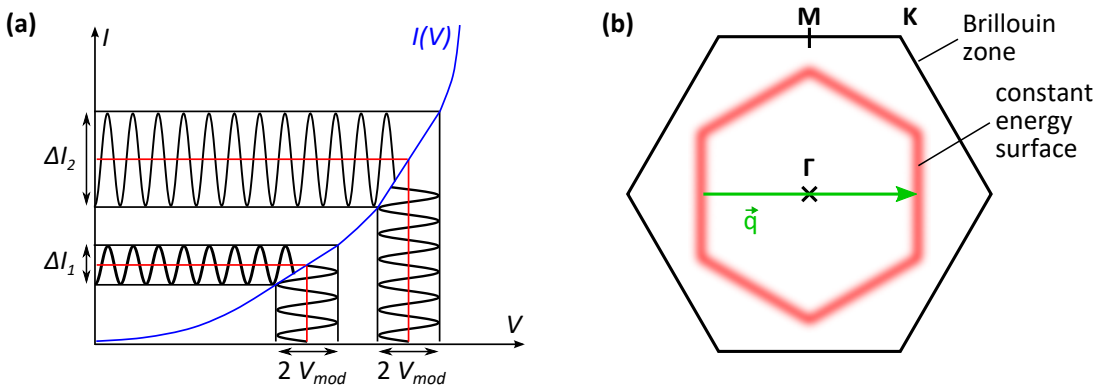

Fig. 4.5.: **(a)** Working principle of measuring the LDOS via the Lock-in technique. By adding a sinusoidal voltage to the bias voltage, the tunneling current oscillates with an amplitude ΔI that is proportional to dI/dV and therefore to the LDOS. The magnitude of ΔI is recorded by the Lock-in amplifier. **(b)** Illustration of elastic scattering in presence of defects in a 2DES. Possible scattering vectors $\vec{q}$ as the one exemplarily shown connect parallel parts of a constant energy surface. This scattering vector can be rediscovered in the FFT of LDOS maps, thereby adding the possibility to trace electronic dispersions via STS.

to the tunneling bias allowing the Lock-in amplifier to constantly record the LDOS during a constant-current measurement. By repeating scans at different bias voltages, spatial and electronic information can be collected in a similar manner as with CITS. The difference between the two techniques is rooted in the role of the setpoint. While LDOS maps are always taken at the bias voltage of the respective topographic measurement, CITS has a global setpoint that defines the tip–sample separation for the entire electronic spectrum. This effect can be reduced by investigating the normalized spectra $(dI/dV)/(I/V)$ instead [98]. On the other hand, this quantity approaches unity for small voltages making it unsuitable for the identification of bandgaps or the investigation of low-energy behavior in general.

Experimental resolution of STS

Using a bias voltage with an additional modulation will naturally influence the energy resolution of the experiment. As can be seen in Fig. 4.5(a), a bigger modulation voltage results in a bigger voltage range that is sampled for the determination of the LDOS. Aside from the modulation voltage, the resolution is also limited by the finite temperature which affects the occupation of states around the Fermi level [106]:

$$\Delta E = \sqrt{\Delta^2_{therm} + \Delta^2_{mod}} = \sqrt{(3.5 k_B T)^2 + (2.45 e V_{rms})^2}. \tag{4.29}$$

Here, k_B is the Boltzmann constant and V_{rms} is the root mean square of the sinusoidal modulation voltage. If not stated otherwise, $V_{rms} = 10\,\mathrm{mV}$ was used for all experiments.

Quasiparticle Interference

In terms of electronic properties both STM and STS are only sensitive to the LDOS of a sample as defined in Eq. 4.21. For a Bloch state the LDOS is spatially uniform and therefore it is impossible to gain information about the electronic dispersion by a local measurement [107]. However, when defects are present on the surface, states with different wave vector $\vec{k}$ are mixed through elastic scattering. This leads to spatial oscillations of the LDOS which can be linked to the electron dispersion. They were firstly demonstrated by Crommie et al. for the surface state of Cu(111) [108]. Their origin can be understood from basic quantum-mechanical considerations [109]. If a free 2D electron gas in the $x-y$ plane is reflected at an infinite potential wall extending in the y direction, its wave function has the form

$$\Psi_k(x,y) = Ne^{ik_y y}(e^{ik_x x} - e^{-ik_x x}) \tag{4.30}$$

where N is a normalization constant. Putting the wave function into Eq. 4.21 results in

$$\mathrm{LDOS}(E, \vec{r}) \propto 1 - J_0(2k_E x). \tag{4.31}$$

Here, J_0 is a Bessel function that behaves like a decaying sine wave, and k_E is a wave vector of the 2DES that complies with its dispersion relation. In other words, a differential conduction map taken at a certain energy will contain a contribution oscillating with a wavelength $\lambda = 2\pi/|\vec{q}|$ where the scattering vector $\vec{q}$ connects parallel parts of a constant energy surface in the BZ as depicted in Fig. 4.5(b). By performing a 2D fast Fourier transform (FFT) of a measured differential conduction map, the scattering vectors can be directly extracted which grants an indirect access to the dispersion relation.

4.3. Low-energy electron diffraction

In a LEED experiment electrons with an energy of typically 30-200 eV are shot onto a crystalline sample in order to analyze the resulting diffraction pattern. A first successful demonstration of LEED was already done in 1927 by Davisson and Germer [110], but only the advances in electron detection and vacuum science made during the 1960s rendered it one of the most wide-spread techniques in surface physics [111]. As LEED is capable to identify different surface reconstructions, it plays a fundamental role in the analysis of 2D adatom systems. Therefore, essential technical requirements of a LEED device and key concepts of diffraction will be briefly reviewed in the following. A sketch of an experimental setup is depicted on the left side of Fig. 4.6. Electrons from a hot filament are accelerated to a defined energy and perpendicularly hit the surface of the sample to be investigated. After diffraction, the electrons are drifting through a field-free zone towards a series of three electronic grids. The second grid acts as a suppressor which deflects inelastically scattered electrons using a retardation field. Electrons passing the grids are finally accelerated onto a phosphor screen which acts as a detector.

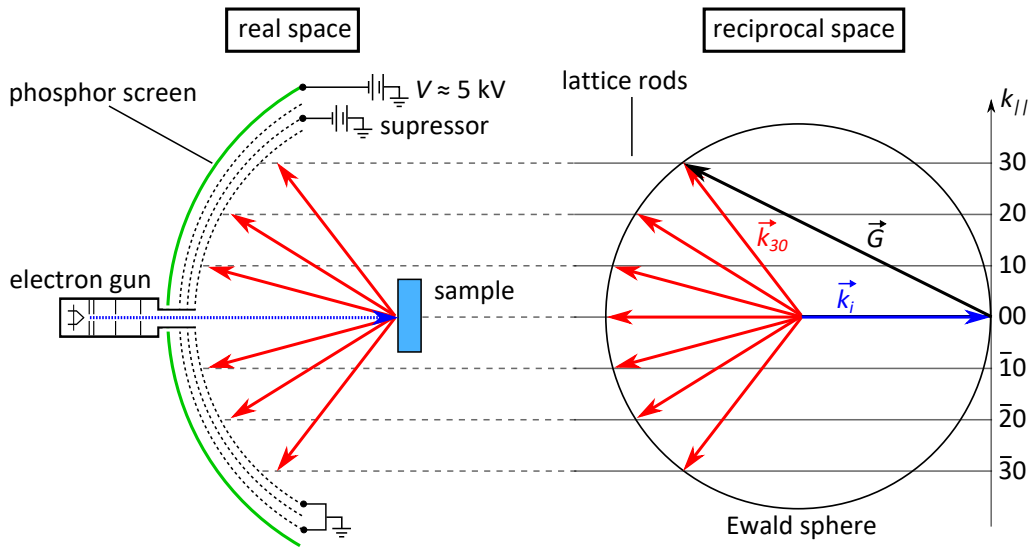

Fig. 4.6.: A LEED experiment in real space (left) and reciprocal space (right). Electrons are accelerated perpendicularly onto the sample plane. Diffracted electrons meeting the Laue condition interfere constructively and create a series of reflexes that can be captured on a phosphor screen. The diffracted beam associated to the (3 0) rod is labeled exemplarily.

The discussion here will be limited to kinematic diffraction theory which only considers single scattering on a 2D lattice. This is sufficient to capture the symmetry of the surface including any superstructures due to the arrangement of adatoms on a substrate. If scattering is considered only for a surface, the reciprocal lattice collapses to a series of rods that are located at the reciprocal lattice points of the 2D lattice and oriented perpendicular to the sample plane. In order to interfere constructively, scattered electrons must fulfill the Laue condition:

$$\Delta\vec{k} = \vec{k_i} - \vec{k_f} = \vec{G} \text{ with } |\vec{k_i}| = |\vec{k_f}|. \tag{4.32}$$

Here $\vec{k_i}$ and $\vec{k_f}$ are the wave vectors of the incident and diffracted electron, respectively, and $\vec{G}$ is a reciprocal lattice vector of the examined surface lattice. The Laue condittion can be easily visualized using the Ewald construction as seen on the right side of Fig. 4.6. A circle with radius $|\vec{k_i}|$ is drawn with the $k_{||}$ axis of the reciprocal lattice acting as a tangent. Wherever the circle intersects with one of the lattice rods, the Laue condition is fulfilled and the angle of a LEED spot is fixed. The spots are usually labeled according to the coordinates of the associated reciprocal rod as exemplarily done for the $|\vec{k}_{30}|$ beam. The intensity of each LEED spot is modulated by a structure factor. Accordingly, LEED energies in this thesis are chosen such that all reconstructions present on the surface are represented in the diffracted image.

5. Substrate-enhanced electronic correlations in $\sqrt{3}_\alpha$-Sn/SiC(0001)

This chapter deals with the highly-correlated 2DES $\sqrt{3}_\alpha$-Sn/SiC(0001). Electronic correlations are boosted by the substrate through its partial ionic nature and weak screening capabilities. For the first time the k-resolved spectral function measured with ARPES is shown. As it does not feature any simple backfolding due to potential magnetism, this system remains a candidate for the realization of a more exotic ground state.

5.1. Triangular lattices on SiC(0001)

The 2DES Sn/SiC(0001) is a new member in the family of group IV triangular lattices since the realization of this adatom system is tied to the newly established preparation of the substrate presented in Sect. 2.2 and Ref. [A5]. However, the closely related systems $\sqrt{3}_\alpha$-Si/SiC(0001) as well as the bare SiC(0001) 1×1 surface which also hosts a 2DES with triangular geometry have been investigated in the past. The $\sqrt{3}_\alpha$-Si/SiC(0001) system was firstly investigated by a Swedish group via PES [50, 112] and STM [113] in the mid 1990s. They already concluded that it forms a triangular lattice with a adatom coverage of 1/3 ML and a half-filled surface state. Since the highest occupied state was found to be located 1.2 eV below the Fermi level in ARPES measurements, it was identified as a LHB and the authors noted the necessity to include electronic correlations when describing the electronic structure of the system. Measurements of the unoccupied band structure via inverse PES showed a Si-derived state 1.1 eV above the Fermi level which means that the two Hubbard bands are almost symmetrically distributed in terms of their energy position [114]. This was also confirmed by STS experiments which found both the LHB and the UHB close to the energies expected from the preceding studies [52]. Accompanying these experimental results, the system was also tackled theoretically and researchers needed a Hubbard-U_0 between 1.6 and 2.5 eV (depending on the respective theoretical method) to achieve a good agreement with experimental evidence [115–117].

If a SiC crystal is truncated perpendicular to the [0001] direction or if the hydrogen layer is removed from an H-terminated H/SiC(0001) surface, the unsaturated dangling bonds of the topmost Si layer also form a 2D triangular lattice system. For the case of thermal hydrogen desorption, it was speculated that it is impossible to prevent an – in this case unwanted – $\sqrt{3} \times \sqrt{3}R30°$ reconstruction [118]. However, very recent experiments suggest that the unreconstructed 1×1 surface can be realized after all [54]. Nevertheless, said surface

could also be produced with light-stimulated desorption of hydrogen using high-intensity synchrotron radiation, thereby avoiding a thermal treatment [119]. Although the atomic sites of this half-filled surface state are much closer to each other than in the $\sqrt{3} \times \sqrt{3}R30°$ case, the band structure does not show any spectral weight at the Fermi level. Instead, a state associated to the dangling bonds was found 1.7 eV below the Fermi level, indicating that it is strongly correlated as well. All the SiC-based triangular lattices investigated so far show significant band gaps pointing towards likewise strong electronic correlations. As stated in Chap. 1, a concomitance of strong SOC can trigger the emergence of exotic ground states. By choosing the heavy element tin as an adatom this will be investigated in the following.

5.2. Preparation of $\sqrt{3}_\alpha$-Sn/SiC(0001)

The preparation of $\sqrt{3}_\alpha$-Sn/SiC(0001) starts off with a freshly etched sample of hydrogen-terminated SiC(0001) as described in Sect. 2.2. Then tin is evaporated onto the surface using an e-beam evaporation source with an ion flux of 100 nA for 15 min. Without the availability of a quartz micro balance the amount of tin deposited is unknown. However, it can be calibrated using LEED for $\sqrt{3}_\alpha$-Sn/Si(111) which will be investigated in Chap. 7. Assuming the reading of the flux monitor is directly proportional to the amount of tin deposited, one ends up with approximately 3.7 ML of tin on top of H/SiC(0001). Afterwards, the sample is annealed at 750°C for 3 min. At this temperature the hydrogen layer is removed from the sample. Without any tin on the surface this procedure would lead to the formation of $\sqrt{3}_\alpha$-Si/SiC(0001). But the considerable amount of Sn atoms present instead favors a formation of different Sn-based reconstructions. After this annealing step, three different phases were identified on the surface, namely $6\sqrt{3} \times 6\sqrt{3}R30°$, 3×3 and $\sqrt{3}_\alpha$-Sn/SiC(0001) which all coexist with domains of several ten nanometers in size [49]. Then the sample is annealed at 775°C for another 3 min which removes the $6\sqrt{3} \times 6\sqrt{3}R30°$ phase from the surface. Finally, after annealing at 800°C for 3 min, only $\sqrt{3}_\alpha$-Sn/SiC(0001) is left on the surface which is again verified by LEED. The corresponding temperature profile and the LEED images after each step of the preparation are summarized in Fig. 5.1(a).

Now the sample is ready for the investigation with STM. Figure 5.1(b) shows an overview image of its surface. There is only the $\sqrt{3}_\alpha$-phase present which means spatially averaging techniques are suitable for characterization, too. It has a terraced appearance that is already known from the bare substrate, documented in Fig. 2.3(b). To give a better insight into the surface morphology, the full range of the color code is limited to the central terrace. It features two domain boundaries (red arrows) that separate different rotational domains [49] and some charge inhomogeneities of different size (green arrows). Similar features are also found on the bare substrate where they are associated to defects at various depths [120]. Therefore, it is not surprising that they remain visible if 1/3 ML of Sn is added to the surface. At the chosen bias voltage $V = -3$ V they can raise the apparent height of the

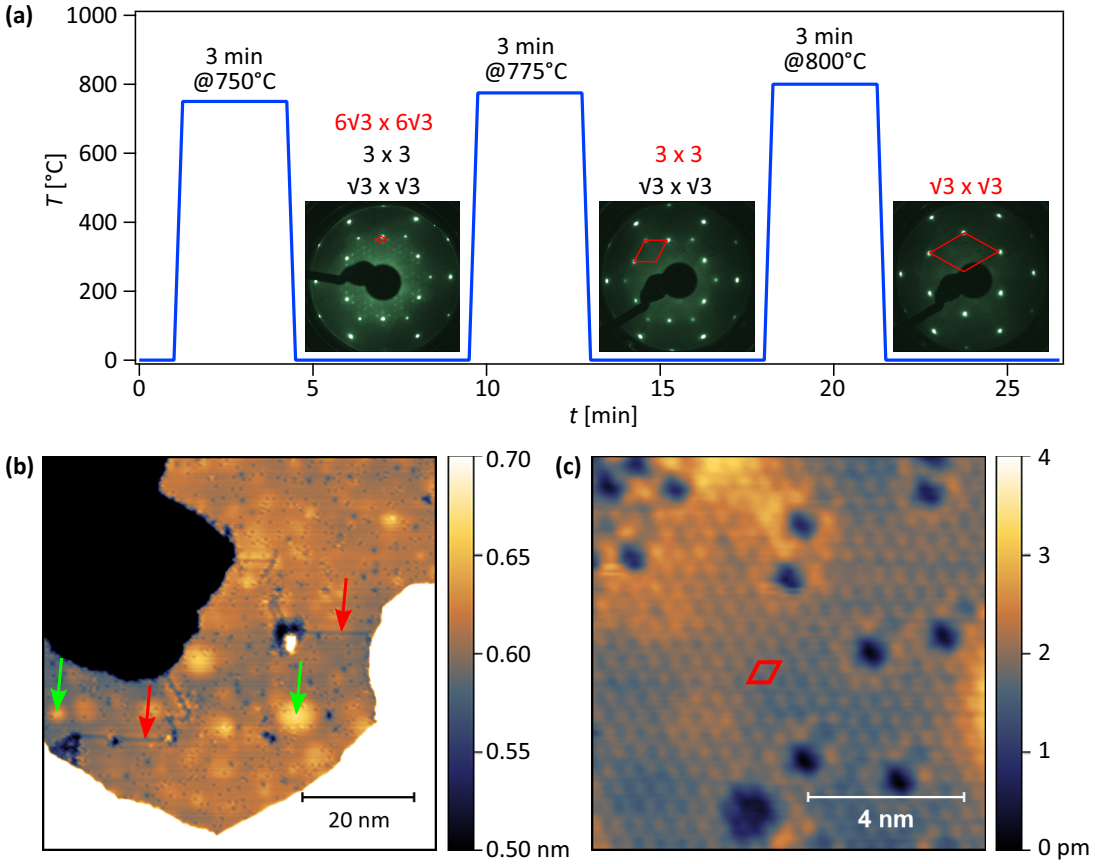

Fig. 5.1.: **(a)** Temperature profile driven during the preparation of $\sqrt{3}_{\alpha}$-Sn/SiC(0001). After annealing for 3 min at 750°C three different phases, namely $6\sqrt{3}\times6\sqrt{3}R30°$ (surface BZ in red), 3×3 and $\sqrt{3}_{\alpha}$-Sn/SiC(0001) coexist on the sample. After annealing at 775°C for 3 min, the $6\sqrt{3}\times6\sqrt{3}R30°$ phase has vanished. The surface BZ of 3×3 Sn/SiC(0001) is marked with red lines. Finally, after annealing at 800°C for 3 min, only the desired $\sqrt{3}_{\alpha}$-Sn/SiC(0001) (surface BZ in red) is left on the surface. The electron energy was set to 57 eV for all three LEED images. **(b)** Topographic STM overview scan of Sn/SiC(0001). To offer the best possible contrast within a substrate terrace, the color code does only span over one terrace. $V = -3\,\mathrm{V}$, $I = 50\,\mathrm{pA}$ and $T = 77.5\,\mathrm{K}$. **(c)** Detailed STM image of the surface where individual Sn atoms are resolved. $V = -3\,\mathrm{V}$, $I = 100\,\mathrm{pA}$ and $T = 77.5\,\mathrm{K}$.

Sn atoms by up to 50 pm. Furthermore, one finds several smaller defects in the film that mostly appear as black dots. A STM scan on a smaller scale, see Fig. 5.1(c), reveals them in more detail. Most of the defects are depressions surrounded by a ring of brighter atoms. This defect type is also known from the $\sqrt{3}_\alpha$-Sn/Si(111) surface where it was identified as a Si atom substituting a Sn atom of the triangular lattice [121]. In the $\sqrt{3}_\alpha$-Sn/SiC(0001) system this defect type might be even more common since a Si/SiC(0001) system would form during preparation if there wasn't an abundance of Sn atoms present on the surface. It is also possible to identify the arrangement of the Sn atoms in the triangular lattice. The corresponding $\sqrt{3} \times \sqrt{3}R30°$ unit cell is indicated in the center of the image. Finally, it is noted that the appearance of the lattice does not change qualitatively with the sample bias or the temperature for $T = \{4.3\,K, 77.5\,K, 300\,K\}$ [49] which excludes any structural distortions or the formation of CO for the respective temperatures.

5.3. Spectroscopic properties of $\sqrt{3}_\alpha$-Sn/SiC(0001)

After the growth of Sn/SiC(0001) has been successfully established, we can examine its electronic properties to elucidate the role of electronic correlations. This is done using ARPES which grants direct access to the spectral function. A measurement along the high-symmetry directions of the $\sqrt{3} \times \sqrt{3}R30°$ BZ is shown in Fig. 5.2(a). Here, only the surface state derived from the half-filled dangling bonds which is in the center of this study is visible. It forms a very broad feature centered about 0.9 eV below the Fermi level. The exact energy position of the state varied slightly among various samples within an binding energy range of $[0.9\,eV; 1.1\,eV]$ which is likely related to a different pinning of the Fermi level. Nevertheless the spectrum is always gapped which led to the conclusion that strong electronic correlations are governing the physics of this system. Accordingly, the state investigated here is the LHB of a Mott insulator [A6].

The spectral function shows some intensity variations and the spectral weight is steeply declining around the boundaries of the first BZ which is likely related to the associated matrix elements. While the raw spectrum does not evidently show a $\sqrt{3}\times\sqrt{3}R30°$ symmetry that is expected from LEED and STM images, a gaussian fit with a linear background performed for the energy distribution curves (EDCs) reveals the expected dispersion. The maxima of the gaussian curves are depicted as white dots in Fig. 5.2(b) and the symmetric behavior around the $\sqrt{3} \times \sqrt{3}R30°$ high-symmetry points of the BZ is clearly confirmed. An excerpt of selected EDCs including the resulting fit function is compiled in Fig. 5.2(c). However, it is also possible to visualize the dispersion without the necessity of a fitting procedure. By normalizing each EDC with its total spectral weight inside the energy interval [-0.6 eV;-1.2 eV] which is applied for the color plot in Fig. 5.2(b), the sought-after $\sqrt{3} \times \sqrt{3}R30°$ symmetry of the state is revealed as well.

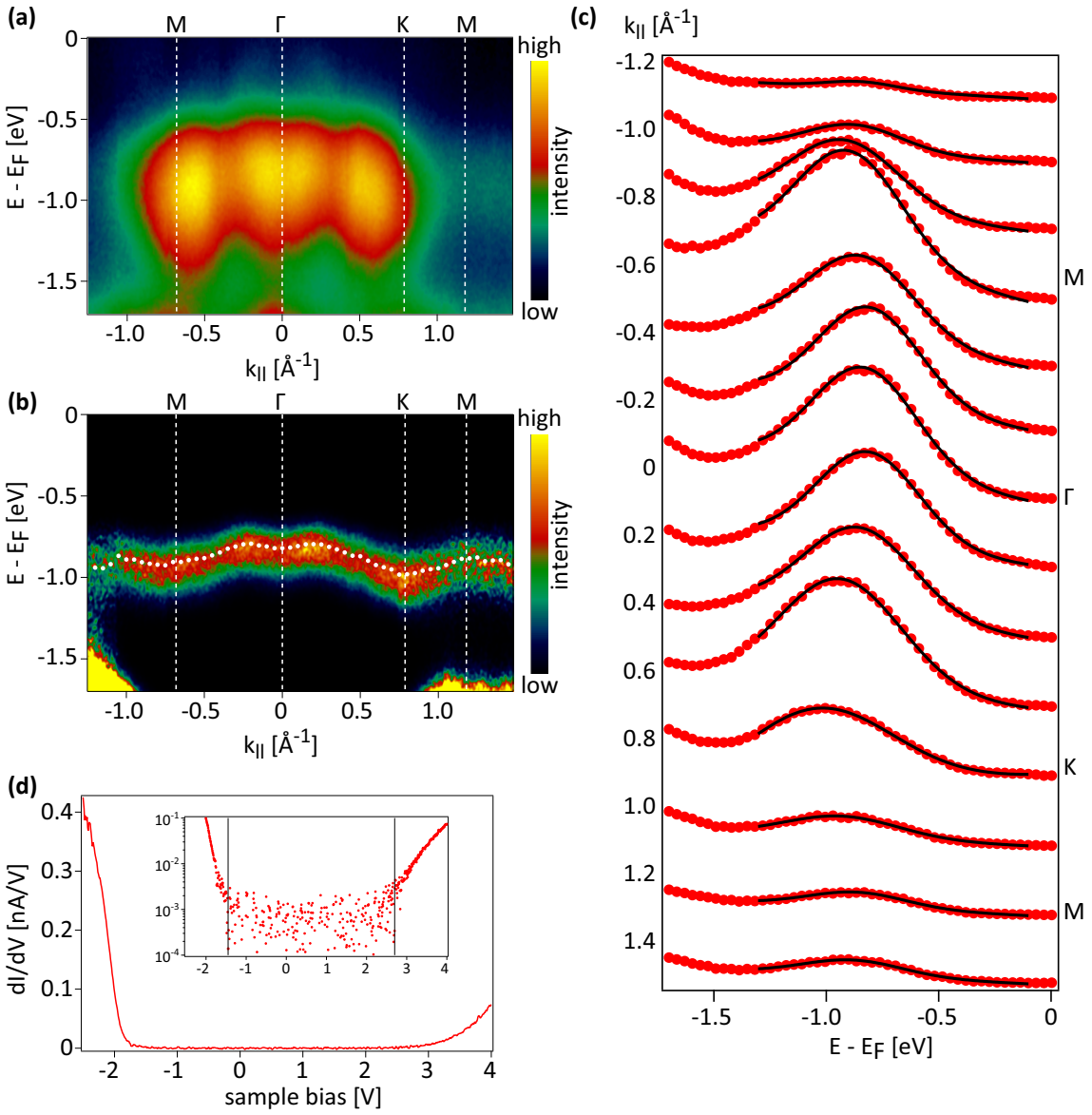

Fig. 5.2.: **(a)** ARPES of the surface state found on $\sqrt{3}_\alpha$-Sn/SiC(0001). The high-symmetry points of the $\sqrt{3}\times\sqrt{3}R30°$ BZ are labeled. $h\nu = 21.2\,\mathrm{eV}$, $T = 300\,\mathrm{K}$. **(b)** Same data as in Panel (a), but the total spectral weight inside an energy corridor [-0.6 eV;-1.2 eV] has been used to normalize each EDC. Although this procedure voids any information contained in the distribution of spectral weight, it helps to visualize the actual dispersion of the state without relying on any other procedures. The white dots are the maxima of all gaussian fits of EDCs of which some are presented in Panel (c). **(c)** Selected EDCs (red dots) from the spectral function in Panel (a). Each EDC has been fitted with a gaussian function allowing for a linear background (black solid lines) in order to determine the energy position of the surface state. There is a higher background in the center of the BZ because it contains a HeI satellite of the SiC bulk band. The spectra are offset vertically for clarity and are labeled with the $k_{||}$ value they are taken at. Each EDC was integrated over an angular width of $0.025\,\mathrm{Å}^{-1}$. **(d)** STS of $\sqrt{3}_\alpha$-Sn/SiC(0001). Setpoint $V = -2.4\,\mathrm{V}$, $I = 150\,\mathrm{pA}$ and $T = 77.5\,\mathrm{K}$. Inset: Logarithmic plot of the data. The band gap is 4.15 eV wide, clearly exceeding the substrate bulk band gap of 3.26 eV. The band positions are likely shifted by tip-induced band bending.

The LHB does not show any other symmetry such as a characteristic backfolding which was observed in Sn/Si(111) and helped to identify the row-wise antiferromagnetic ground state [10]. Independent of a critical temperature for such a magnetic state, ARPES spectra of $\sqrt{3}_\alpha$-Sn/SiC(0001) look clearly different than in Si- or Ge-based systems which feature a low intensity around the Γ point [10, 122]. Many-body calculations of the k-resolved spectral function may resolve where this discrepancy originates from in future studies. Since the LHB is a very broad feature and at the same time only weakly dispersing, possible shadow bands of common superstructures such as $2\sqrt{3} \times 2\sqrt{3}R30°$ and 3×3 are naturally difficult to resolve.

As a complementary approach, a measurement of the LDOS using STS was conducted. Unfortunately, it did not yield a meaningful result, see Fig. 5.2(d), as the spectra do not show any states around $V = -1\,\mathrm{V}$ where the LHB was found in ARPES. The total gap found here is 4.15 eV as deduced from the inset of Fig. 5.2(d) which shows the data on a logarithmic scale. This exceeds the bulk band gap of the 4H-SiC substrate by about 0.9 eV [47]. Therefore, the spectra cannot quantitatively reflect the electronic properties of the examined sample. A similar behavior was also observed for the hydrogen-terminated substrate surface [120] and it is likely caused by tip-induced band bending. Further investigations using STS were thus not undertaken.

5.4. Enhancement of electronic correlations through the SiC substrate

To get a deeper insight into the physics of $\sqrt{3}_\alpha$-Sn/SiC(0001), its band structure is modeled with DFT. Although this approach is not able to reproduce the spectrum measured in ARPES as Coulomb correlations are not included, it can nevertheless give an instructive insight into some important aspects. The calculations for the half-filled surface state are depicted in Fig. 5.3(a). Although the lattice constant on the surface of SiC(0001) is 20 % smaller than on Si(111), the bandwidth of the DFT calculation is reduced from $\approx 0.50\,\mathrm{eV}$ in $\sqrt{3}_\alpha$-Sn/Si(111) [9] to $\approx 0.29\,\mathrm{eV}$ in Sn/SiC(0001). Therefore, it is clear that indirect hopping processes through the substrate must be considered as well, a mechanism already deemed important in Sn/Si(111) [123]. Due to the partly ionic character of the bonds in SiC the hybridization with the adatom system on top is reduced [A6]. Thereby the effective hopping amplitude is decreased which promotes the localization of electrons.

A second contribution of the substrate to suppress the conductivity in the 2DES comes from its relatively large band gap. The effective Coulomb repulsion between electrons is affected by the dynamic screening capabilities of the respective material which are captured in the electronic dielectric constant ε_∞. The general trend is that it decreases with an increasing band gap [124]. This leads to $\varepsilon_\infty(SiC) \approx 6.5$ compared to $\varepsilon_\infty(Si) \approx 11.7$ [125, 126] which reduces the screening by approximately 50 %. With this information, the angle-integrated spectral function of the system was simulated using dynamical mean field theory

for different parameters of the effective Coulomb interaction U_0, see Fig. 5.3(b). Assuming a symmetric distribution of LHB and UHB with respect to the Fermi level, $U_0 = 2\,\text{eV}$ yields a good agreement with experimental data. This means that the effective Coulomb repulsion is about three times bigger than in Sn/Si(111) [10] although the 2DES is hosted by Sn $5p_z$ orbitals in both cases.

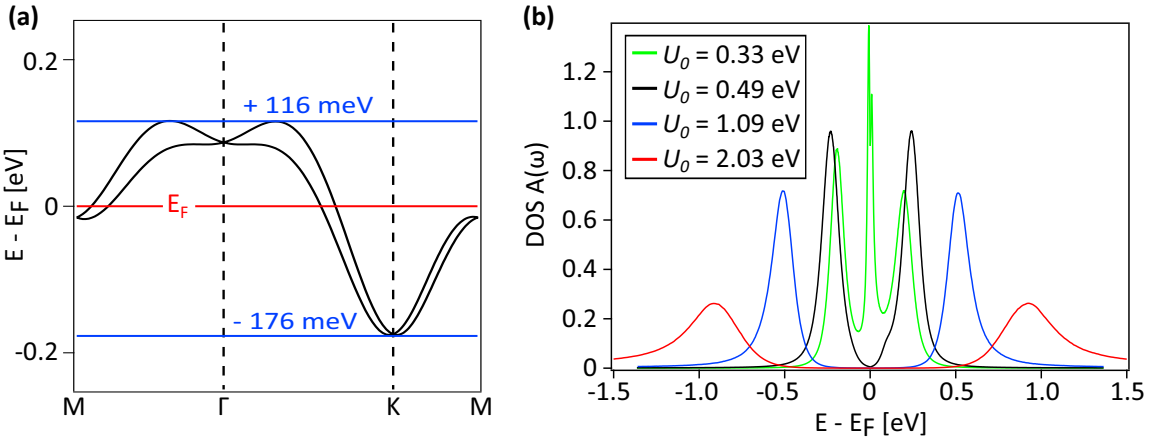

Fig. 5.3.: **(a)** DFT calculation of $\sqrt{3}_\alpha$-Sn/SiC(0001) including SOC. Only the relevant $5p_z$ state is shown here. The Fermi level is set to result in half filling. Calculation done by A. Fleszar. **(b)** LDA+DMFT calculation of the spectral function of $\sqrt{3}_\alpha$-Sn/SiC(0001) for different values of the Coulomb repulsion U. Assuming a symmetric distribution of LHB and UHB with respect to the Fermi level $U = 2\,\text{eV}$ yields a good agreement with experimental data. Calculation done by G. Li. From Ref. [A6].

It remains unclear how these numbers affect the ground state of $\sqrt{3}_\alpha$-Sn/SiC(0001). Since there is no evidence for a transition to a charge-ordered state, the system remains an arrangement of unpaired spins on a frustrated lattice that can potentially reduce its energy by establishing some kind of magnetic order. As the size of the SOC compared to the bandwidth in $\sqrt{3}_\alpha$-Sn/SiC(0001) is more than two times bigger than in related systems [A6], exotic ground states might be triggered, too [127, 128]. Including direct exchange and Dzyaloshinskii-Moriya interaction into a model Hamiltonian, Badrtdinov et al. propose that the system is a candidate for a spiral spin order that would host skyrmions if exposed to a strong magnetic field [18]. The minimal experimental conditions for the observation of this state are calculated to be a magnetic field of at least 7 T and a temperature of about 1 K which can both be reached in specialized STM setups.

In summary, $\sqrt{3}_\alpha$-Sn/SiC(0001) is a 2D triangular lattice with both strong electron correlations and strong SOC. The small inter-site hopping and the large effective Coulomb repulsion are boosted by the properties of the SiC substrate. The spectral function measured in ARPES has an intensity distribution that makes it stand out from the family of group IV triangular lattices. Since the spectral function also contains evidence of the ground state

an investigation of $\sqrt{3}_\alpha$-Sn/SiC(0001) with dedicated many-body calculation techniques could shed light on this unresolved question. Besides theoretical efforts, spin-resolved STM might be able to resolve the spin structure at low temperature (LT) in real space and find indications of the predicted skyrmion state.

6. Electronic correlations in triangular lattices of Pb/Si(111)

In this chapter a detailed investigation of the LT phase of $\sqrt{3}_\alpha$-Pb/Si(111) is presented. By careful analysis of STM and STS data, a charge-ordered state driven by electronic correlations and associated with a topographic surface corrugation 2-up/1-down is detected. Using anchor points from quasiparticle interference (QPI) measurements, the spectral function is calculated via the newly developed XVCA. Finally, electronic correlations are confirmed to also play a role in the dilute $\sqrt{3}_\gamma$-Pb/Si(111) system by a combined study with ARPES and STS.

6.1. Phases of Pb/Si(111) in the (sub-)monolayer regime

(Sub-)monolayer phases of Pb/Si(111) were studied for the first time in 1964 since scientists expected "interesting electrical properties" due to the difficulty of saturating all the dangling bonds on a Si(111) surface [31]. However, the limited capabilities of surface analysis techniques at the time did not allow for a thorough investigation. The interest in these surface systems recovered in the mid 1980s when improved analysis techniques and especially the availability of the scanning tunneling microscope permitted a first glimpse at the rich phase diagram of Pb/Si(111) [129, 130]. Since there are many different phases which partially share the $\sqrt{3} \times \sqrt{3}R30^\circ$ reconstruction and can in addition be coexisting, only careful studies with STM eventually shed more light on their configuration on the atomic level [131, 132]:

- The structure of $\sqrt{3}_\alpha$-Pb/Si(111), see Fig. 6.1(a), was already introduced in Sect. 2.3. The 3×3 phase which emerges below 86 K [133] is in the focus of this section.
- Aside from this, the dilute triangular lattice $\sqrt{3}_\gamma$-Pb/Si(111) where the adatoms are Pb and Si in equal shares, see Fig. 6.1(b), will also be investigated.
- Pb/Si(111) with a coverage of up to 4/3 ML shows a complex variety of phases. At exactly 1 ML there is a phase which has a 1×1 reconstruction at RT that transforms into $\sqrt{7} \times \sqrt{3}$ at approximately 270 K [134–136], see Fig. 6.1(c). Since LEED images in this thesis are all taken at RT, they do not show the $\sqrt{7} \times \sqrt{3}$ reconstruction although it is predominantly found in the respective STM images. If more Pb is added, the surface keeps the $\sqrt{7} \times \sqrt{3}$ reconstruction up to 1.2 ML which led to some misunderstanding until

it was suggested that there are indeed two different phases sharing this reconstruction [134]. That is, however, not a unique finding as a congeneric behavior was also reported for In/Si(111) [137].

- The phases with even higher Pb coverage, i.e., between 1.2 ML and 4/3 ML, are a realization of a so-called devil's staircase (DS), a special mathematical function which – in the case of Pb/Si(111) – links the chemical potential to the absolute coverage [138, 139]. The DS consists of two building blocks, namely the just mentioned $\sqrt{7} \times \sqrt{3}$ with 1.2 ML and $\sqrt{3}_\beta$-Pb/Si(111) with 4/3 ML coverage, see Fig. 6.1(d). Theoretically, any linear combination of these two building blocks is allowed, leading to an infinite amount of phases with correspondingly huge unit cells in this coverage regime. Two particular phases of this DS were part of a study that first showed superconductivity in a true 2DES, with critical temperatures slightly above 1.5 K [140].

A summary of the mentioned phases and transitions is compiled in the phase diagram in Fig. 6.1(e).

6.2. Correlation-driven charge order in a two-dimensional adatom lattice

The interest in the family of group IV triangular lattices was boosted by the fact that some of the α-phases show a phase transition from $\sqrt{3} \times \sqrt{3}R30°$ to 3×3 when cooled below a critical temperature [4, 5]. In 1999, this was also confirmed for $\sqrt{3}_\alpha$-Pb/Si(111) when the corresponding reflexes where observed in a study using reflection high-energy electron diffraction [141]. Unfortunately, it turned out that $\sqrt{3}_\alpha$-Pb/Si(111) cannot be realized in patches big enough to allow for spatially averaging techniques [142–144]. It is always coexisting with either $\sqrt{7} \times \sqrt{3}$ Pb/Si(111) or an extremely defect-rich $\sqrt{3}_\alpha$-Pb/Si(111). This leaves STM as one of the few probes to collect detailed information about its topographic and electronic properties. A following study verified that the phase transition is an intrinsic property of the system, i.e., defects are not required as nucleation points, and has a critical temperature of 86 K [133]. The driving force of this phase transition and the nature of the ground state are subject to an ongoing discussion in literature.

A first explanation was given by Brihuega et al. who suspected a topographic phenomenon mediated by a surface soft phonon [133]. It is based on the *dynamical fluctuation model* which was originally proposed to explain a transition from a RT 2×1 to a LT $c(4 \times 2)$ phase observed in STM measurements on Si(001) [145]. Dimers on the Si(001) surface perform a thermally activated "flip-flop" motion that freezes out at 65 K, thereby lowering the symmetry of the system. The frequency of this oscillation is much higher than the corresponding measurement times of a single pixel in a typical STM experiment (order of a few ms). Therefore, an image taken above the critical temperature will be averaged over several oscillation periods, effectively showing a state with higher symmetry in STM. This

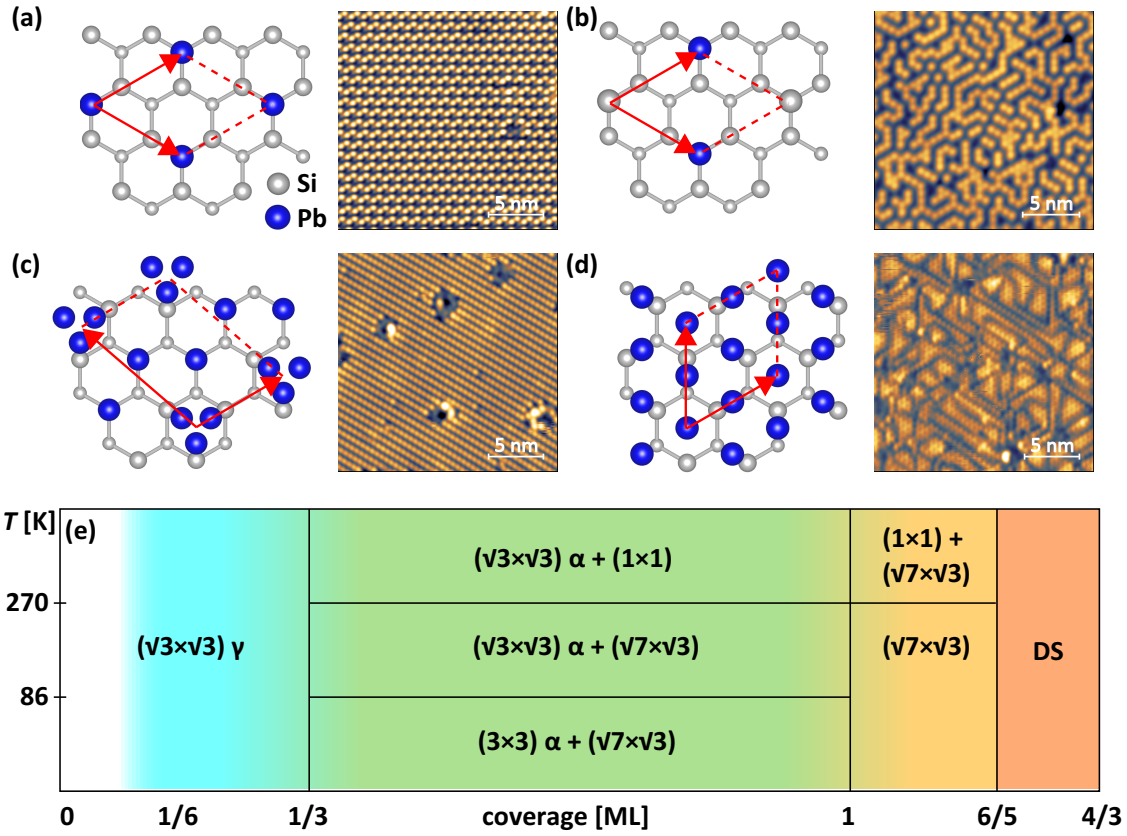

Fig. 6.1.: Structure models and corresponding STM images as well as a phase diagram of Pb/Si(111) in the coverage regime below 4/3 ML. **(a)** Structure model of $\sqrt{3}_\alpha$-Pb/Si(111). The corresponding STM image is taken below the critical temperature and therefore shows a 3×3 reconstruction. Tunneling conditions were $T = 4.3\,\mathrm{K}$, $V = -0.05\,\mathrm{V}$ and $I = 200\,\mathrm{pA}$. **(b)** Structure model of $\sqrt{3}_\gamma$-Pb/Si(111). Although the system shows a $\sqrt{3} \times \sqrt{3}R30°$ reconstruction in LEED, Pb and Si atoms are not distributed in a regular fashion. Nevertheless certain patterns of meandering chains are preferred as can be seen in the corresponding STM image. Tunneling conditions were $T = 4.3\,\mathrm{K}$, $V = 2.25\,\mathrm{V}$ and $I = 200\,\mathrm{pA}$. At this bias voltage, Pb atoms are visible as bright protrusions while the Si atoms remain invisible [132]. **(c)** Structure model of $\sqrt{7} \times \sqrt{3}$ Pb/Si(111) with a coverage of 1 ML. This is the phase coexisting and competing with $\sqrt{3}_\alpha$-Pb/Si(111). Only the trimers are visible in the corresponding STM image, giving it a chain-like appearance [135]. Tunneling conditions were $T = 77.5\,\mathrm{K}$, $V = 1.6\,\mathrm{V}$ and $I = 100\,\mathrm{pA}$. **(d)** Structure model of $\sqrt{3}_\beta$-Pb/Si(111) which is one of the building blocks of the DS. It has not been realized as a pure phase so far, instead the corresponding STM image shows the so-called striped-incommensurate phase which has a coverage around 1.3 ML [136]. Tunneling conditions were $T = 77.5\,\mathrm{K}$, $V = 1.4\,\mathrm{V}$ and $I = 100\,\mathrm{pA}$. **(e)** Phase diagram of Pb/Si(111) in the coverage regime up to 4/3 ML. The boundaries between different phases are partly drawn as smooth transitions since they have barely been explored so far and it is thus not clear when and how different phases are formed in the transition regions.

explanation was then used to elucidate on the occurrence of LT reconstructions (or the lack thereof) in $\sqrt{3}_\alpha$-Sn/Ge(111) and $\sqrt{3}_\alpha$-Sn/Si(111) [146]. Equivalently, the Pb atoms on $\sqrt{3}_\alpha$-Pb/Si(111) might be oscillating vertically above a critical temperature. Based on generalized gradient approximation (GGA)-DFT calculations, Brihuega et al. find an energy gain associated with a small vertical displacement of the Pb atoms leading to a 1-up/2-down configuration which is seemingly in line with the LT topographic STM images shown [133].

Another explanation would be the formation of CO, either driven by electronic correlations as suspected by a theoretical study from Hansmann et al. [7], or driven by Fermi surface nesting as was suggested for Pb/Ge(111) [4]. Although not elucidating the driving force of the transition, Tresca et al. were the first to back up their band structure calculations with experimental evidence from QPI [56]. They also noted the importance of SOC, possibly leading to a spin-split Fermi surface. So far, the full repertoire STM and state-of-the-art many-body calculation techniques have to offer has not been applied to $\sqrt{3}_\alpha$-Pb/Si(111). The goal of this section is to provide experimental and theoretical evidence that the system indeed undergoes a transition to CO which is driven by electronic correlations while the adatoms concomitantly experience a small vertical displacement leading to a buckled surface. At the same time, some of the flaws of other explanations will be exposed.

6.2.1. Preparation of almost defect-free $\sqrt{3}_\alpha$-Pb/Si(111) patches

As already stated above, $\sqrt{3}_\alpha$-Pb/Si(111) cannot be fabricated without other phases coexisting. Thus, the goal is to prepare a surface where the patches of $\sqrt{3}_\alpha$-Pb/Si(111) are frequent enough to be quickly found with STM, and have a low defect rate to study the intrinsic properties of the system. As QPI experiments are also intended, sporadic defects which can act as scattering centers are nevertheless desirable.

Starting from a freshly flashed Si(111) substrate (as described in Sect. 2.1), Pb is deposited from an e-beam evaporation source with a flux of 1 μA for 10 min onto a substrate held at RT. The amount of Pb deposited was surveyed using a characteristic LEED pattern that results when Pb atoms are aligned with the Si 7×7 reconstruction forming an ordered overlayer with a coverage of less than 3 ML [131]. It turns out that the exact coverage at this stage of the preparation is not crucial since any excess Pb can be easily desorbed during the subsequent annealing step. However, this required some optimization which lead to heating for 3 min at 450°C for substrates with a resistivity below 0.02 Ωcm. For substrates with higher resistivity the annealing temperature was reduced by a few degrees due to the change in emissivity [147].

Then the sample is examined with LEED, where a mix of a 1×1 and $\sqrt{3} \times \sqrt{3}R30°$ reconstruction is expected at RT, see Fig. 6.2(a). Afterwards the sample is cooled down for the investigation by STM. The overview scan in Fig. 6.2(b) shows the typical morphology of these samples, with insular patches of 3×3 Pb/Si(111) with a small amount of defects, surrounded by ample areas of $\sqrt{7} \times \sqrt{3}$ Pb/Si(111). One can also find patches where the

transition to 3×3 is strongly affected or suppressed by numerous defects, as can be seen in the lower left part of Fig. 6.2(b).

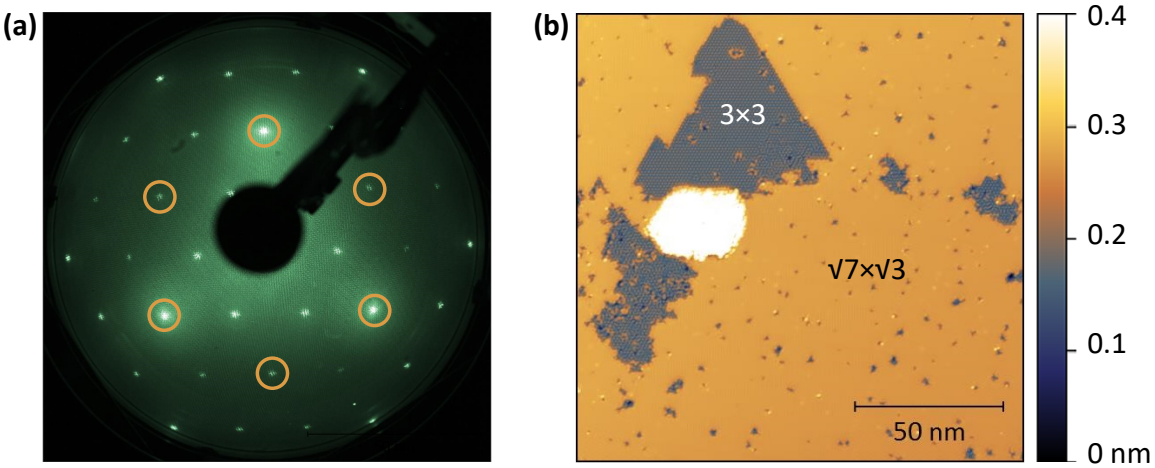

Fig. 6.2.: **(a)** LEED image of Pb/Si(111) taken with an electron energy of 80 eV. The image shows reflexes of a 1×1 and $\sqrt{3} \times \sqrt{3}R30°$ reconstruction, with the former being marked by yellow circles for orientation. The experiment was conducted at RT, i.e., above the transition temperature to both the $\sqrt{7} \times \sqrt{3}$ and 3×3 reconstruction. **(b)** Topographic STM map of a sample prepared in a way to promote large domains of the desired 3×3 $\sqrt{3}_\alpha$-Pb/Si(111). Even under the best preparation conditions the sample is mostly covered with the metallic $\sqrt{7} \times \sqrt{3}$ phase. The image was taken at $T = 4.3\,\mathrm{K}$, $V = 1\,\mathrm{V}$ and $I = 50\,\mathrm{pA}$.

6.2.2. Detection of a charge-ordered state in $\sqrt{3}_\alpha$-Pb/Si(111)

At first, the phase transition from $\sqrt{3} \times \sqrt{3}R30°$ to 3×3 will be examined. Therefore, the system was investigated via STM at RT and LT. The data is shown in Fig. 6.3 and the topographic measurements confirm the results already established in literature, namely that there is a transition from a $\sqrt{3} \times \sqrt{3}R30°$ reconstruction at RT, see Fig. 6.3(a), to a 3×3 reconstruction at LT as in Fig. 6.3(b). Effects of this phase transition on the electronic structure were not documented so far until a very recent study revealed some features using STS and QPI [56]. Here, we take a dedicated look on the spatial distribution of the signal both in topography and LDOS maps to track down the characteristics of the 3×3 reconstruction. Looking at the LDOS maps, one notices that the reconstruction also changes from $\sqrt{3} \times \sqrt{3}R30°$ to 3×3 as can be seen in Fig. 6.3(c), (d). This indicates that charge is redistributed and the phase transition is partly happening on an electronic level, i.e., CO emerges. There are three Pb atoms within the 3×3 Wigner-Seitz (WS) unit cell of the LT phase of $\sqrt{3}_\alpha$-Pb/Si(111). Given its position in the unit cell, one is coined the center atom. It has – at the chosen bias voltage of $-0.3\,\mathrm{V}$ – an increased LDOS compared to the other two adatoms. The other two, which are again coined according to their position as corner atom, are identical in terms of their electronic behavior. As the center atom

appears elevated both in the LT topographic and the LT LDOS map, a bare structural phase transition is ruled out since effects of the local barrier height would have an opposite effect [98]. This will be investigated in more detail in Sect. 6.2.3.

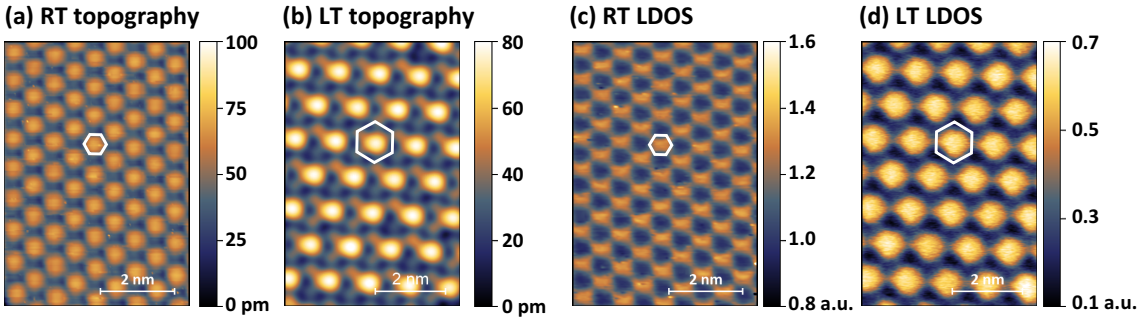

Fig. 6.3.: **(a, b)** Topographic maps and **(c, d)** corresponding DOS maps of $\sqrt{3}_\alpha$-Pb/Si(111) measured at RT and at LT, respectively. One can clearly identify the phase transition which is associated with a switch from a $\sqrt{3} \times \sqrt{3}R30°$ to a 3×3 reconstruction for both topography and DOS maps. The corresponding WS unit cells are marked in each panel. This manifests the detection of a charge-ordered state. Drawing conclusions about a topographic reordering of the adatoms requires further analysis. The settings were $V = -0.3\,\mathrm{V}$, $I = 100\,\mathrm{pA}$ for the RT and $V = -0.3\,\mathrm{V}$, $I = 50\,\mathrm{pA}$ for the LT measurement.

Now that we have demonstrated the ground state of $\sqrt{3}_\alpha$-Pb/Si(111) to be CO, an obvious tool for a more detailed characterization is the analysis of the site-specific LDOS via CITS. The spectra are shown in Fig. 6.4(a). To generate these, several I-V curves measured at nominally identical sites were averaged. A small vertical offset of 0.6 pA from $(I, V) = (0, 0)$, likely caused by a small leakage current, is corrected for. Afterwards, the dI/dV curve was computed by numerical differentiation. The CO state is clearly confirmed by these spectra. In the occupied part of the spectrum the curves are vastly different, with a significantly higher LDOS for the center atoms. This is in line with the DOS map shown in Fig. 6.3(d), where the atoms in the center of the WS unit cell are the ones that carry the higher signal. By repeating the STS measurements with varying tunneling currents, effects of the STM probe tip obscuring the intrinsic sample spectrum, as observed in the related system $\sqrt{3}_\alpha$-Si/SiC(0001) [52], have been excluded.

Close to the Fermi level the signal is almost identical for the two sites and exhibits a small but non-zero differential conductivity, indicating a metallic state. In the unoccupied part the center atoms again generate a higher signal for most of the covered voltage regime but both curves share a similar trend with a peak at $V = 0.32\,\mathrm{V}$ and a negative differential conductivity for $V \gtrapprox 0.85\,\mathrm{V}$. Technically, the latter would correspond to a negative DOS which is an unphysical result. The phenomenon is, however, observed both by another group and in similar material systems, too [40, 56, 148]. Its origin is thus possibly intrinsic to the STM measurement. If the Pb-induced surface state is energetically well separated from the silicon conduction band, there are no states in an energy window immediately above this

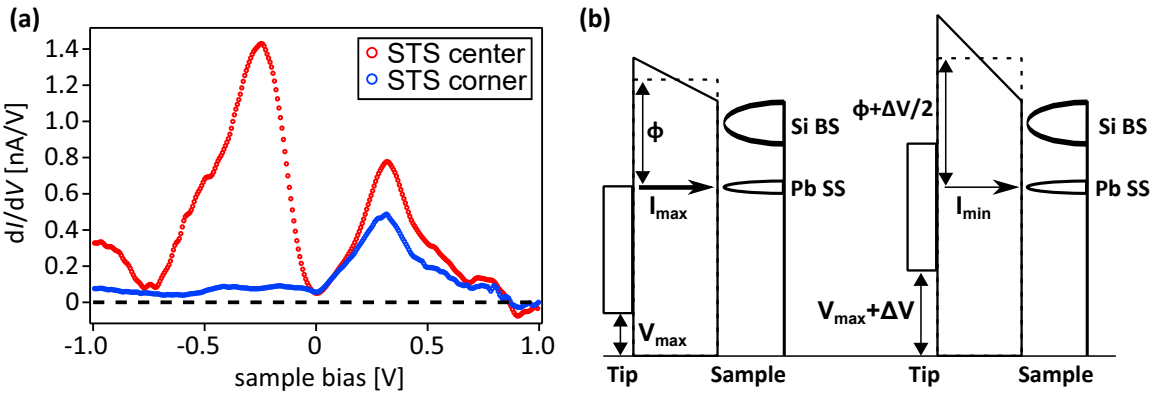

Fig. 6.4.: **(a)** dI/dV spectra of $\sqrt{3}_\alpha$-Pb/Si(111) measured on atoms in the center (red) of the WS unit cell and on atoms in its corner (blue). Center atoms show an increased LDOS over a major part of the spectrum with a prominent peak in the occupied states at $V \approx -0.25\,\mathrm{V}$. The negative differential resistivity observed above $V = 0.85\,\mathrm{eV}$ is explained in terms of an artifact caused by a changing tunneling barrier height within an energy gap above the Fermi level. The setpoint was $V = 0.1\,\mathrm{V}$ and $I = 10\,\mathrm{pA}$. $T = 4.3\,\mathrm{K}$. **(b)** Possible energy diagram of the tunneling conditions in $\sqrt{3}_\alpha$-Pb/Si(111). The lack of states within a small energy window inside the bulk band gap can serve as an explanation for the per se unphysical situation of a negative DOS. The tunneling current reaches its maximum when the Fermi level of the tip is aligned with the top of the Pb surface state (Pb SS) and it becomes minimal just before it is aligned with the bottom of the Si bulk states (Si BS) of the conduction band. Picture adapted from Ref. [148].

surface state. The dI/dV curve, which is proportional to the DOS, will therefore be zero. Increasing the bias voltage further raises the barrier height for tunneling electrons, leading to a decreasing tunneling current. This consequently results in a dI/dV curve dropping below the zero line. It will increase again only after states from the silicon conduction band contribute to the tunneling process. Fig. 6.4(b) illustrates this situation for the case of a one-dimensional trapezoidal barrier. The tunneling current reaches its maximum when the Fermi level of the tip is energetically aligned with the top of the Pb surface state (Pb SS). The minimal tunneling current is reached just before electrons from the Fermi level of the tip can elastically tunnel into Si bulk states (Si BS). In this energy range the effective height of the tunneling barrier for electrons from the Fermi level of the tip is described by $\Phi(V) = \frac{\Phi_s+\Phi_t}{2} + \frac{eV}{2}$ [98].

Concerning the energy position it is reasonable to assign the rise at around 1 eV to Si bulk states since this behavior is also found for other surface systems grown on Si(111) [40, 149]. The total weight of the dI/dV curve of center atoms in Fig. 6.4(a) is a lot larger than for corner atoms although both sites should in principle be able to host two electrons in their p_z-states. This should not be of concern for two reasons. On the one hand, STS does not probe the DOS uniformly, since the tunneling matrix element is bigger for states close to the center of the BZ. On the other hand, the relative weight of the curves is dictated by the setpoint chosen for the measurement.

Examination of the 3×3 island boundary

As we have seen at the beginning of this chapter in Fig. 6.2, the area covered by $\sqrt{3}_\alpha$-Pb/Si(111) makes up only a small fraction of the whole sample. The 3×3 - reconstructed islands are surrounded by a weakly metallic $\sqrt{7} \times \sqrt{3}$ phase and naturally there is some kind of boundary region between the two. A closer inspection of this boundary is worthwhile since $\sqrt{3}_\alpha$-Pb/Si(111) may host an exotic superconducting state featuring edge modes (see Chap. 1). Therefore, a study of the edges of the now established CO phase is the basis of understanding any possible further effects. While the transition between different Pb/Si(111) phases is smooth in some cases, e.g., for the building blocks of the DS [138], there is a clear boundary between $\sqrt{3}_\alpha$-Pb/Si(111) and the surrounding $\sqrt{7} \times \sqrt{3}$ phase. For certain bias voltages this is even apparent in large-scale STM scans such as Fig. 6.5(a) where the boundary is visible through its increased apparent height. When looking at the whole boundary region, it becomes clear that it is not linked to a clean α-phase because it is alike present in the upper right side or around some smaller islands which are both rich of defects.

A closer examination of the boundary is made in Figs. 6.5(b)-(e). Panel (b) shows a detailed topographic scan of a boundary between $\sqrt{7} \times \sqrt{3}$ (bottom) and 3×3 Pb/Si(111) (top). A height profile taken along the blue line in Panel (b) and graphed in the same color in Panel (c) can give more insight into the nature of the boundary. One immediately notices the periodic intensity variations with a pronounced dip every 1.9 nm. The regions in between those dips show an intensity variation, too. This is clearly related to the adjacent $\sqrt{7} \times \sqrt{3}$ phase because the green profile along the same crystal direction in said phase shows the same behavior. To extract further information, a FFT of the height profile is calculated, see Fig. 6.5(d). It reveals that two other characteristic periodicities can be found within the edge region, viz. 3.8 Å and 6.4 Å which are the interatomic distances in 1×1 and $\sqrt{3} \times \sqrt{3}$ Pb/Si(111), respectively. A slight deviation from the actual value of 6.65 Å for $\sqrt{3}_\alpha$-Pb/Si(111) is due to the limited number of pixels in the experiment which affects the FFT spectrum, too. The other noticeable features in Fig. 6.5(d) are higher-order contributions of the first-mentioned periodicity.

Therefore, it is concluded that the phase boundary consists of 1×1 Pb/Si(111) where the intensity of the atoms is modulated by the adjacent environment. The appearance of this boundary can vary based on the exact alignment of the two involved phases with the Si(111) surface. This can be seen on the left side of Fig. 6.5(b) where the intensity variations in the boundary are greatly reduced and single atoms can be identified (within the red circle). As a side note, the high spatial resolution of Fig. 6.5(b) also grants an impression of the trimer structure of the $\sqrt{7} \times \sqrt{3}$ phase introduced in the beginning of this chapter. This is often not captured in STM and the phase only appears as a series of lines as in Fig. 6.1(c).

In order to complete the picture, STS is performed on the atoms of the boundary and the $\sqrt{7} \times \sqrt{3}$ phase. The data is presented in Fig. 6.5(e) and was taken at a site similar to the one shown in Panel (b). Above the Fermi level both spectra show a broad feature

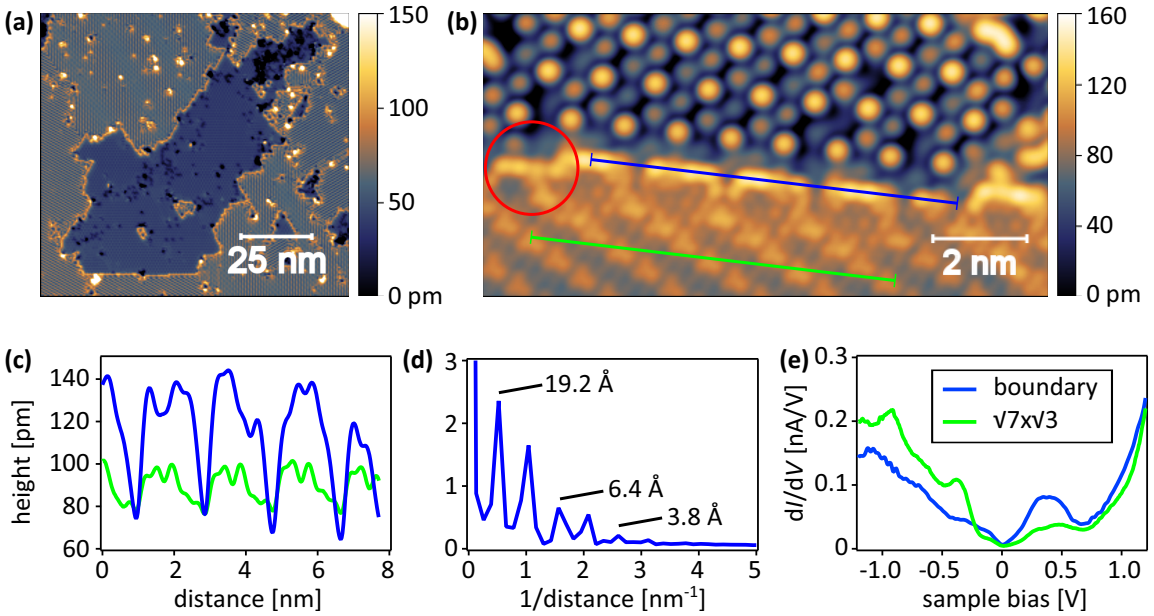

Fig. 6.5.: **(a)** Topographic map of a huge $\sqrt{3}_{\alpha}$-Pb/Si(111) island surrounded by $\sqrt{7}\times\sqrt{3}$ Pb/Si(111). The color code is chosen in a way to highlight the boundary between the two phases. The tunneling conditions were $V = 1\,\mathrm{V}$ and $I = 10\,\mathrm{pA}$. **(b)** Detailed topographic map including such a boundary with tunneling conditions $V = -0.5\,\mathrm{V}$ and $I = 100\,\mathrm{pA}$. Using the height profiles marked in this image and graphed in Panel **(c)**, it was possible to identify the phase boundary as 1×1 Pb/Si(111). Atoms with the corresponding spacing can be identified, e.g., in the red circle. **(d)** FFT spectrum of the blue height profile shown in Panel (c). **(e)** STS from a region similar to the one shown in Panel (b). $I(V)$ curves of measurements on several atoms of the respective phase were averaged and differentiated numerically. Setpoint $V = 1.5\,\mathrm{V}$ and $I = 300\,\mathrm{pA}$. $T = 4.3\,\mathrm{K}$ for all panels.

at $V \approx 0.35\,\mathrm{V}$ while Si bulk states dominate for higher bias voltages. In the occupied states the $\sqrt{7}\times\sqrt{3}$ phase has two peaks at -0.38 and $-0.93\,\mathrm{V}$, respectively, whereas the spectrum of the boundary is almost featureless up to $V = -1\,\mathrm{V}$. It has to be noted, however, that it was averaged over several atoms in different configurations. There is some variation among the single spectra as one can already expect from their different appearance in topographic measurements. Since the edge region is weakly metallic and the LDOS of individual atoms varies slightly, it will be difficult to prove the existence of additional states in case topological superconductivity is ever realized or found in this system. Maybe the characteristic decay length of topological states which was, e.g., analyzed for the topological insulator bismuthene can be used to provide supporting evidence [150].

6.2.3. Decoding the topographic buckling

The results from Sect. 6.2.2 did not clarify whether the formation of CO goes along with a topographic rearrangement of Pb atoms. It is known that the contrast of topographic STM

scans inverts when switching the bias voltage from $V = -0.5\,\mathrm{V}$ to $V = +0.5\,\mathrm{V}$ [142]. Thus, there must be some kind of transition region which will be investigated in the following in order to resolve this issue. The contrast inversion of the topographic images is found at a bias voltage $V \approx -125\,\mathrm{mV}$, the transition region is examined in Fig. 6.6(a)-(c). Starting at negative bias of $V = -100\,\mathrm{mV}$, Fig. 6.6(a), the atom in the center of the WS unit cell appears lower than neighboring atoms. Since there is only little contribution from the integrated LDOS at low bias voltages, this qualitatively reflects the true corrugation of the sample surface, i.e., Pb atoms are arranged in a "2-up/1-down" configuration. This is also confirmed by a measurement at very small bias voltage depicted in Fig. 6.6(d) that was not part of this measurement series, i.e., it was measured on a different sample with a different tip. The pattern in the LDOS map is not linked to the atomic positions, indicating that the appearance of the topographic measurements is dominated by the atomic corrugation. With increasing absolute bias voltage, the CO state progressively imprints its charge distribution onto the topographic maps, raising the apparent height of the atom in the center of the WS unit cell. Eventually, for $V = -150\,\mathrm{mV}$, this atom appears higher than surrounding atoms, see Fig. 6.6(c), rendering the topographic maps completely dominated by LDOS effects. Thus, there is a weak topographic lattice distortion with a specific pattern which is out of phase from the CO pattern.

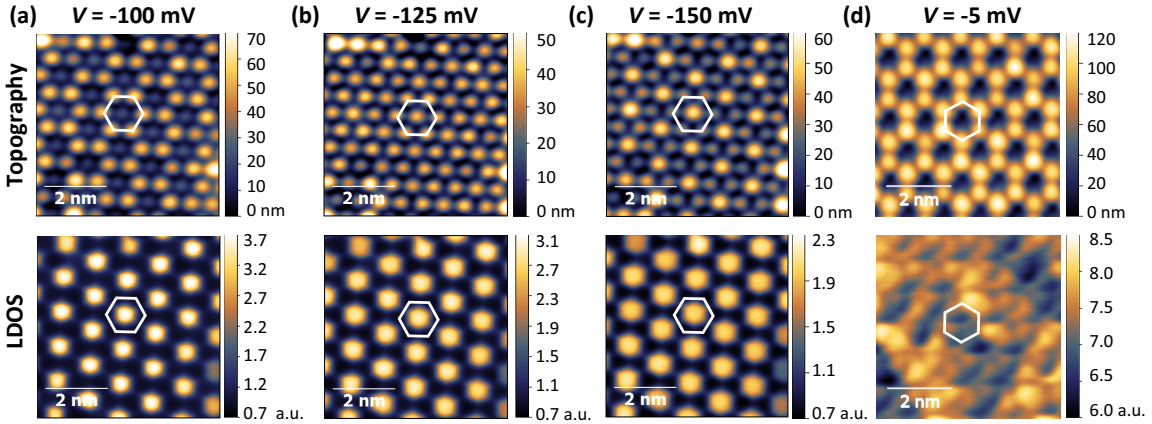

Fig. 6.6.: Topography (top) and the corresponding LDOS maps (bottom) of Pb/Si(111) for bias voltages (a) $V = -100\,\mathrm{mV}$, (b) $V = -125\,\mathrm{mV}$, (c) $V = -150\,\mathrm{mV}$ and (d) $V = -5\,\mathrm{mV}$. A 3×3 WS unit cell is marked in each panel. While the measurements in Panels (a)-(c) are made at the exact same sample spot with an unchanged tip configuration, the data in Panel (d) is from a different sample. For higher absolute bias voltage the LDOS maps show the CO state with a qualitatively unchanged appearance, the contrast in the topographic maps switches due to the interplay of LDOS effects from the CO state with the concomitant topographic buckling. For very low bias voltage the dominating pattern of the LDOS map is no longer linked to the symmetry of the adatom system, pointing towards LDOS effects not playing a role for the appearance of the topographic measurements. $I = 200\,\mathrm{pA}$ and $T = 4.3\,\mathrm{K}$ for all measurements. Adapted from Ref. [A1].

The measurements were not limited to the bias voltages shown in Fig. 6.6(a)-(c), the whole bias series can be found in the appendix in Fig. A.1. Apart from the bias voltage, all other experimental settings including the tip configuration were kept constant for this series of measurements, allowing for a direct comparison. The goal is to track the evolution of the apparent height in topographic measurements and link it to the results from LDOS maps and CITS for the two different Pb sites "up" and "down". This way one can get an estimate for the topographic buckling which can be used as a cross check for the conclusions drawn above. The relevant curves for this are compiled in Fig. 6.7. Topography and LDOS maps are always measured simultaneously at the previously specified voltage while CITS has a global setpoint that governs the appearance of a tunneling spectrum over its bias range. In order to compare spectroscopy data from LDOS maps and CITS, one has to get rid of these setpoint effects inherently associated with CITS. Depending on the setpoint, the distance between the tip and different adatoms might vary, resulting in a site-selective enhancement of the dI/dV signal. By normalizing the dI/dV spectra with the conductivity I/V this can be overcome to a good approximation. In addition, for bias voltages far away from the Fermi level the normalized differential conductivity is also closer to the actual DOS of the sample [98, 151]. The drawback is that spectra converge to a value of 1 for $V \to 0$, making them unsuitable for an analysis of the low-energy behavior. As the goal of this section is the comparison of CITS with the signal from LDOS maps, getting rid of setpoint effects has a high priority. Therefore, the normalized differential conductivity is chosen to compare the signal from LDOS maps with CITS in Fig. 6.7(a). The data points from LDOS maps were scaled to similar values as the corresponding tunneling spectra.

However, it is not the absolute, but rather the relative value of the LDOS of different adatom sites that determines the apparent height difference in topographic measurements. Thus, we have to focus on the difference spectra of the data in Fig. 6.7(a) which are plotted as purple solid line and dots in Fig. 6.7(b), associated with the left ordinate. The good agreement between the data points extracted from DOS maps (purple dots) and the difference spectra from CITS (solid purple line) proves that the normalization described above is an effective tool to minimize setpoint effects.

As delineated in Eq. 4.23, the tunneling current is affected by an integral over the sample's DOS. Therefore, the integral $\Delta(V)$, defined in the following Eq. (6.1), gives a good estimate of the contribution of DOS effects to the apparent height in topographic measurements:

$$\Delta(V) = \int_0^V LDOS_{center}(V') - LDOS_{corner}(V')\ dV' \ . \tag{6.1}$$

The apparent height difference between "up" and "down" atoms depending on the bias voltage is also plotted in Fig. 6.7(b) as green dots with a separate ordinate on the right side. Calculating the integral $\Delta(V)$ from Eq. 6.1 results in a curve that predicts the development of this apparent height difference based on the data from STS. In order to be be matched with the experimental values, $\Delta(V)$ has to be scaled by a factor a that connects a certain change in the LDOS with the resulting movement of the tip to keep the tunneling current

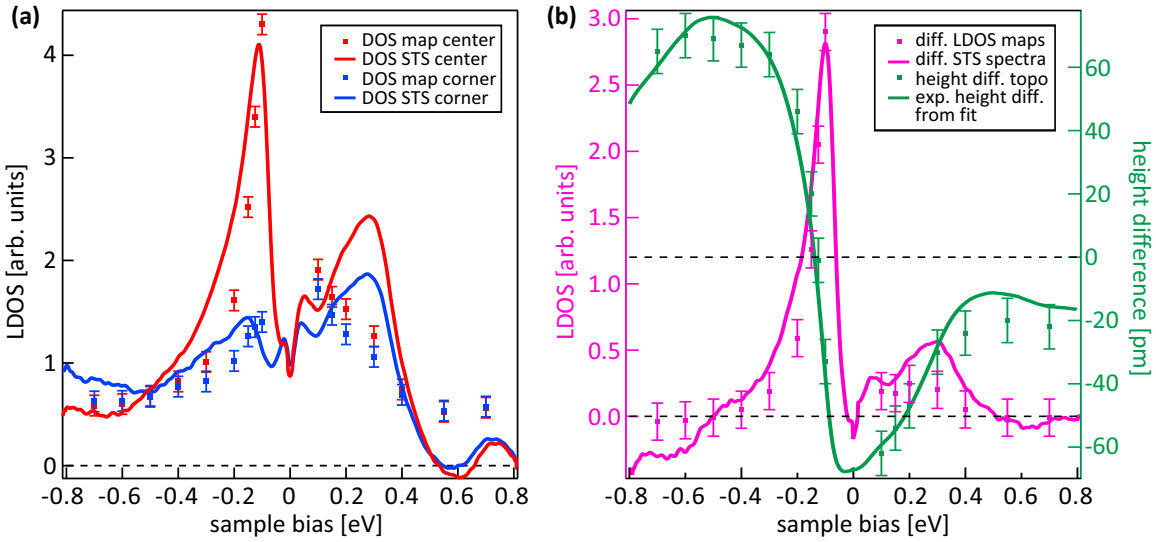

Fig. 6.7.: **(a)** Site-resolved tunneling spectra $(\mathrm{d}I/\mathrm{d}V)/(I/V)$ of $\sqrt{3}_\alpha$-Pb/Si(111) plotted as solid lines. Tunneling setpoint $V = -0.8\,\mathrm{V}$ and $I = 200\,\mathrm{pA}$. In addition, values from LDOS maps of the data series in Fig. A.1 are shown as dots. The data in the graph is scaled to a similar amplitude in arbitrary units. The error bars reflect the variations of the LDOS on nominally identical sites of the lattice. **(b)** Purple line/dots: Difference curves of the respective spectra shown in Panel (a), i.e., the difference of the red and blue line yields the purple line and the same is true for the dots. The conformity of both curves verifies that the signal from the DOS maps is well captured by the normalized LDOS, i.e., $(\mathrm{d}I/\mathrm{d}V)/(I/V)$. By integrating over the difference spectrum one retrieves a curve (green solid line) that reflects the LDOS contribution to the apparent height. By properly scaling this curve to the measured height difference (green dots), one finds that the bias-dependent changes in the apparent height closely follow those in the integrated LDOS difference. For $V \to 0$, the LDOS contribution almost vanishes which allows to extract an estimate of the true corrugation of $67(\pm 7)\,\mathrm{pm}$. The error bars again reflect the variations in LDOS or apparent height on nominally identical sites of the lattice.

constant. This factor depends on the transmission coefficient and the DOS of the tip, making a comparison with experimental data the only way to grasp it. The scaled curve then has to be shifted by an amount b which reflects the actual corrugation of the surface. To summarize, $a \times \Delta(V) + b$ is fitted to the apparent height difference and added to Fig. 6.7(b) as a green solid line. The fit reveals that this procedure is well suited to model the development of the apparent height based on data from STS since the green curve lies almost entirely within the error bars of the height difference measured from the topographic maps. A readout of $\Delta(0)$ yields that the center atoms are located about 67 pm lower than the surrounding corner atoms, i.e., $\sqrt{3}_\alpha$-Pb/Si(111) adopts a 2-up/1-down configuration in its ground state.

However, the exact value has to be taken with caution since it can be influenced by several factors. Since the corner atoms are located slightly higher than the center atom, the configuration of the tip, especially its sharpness and orbital configuration, may change

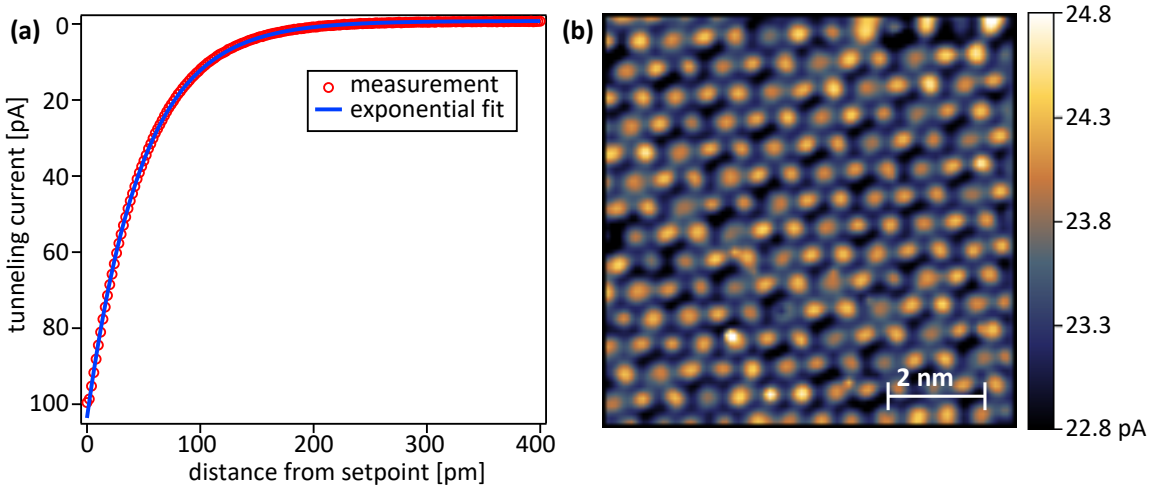

Fig. 6.8.: **(a)** Measurement of tunneling current as function of the distance from the setpoint for center and corner atoms and the exponential fit of the data. Both measurements look identical to the bare eye. Only the extraction of the fitting parameters reveal the subtle differences. **(b)** Current map $I(x, y)$ for a fixed distance $z = 70\,\mathrm{pm}$ from the setpoint. Center and corner atoms appear with an almost equally strong signal, demonstrating that variations of the local tunneling barrier height only have a negligible influence.

the result. In this sense, it is expected that sharper tips gather less signal from surrounding atoms, rendering the result obtained here a lower limit for the corrugation. Secondly, there might be a small difference in the LDOS at the Fermi level. As can be seen in the purple curve in Fig. 6.7(b) the signal is not exactly zero for $V = 0$. Although the deviation is small, the result could be altered by a few picometers. Last but not least, it is known that the local tunneling barrier height varies on a buckled surface, making the tunneling current decay stronger with increasing tip–surface separation above a local protrusion [98]. To verify that this is not an issue for the conclusions drawn above, the decay of the tunneling current with the tip–sample separation was measured by performing a grid spectroscopy $I(z)$ on the sample. Fig. 6.8(a) shows the data and an exponential fit for center and corner atoms. The results for the two atom types cannot be distinguished within this graph because the differences are too small. Instead, a 2D map at a distance 70 pm from the setpoint is shown in Fig. 6.8(b). Although the corresponding topographic map shows a 3×3 reconstruction, the atoms here feature an almost equal signal leading to a $\sqrt{3} \times \sqrt{3}R30°$ reconstruction. A determination of the decay length $\lambda = z \ln^{-1}(I(0)/I(z))$ via an exponential fit for "center" and "corner" sites separately yields $\lambda_{center} = (47.96 \pm 0.11)\,\mathrm{pm}$ and $\lambda_{corner} = (47.42 \pm 0.11)\,\mathrm{pm}$, respectively. As predicted theoretically [98], the decay length from the lower lying atoms is slightly higher. The difference is, however, only 1 %, meaning that the effect on the apparent height is below the resolution limit of STM.

Even if the exact value of the corrugation cannot be ultimately resolved, the qualitative result, i.e., the center atom being located lower than the surrounding corner atoms, is

already significant on its own. There haven't been any experimental studies on the corrugation so far, but DFT calculations based on the GGA functional have reported a contrary behavior with the center atom elevated with respect to its neighbors [133, 152]. With the experimental evidence presented here, it is obvious that the calculations done so far do not capture the physics of this system sufficiently.

6.2.4. Tracing the spectral function via quasiparticle interference

As already stated before, the patches on the surface of $\sqrt{3}_\alpha$-Pb/Si(111) manifesting the 3×3 CO are too small to permit the application of spatially averaging techniques such as ARPES. Instead, QPI is used to gain at least an indirect access to the spectral function. For energies within 50 meV around the Fermi energy, LDOS maps that reveal a distinct set of scattering vectors in their FFT images are recorded. One series of measurements is shown in Fig. 6.9, where the FFT images of LDOS maps recorded at six different bias voltages are depicted. Various sample spots were probed using a tip that has been reshaped multiple times on a Ag(111) crystal to exclude that the pattern originates from some kind of artifacts, either generated by specific defects or an unfortunately structured tip. The QPI pattern is dominant especially for energies close to the Fermi level, i.e., $V = \pm 10$ mV, but even for most of the higher voltages it was possible to extract scattering vectors – usually at the cost of larger error bars. The Bragg peaks of the 3×3 reconstructed surface, which are present in every FFT image, could be used as a natural scale bar since they are directly related to the lattice constant of silicon. Since the scanning tunneling microscope is well calibrated, they could be easily identified by their placement in reciprocal space. For bias voltages farther away from the Fermi level it was not possible to record LDOS maps where any distinct scattering vectors associated with QPI could be extracted. A possible reason is that the CO pattern gets more intense with increasing absolute bias voltage, potentially causing a weak signal from QPI to fade into the background noise.

Although the scattering pattern seems fairly complex, it can be explained by a single scattering channel. As indicated by the red circles in the bottom right half of Fig. 6.10(a), the whole pattern can be reconstructed by means of almost circular features centered around the Bragg peaks of the FFT image. This means that in addition to the scattering within the BZ which is visible in any QPI experiment, there is a particularly strong contribution of quasiparticles scattered by an additional reciprocal lattice vector. A closer analysis of measurements at different bias voltages, see Fig. 6.10(b), reveals that the length of scattering vectors increases for more positive bias voltages, pointing towards an electron-like dispersion. Since QPI patterns were found also at the smallest bias voltages, the ground state of $\sqrt{3}_\alpha$-Pb/Si(111) must be metallic CO. As already suggested from the good agreement of the QPI pattern with a model based on circles, the analysis with regard to the two high symmetry directions $\overline{\Gamma M}$ and $\overline{\Gamma K}$ does not yield a different length of the respective scattering vectors within the margin of error. The scattering vector along $\overline{\Gamma M}$ has been evaluated from the central (0,0) Bragg spot as it is usually performed for FFT images of

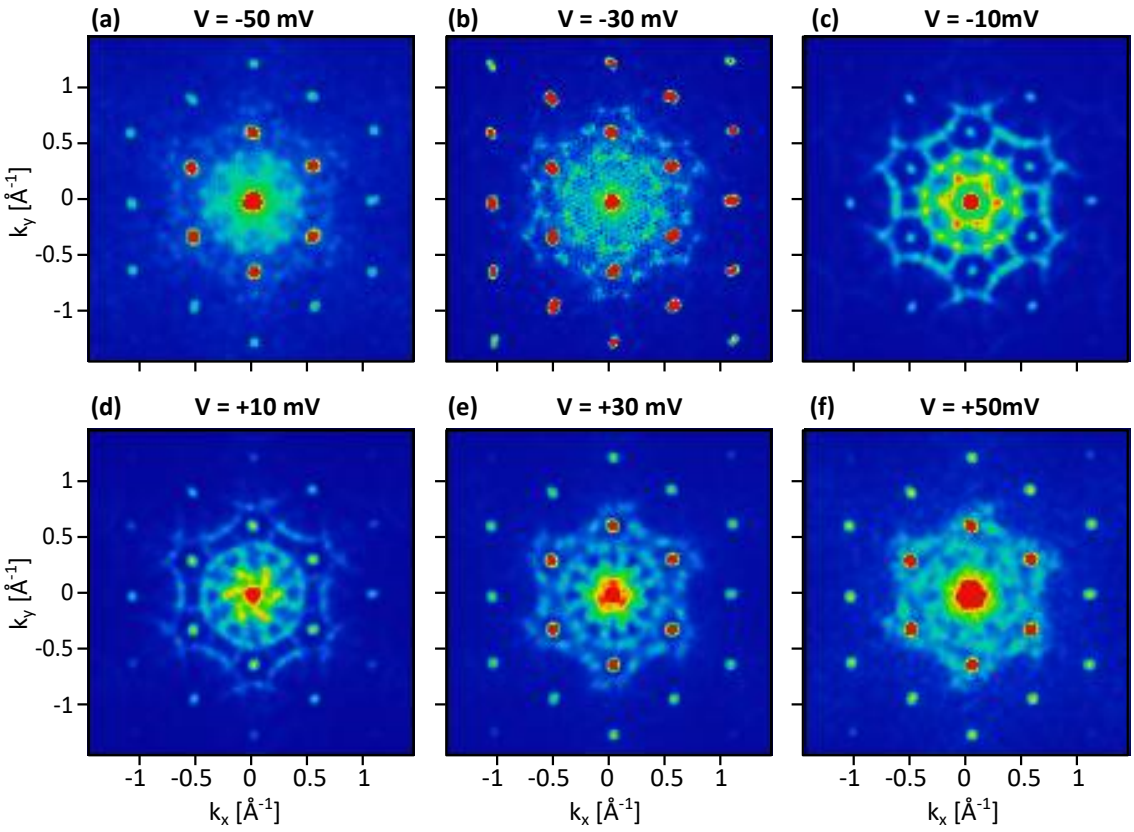

Fig. 6.9.: FFTs of dI/dV-maps measured at bias voltages between -50 mV (a) and +50 mV (f). Each FFT image features a distinct QPI pattern as well as Bragg reflexes of the 3×3 reconstructed surface. The FFT images were symmetrized to reflect the 3-fold symmetry of the substrate and smoothed with the 3-pixel Gauss filter. The tunneling conditions of the measurements these FFT images are based on are $I = 100\,\mathrm{pA}$, $V_{rms} = 2.5\,\mathrm{mV}$ and $T = 4.3\,\mathrm{K}$. Adapted from Ref. [A1].

this kind. The error bars vary between different measurements depending on the characteristic of the peak profile. For the $\overline{\Gamma K}$ direction, the scattering vector was determined in the second order (see Fig. 6.10(a) for clarification) because the identification of a clear peak turned out to be difficult for some bias voltages when only considering the lower orders. Here, the peak characteristics are very similar for each measurement, resulting in a constant error bar across all bias voltages. By interpolating the data points, one finds a scattering vector of $0.44 \pm 0.08\,\mathrm{Å}^{-1}$ at the Fermi level, again with no notable deviation with regard to the crystal direction.

Role of defects

Since the presence of defects as scattering centers is indispensable for the QPI experiments shown above, it is worth taking a closer look at their influence on the local atomic

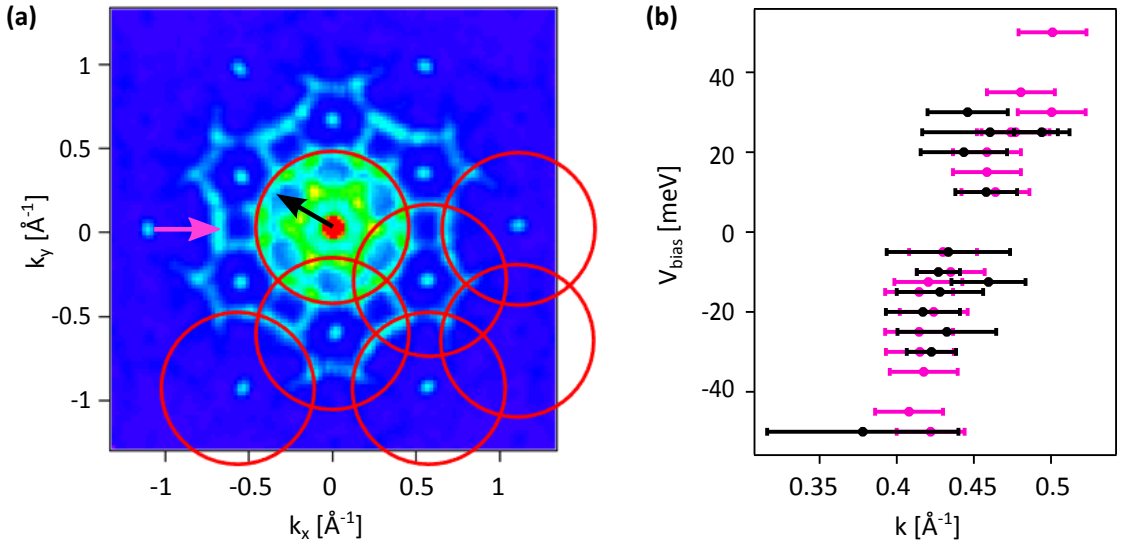

Fig. 6.10.: **(a)** Closer analysis of the QPI pattern already shown in Fig. 6.9(c). As indicated by the red circles in the bottom right part of the panel, the whole image can be qualitatively reconstructed by circular features centered at each Bragg spot. The scattering vectors are evaluated along the two 3×3 high symmetry directions $\overline{\Gamma M}$ (black arrow) and $\overline{\Gamma K}$ (purple arrow). The latter one is determined in the second order, as indicated by the arrow, because the evaluation was not possible for the first or zeroth order for many bias voltages. From Ref. [A1]. **(b)** Evaluation of the scattering vectors from different sample spots and additional bias voltages. The data is color-coded according to the scattering vectors in Panel (a).

environment. For the related system $\sqrt{3}_\alpha$-Sn/Ge(111), it has been shown that there is a temperature-dependent interplay between defects and the arrangement of the 3×3 reconstruction [153, 154]. This could of course be very relevant for QPI measurements if the intrinsic properties of the system are obscured by long-range effects originating from defects. Related studies suggest that this is not the case for $\sqrt{3}_\alpha$-Pb/Si(111) [142], but the authors did not gather results down to 4 K which is the working temperature of the QPI experiments.

In Fig. 6.11 a topographic map (a) and the corresponding LDOS map (b) of a domain with a few defects is shown. Both measurements suggest that the influence of defects is very short-ranged as the majority of the examined atoms remains unaffected by the scattered defects. This is confirmed by the line profile taken along the green path and depicted in Fig. 6.11(c). The defect itself and the directly adjacent center atoms have a modified LDOS, whereas the next-nearest neighbors of this kind all share the same signal in the LDOS map and can therefore be considered as unaffected. This was also verified for other bias voltages and various defects found during the measurements at 4 K.

The situation can, however, change when experiments are carried out close to the temperature of the phase transition, e.g., at the easily accessible 77.5 K. This is shown in the topographic and LDOS map presented in Fig. 6.11(d), (e). Several small defects can be

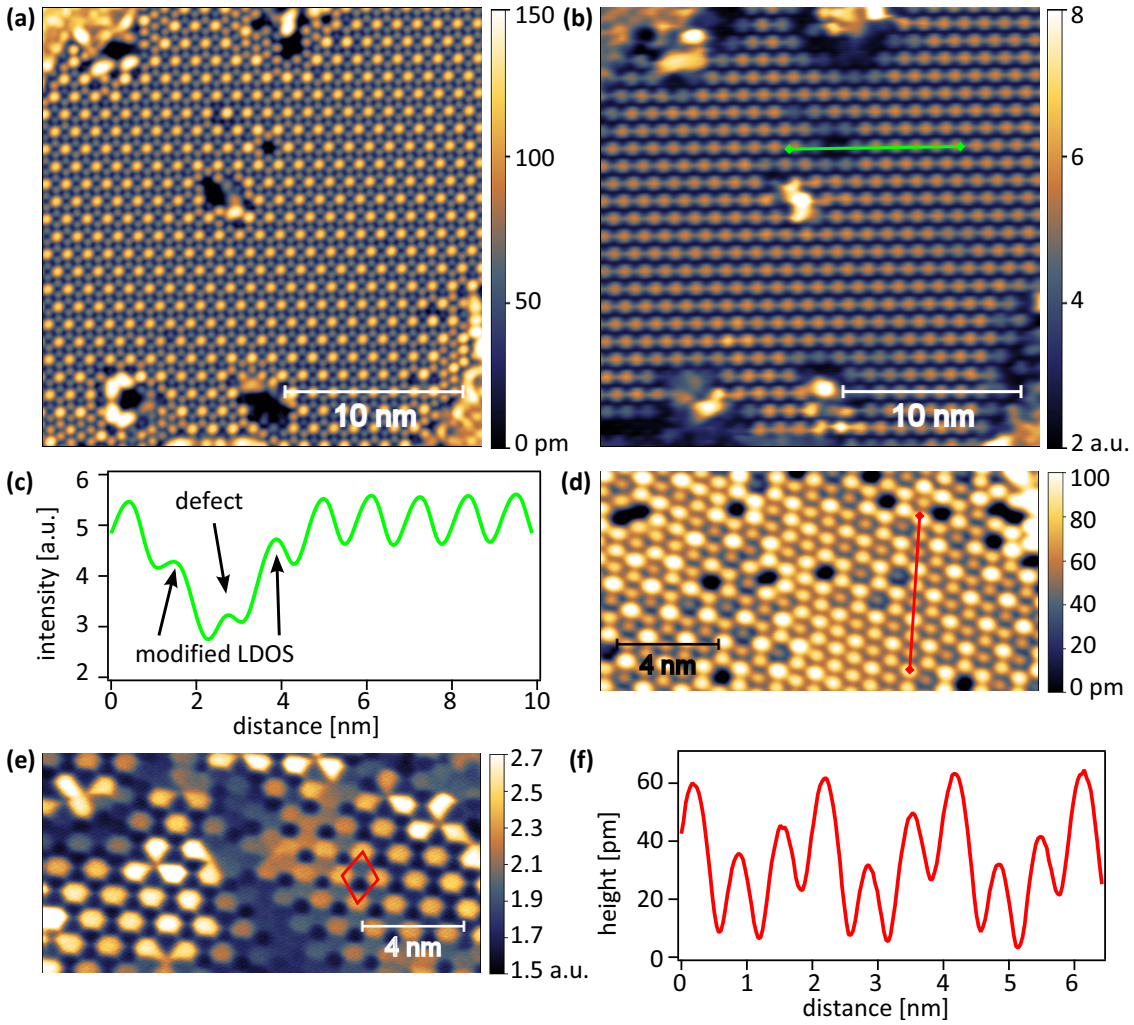

Fig. 6.11.: **(a)** Ample domain of 3×3 Pb/Si(111) as used for the QPI experiments presented earlier. Tunneling conditions were $V = -0.2\,\mathrm{V}$, $I = 200\,\mathrm{pA}$ and $T = 4.3\,\mathrm{K}$. **(b)** Conductance map taken simultaneously with the data in Panel (a). Although there are several defects, their impact mostly decays within one unit cell at LT. **(c)** Profile taken along the path indicated in Panel (b) from left to right. The distortions created by the defect only effects its immediate vicinity, i.e., the next-nearest "center" atoms remain unaffected. **(d)** Cutout of a domain of $\sqrt{3}_\alpha$-Pb/Si(111) that is heavily affected by the defects present. This was only observed at temperatures close to the phase transition at 86 K. Tunneling conditions were $V = -0.2\,\mathrm{V}$, $I = 200\,\mathrm{pA}$ and $T = 77.5\,\mathrm{K}$. **(e)** LDOS map taken simultaneously with the data in Panel (d). The defects change the energetics on the surface and even allow for a different kind of reconstruction on parts of the surface, e.g., a phase with three different types of Pb atoms within a unit cell (indicated in red). **(f)** Height profile taken along the path indicated in Panel (d) from the bottom upwards. It can be clearly identified that there are three types of atoms which differ in their apparent height. The apparent height is at least partly governed by electronic effects as the conductivity map in Panel (e) also shows three types of adatom sites in this area.

found in this region of the sample and they heavily impact the atomic reconstruction. As shown in the LDOS map in Fig. 6.11(e), the reconstruction changes locally depending on the electronic environment which is also governed by defects. On the right side of the panel there is even a new kind of 3×3 reconstruction established which features three mutually different sites both regarding their LDOS and also their apparent height as is shown in the height profile taken along the red path and shown in Fig. 6.11(f). This indicates that the energetics of $\sqrt{3}_\alpha$-Pb/Si(111) are prone to subtle changes and new phases can be induced locally by static defects for temperatures close to the phase transition. It has been shown that a phase with three mutually different sites within a unit cell, in this case a charge-ordered insulator, even is part of the regular phase diagram of the related group IV system $\sqrt{3}_\alpha$-Sn/Ge(111) where it appears at temperatures around 60 K [155].

6.2.5. Theoretical modeling of the spectral function

For a better insight into the STM results, the band structure of $\sqrt{3}_\alpha$-Pb/Si(111) is modeled theoretically. The goal is a description within an extended Hubbard model, see Eq. 3.2, in order to capture the many-body physics governing this system. As a starting point, the band structure was determined using local density approximation (LDA)-DFT simulations, see Fig. 6.12, which were performed by A. Fleszar. Concerning the Pb $6p_z$ surface state, a parametrization in terms of a tight-binding model leads to a perfect match with DFT as can be verified by tracing the red dotted dispersion in Fig. 6.12. This yields the parameters t_n which are the hopping integrals between the nth neighboring Pb atoms and which will be used for the many-body calculations described in the following. The tight binding dispersion with hoppings up to the fourth nearest neighbor is:

$$\begin{aligned} E(\boldsymbol{k}) = \; & 2t_1\left[\cos(k_x) + 2\cos\left(\frac{k_x}{2}\right)\cos\left(\frac{\sqrt{3}}{2}k_y\right)\right] \\ & + t_2\left[\cos(\sqrt{3}k_y) + 2\cos\left(\frac{3}{2}k_x\right)\cos\left(\frac{\sqrt{3}}{2}k_y\right)\right] \\ & + 2t_3\left[\cos(2k_x) + 2\cos(k_x)\cos(\sqrt{3}k_y)\right] \\ & + 2t_4\left[\cos(2k_x)\cos(\sqrt{3}k_y) + \cos\left(\frac{k_x}{2}\right)\cos\left(\frac{3\sqrt{3}}{2}k_y\right)\right. \\ & \left. + \cos\left(\frac{5}{2}k_x\right)\cos\left(\frac{\sqrt{3}}{2}k_y\right)\right] . \end{aligned} \tag{6.2}$$

The resulting hopping parameters from the fit to the DFT calculation described above are summarized in Tab. 6.1. It also contains the hopping parameters for the isostructural $\sqrt{3}_\alpha$-Sn/Si(111) which will be used as a benchmark for our results on $\sqrt{3}_\alpha$-Pb/Si(111)

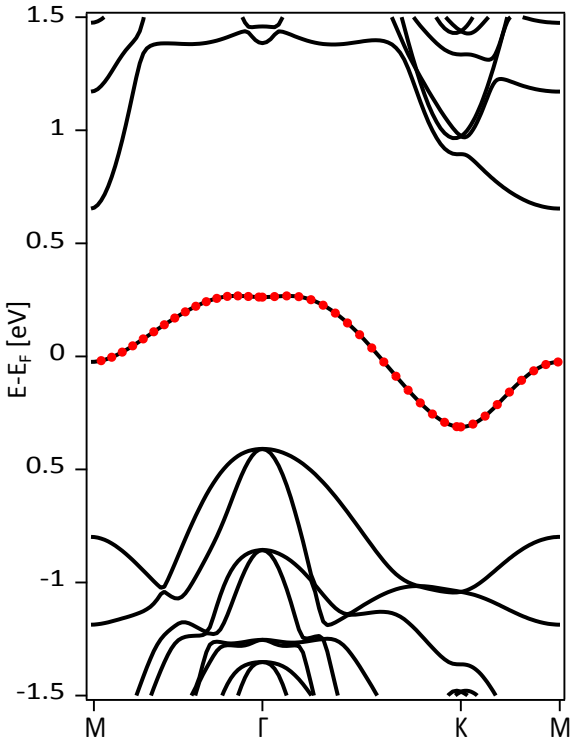

Fig. 6.12: Band structure calculation for $\sqrt{3}_\alpha$-Pb/Si(111) using LDA/DFT, depicted with black solid lines. The band crossing the Fermi level, formed by Pb $6p_z$ orbitals, is the surface state in the focus of this study. It can be perfectly described by a tight binding calculation (shown with red dots) as given in Eq. 6.2 using the hopping parameters from Tab. 6.1. The chemical potential is set to result in a half-filled surface state. Calculation performed by A. Fleszar.

since it has been intensively studied in the past and many relevant properties are already known (see Sect. 7.1 and the references therein). Regarding the tight binding dispersion, both surface systems have fairly similar hopping integrals. Nevertheless, they show different ground states, which will be captured within the many-body calculations presented in the upcoming paragraphs.

System	t_1	t_2	t_3	t_4
Pb/Si(111)	0.0585 eV	−0.0224 eV	0.0073 eV	−0.0014 eV
Sn/Si(111)	0.0522 eV	−0.0203 eV	0.0074 eV	−0.0014 eV

Tab. 6.1.: Hopping integrals for $\sqrt{3}_\alpha$-Pb/Si(111) and the closely related system $\sqrt{3}_\alpha$-Sn/Si(111). t_n is the hopping integral between a site and its nth nearest neighbor.

In recent years, there have been several efforts to calculate the spectral function of group IV triangular lattice systems. Since some of the systems are not metallic despite having a half filled surface state, electronic correlations have to be included into the calculations using dedicated many-body calculation techniques. So far, any efforts have been limited to specific systems or ground states because most methods are unable to treat the two most common phenomena, viz. magnetism and CO, on equal footing. Antiferromagnetic ground

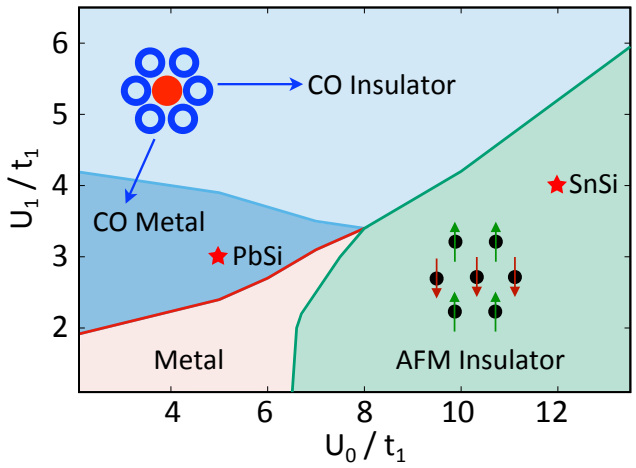

Fig. 6.13: U_0/t_1 vs. U_1/t_1 phase diagram obtained within the XVCA. For dominant onsite-repulsion U_0 an antiferromagnetic insulator with row-wise order is found, for sufficiently strong nearest-neighbor repulsion U_1 a charge-ordered insulator. For weaker interactions also metallic regimes are present. Parameters used are $t_2/t_1 = -0.383$, $t_3/t_1 = 0.125$ with $(U_0/t_1, U_1/t_1) = (5, 3)$ for PbSi and $(12, 4)$ for SnSi. The energy scale for PbSi (SnSi) is set by $t_1 = 58.5\,\text{meV}$ ($t_1 = 52.7\,\text{meV}$). From Ref. [A1].

states have an enlarged unit cell which has to be correctly implemented into many-body calculation techniques, e.g., by using cluster methods. This was done in a study by Li at al., where the Dynamical Cluster Approximation was used to calculate the spectral function of Sn/Si(111) [10]. By comparison with experimental data retrieved by ARPES, the authors found that the ground state features a row-wise antiferromagnetic spin alignment, in contrast to the 120° spiral order predicted elsewhere [156]. CO, on the other hand, can only be realized if the nearest neighbor Coulomb interaction U_1, a quantity not included in the most simple Hubbard model (Eq. 3.1), is sufficiently strong. By using an extended Hubbard model that includes the Coulomb interaction between neighboring sites, Hansmann et al. were able to set up a phase diagram of group IV triangular lattice systems on Si(111) [7]. While smaller adatoms clearly favor a Mott-insulating ground state, $\sqrt{3}_\alpha$-Pb/Si(111) is positioned in a transition region between CO, Mott-insulating and metallic phases. In light of the close energetics, the study does not yield a definite answer regarding the ground state of $\sqrt{3}_\alpha$-Pb/Si(111).

Our approach is to treat all group IV triangular lattices within a single numerical framework which we coined XVCA. It extends a well-known cluster technique, viz. the VCA, by including non-local Coulomb interaction (see Sect. 3.2 for more details). The calculations were performed by S. Rachel and M. Laubach. They map out the interacting U_0–U_1 phase diagram (see Fig. 6.13) of Hamiltonian Eq. 3.2 for single particle parameters $t_2/t_1 = -0.383$ and $t_3/t_1 = 0.125$ which are the values for $\sqrt{3}_\alpha$-Pb/Si(111) from Tab. 6.1. Although its sister compound $\sqrt{3}_\alpha$-Sn/Si(111) exhibits different hopping integrals, it turns out that the ratios t_2/t_1 and t_3/t_1 are essentially identical (with negligible t_4/t_1) for both compounds, allowing for a universal interacting phase diagram containing both $\sqrt{3}_\alpha$-Pb/Si(111) and $\sqrt{3}_\alpha$-Sn/Si(111). Other systems with a similar tendency can in principle also be added to this phase diagram in future studies.

The phase diagram reveals metallic and insulating phases. For dominating on-site interaction ($U_1/U_0 \ll 1$) we find – as expected – a conventional Mott insulator. The spin arrangement in presence of the geometric frustration turns out to favor row-wise antiferromagnetism as it is realized in $\sqrt{3}_\alpha$-Sn/Si(111) [10]. This arrangement is predicted by other theoretical methods as well [9]. In contrast, for dominating nearest neighbor interaction electrons try to avoid singly occupied sites which leads to insulating CO. For the parameters shown here, a configuration where one site per unit cell has an increased charge and the other two sites have a lower but equal charge is energetically favorable to deal with the frustrated geometry. In the insulating regime, we find the first order phase transition from CO to antiferromagnetism for $U_1/U_0 \approx 0.43$. If interactions remain weak the system becomes metallic. There is also an intermediate regime where the interactions are not strong enough to drive the system into an insulating regime. Nevertheless CO arises from the competition of local U_0 and non-local U_1.

Besides $\sqrt{3}_\alpha$-Pb/Si(111) discussed in this section, we use $\sqrt{3}_\alpha$-Sn/Si(111) which is also investigated in Chap. 7 as a second reference point. Obtaining the values U_0, U_1 from pure ab-initio methods is usually very difficult. Furthermore, the values might depend on the methodology. An example for this is already documented in literature for the correlation strength in $\sqrt{3}_\alpha$-Sn/Si(111). Using ab-initio methods the local Coulomb interaction was computed to be 1.0 eV [7] while calculations based on the Dynamical Cluster Approximation found best agreement with experiment for $U_0 = 0.66\,\text{eV}$ [10]. Thus, the correlation parameters U_0 and U_1 will be determined by comparison with experimental data. As the nearest neighbor interaction U_1 is included in the XVCA, a new and different value of U_0 is now also expected for $\sqrt{3}_\alpha$-Sn/Si(111) due to the interplay of these two correlation parameters.

The XVCA method is used to compute the k-resolved single-particle spectral function. Simulated plots on the (U_0, U_1) manifold compared with the experimental data allow us to locate the position of $\sqrt{3}_\alpha$-Pb/Si(111) and $\sqrt{3}_\alpha$-Sn/Si(111) in the phase diagram of Fig. 6.13. The best match between QPI and XVCA is obtained for interaction parameters $(U_0/t_1, U_1/t_1) = (5, 3)$. The resulting spectral function along high symmetry directions is depicted in Fig. 6.14(a). In the enlargements in Fig. 6.14(b), (c), a comparison between the relevant part of the theoretical spectral function and the scattering vectors found in QPI, see Fig. 6.10(b), is shown, demonstrating consistency over the whole energy range covered.

Since we have selected a spectral function from the $U_0 - U_1$ phase diagram it is now also possible to compare the site-specific spectra from theory with the STS data. As discussed in Sect. 4.2.3, there are certain deviations between the measured signal and the actual spectral function, which makes a comparison less significant. Therefore, the route taken here, viz. choosing the correlation parameters U_0, U_1 on basis of the QPI data and using STS as a qualitative verification is advisable. The spectra are compiled in Fig. 6.15. The occupied states are reproduced fairly well for both sites with the corner atoms acquiring very little signal while the center atoms feature a broad peak with a maximum at $V \approx -0.25\,\text{V}$. Even its overall shape is very well captured in the XVCA calculations. Note that the calculations

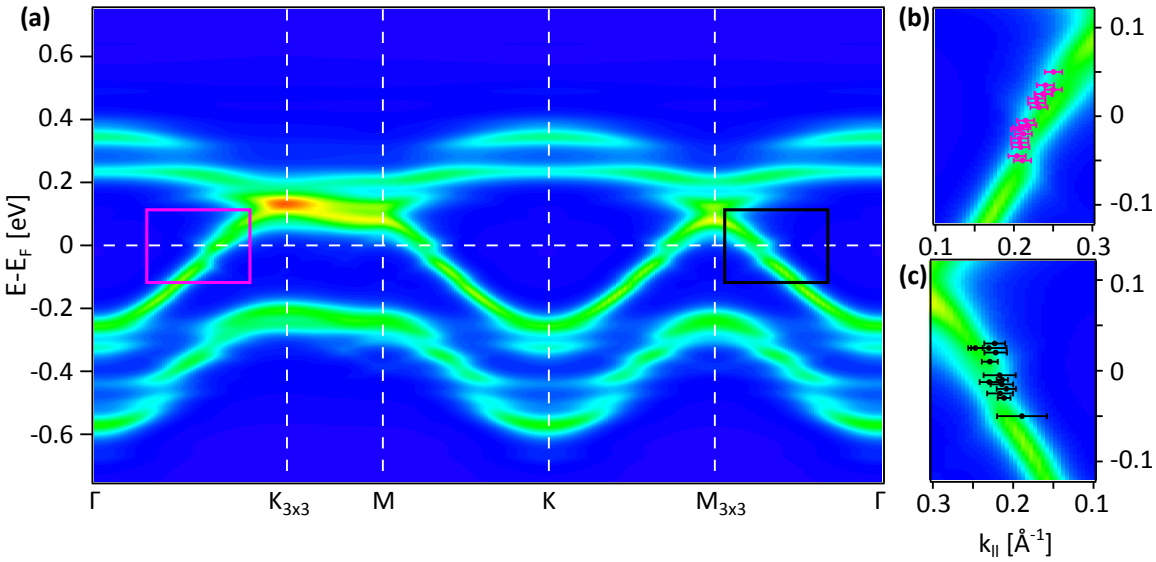

Fig. 6.14.: **(a)** Spectral function of $\sqrt{3}_\alpha$-Pb/Si(111) calculated by the XVCA using $(U_0/t_1, U_1/t_1) = (5, 3)$. These parameters were selected based on the agreement with the QPI data collected. **(b)** Enlargement of the purple box from Panel (a). The purple dots represent the wave vectors extracted from the FFT images of LDOS maps. Here, only data along the $\sqrt{3}\,\overline{\Gamma M}$ direction is displayed. **(c)** Enlargement of the black box from Panel (a). The black dots represent the wave vectors extracted from the FFT images of LDOS maps. Here, only data along the $\sqrt{3}\,\overline{\Gamma K}$ direction is displayed. Both Panel (b) and (c) show an excellent agreement between experiment and theoretical calculations. From Ref. [A1].

just result in a series of delta peaks which are broadened artificially to reflect experimental conditions. In addition, due to the limited size of the cluster used for the calculation, the signal may contain artifacts which arise as peaks in the substructure of the LDOS. For the unoccupied states, however, the agreement is not as good. Since a significant part of states in this energy regime is found far away from the Γ-point this is does not come completely unexpected and might be related to the k-dependence of the tunneling current. In addition, it is not clear to what extent other states, e.g., silicon substrate states that are not included in the XVCA, contribute to the measured LDOS.

For $\sqrt{3}_\alpha$-Sn/Si(111) the spectral function is available from ARPES which allows an even better matching with a theoretical counterpart from the XVCA because the whole electron-removal part can be utilized. Here, we take data measured with synchrotron radiation because the contribution of Si bulk bands in the relevant energy window can be effectively decreased by choosing 130 eV as photon energy. The high photon energy also allows to capture the spectral function along a chosen direction within a single measurement, thereby eliminating variations due to a changing measurement geometry. Furthermore, synchrotron radiation can provide spectra with the highest quality since the illuminated spot on the sample is usually smaller than in lab-based experiments and can be chosen accordingly.

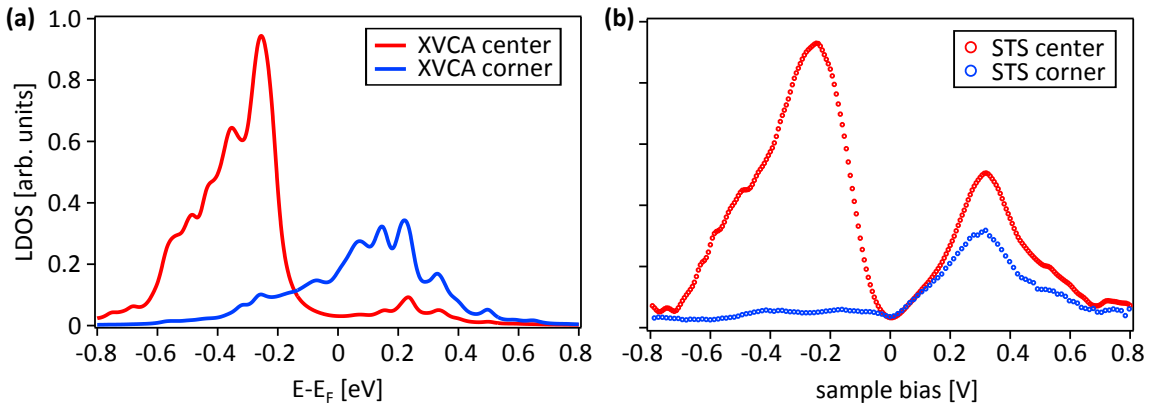

Fig. 6.15.: **(a)** LDOS of $\sqrt{3}_\alpha$-Pb/Si(111) for the two atomic sites "center" (red) and "corner" (blue) calculated by the XVCA for $(U_0/t_1, U_1/t_1) = (5, 3)$ using the spatial resolution on the cluster. **(b)** dI/dV spectra measured at the corresponding atomic sites via STS. This data was already shown in Fig. 6.4 and is just reprinted for comparison. From Ref. [A1].

The data shown in Fig. 6.16(a) is the same as the one published in Ref. [10]. For selecting a pair of values $(U_0/t_1, U_1/t_1)$, coinciding maxima of EDCs taken at different high symmetry points were used as a criterion. This resulted in the choice of $(U_0/t_1, U_1/t_1) = (12, 4)$ and the associated spectral function is depicted in Fig. 6.16(b). This means that $\sqrt{3}_\alpha$-Sn/Si(111) is located on the far right side of the phase diagram Fig. 6.13. In this region, the XVCA predicts row-wise antiferromagnetism as the ground state, in line with the experimental evidence [10]. The correlation parameter U_0 changed marginally from 0.66 eV in Ref. [10] to 0.63 eV in this work. Since U_1 enters the calculations as a new parameter, such small variations are expected. The two curves in Fig. 6.16 show a good agreement in their dispersion and even fine details like the increased intensity around the M-point are captured within the theoretical model. Other features, however, like the width of the band or the intensity of the shadow band around the Γ-point are not reproduced with the same accuracy.

In summary, the XVCA method is a universal tool to calculate the spectral function of 2D triangular lattices. Both charge- and spin-ordered ground states are predicted correctly by this method using $\sqrt{3}_\alpha$-Pb/Si(111) and $\sqrt{3}_\alpha$-Sn/Si(111), respectively, as prototype systems. The phase diagram in Fig. 6.13 can be used in the future to predict ground states of related adatom systems or look for specific correlation parameters in the search for exotic phases, e.g., upon doping.

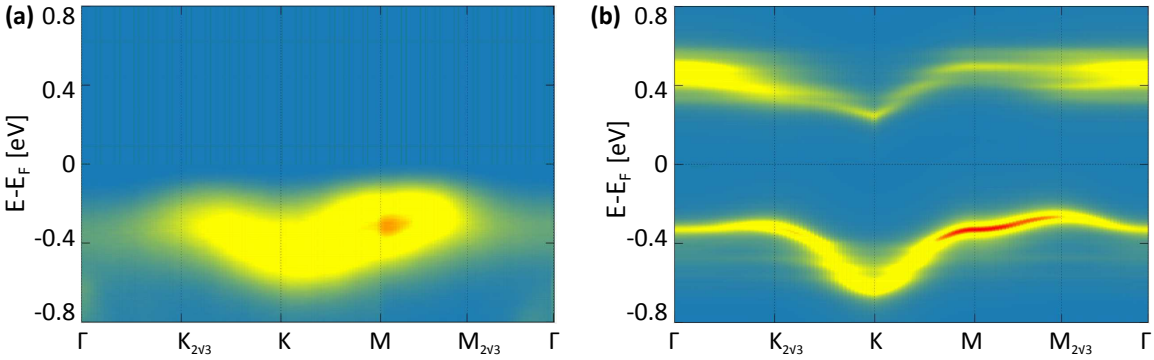

Fig. 6.16.: **(a)** Spectral function of $\sqrt{3}_\alpha$-Sn/Si(111) measured with ARPES. Collinear antiferromagnetism was identified based on the backfolding at the $2\sqrt{3} \times 2\sqrt{3}$ zone boundaries. The graph was reproduced using data from Ref. [10]. The photon energy was 130 eV, the sample temperature 60 K. **(b)** Spectral function of $\sqrt{3}_\alpha$-Sn/Si(111) calculated within the XVCA for the selected correlation parameters $(U_0/t_1, U_1/t_1) = (12, 4)$. The corresponding ground state according to the phase diagram in Fig. 6.13 is collinear antiferromagnetism as well. From Ref. [A1].

6.2.6. Influence of substrate doping and temperature

Doping a group IV triangular lattice does not necessarily require the deposition of donors or acceptors as it is performed for $\sqrt{3}_\alpha$-Sn/Si(111) in Chap. 7. It was shown that dopants in the substrate can already affect the electronic structure of the adatom system using the example of $\sqrt{3}_\alpha$-Sn/Si(111) [27, 40, 157]. Therefore, pertinent experiments were also conducted for $\sqrt{3}_\alpha$-Pb/Si(111) within this thesis. The resulting tunneling spectra are shown in Fig. 6.17. Note that substrates with a low doping concentration do not offer sufficient conductivity at $T = 4.3$ K to measure the intrinsic properties of an adatom system grown thereon [41]. Consequently, this comparison is made at 77.5 K while data taken at 4.3 K can serve as a reference to detect temperature-induced effects.

By comparing the purple and orange spectra in Fig. 6.17, i.e., STS of films grown on substrates of high and low p-doping, respectively, it becomes evident that substrate doping does not play a crucial role for the electronic properties of $\sqrt{3}_\alpha$-Pb/Si(111) when probed at 77.5 K, at least within the range of available substrates within this thesis. Both experiments reveal a very similar behavior around the Fermi level and small differences might be attributed to the different respective setpoints. At higher energies ($|V| > 0.4$ eV) the spectra from the highly-doped substrate show significantly more weight. As this is seen both for center and corner atoms in a similar fashion, a contribution of additional tip states is likely, especially because effects of substrate doping are expected rather close to the Fermi level. This reasoning is also supported by comparing with measurements at 4.3 K (blue spectra) which show a lower signal at these high energies despite being performed on a substrate with the same specification.

Extending this comparison to the region around the Fermi level, however, reveals that the dominant peak in the unoccupied states is accompanied by a small side peak at lower

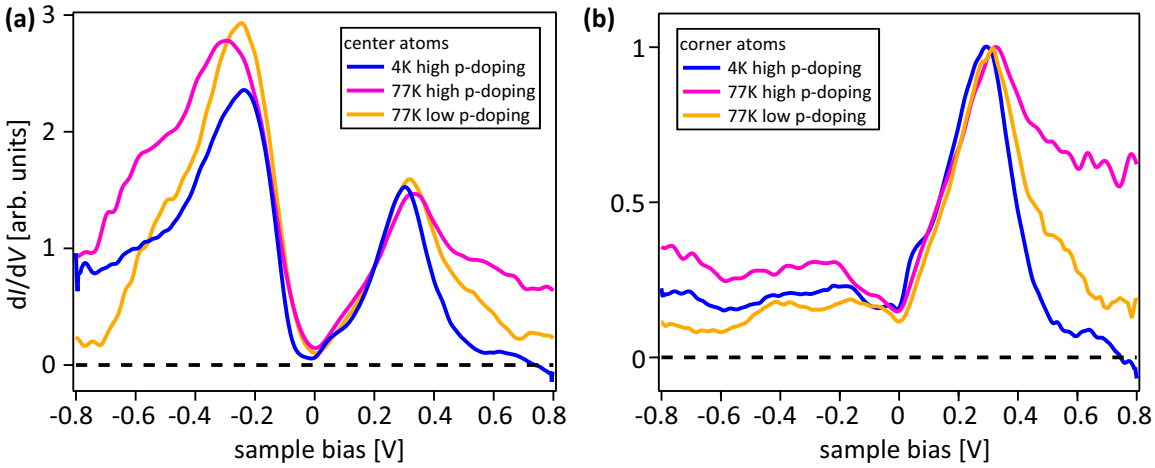

Fig. 6.17.: STS of $\sqrt{3}_\alpha$-Pb/Si(111) on substrates of high and low p doping, measured at different temperatures. Note that substrates with low doping cannot be used for measurements at 4.3 K because their conductivity at low temperature is not sufficient. Panels (a) and (b) show spectra taken on center and corner sites of the 3×3 reconstructed surface, respectively. To improve comparability, the height of the dominating peak in the unoccupied states of corner atoms has been normalized to 1. Spectra from center atoms have been normalized accordingly with the resultant numbers. The setpoints for the CITS measurements were $V = 0.1$ V and $I = 10$ pA for the highly doped substrates at 4.3 K, $V = 0.1$ V and $I = 10$ pA for the highly doped substrates at 77.5 K and $V = -0.125$ V and $I = 20$ pA for the lowly doped substrates at 77.5 K.

energy at LT. A comparison with spectra measured on strongly n-doped samples at 4.3 K, see Sect. 6.2.8 and Ref. [56], reveals that this peak appears for strong n-doping, too. It has to be noted that the side peak being invisible at $T = 77.5$ K is not just an effect of the thermal influence on the resolution because $k_B T$ only amounts to 6.6 meV at 77.5 K, which is considerably lower than the width or the separation of the two peaks. Therefore, the feature is possibly sensitive to other temperature-dependent scattering processes that lead to the observed suppression. The peak has a similar energy as the substrate-induced peak (SIP) observed in $\sqrt{3}_\alpha$-Sn/Si(111), both within this thesis (see Sect. 7.2.4) and in Ref. [40]. Nevertheless, in the case of $\sqrt{3}_\alpha$-Pb/Si(111) this feature is not detectable at 77.5 K and in general less pronounced when compared to $\sqrt{3}_\alpha$-Sn/Si(111) at the same substrate doping levels. Furthermore, it does hardly change the signal strength at the Fermi level. This is also in contrast to the findings in $\sqrt{3}_\alpha$-Sn/Si(111) where the system becomes more metallic with increased p-doping. Thus, this feature cannot be attributed to a SIP and its origin remains open for future studies.

When comparing the energy position of the most prominent peaks, a slight shift among the different spectra stands out. Including also other measurements not shown here reveals that slightly different energy positions can be found across all measurements. There is no consistent trend of the peak positions with regard to the examined domain size, the chosen setpoint or the magnitude of the applied tunneling current. As seen in Fig. 6.17, it also

does not depend solely on the substrate doping or the temperature. Therefore, it is either due to a complex interplay of multiple parameters or related to small variations of the tip properties which can not be kept completely unchanged over the course of an extensive series of measurements.

6.2.7. Other mechanisms able to drive a phase transition

Besides CO driven by electronic correlations, there are two other mechanisms which are in principle able to provoke such a phase transition towards a 3×3 reconstruction, viz. a CDW driven by Fermi-surface nesting and dynamical fluctuations of atoms that are frozen at a critical temperature. Both mechanisms have also been discussed for other group IV triangular adatom systems [4, 5, 158]. The following section will provide arguments why they are not relevant for the phase transition in $\sqrt{3}_\alpha$-Pb/Si(111).

To check for the possibility of Fermi surface nesting, we calculated the electronic susceptibility $\chi_0(\vec{q})$ within the $\sqrt{3} \times \sqrt{3}R30°$ BZ based on the DFT band structure presented in Sect. 6.2.5. The results are shown in Fig. 6.18 for the situation (a) without and (b) with SOC. The ordering vector of the CO state observed in experiment is $\vec{Q} = (\Gamma, K_{\sqrt{3}})$. The susceptibility does not show any divergencies or maxima close to the corners of the BZ which would indicate the tendency to form a CDW mediated by Fermi surface nesting. Since the influence of SOC in this system can be described almost entirely by the Rashba effect [56], the close resemblance of the two panels in Fig. 6.18 is not surprising. The idea of a CDW driven by Fermi surface nesting as an origin of the 3×3 reconstruction was also discarded for other group IV triangular lattices for the very same reason. Although claimed initially [4], a close inspection of the Fermi surface did not result in a sufficiently strong nesting for Ge-based systems [5, 122]. In summary, electronic nesting is currently not held responsible for the transition to a 3×3 phase found in many group IV triangular lattice systems, indicating that many-body physics could play an important role for all of them.

A second mechanism to be considered is based on dynamical fluctuations of adatoms, a model already mentioned in the beginning of Sect. 6.2. Below a critical temperature, this vertical motion is frozen and the adatoms are arranged in the energetically most favorable configuration. Since these fluctuations would happen on a timescale of picoseconds [158], STM measurements are not suitable to give a definite answer on the validity of this model. It is, however, possible to take a look from a theoretical point of view. Arguments favoring a vertical distortion as the origin of the LT phase in $\sqrt{3}_\alpha$-Pb/Si(111) are based on DFT calculations which predict a 1-up/2-down configuration for the ground state [56, 133, 152, 159]. However, it should be noted that this result requires the use of the GGA functional while no distortion is found using LDA. For $\sqrt{3}_\alpha$-Sn/Ge(111) it was even shown that the inclusion of electronic correlations can result in a disappearance of a topographic buckling on the DFT+U level [6]. Since the result of the calculation seems to depend critically on the employed functional or the inclusion of electronic correlations, the predictive power of DFT seems to be very limited in this regard. As the experimental evidence in Sect.

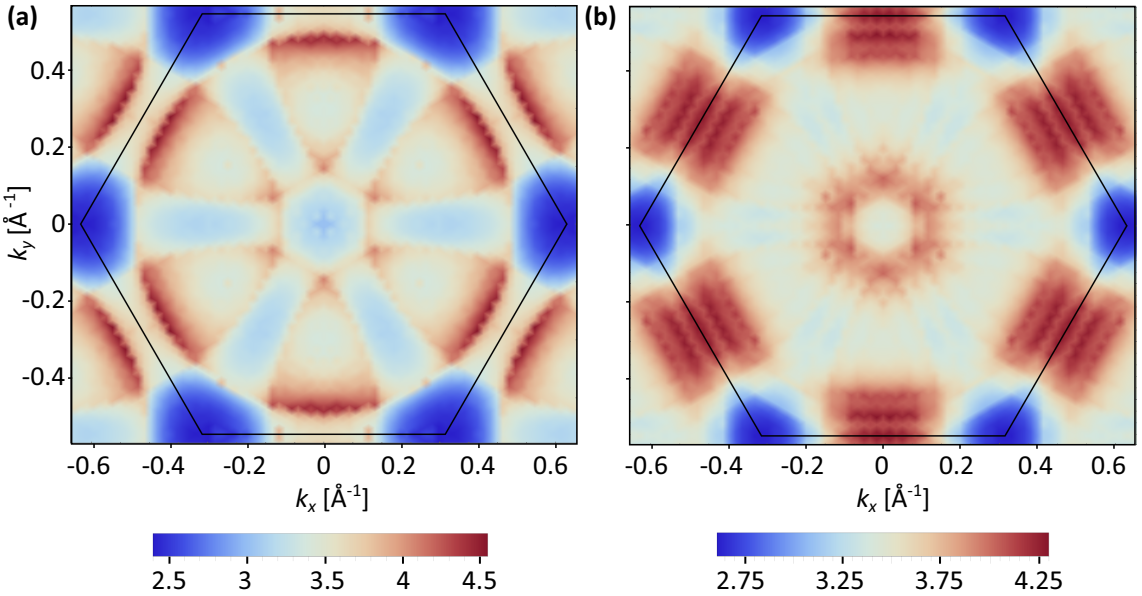

Fig. 6.18.: **(a)** Electronic susceptibility of $\sqrt{3}_\alpha$-Pb/Si(111) based on DFT calculations of the $\sqrt{3} \times \sqrt{3}R30°$ reconstructed surface, i.e., the system is not in the CO state. The corresponding BZ is marked with black lines. The ordering vector observed in experiments $\vec{Q} = (\Gamma, K_{\sqrt{3}})$ is associated with a minimum in the susceptibility calculations, excluding a phase transition driven by nesting. **(b)** Analogous data when SOC is included in the DFT calculations. Calculations performed by S. Rachel. From Ref. [A1].

6.2.3 indubitably revealed a 2-up/1-down configuration instead, more elaborate theoretical methods are required to resolve the question of the atomic buckling theoretically.

6.2.8. Comparison with other published results

The $\sqrt{3}_\alpha$-Pb/Si(111) system has already been investigated by other groups before and this section will serve as a compilation of important results from the literature in view of the novel insights collected within this thesis. Due to a similar approach, i.e., STS and QPI supported by theoretical calculations, the recent paper by Tresca et al. [56] is a natural first candidate for this comparison. Since the authors used substrates with high n-doping, their tunneling spectra can serve as another benchmark to study the influence of substrate doping on the properties of the adatom system on top. Spectra averaged over several unit cells, i.e., including both center and corner sites, are shown in Fig. 6.19. There is a remarkably close correspondence in the unoccupied states. Therefore, this voltage range was used to scale the spectra with respect to each other. Both spectra show a negative differential resistance at about 0.75 V and a small shoulder right above the Fermi level. In Sect. 6.2.6 this was not attributed to substrate doping but instead interpreted as a temperature effect, despite its similarities with the SIP found in $\sqrt{3}_\alpha$-Sn/Si(111) which is heavily depending

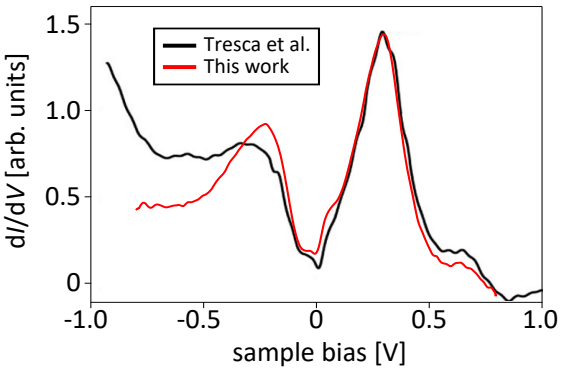

Fig. 6.19: Comparison of STS on $\sqrt{3}_\alpha$-Pb/Si(111) between data measured within this work (red) and data published in Ref. [56] (black). The latter consists of spectra averaged in an area of $9\,\mathrm{nm}^2$ (setpoint $V = -1\,\mathrm{V}$, $I = 200\,\mathrm{pA}$) while the data from this work is an average of spectra from corner and center sites, weighted 2:1 in accordance with their relative occurrence (setpoint $V = -0.125\,\mathrm{V}$, $I = 20\,\mathrm{pA}$). Differences, prominent especially for negative bias voltage, are likely associated to tip effects. Reprinted with permission from Ref. [56]. Copyright (2020) by the American Physical Society.

on the substrate doping. This interpretation is consequently strengthened in view of this comparison. There is also a small offset between the curves at the Fermi level. This can be related to the different setpoints used for both measurements or the way spectra are averaged in the respective case. While Tresca et al. included all spectra within a small area, the data from this work is an average of spectra that were measured exactly on corner and center sites and weighted according to their relative occurrence. In the occupied states the agreement is less striking, but could certainly be explained within the typical variance associated with tip preparation. In summary, the consistency of both experiments is not in doubt.

This leads us to the comparison of the QPI results. By performing CITS in an energy range of 5 meV around the Fermi level, Tresca et al. were able to retrieve a dI/dV map that is used to reconstruct a possible Fermi surface. Assuming that they missed a factor of $\sqrt{3}$, which is likely when looking at the manuscript as a whole, their result for the scattering vector at the Fermi level agrees well with the value determined in Sect. 6.2.4. However, there are also differences since Tresca et al. interpret their findings in terms of a spin-split Fermi surface. The scattering of quasi-particles conserves spin if defects are non-magnetic, leading to a suppression of scattering channels that are exclusively present in the case of a spin-split Fermi surface [160, 161]. A smoking-gun test, e.g., QPI measurements with magnetic defects, is still missing and could be a fruitful experiment for future studies. However, this can be a laborious study as the appearance of additional scattering channels can depend delicately on the type of system or adatoms [162, 163]. With Pb being a very heavy atom, SOC is expected to be of substantial importance and a band structure not degenerate in spin seems plausible. Nevertheless, the data presented in Ref. [56] does not allow for this conclusion and, as we have seen in this chapter, all experimental findings can be explained in a picture without SOC so far.

Now the results regarding the vertical displacement of atoms of the 3×3-reconstructed surface is compared with other experimental studies. In pertinent publications the evidence

is almost exclusively based on results from DFT calculations. The sole exception seems to be Ref. [159] where X-ray photoemission spectroscopy (XPS) and photoelectron diffraction of the Pb 5*d* core level are used to get an insight into the surface morphology. According to the authors, the Pb 5*d* core level at a total coverage of 1/3 ML can be modeled by two (spin-split) peaks that can be attributed to the "up" and "down" atoms, respectively. By comparison with theoretical models they find the configuration to be 2-up/1-down in agreement with the conclusions drawn in Sect. 6.2.3. In those samples, however, the LT 3×3 does not form due the presence of Si defects which account for up to 10% of the total adatoms [159]. The authors claim that the structural properties are altered around defects and Pb atoms are pushed up in vicinity of Si adatoms. Accordingly, the intrinsic configuration without defects would still be 1-up/2-down. Since the surface examined in this study hardly contains any 3×3 reconstructed areas, the significance of this results for the α-phase without any defects is low. Therefore, the findings made within this thesis provide the first experimental evidence of the atomic configuration which is 2-up/1-down.

As discussed above, there were several attempts to model the band structure of $\sqrt{3}_\alpha$-Pb/Si(111) but for a meaningful comparison with our results a spectral function as calculated in Ref. [7] is necessary. The authors of said study also set up a phase diagram of the electronic interaction parameters (U_0, U_1) for group IV triangular lattices. In this case dynamical mean-field theory is used to calculate the associated spectral functions. The individual representatives $\sqrt{3}_\alpha$-X/Si(111) (X = C, Si, Sn, Pb) are placed on the phase diagram at values (U_0, U_1) based on results from ab-initio calculations. Although the actual interaction parameters for the formation of certain ground states are different, the qualitative appearance of the phase diagram is very similar to the one in Fig. 6.13. $\sqrt{3}_\alpha$-Pb/Si(111) is also located in a region between metallic, CO and Mott-behavior, however, the associated spectral functions (both an insulating and a metallic solution are presented) do not match with the experimental evidence. As the STS results in this thesis show, an insulating solution is not correct and the metallic solution features an extremely flat band at the Fermi level in disagreement with the dispersion found in Fig. 6.10. This demonstrates the difficulty to retrieve the correct values of the correlation parameters (U_0, U_1) and the challenges that arise when comparing results obtained with different numerical methods. Fitting unknown parameters to the experimental evidence as done in Sect. 6.2.5 naturally leads to the best agreement between measurements and calculations.

In summary, this work provides evidence that the ground state of Pb/Si(111) is CO driven by electronic correlations. While this was already proposed elsewhere, viz. Ref. [7], this study is using STS and QPI to set corner points for the subsequent calculation of the spectral function with the newly developed XVCA. These findings are consistent with all pertinent experimental evidence, indifferent if found here or in literature. Other approaches are at least partly in conflict with the results found in Sect. 6.2.3 or 6.2.4. The impact of SOC on the band structure remains still under debate because experimental evidence of spin-polarized bands is missing so far.

6.3. Insulating behavior in a dilute Pb lattice at half filling

Along with their interest in the α-phases of the various group IV triangular lattices, people found that there is another stable phase with lower coverage for some representatives which is usually referred to as mosaic or γ-phase [164–166]. The key difference is that half of the original adatoms are substituted by atoms from the substrate, leading to an effective coverage of 1/6 ML. However, the different elements are not distributed regularly within the triangular lattice, i.e., the system is chemically disordered. For Pb/Si(111), such a system can be realized as well [131, 132] and its electronic properties will be investigated in the following. The structure was already introduced at the beginning of Chap. 6 in Fig. 6.1(b). With our knowledge from the previous chapter, an investigation of possible reconstructions or CO when Pb adatoms are partly replaced by silicon can be instructive.

6.3.1. Preparation of $\sqrt{3}_\gamma$-Pb/Si(111)

The preparation of $\sqrt{3}_\gamma$-Pb/Si(111) is closely following the recipe already given in Sect. 6.2.1 for the α-phase and only the annealing step has to be altered. A few monolayers of Pb are evaporated on a freshly flashed Si 7×7 substrate held at RT and subsequently the sample is annealed at 500°C for 3 min. Due to its high thermal stability, $\sqrt{3}_\gamma$-Pb/Si(111) is the only phase remaining on the surface when annealing at this temperature [131], allowing for an investigation with spatially averaging techniques. A successful preparation is then verified by LEED which features a $\sqrt{3}\times\sqrt{3}R30°$ reconstruction as depicted in Fig. 6.20(a). The diffraction pattern empirically shows an increased intensity for the central $\sqrt{3}\times\sqrt{3}$ as well as three of the 1×1 spots [131] at an electron energy of 80 eV, which can be used to further verify a successful preparation already by means of LEED. However, since other Pb/Si(111) phases have the same reconstruction this can only act as a preliminary test. An inspection with STM reveals a surface as the one shown in Fig. 6.20(b) covering the whole sample. An investigation of an interface of $\sqrt{3}_\gamma$-Pb/Si(111) and Si 7×7 revealed that the Pb atoms are associated with the bright protrusions while Si atoms have a lower apparent height at the bias voltage chosen here [132]. The Pb atoms are hence not distributed randomly on the surface but they tend to form structures of meandering chains. By counting Pb atoms in a 900 nm^2 section of Fig. 6.20(b), the stoichiometry of the surface was examined. The result was that 49 % of the adatoms are Pb which is close to the nominal value of every other adatom.

6.3.2. Scanning tunneling microscopy of $\sqrt{3}_\gamma$-Pb/Si(111)

To get a deeper insight into this peculiar appearance of the STM images, topographic maps and the corresponding LDOS were measured over a wide range of sample bias voltages. It turns out that there are three sections with regard to the applied bias voltage which show a qualitatively different behavior. A representative image from each section was selected for the compilation in Fig. 6.21.

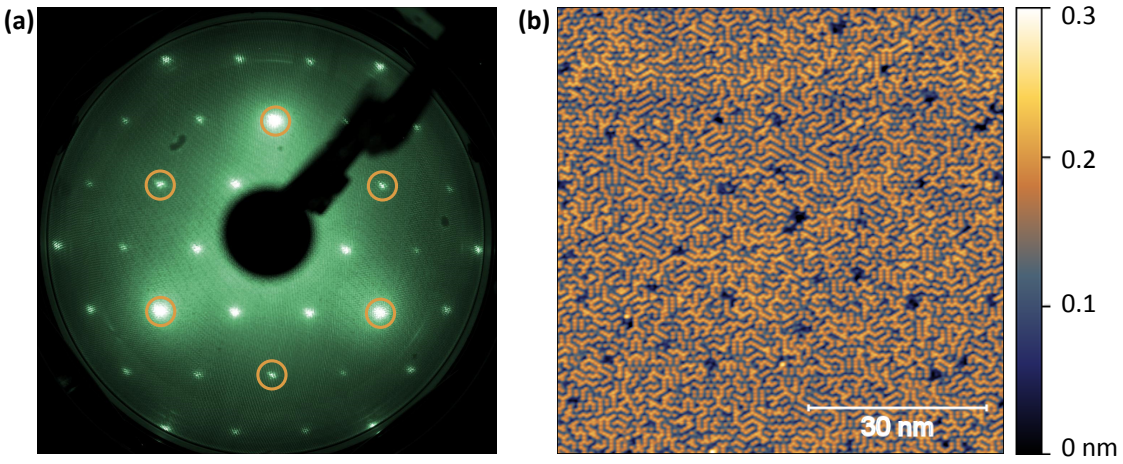

Fig. 6.20.: **(a)** LEED image of $\sqrt{3}_\gamma$-Pb/Si(111) taken with an electron energy of 80 eV. The image shows reflexes of a 1×1 and $\sqrt{3} \times \sqrt{3}R30°$ reconstruction, with the former being marked by yellow circles for orientation. **(b)** Corresponding topographic STM map showing the characteristic chain-like pattern of $\sqrt{3}_\gamma$-Pb/Si(111). The image was taken at $T = 4.3\,\mathrm{K}$, $V = -1\,\mathrm{V}$ and $I = 20\,\mathrm{pA}$. At this bias voltage, Pb atoms appear as bright protrusions and Si atoms as depressions in between. There are no other phases present on the surface.

- For bias voltages $V > 1.75\,\mathrm{V}$, as in Fig. 6.21(a), (b), Pb atoms appear brighter than Si atoms. The pattern of the Pb atoms is also explicitly visible in the corresponding LDOS map. Nevertheless, there is also some spatial variation of the LDOS evident which ranges over the distance of several adatoms. It does not seem to be influenced by the local configuration of Pb and Si adatoms but could rather be related to vacancies or defects in the underlying substrate. The distribution of vacancies, well visible as dark holes in Fig. 6.21(c), is at least somewhat correlated with an increased LDOS in the Fig. 6.21(b).

- For bias voltages $1.5\,\mathrm{V} > V > 0.5\,\mathrm{V}$, as in Fig. 6.21(c), (d), Pb and Si atoms can hardly be distinguished, neither in the topographic nor in the LDOS maps. Only some Pb atoms have a clearly increased apparent height. Here, this is related to the local atomic configuration since Pb atoms that appear bright in Fig. 6.21(c) have many other (in most cases four) Pb atoms as their nearest neighbor. This is illustrated by means of three examples in Figs. 6.21(a), (c) where the positions of identical atoms are marked in both images by red circles.

- For bias voltages $V < -0.4\,\mathrm{V}$, as in Fig. 6.21(e), (f), Pb atoms again appear mostly brighter than Si atoms while the atomic pattern cannot be rediscovered in the LDOS maps. However, some exceptions can be found, where Si atoms appear higher than Pb atoms in the topographic maps. This happens in areas where a Pb atom has only Si atoms as nearest neighbors, pointing again towards a strong influence of the local chemical

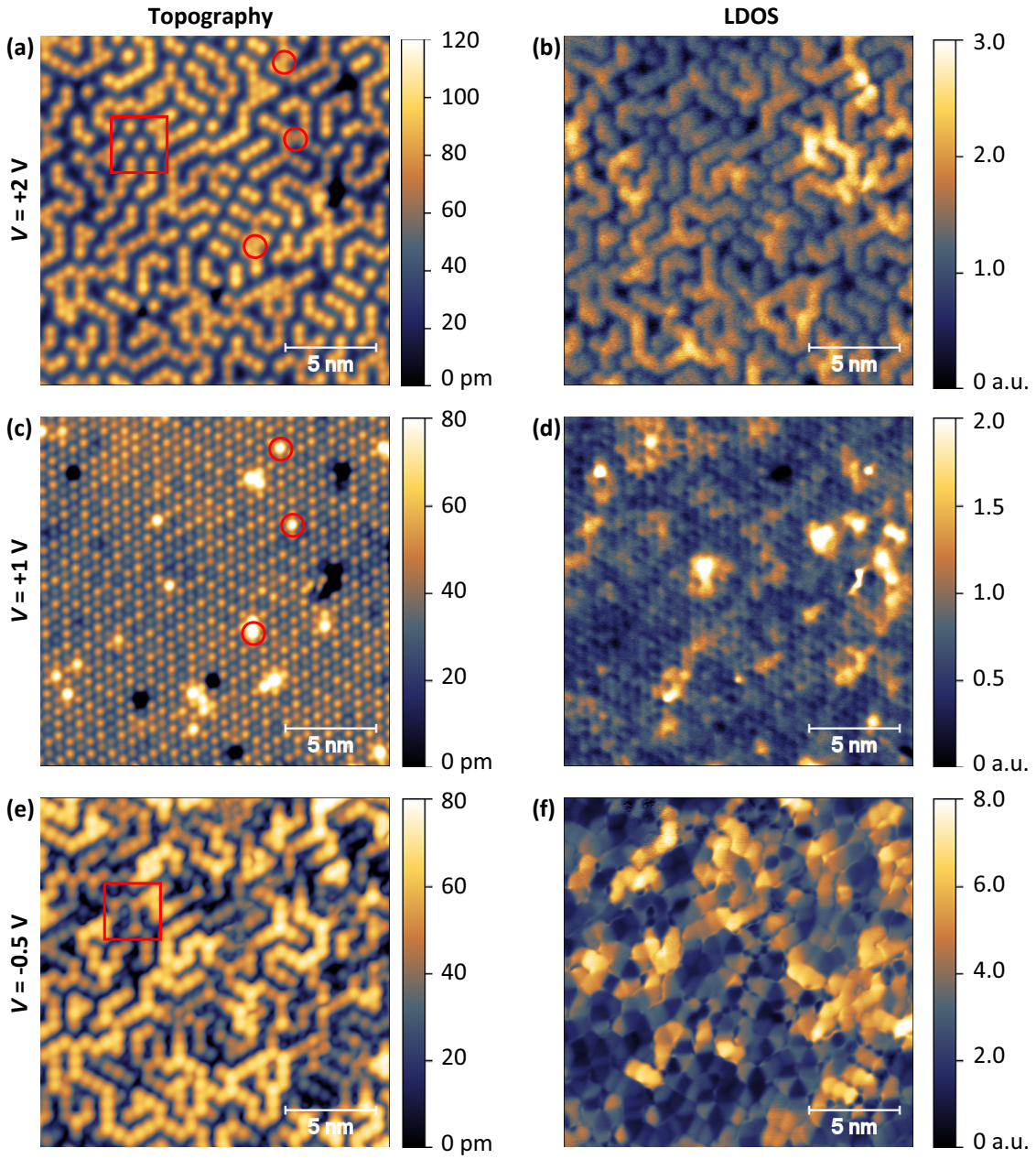

Fig. 6.21.: Topographic scans (left) and corresponding LDOS maps (right) of $\sqrt{3}_\gamma$-Pb/Si(111) at bias voltages (a, b) $V = +2.0\,\mathrm{V}$, (c, d) $V = +1.0\,\mathrm{V}$ and (e, f) $V = -0.5\,\mathrm{V}$. Apart from a minuscule shift due to thermal drift, each panel shows the exact same region on the sample. The red circles in Panels (a) and (c) mark Pb adatoms that show an increased apparent height at $V = +1.0\,\mathrm{V}$. By tracking their position it was found that they all share a high number of Pb atoms as nearest neighbors. The red boxes in Panels (a) and (e) indicate an area where Si atoms show an increased apparent height for $V = -0.5\,\mathrm{V}$, even higher than some of the Pb atoms nearby. By again tracking their positions and comparing with Panel (a), it becomes evident that this happens close to Pb adatoms which have only Si atoms as nearest neighbors. All measurements were performed at $T = 4.3\,\mathrm{K}$ and $I = 200\,\mathrm{pA}$.

environment. An example for this is highlighted in Figs. 6.21(a), (e) where the red boxes mark identical areas on the sample with Si atoms having a higher apparent height than some Pb atoms nearby.

For bias voltages $0.5\,\mathrm{V} > V > -0.4\,\mathrm{V}$, it is not possible to perform STM due to the insulating behavior of the surface. In summary, the $\sqrt{3}_\gamma$-Pb/Si(111) system shows a complex behavior, both regarding topographic measurements and LDOS maps. While some effects only depend on the immediate neighborhood of an adatom, there are other variations that extend over a few nanometers. This can of course also influence the vertical positions of adatoms, adding another variable. In the next section results from CITS will be included to further help our understanding.

6.3.3. Local electronic properties of $\sqrt{3}_\gamma$-Pb/Si(111)

From the LDOS maps in the last section it already became clear that the local chemical environment has a significant impact on the properties of adatoms in $\sqrt{3}_\gamma$-Pb/Si(111). By performing CITS and selecting spectra not only by the element of the examined adatom but also under consideration of surrounding elements, this finding is now substantiated. Fig. 6.22(a) shows spectra of Pb atoms assorted by the number of directly neighboring Pb adatoms. Pb atoms with five or even six neighboring Pb atoms are only found very rarely and are not included here. As already pointed out in the preceding section, $\sqrt{3}_\gamma$-Pb/Si(111) is insulating. The band gap found in the LDOS measured on individual atoms, however, varies considerably. The spectra mostly show three prominent peaks which, for the sake of convenience, will be referred to as peak A, B and C as labeled in Fig. 6.22(a). In the occupied states their position follows a clear trend, viz. peak A and B are shifted closer to the Fermi level with an increasing number of Pb nearest neighbors. However, it is not a rigid shift of the whole spectrum because the energy splitting between the peaks is not constant.

For the unoccupied states the situation is less clear. Although the energy position of Peak C also changes with the number of Pb nearest neighbors, there is no clear trend. The spectrum from the adatom with four Pb neighbors even shows an additional peak, which makes an undoubtful assignment of Peak C impossible in this case. Comparing single spectra with one another reveals a bigger variation than known from $\sqrt{3}_\alpha$-Pb/Si(111) where all spectra look almost identical. It was already pointed out that the chemical environment on a bigger scale as well as the exact configuration of the atoms do also have an influence on the spectra which accounts for the observed differences in single spectra [149]. The exact energy positions of all peaks as well as the calculated energy splittings between peak A and B are summarized in Tab. 6.2.

It is known from PES measurements that the Pb $5d_{5/2}$ (and likewise Pb $5d_{3/2}$) core level only consists of a single peak for the γ-phase while it can be modeled by two or three peaks with varying binding energies and intensities for higher Pb coverages [159, 167]. Therefore,

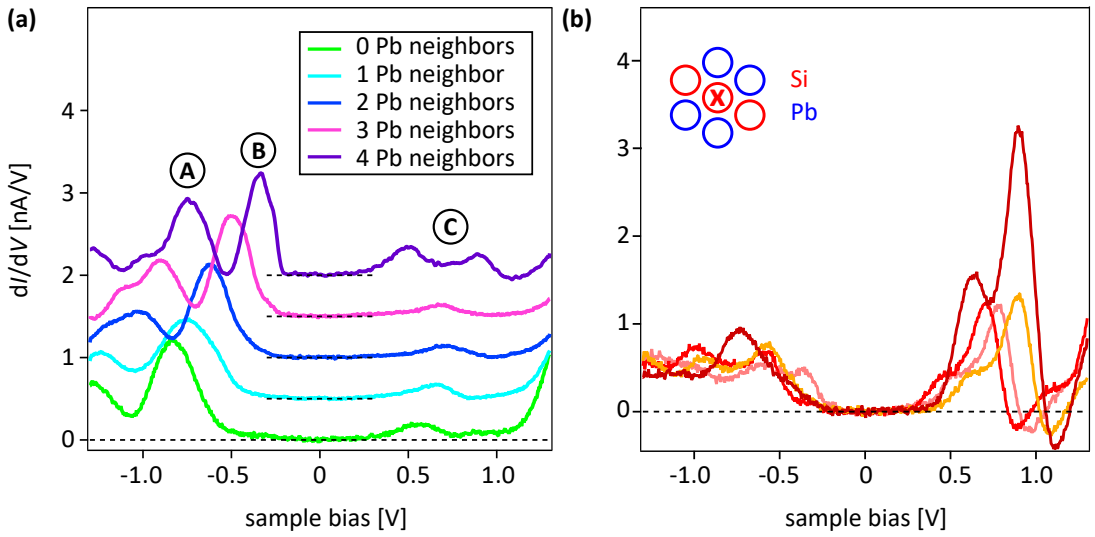

Fig. 6.22.: **(a)** STS of $\sqrt{3}_\gamma$-Pb/Si(111) taken exclusively on Pb adatoms. The spectra are averaged over several atoms with the same number of Pb atoms as nearest neighbors (only the one with four Pb neighbors is a single spectrum). The spectra are offset vertically for clarity. A, B and C label the peaks referred to in the main text. **(b)** STS of $\sqrt{3}_\gamma$-Pb/Si(111) taken exclusively on Si adatoms. All spectra shown here are single spectra taken on Si atoms that have two Si atoms and four Pb atoms as their nearest neighbor. Furthermore, they all share the identical configuration as shown in the pictograph, i.e., the examined (marked by X) and the two neighboring Si atoms can be connected by a straight line. The setpoint for the whole CITS map was $V = -1.3\,\mathrm{V}$, $I = 150\,\mathrm{pA}$ and $T = 4.3\,\mathrm{K}$.

it was argued that Pb only exists in a single, insulating state in the γ-phase while there are metallic sites in the α-phase as well. The measurements here reveal that although all Pb atoms share a lack of spectral weight at the Fermi level, the peak positions in the valence band can differ by up to 0.5 eV which is comparable to the observed chemical shifts within the Pb $5d$ core level in Pb/Si(111) phases with higher coverage. This means that although all the different Pb atoms of the γ-phase have their $5d$ core level at the same energy, their low-energy characteristics are diverse. It is also clear that the spectra of $\sqrt{3}_\gamma$-Pb/Si(111) do not converge to a spectrum of $\sqrt{3}_\alpha$-Pb/Si(111) if the number of Pb neighbors is increased since the α-phase only features a single peak in the occupied states. This also makes clear that the chemical environment on a bigger scale is important for the properties of the system.

A series of peaks in the tunneling spectra of Pb atoms of the mosaic phase at negative bias voltage was already observed in Ref. [168] but they did not make a detailed analysis regarding the local environment of the examined atoms. Later, the same group included this important aspect but did not observe the second peak at higher binding energies although it was predicted by their theoretical calculations of the projected DOS [149]. In contrast to the results here, they also found metallic behavior in the case of four Pb atoms as

Pb neighbors	Peak A (V)	Peak B (V)	Peak C (V)	Splitting $B - A$ (V)
0	-0.74	-0.40	0.56	0.34
1	-0.90	-0.49	0.65	0.41
2	-1.04	-0.62	0.71	0.42
3	-1.24	-0.75	0.68	0.49
4	-1.29	-0.83	0.50 (0.89)	0.46
$\sqrt{3}_\alpha$-Pb "center"	–	-0.25	0.30	–

Tab. 6.2.: Peak positions in tunneling spectra of Pb adatoms: Peaks A, B and C labeled according to their appearance in each spectrum starting from $V = -1.3\,\mathrm{V}$ as well as the energy splitting between Peak A and B, both as a function of the number of Pb atoms as nearest neighbors. Since the spectrum with four Pb neighbors has two peaks in the unoccupied states it is unclear which one should rather be assigned as Peak 3. For comparison the values from a "center"-atom of $\sqrt{3}_\alpha$-Pb/Si(111) are also listed, see Fig. 6.4(a). This spectrum, however, features only two peaks.

nearest neighbor. In any case, the available data set is extended which can promote further understanding, especially if the reason for the just mentioned deviations with other work can be resolved.

A similar approach was taken for the analysis of spectra from Si adatoms. It quickly became clear that, in contrast to the Pb atoms, tunneling spectra on Si adatoms can look vastly different even if they are taken on atoms with a similar local environment. An example is presented in Fig. 6.22(b) where single spectra of Si atoms with four Pb atoms and two Si atoms as their nearest neighbor are shown. Even the configuration of the surrounding atoms was identical, i.e., the examined Si adatom and the two neighboring Si atoms could be connected by a straight line, just as illustrated in the pictograph in the top left of Fig. 6.22(b). This suggests that the chemical environment on a bigger scale, i.e., the neighbors of the adjacent Pb atoms, is also relevant for the Si atoms, potentially in an even more significant way than known from the Pb atoms. In conclusion, it would require a significantly bigger data set to grasp any systematic behavior in the STS of the Si atoms which is beyond the scope of this thesis.

Since all tunneling spectra show insulating behavior, there has to be a mechanism at work to drive the half filled band into this state. Analyzing the detailed shape of the Si $2p$ core level, it was argued that the system exhibits CO where charge is transferred from Si to Pb atoms [169]. The same is concluded based on the results from STS where Pb atoms show a large peak in the occupied states while Si atoms have the majority of spectral weight above the Fermi level [170]. This is in line with the spectra provided in Fig. 6.22 but it was also shown that the electronic landscape is quite complex, see Fig. 6.21, making an

unambiguous interpretation difficult which is also pointed out in Ref. [149]. As a matter of fact, an alternative model based on the rearrangement of bonds casts doubt on the existence of CO in the closely related $\sqrt{3}_\gamma$-Pb/Ge(111) system [164]. When it comes to the theoretical treatment of $\sqrt{3}_\gamma$-Pb/Si(111), dedicated many-body calculation techniques have not been applied so far. This is certainly related to the disordered chemistry on the surface which has to be modeled in line with available computer resources. Nevertheless, the insights gained from such a treatment could be as important as in the related α-phases. Although a comparison with results from many-body calculations is thus not possible so far, there is no reason to believe that electronic correlations do not play a role in $\sqrt{3}_\gamma$-Pb/Si(111) as well.

To date, it has not been resolved if the complex LDOS pattern involves a vertical displacement of adatoms as observed in $\sqrt{3}_\alpha$-Pb/Si(111). A theoretical study predicted a subtle shift among the Pb atoms depending on the number of neighboring Pb atoms [149]. The relative height difference between Pb atoms according to this study is on the order of 10 pm. Within the electronic landscape found in $\sqrt{3}_\gamma$-Pb/Si(111) in this chapter which features a wide range of spectra and band gaps among the individual atoms, it is not possible to disentangle the topographic information from LDOS effects precisely enough to experimentally verify such a small distortion using STM. Apart from height differences among the Pb atoms, there could be a general height difference between Pb and Si adatoms. However, one also has to consider the different size of the atoms. Both the actual atomic radii of the two elements [171] as well as typical cutoff radii used in DFT calculations [149] differ by up to 70 pm. This is close to the apparent height difference of Pb and Si atoms in Fig. 6.21(a), giving the whole concept an ambivalent character.

6.3.4. Angle-resolved photoemission on $\sqrt{3}_\gamma$-Pb/Si(111)

Shortly after the discovery of the mosaic phase of Pb/Si(111), scientists started to investigate the system with PES, examining both core levels and the valence band spectrum [159, 169, 172, 173]. The Pb 5*d* and Si 2*p* core levels have been studied in great detail using synchrotron radiation which is why lab-based experiments will not be able to make a meaningful contribution to this subject. On the other hand, ARPES measurements published for this system were all made before 2D detectors were commonly available in the relevant setups. Therefore, it is worthy to revisit $\sqrt{3}_\gamma$-Pb/Si(111) in this matter and compare data among one another.

Fig. 6.23(a) shows a band map of $\sqrt{3}_\gamma$-Pb/Si(111) covering the two high-symmetry directions of the momentum space of a triangular lattice. The measurement path can be retraced via the inset in Fig. 6.23(b). Apart from the hole-like Si bulk bands at the Γ point, an adatom-derived band at an energy of around -0.5 eV is most dominant. In accordance with related systems such as $\sqrt{3}_\alpha$-Sn/Si(111) this band is assigned to the dangling bonds on the surface, a conclusion already drawn elsewhere [169]. Despite being half-filled, it does

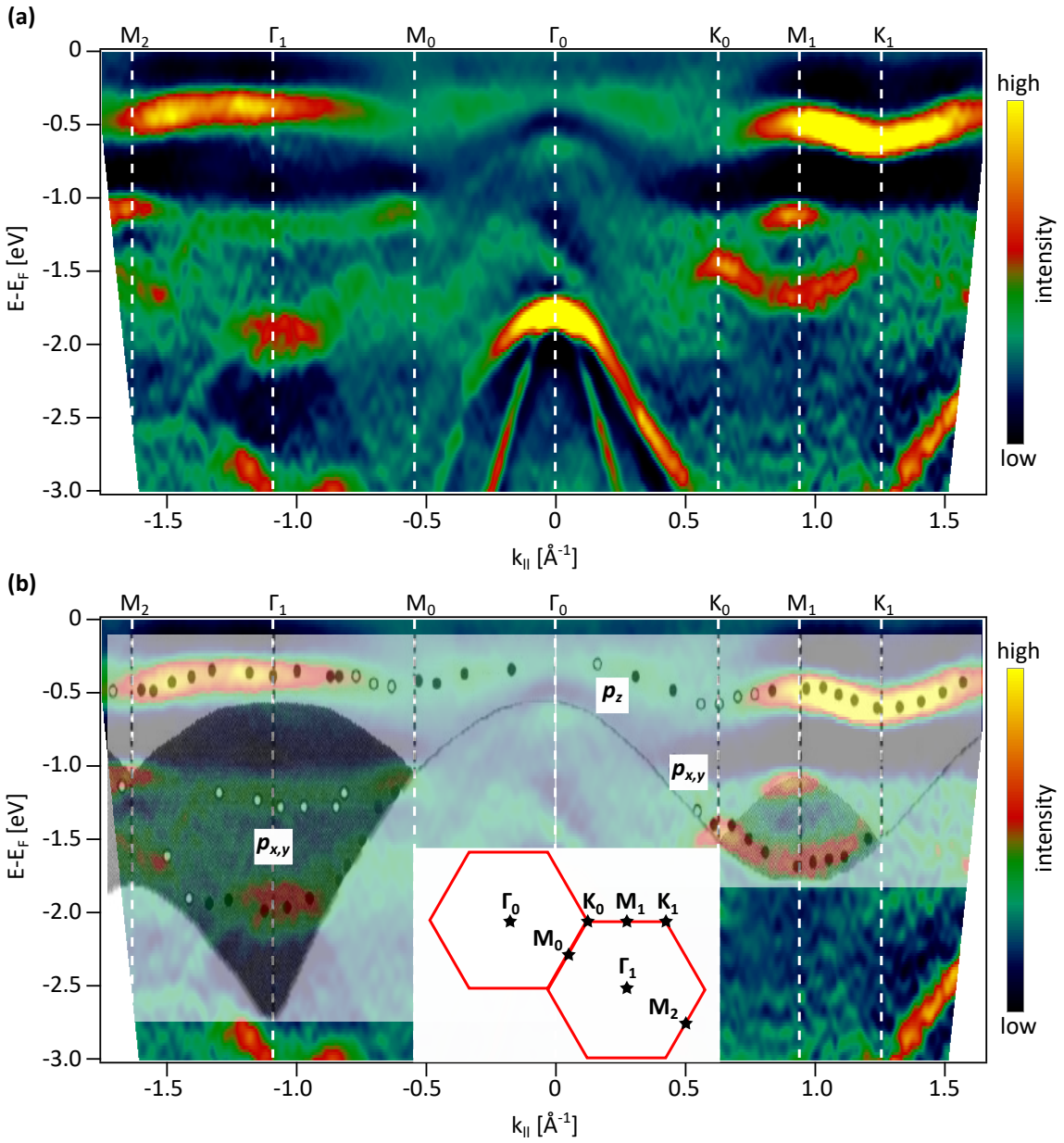

Fig. 6.23.: **(a)** ARPES band map of $\sqrt{3}_\gamma$-Pb/Si(111) along the high-symmetry directions within the surface BZ. The positions of high-symmetry points of the $\sqrt{3} \times \sqrt{3}R30°$ are marked. There are no signs of any further backfoldings that would indicate some kind of superstructure. The data is plotted as the 2nd derivative of the intensity with respect to the energy to improve the visibility of the surface state especially in the center of the BZ. The raw data can be found in the appendix in Fig. A.2. $h\nu = 21.2\,\mathrm{eV}$, $T \approx 20\,\mathrm{K}$. **(b)** The data of Panel (a) in overlay with data points from Ref. [169] which was measured with the same photon energy. The overlay is shifted downwards by 0.07 eV to correct for a difference in the respective Fermi levels. Both measurements agree well for all the adatom-derived states. Inset: Sketch of the reciprocal space to retrace the measurement path along the high-symmetry points of the $\sqrt{3} \times \sqrt{3}$ BZ. Reprinted with permission from Ref. [169]. Copyright (2020) by the American Physical Society.

not cross the Fermi level, confirming a key result from Sect. 6.3.3 also by PES[7]. In addition to that, the spectral function has a similarly broad appearance as in $\sqrt{3}_\alpha$-Sn/Si(111), see Fig. 6.16(a). This corroborates the statement that the inclusion of electronic correlation effects is essential for the description of $\sqrt{3}_\gamma$-Pb/Si(111) and the observed state is the LHB of a correlated 2DES. The spectral function is also essential for the identification of ground states and phase transitions in group IV triangular lattices [10, 175] as it is sensitive to a broken symmetry on the surface, e.g., due to magnetic order. In this case one would expect a backfolding of spectral weight between the Γ point and the adjacent M or K points which is not observed here. Therefore, simple commensurate superstructures like a 3×3 or $2\sqrt{3} \times 2\sqrt{3}$ spin order, which in principle can occur in such a system [8, 9], can be excluded. If there is an additional potential due to short-range order based on the two types of adatoms, it is too weak to have a measurable effect on the spectral function.

Since there are already pertinent experiments available in literature [169], a comparison between the results from this publication and the data measured in the context of this thesis is made in Fig. 6.23(b) by directly overlaying the two data sets. In order to achieve the depicted agreement the data from Ref. [169] has to be shifted downwards by 0.07 eV which was determined concordantly by comparing the positions of the Si valence band maximum and the position of the K_1 point which apparently has the best signal-to-noise ratio in this experiment. Such an offset is not remarkable since the respective systems were prepared in a different way on substrates with different dopants and measured at different temperatures. All of this might have an influence on the position of the Fermi level. Apart from that, the agreement is excellent and the two dispersions match very well. This evidently also extends to the deeper-situated bands which have mostly $p_{x,y}$ character [169]. There are also similarities in terms of the intensity of bands which is coded via the dot color in Ref. [169] as high (black dots) and low (white/empty dots). This agreement makes sense since the same photon energy is used in both experiments. However, some differences may arise due to polarization effects or an unequal measurement geometry.

Finally, the results from ARPES and STS will be compared. Fig. 6.24 compiles spectra from both techniques. Therefor, ARPES spectra were integrated along the high-symmetry directions of a BZ, while the STS spectrum is a weighted average of the spectra shown in Fig. 6.22(a). In ARPES the p_z and the $p_{x,y}$-like bands are separated creating a minimum 0.8 eV below the Fermi level. On the other hand, there is strong contribution towards the LDOS measured in STS from adatoms with zero, one or four Pb atoms in their neighborhood. Thus, the STS signal does not translate to the ARPES signal in a straight-forward manner. Including Si adatom spectra to the considerations will not change the picture qualitatively as they do not have dominant features in the energy range in question. In fact, the ARPES spectrum of $\sqrt{3}_\gamma$-Pb/Si(111) looks more similar to a corresponding measurement of $\sqrt{3}_\alpha$-Sn/Si(111), see Fig. 6.24, which does not feature this kind of chemical disorder. However, without a deeper understanding of the $\sqrt{3}_\gamma$-Pb/Si(111) system, it is not possible to fathom

[7] As the system is known to be gapped [174], bands do also not cross the Fermi level elsewhere in the BZ.

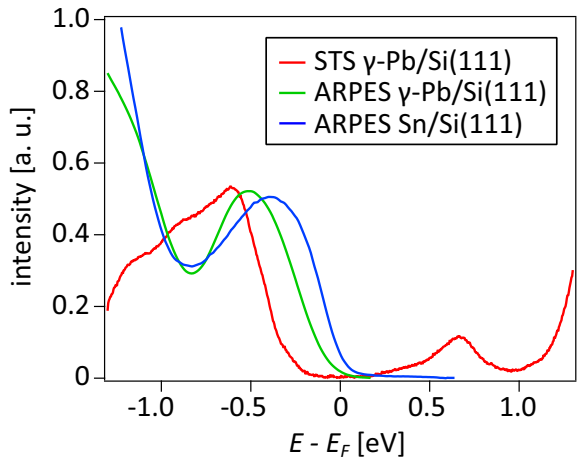

Fig. 6.24: Comparison between STS and PES of $\sqrt{3}_\gamma$-Pb/Si(111) and $\sqrt{3}_\alpha$-Sn/Si(111). STS is only taken from Pb atoms. The spectra from atoms with a different number of Pb neighbors are weighted according to Ref. [149] and then summed up to the spectrum depicted here. The photoemission spectra are produced by integrating ARPES band maps along the measured high-symmetry directions in the second BZ, thereby avoiding contribution of the Si bulk band in the center of the first BZ.

the physical reasons for the differences between the two PES spectra. Regarding the spectra of $\sqrt{3}_\gamma$-Pb/Si(111) measured with PES and STS, the differences in the measurement process of the two techniques must be responsible for the observed discrepancy which also requires future studies for a comprehensive explanation.

In summary, the ARPES measurements reveal a surface state with the typical dispersion of a triangular lattice. Since it does not cross the Fermi level despite half filling, it is interpreted as a LHB just as in related compounds such as $\sqrt{3}_\alpha$-Sn/Si(111). Its broad appearance supports the importance of electronic correlations to correctly describe this system as well. STS confirms the insulating character of the system. However, it also reveals that the local chemical environment of the Pb adatoms strongly affects their LDOS. The two peaks in the occupied part of the spectrum are located closer to the Fermi level if there are more Pb atoms in the immediate neighborhood. While tunneling spectra show states over the whole energy window from -0.2 down to -1.2 V, there is a clear gap between the p_z and $p_{x,y}$ states in PES which lacks a clear explanation so far. Therefore, a lot more work has to be done to understand the relation between STS and PES in this system and in correlated electron systems in general.

7. Electron doping of $\sqrt{3}_\alpha$-Sn/Si(111) via potassium adsorption

In this chapter the effects of potassium evaporation on $\sqrt{3}_\alpha$-Sn/Si(111) are examined. Instead of developing a metallic QPP as anticipated from simple Mott theory, potassium only has a local influence on the electronic structure. The K atoms were found to be adsorbed on empty T_4 sites of the substrate which lead to the formation of two well ordered K-Sn alloys with a relative K content of 1/3 and 1/2, respectively. In a combined study of STM and ARPES it is shown that the half-filled Mott insulator $\sqrt{3}_\alpha$-Sn/Si(111) eventually turns into a band-insulating K-Sn/Si(111) system.

7.1. The pristine $\sqrt{3}_\alpha$-Sn/Si(111) system

The research on (sub-)monolayer phases of Sn/Si(111) was initiated in 1964 with the same paper that also contained the first study on Pb/Si(111) [31]. The authors found different phases with a $\sqrt{3} \times \sqrt{3}R30°$ as well as a phase with $2\sqrt{3} \times 2\sqrt{3}R30°$ reconstruction. Since the study is only based on the analysis of LEED images, an undoubtful assignment of phases found therein is not possible because several phases share the $\sqrt{3} \times \sqrt{3}R30°$ surface reconstruction. Given the temperature steps used during the annealing cycles, it is likely that the authors realized an insulating $2\sqrt{3} \times 2\sqrt{3}R30°$ phase which has a coverage of 7/6 ML [176] as well as the mosaic γ-phase which is chemically disordered just like its Pb counterpart, see Sect. 6.3. A large-scale realization of $\sqrt{3}_\alpha$-Sn/Si(111) is more difficult because it requires a well adjusted deposition amount of 1/3 ML of Sn. One of the first demonstrations of successful preparation was given in 1990 when Kubby et al. presented STM images of different Sn/Si(111) phases [165]. Along with the progression of the respective analysis techniques throughout the last 30 years, $\sqrt{3}_\alpha$-Sn/Si(111) became a standard system for the exploration of surface physics.

The $\sqrt{3}_\alpha$-Sn/Si(111) system consists of Sn atoms occupying one out of three T_4 positions on the surface of Si(111), resulting in a $\sqrt{3} \times \sqrt{3}R30°$ reconstruction as already introduced in Sect. 2.3. With three bonds being saturated through backbonds to the substrate, a half filled p_z orbital per unit cell is left to form a 2DES at the surface that is essential for the description of the physics in $\sqrt{3}_\alpha$-Sn/Si(111). In contrast to many other group IV triangular lattices, the $\sqrt{3} \times \sqrt{3}R30°$ reconstruction is preserved down to at least 0.5 K, the lowest temperature investigated thus far [27]. At these temperatures $\sqrt{3}_\alpha$-Sn/Si(111) was found to be insulating with a band gap of 40 meV despite the half-filled orbitals, pointing

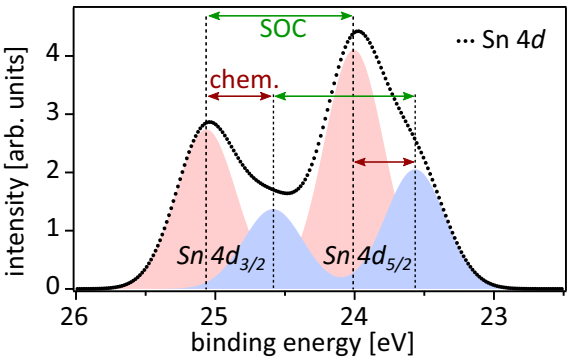

Fig. 7.1: Illustrative sketch of composition of the Sn 4*d* core level of pristine $\sqrt{3}_\alpha$-Sn/Si(111). The peak consists of two components (red and blue) that are chemically shifted with respect to each other. Furthermore, the spectrum features a splitting due to SOC whereas the two left(right) peaks originate from the Sn $4d_{3/2}$(Sn $4d_{5/2}$) level. Their ratio can be changed by doping with alkaline metals or halogens as described in the main text. The spectrum is artificially generated for illustrative purposes only and not based on any measurement.

towards the importance of electronic correlations [104]. At 70 K the system exhibits an insulator-to-metal transition and a pseudo-gap-like behavior develops that prevails up to RT [104]. This is in line with simultaneously published ab-initio calculations which did not find any structural distortion and suggested that the system is an antiferromagnetic Mott insulator at LT [6]. Later, this was refined by a study using STS and two-probe conductivity measurements via a modified STM tip [177]. Utilizing substrates with very low doping the authors found that the gap has a size of 70 meV in the ground state. Above 40 K, the insulating nature of the system vanishes and tunneling spectra can be modeled based on a dynamic Coulomb blockade.

Although there is an agreement in literature concerning an insulating ground state, its complex physical nature is still an active research area. The discussion is centered around two experimental clues that have been reproduced in several PES experiments: The spectral function features a backfolding of spectral weight towards the Γ-point [10, 16, 178] and the Sn 4*d* core level can be modeled using two (spin-split) peaks which are shifted with respect to each other by approximately 0.45 eV [121, 179–181]. In pristine $\sqrt{3}_\alpha$-Sn/Si(111) the peak at higher binding energy has twice the spectral weight as the one at lower binding energy, see Fig. 7.1 for an illustrative sketch. Therefore, it was speculated that there might be a reconstructed ground state at even lower temperatures [121].

The whole data was first interpreted within the dynamical fluctuation model already introduced in Sect. 6.2 as a possible explanation for the reconstruction of $\sqrt{3}_\alpha$-Pb/Si(111). The Sn atoms might flip between two different vertical positions whose signatures could be measured as a chemical shift of the Sn 4*d* core level in XPS. Since the photoemission process is happening on time scales orders of magnitude faster than the fluctuations, the spectrum would essentially consist of only two peaks, as observed. This geometrical distortion would also result in a momentary 3×3 reconstruction that induces a backfolding in the spectral function [178]. A more detailed analysis, however, showed that the backfolding is in discrepancy with a 3×3 reconstruction [10]. In agreement with many-body calculations this study concluded that the backfolding appears due to a collinear antiferromagnetic state

that effectively results in a $2\sqrt{3} \times 2\sqrt{3}$ reconstruction. Later, this argument was strengthened by an analysis of the spin structure of the surface state which showed a splitting into two spin-polarized bands [16]. Nevertheless, a direct measurement of the spin pattern in real space is still missing to date. Furthermore, an analysis of the vibration signatures via Raman spectroscopy and theoretical simulations thereof shows that the vibrational spectrum is more complex than a simple vertical movement of Sn atoms [105, 182]. The system was also reinvestigated within this thesis using the newly developed XVCA. A comparison with the experimental spectral function also predicted collinear antiferromagnetism as the ground state of $\sqrt{3}_\alpha$-Sn/Si(111), see Fig. 6.16.

Another explanation features the fluctuations of charges between the Sn atoms – too fast to be detectable via STM, but again quasi-static on the timescale of photoemission [183]. While this is a promising approach to explain both the experimental clues mentioned before, it does not withstand a strict quantitative comparison with experimental data. Finally, it was also speculated that the system is a Slater insulator facilitated by superexchange interactions and the physics can be explained without the need for electronic correlations [123]. This was criticized since neither a strong hybridization of Sn and Si bands nor a nesting of helical states has been observed in ARPES [16].

In summary, $\sqrt{3}_\alpha$-Sn/Si(111) is a 2DES with a complex interplay of electronic correlations, magnetic ordering, and phononic degrees of freedom. The p_z surface state that can be observed with spectroscopic techniques such as PES or STS is almost unanimously interpreted as the LHB of a Mott-insulating system. While individual theories or experiments excel at explaining certain aspects, other characteristics often cannot be captured simultaneously.

Previous doping studies

In order to get novel insights into the physics of $\sqrt{3}_\alpha$-Sn/Si(111), researchers started to examine the response of the system to doping. After a possible realization of exotic ground states in doped triangular lattices was predicted, see Chap. 1, these experiments got a second, likely even bigger incentive. In general, there are four different approaches of doping such a surface system:

- Evaporate elements with very low/high electronegativity on top of $\sqrt{3}_\alpha$-Sn/Si(111) which can then act as electron donors/acceptors [179–181, 184]. In the ideal case, other properties of the surface would remain unaffected. Typical choices are alkali metals acting as donors and halogens acting as acceptors.

- Substitute a fraction of the Sn atoms on the surface with atoms from group III or group V [184]. This mechanism is responsible for the doping of the substrates used in this thesis and widely spread in the semiconductor industry.

- Change the electron filling of the adatom system by using a substrate with an extremely high doping concentration [27, 40, 157]. Since the Sn atoms are chemically bound to the top layer of the substrate, a lack or excess of electrons in the substrate can translate to the Sn layer.
- Use a bottom gate to change the electron filling via a bias voltage. This doping approach has not been realized for group IV triangular lattices so far.

Due to the common availability and easy handling of alkali metal dispensers, the first approach has been widely used and was also applied to related systems like $\sqrt{3}_\alpha$-Sn/Ge(111) [185]. Studies mostly focused on the evolution of the line shape of the Sn 4*d* core level upon doping with K or Na. As introduced above in Fig. 7.1, the Sn $4d_{5/2}$ (and likewise Sn $4d_{3/2}$) core level can be modeled by two peaks. Evaporation of K onto the surface gradually shifts spectral weight from the red to the blue-colored peak until the former has vanished almost completely [179, 180]. At this point, the spectral shape of the Sn 4*d* peak does not change any further, suggesting that the surface is now somehow electronically saturated. The amount of K needed to reach this state is quantified as approximately 1/3 ML, i.e., one K atom per Sn atom [179]. The original spectral shape can be restored by adsorbing iodine on the surface [180].

Although these results are interesting on their own, the eventual goal is to directly study how doping affects the low-energy physics of the 2DES. So far, this has only been investigated using a micro-four-point probe to explore the electronic transport properties of the system [184]. The authors find metallic behavior for temperatures above 260 K both upon doping the surface via Na adsorption or substitutional doping with In. For lower temperatures the system becomes insulating due to carrier localization caused by the disorder introduced by the dopants themselves. However, the dopant concentration in this study was only 10 %, i.e., far away from the saturation point described above. In terms of STM studies, alkali-doped $\sqrt{3}_\alpha$-Sn/Si(111) has been barely investigated in literature so far. Disregarding some incidental measurements of Na-Sn/Si(111) in the aforementioned transport study, the first pertinent results were produced almost simultaneously within this thesis and Ref. [186]. The latter one is focused exclusively on K-Sn/Si(111) at a specific K coverage of 1/6 ML and its behavior at different temperatures up to RT. In corresponding measurements this study agrees well with the results shown here.

The use of a highly doped substrate to change the electron filling of the 2DES grown on top has also been successfully applied to $\sqrt{3}_\alpha$-Sn/Si(111). Using STS, Ming et al. showed that the system develops a higher spectral weight at the Fermi level when the hole doping of the Si substrate is increased [40]. A peak slightly above the Fermi level was found to scale with the substrate doping and was therefore identified as a QPP. This feature is also observed in tunneling spectra measured within this thesis. In a follow-up study the same group finds that the maximum hole-density is increased even further in small domains where STS measurements at LT show a zero-bias anomaly [157]. This can be an indication for superconductivity but the authors point out that modeling the data with a

dynamic Coulomb blockade yields decent agreement, too. Very recently said group studied the system at ultra-low temperatures down to 0.5 K and magnetic fields up to 10 T and found typical hallmarks of a 2D superconductor [27]. Therefore, this system is a promising candidate to study potentially unconventional superconductivity in a structurally simple 2D system which might simplify the search for the essential ingredients.

7.2. Local doping of $\sqrt{3}_\alpha$-Sn/Si(111) via potassium adsorption

As outlined in the previous section, the doping of $\sqrt{3}_\alpha$-Sn/Si(111) via alkaline adsorption has proven to effect the line shape of the Sn 4*d* core level as well as the conductivity characteristics. However, a pertinent study directly probing the states around the Fermi level using PES or STS is missing so far apart from the aforementioned study containing tunneling data of K-Sn/Si(111) at a specific K coverage of 1/6 ML that became available while this section was written [186]. In the following, a detailed analysis on the effects of potassium adsorption on $\sqrt{3}_\alpha$-Sn/Si(111) will close this gap and provide new insights into the doping mechanisms of 2D triangular lattices. By examining the spectral function, which carries essential information about the electronic correlations and ground state properties, via ARPES and likewise tracking the potassium adsorption and its electronic effects in real space via STM and STS, a complete picture of the doping process will be developed.

7.2.1. Preparation of $\sqrt{3}_\alpha$-Sn/Si(111) and potassium deposition

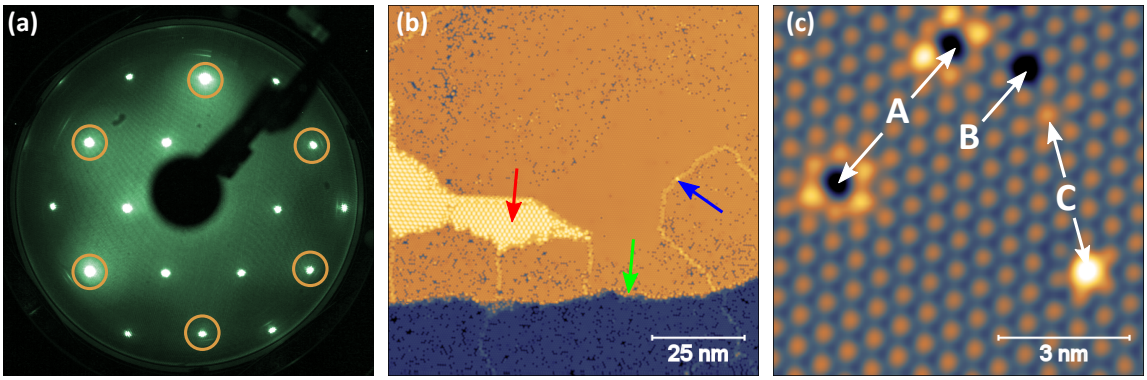

Fig. 7.2.: **(a)** LEED image of a freshly prepared $\sqrt{3}_\alpha$-Sn/Si(111) sample taken at an electron energy of 48 eV. The 1×1 reflexes with respect to the substrate are highlighted for orientation. It also shows reflexes of the $\sqrt{3}\times\sqrt{3}R30°$ reconstruction but no traces of $2\sqrt{3}\times2\sqrt{3}R30°$. **(b)** STM overview scan of the same sample. Despite not being recognizable in LEED, a small fraction of the surface is covered with the $2\sqrt{3}\times2\sqrt{3}R30°$ phase (red arrow). The image also features a substrate step (green arrow) and boundaries between different $\sqrt{3}\times\sqrt{3}R30°$ domains (blue arrow). $V = -1$ V, $I = 50$ pA and $T = 4.3$ K. **(c)** Typical defects found on a pristine $\sqrt{3}_\alpha$-Sn/Si(111) surface: Substitutional Si atom (A), vacancy (B), and defects in the subsurface (C). $V = -1.5$ V, $I = 150$ pA and $T = 4.3$ K.

In order to carry out a study on the effects of potassium doping, it is necessary to prepare and characterize a pristine $\sqrt{3}_\alpha$-Sn/Si(111) surface beforehand. To do so, we start out with a freshly flashed Si(111) substrate which is held at RT. In contrast to the preparation of $\sqrt{3}_\alpha$-Pb/Si(111) discussed in Sect. 6.2.1, the amount of adatoms deposited from an e-beam evaporation source is very critical for the success of the preparation because tin can not be easily annealed off without creating numerous defects. Therefore, the amount deposited was calibrated to be close to 1/3 ML via LEED in the following way: An unknown amount of tin was deposited onto a clean substrate. After annealing the sample at 650°C for three minutes two kinds of phases are formed on the surface: The desired $\sqrt{3}_\alpha$-Sn/Si(111) with a coverage of 1/3 ML as well as a $2\sqrt{3} \times 2\sqrt{3}R30°$ phase with a coverage of 7/6 ML. The sample was then examined in LEED with regard to these two reconstructions. The amount of tin deposited on a fresh sample in the next preparation step was then gradually reduced until there were no indications of a $2\sqrt{3} \times 2\sqrt{3}R30°$ phase left in LEED, see Fig. 7.2(a). It turned out that a small residual amount of $2\sqrt{3} \times 2\sqrt{3}R30°$ Sn/Si(111) can still be found on the surface in STM but this is even beneficial for the measurements since small patches of this phase are often accompanied by regions of $\sqrt{3}_\alpha$-Sn/Si(111) which have an extremely low defect concentration. For PES experiments the total coverage of this additional phase is too small to produce a noticeable signal in any spectrum. Fig. 7.2(b) shows a topographic STM scan of a typical $\sqrt{3}_\alpha$-Sn/Si(111) sample after successful preparation.

Nevertheless occasional defects will be present on the pristine $\sqrt{3}_\alpha$-Sn/Si(111) surface and it is helpful to get familiar with the most common ones in order to clearly distinguish them from features that are to be seen once potassium gets evaporated onto the surface. There are three types of defects labeled A, B, and C in Fig. 7.2(c) which are naturally found on $\sqrt{3}_\alpha$-Sn/Si(111) samples prepared within this thesis. At a tunneling bias $V = -1.5\,\mathrm{V}$ they have the following appearance:

- Type A is a dark hole surrounded by a bright hexagon. It is attributed to a substitutional Si atom surrounded by six Sn atoms [121].
- Type B is just a dark hole with no influence on the surrounding atoms. This is attributed to a vacancy in the Sn layer [121].
- Type C is a single protrusion which can appear in varying brightness. Its origin is not yet completely clarified but it is suspected to be due to different defects in the subsurface, e.g., a Sn atom replacing a Si atom of the substrate [187].

Potassium deposition

After a successful preparation of pristine $\sqrt{3}_\alpha$-Sn/Si(111), the samples are ready for the adsorption of potassium. To this end, they are positioned facing a commercial alkali metal dispenser from SAES Getters which releases a smoothly increasing amount of alkali metal when heated at constant current [188]. A typical current sequence used for the potassium

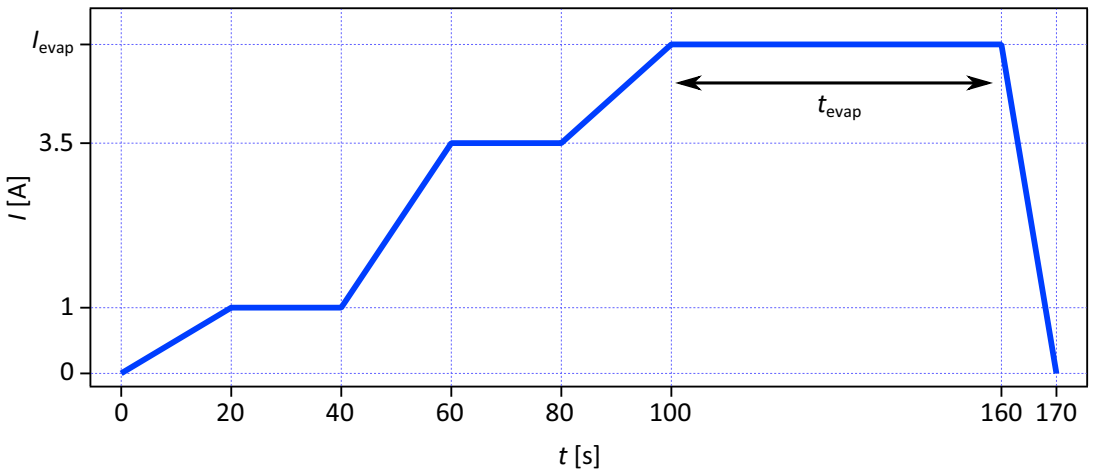

Fig. 7.3.: Current profile for the evaporation of potassium on $\sqrt{3}_\alpha$-Sn/Si(111). Typical evaporation times t_{evap} could range from 30 to 300 s and evaporation currents I_{evap} were between 4.5 and 6.5 A. In the example profile shown here $t_{evap} = 60$ s and $I_{evap} = 5$ A are chosen. The ample intervals arise due to the different distance of sample and dispenser in the respective vacuum chambers and possibly a different response characteristic of the two dispensers in use.

deposition is graphed in Fig. 7.3. In the PES chamber potassium evaporation was performed directly in front of the spectrometer allowing for quick cycles of deposition and measurement. In the STM chamber the potassium evaporation had to be done outside of the cryostat in the preparation chamber. There was no notable difference in the sticking coefficient of potassium between samples at RT and those that were inside the cryostat at LT directly before deposition.

7.2.2. Investigation of K-induced surface reconstructions via STM

In the following, the effects of K deposition on $\sqrt{3}_\alpha$-Sn/Si(111) will be investigated via STM. Fig. 7.4(a) shows a topographic overview scan of a sample with a small amount of tin deposited. Aside from numerous vacancies in the Sn lattice, bright protrusions which have a clearly different appearance than the typical defects shown in Fig. 7.2(c) are visible and are thus attributed to result from K deposition. They are especially gathered on domain boundaries such as in the bottom right of Fig. 7.4(a) but are also found inside patches of the triangular lattice where the analysis of their properties will be made.

In order to get an idea of how potassium interacts with the Sn lattice, we firstly identify the smallest structure originating from K deposition which is a plateau of triangular shape. Several representatives are found on the left side of Fig. 7.4(b) which is an enlargement of the region indicated with a white box in Panel (a). Other features are made up of two or more triangles sharing a corner among each other. A topographic map of a sample with a slightly higher K coverage and measured with an increased spatial resolution that was

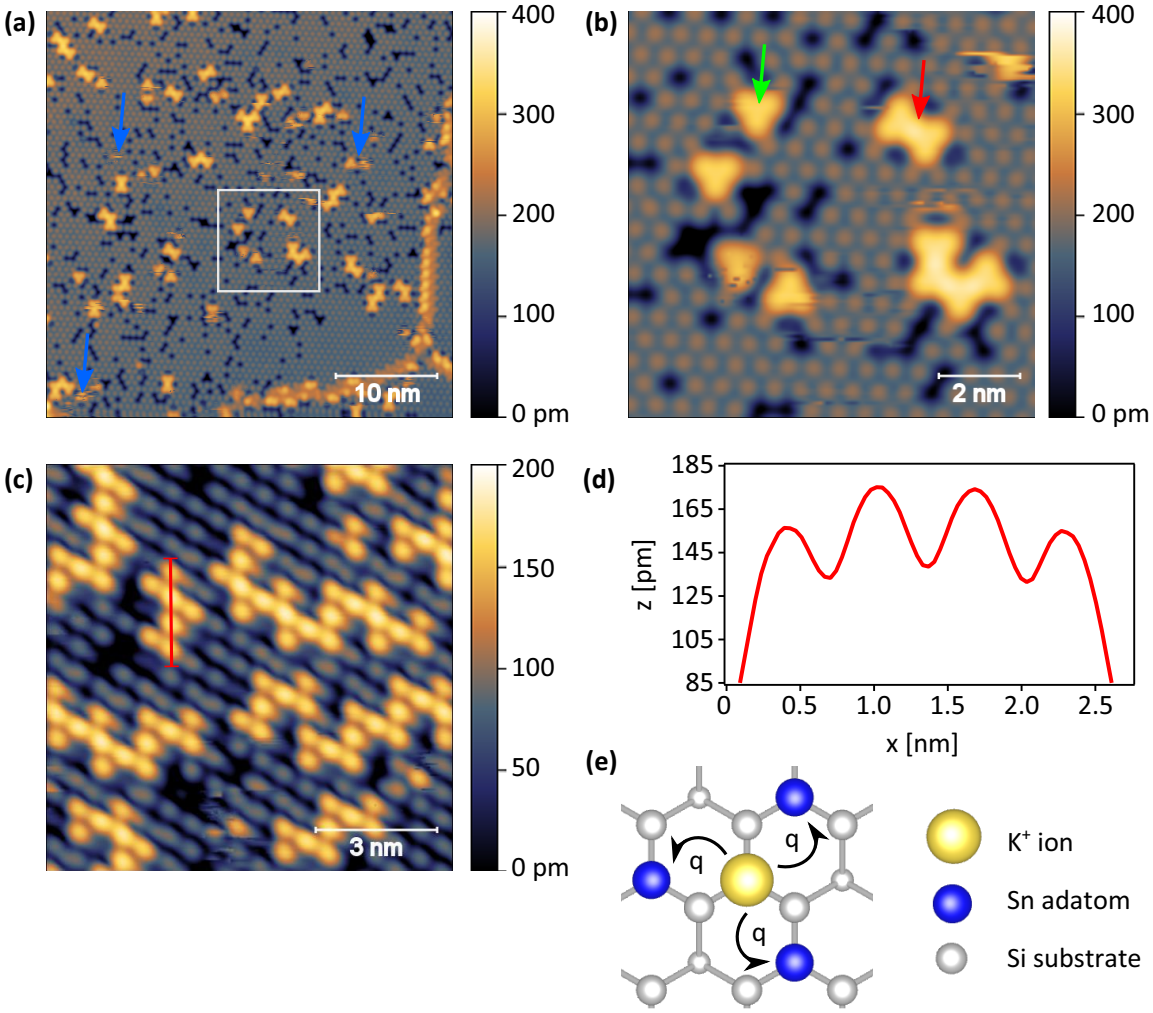

Fig. 7.4.: **(a)** Topographic STM image of $\sqrt{3}_{\alpha}$-Sn/Si(111) doped with approximately 3 % K atoms whose presence results in bright protrusions. The blue arrows exemplarily mark horizontal scars originating from K atoms changing their position. Tunneling conditions $V = -1\,\mathrm{V}$, $I = 100\,\mathrm{pA}$, $T = 4.3\,\mathrm{K}$. **(b)** Enlarged view of the white box in Panel (a). Although bone-like structures (red arrow) are most frequently found at low K concentration, the smallest unit is a triangular feature (green arrow). **(c)** STM data of a sample with a slightly higher K content but measured with an increased spatial resolution that was occasionally achieved. It becomes evident that the K-induced features originate from an increased apparent height of the three adjacent Sn atoms while the K atoms themselves remain invisible at this bias voltage. $V = -2.5\,\mathrm{V}$, $I = 50\,\mathrm{pA}$, $T = 4.3\,\mathrm{K}$. **(d)** Height profile of a K-induced feature, exemplarily shown with the red line in Fig. 7.4(c). The actual data presented here is an average over several features of this kind to correct for the influence of nearby defects and tip anisotropy. **(e)** Model of the smallest unit: A K atom at an unoccupied T_4 position distributing its valence charge evenly among the three adjacent Sn adatoms.

sporadically achieved, see Fig. 7.4(c), provides a deeper insight into the structure: The K-induced feature consists of three protrusions which are exactly at the position of Sn atoms. Since the triangular feature is the smallest building block, it is reasonable to attribute it to the effect of a single K atom. This assumption will be confirmed in Sect. 7.2.3 where the K coverage is verified independently via XPS. For symmetry reasons the K atom has to reside in the center of the triangle, i.e., at an unoccupied T_4 position of the underlying Si substrate. This argument is strengthened by XPS measurements of the Si $2p$ core level where the pronounced change of the spectral shape upon K deposition also hints towards potassium being embedded into the surface geometry [179]. The exact vertical alignment with respect to the Sn atoms, however, remains unresolved for the moment. Dedicated diffraction experiments or DFT calculations might give an insight into this matter in future studies. The three protrusions associated with a nearby K atom can therefore only be Sn atoms with an increased apparent height.

Utilizing the atomically resolved image in Fig. 7.4(c), additional information on the role of potassium on the surface can be collected. Fig. 7.4(d) shows a height profile along features consisting of three connected K-induced triangles as the one marked in Fig. 7.4(c). The profile includes four Sn atoms that are all affected by nearby K dopants but the two atoms in the center appear elevated by approximately 20 pm. These two atoms in the center of the chosen line profile are adjacent to two K atoms, while the other two are only adjacent to one. It is already known from literature that potassium is electronically active on the surface since it affects the shape of the Sn $4d$ core level by sharing its valence electron [179, 180]. Therefore, we conclude that the observed effects are also of electronic origin. The K dopants distribute their valence electron among the three surrounding Sn atoms, thereby increasing the number of occupied states. When performing a STM measurement, this translates to an increased apparent height. Since Sn atoms accumulate charge from all neighboring K ions, the characteristics found in the height profile in Fig. 7.4(d) are adequately explained. Calculations with DFT show that the Sn atoms tend to relax outward when they accumulate electrons from a nearby K atom [186]. Accordingly, an actual corrugation might contribute to the observed apparent height as well. In Fig. 7.4(b) one recognizes that potassium has an influence on the next-nearest neighbors, too. At the chosen bias voltage they appear as depressions, indicating an electronic and/or structural change as well. This will be investigated in more detail in Sect. 7.2.4 via STS. Including the structural considerations above, we conclude that the adsorbed K atoms are located at an unoccupied T_4-site of the Si substrate and distribute their charge mainly among the three neighboring Sn atoms. This is also summarized as a sketch in Fig. 7.4(e).

During STM scans like the one shown in Fig. 7.4(a), the potassium atoms are not completely stationary. This can be seen even in a single image by means of horizontal scars or features that end abruptly within a single scan line. Positional changes mostly go along with these horizontal scars suggesting that the mobility is facilitated by interactions with the tip. Despite this, there are no new features observed which means that the electron transferred to the Sn p_z orbitals is still bound to the K^+ ion nearby, i.e., it is not able to

move freely as intended in an actual doping scenario. A closer examination of this matter will be provided in Sect. 7.2.4. For measurements at 77.5 K, the mobility of K atoms is notably increased compared to 4.3 K, but there are no qualitative changes.

So far, the K atoms only occupy T_4 sites that are at least $2a_{\mathrm{Si}} = 7.68\,\text{Å}$ apart whereas a_{Si} is the surface lattice constant of silicon as defined in Fig. 2.1(b). Fixed adsorption sites for K atoms will naturally lead to an ordered superstructure if the K coverage is sufficiently high. With the rule above, this would entail the formation of four different domains with mutually exclusive adsorption sites. To verify this, K-Sn/Si(111) surfaces with a gradually increasing K content will be investigated. The results are summarized in Fig. 7.5(a)-(f) which shows topographic STM images of samples with increasing K concentration. Each panel is labeled with the relative portion of potassium with respect to tin based on the model developed above and – for higher concentration – in the following. It was often possible to measure the individual stages of K concentration with high spatial resolution as well which is then shown as an inset of the respective panel. The accordance of the two appearances – wether the substructure of the K-induced feature is resolved or not – has been directly observed upon tip changes within a single scan frame.

The K-coverage series starts in Fig. 7.5(a) with a K concentration of 16 %. The bone structures already known from Fig. 7.4(a) can still be found sporadically but longer chains are more common. An ordered lattice, however, does not yet form. Upon increasing the K content, the formation of small domains featuring a honeycomb structure, see Fig. 7.5(b), is observed. This is the expected behavior if the structure model developed above holds. When the K concentration reaches 1/6 ML with respect to the Si substrate, i.e., there is one K atom per two Sn atoms, this structure is complete as seen in Fig. 7.5(c). Since the K atoms are known to be arranged in a honeycomb pattern from the structure model established at lower coverage, this phase will be coined honeycomb phase. The elevated Sn atoms determining the appearance of the STM images, however, constitute a kagome lattice. The same is observed in Ref. [186]. As predicted earlier, the formation of different domains is observed and the resulting domain boundaries are visible both in the upper and lower part of the panel. Only after this honeycomb lattice is completed, a new phase develops on the surface which has a uniform appearance and appears elevated with respect to the honeycomb structure, see Fig. 7.5(d). From the inset it becomes clear that the Sn atom that was recessed in the center of the kagome ring so far, now shares the same apparent height as the other Sn atoms. Hence this uniform phase looks like a pristine $\sqrt{3}_\alpha$-Sn/Si(111) surface, but with all Sn atoms elevated, as can be seen in the inset of Fig. 7.5(e). When more potassium is added, the surface becomes heavily corrugated as seen in Fig. 7.5(f). Apparently it is no longer energetically favorable to incorporate K atoms into the triangular lattice. Instead, they are piled on the surface in a disordered manner.

The observations above verify the assumption on the formation of a long-ranged ordered K-Sn lattice. This leads to the structure model of the honeycomb phase which is depicted in Fig. 7.6(a). As a next step we will take a closer look at the uniform phase in order to develop a structure model as well. In all STM measurements that feature the honeycomb

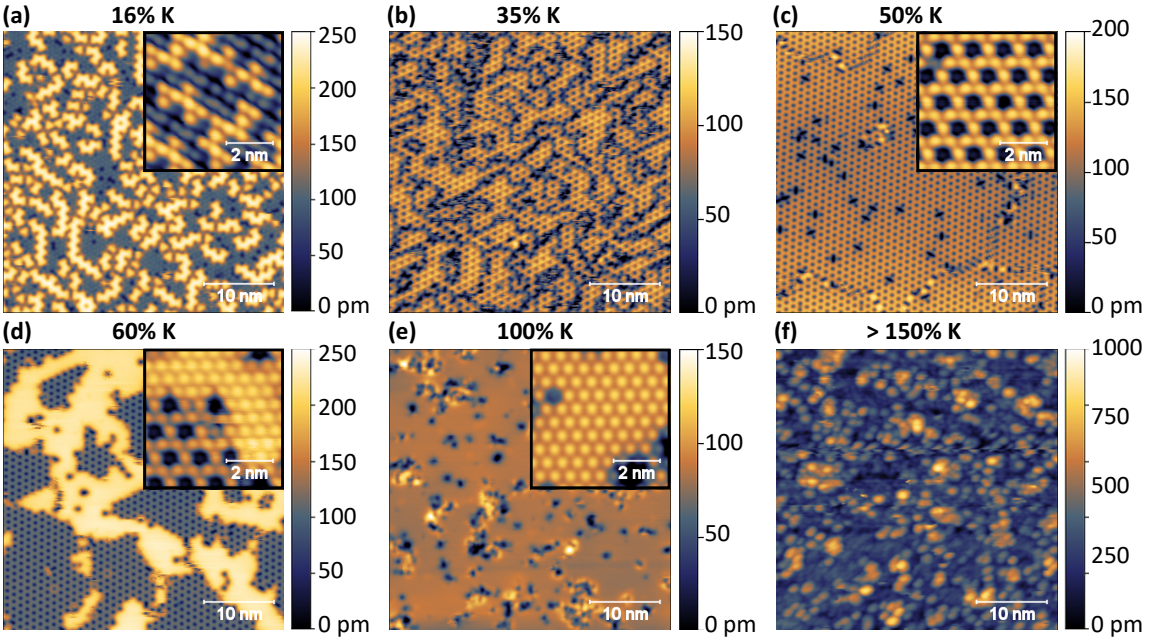

Fig. 7.5.: Evolution of the surface morphology of K-Sn/Si(111) with increasing K concentration. The percentage above each panel reflects the K coverage with respect to the Sn lattice based on the structure model introduced before. The various insets show the same structure as the associated main panel but with an increased spatial resolution that was sporadically achieved. The height scales are only valid for the respective main panel. **(a)** At low coverage the bone structures already known from Fig. 7.4(a) are most common. From the inset it becomes obvious that the K atoms themselves are not visible at this bias voltage but only their effect on adjacent Sn atoms. **(b)** With increasing coverage the K atoms begin to form a honeycomb lattice. **(c)** At 50 % K coverage the honeycomb lattice is complete. **(d)** Only after the honeycomb lattice is completed the center of the honeycomb ring is also elevated due to the presence of – most likely – one or two additional K atoms. The resulting uniform phase appears higher than the adjoining honeycomb phase. **(e)** Once the uniform phase is completed the surface features a $\sqrt{3} \times \sqrt{3}R30°$ reconstruction, i.e., every protrusion has the same apparent height. **(f)** Upon further K deposition the surface becomes disordered. Tunneling conditions: (a) $V = -1\,\mathrm{V}$, $I = 50\,\mathrm{pA}$, inset: $V = -2.5\,\mathrm{V}$, $I = 50\,\mathrm{pA}$. (b) $V = -2.5\,\mathrm{V}$, $I = 50\,\mathrm{pA}$. (c) $V = -2.5\,\mathrm{V}$, $I = 50\,\mathrm{pA}$, inset: $V = -2.5\,\mathrm{V}$, $I = 30\,\mathrm{pA}$. (d) $V = -2.5\,\mathrm{V}$, $I = 100\,\mathrm{pA}$, inset: $V = -2.5\,\mathrm{V}$, $I = 30\,\mathrm{pA}$. (e) $V = -2.5\,\mathrm{V}$, $I = 50\,\mathrm{pA}$, inset: $V = -2\,\mathrm{V}$, $I = 50\,\mathrm{pA}$. (f) $V = -2.5\,\mathrm{V}$, $I = 100\,\mathrm{pA}$. Measurement in (b) done at $T = 77.5\,\mathrm{K}$, others at $T = 4.3\,\mathrm{K}$.

and/or uniform phase such as Fig. 7.5(c)-(e) the center of the kagome ring is either empty like in the honeycomb phase or filled like in the uniform phase. Intermediate fillings were never observed within the regular lattice which suggests that this is the effect of a single K atom adsorbed in the center of the ring, filling up the empty p_z orbital. This would result in a K/Sn ratio of 0.75. The corresponding structure model is depicted in Fig. 7.6(b). However, there are several clues that this is not the case:

- The T_4 position in the center of the kagome ring is already occupied by a Sn adatom. If K adsorption directly above or below this Sn atom happened, the site would be structurally different than surrounding sites, resulting in a $2\sqrt{3} \times 2\sqrt{3}$ reconstruction. This is neither observed in STM images where all atoms in the uniform phase have an identical apparent height nor in pertinent LEED images. Furthermore, vertical stacking of atoms is likely energetically unfavorable.

- It was already observed that the K atoms can switch their position even at LT, suggesting that the corresponding energy barrier is small. Adding potassium to an existing honeycomb phase might thus trigger a reorganization of K atoms into the observed $\sqrt{3} \times \sqrt{3}R30°$ phase. In this case they could still occupy empty T_4 which are already known to be a preferred adsorption site but now with a mutual distance of $\sqrt{3}a_{\mathrm{Si}}$ as seen in the structure model in Fig. 7.6(c). While a mirror symmetry of the system is broken in that case, all Sn and K atoms end up in structurally identical configurations. The model also gives a possible explanation why the uniform phase does not occur before the honeycomb phase is completed. If the energy barrier for switching positions is small for the K atoms extending the size of the honeycomb phase on the sample surface through a positional reorganization might be energetically more favorable than a local formation of the uniform phase.

- The configuration just described has a K/Sn ratio of 1 meaning that all Sn $5p_z$ orbitals can be filled completely by the available electrons. This would result in insulating behavior which is in line with STS and ARPES measurements in the following sections.

Based on this, the model with intertwined triangular lattices of potassium and tin in equal shares is favored. The authors of Ref. [186] express the same conjecture. It has to be noted that there are two possible realizations of the described uniform phase on a given Sn lattice since there are two empty T_4 sites within a $\sqrt{3} \times \sqrt{3}R30°$ unit cell, see Fig. 7.6(c). A domain boundary within the uniform phase has, however, not been observed so far. Therefore, a concluding assessment of the structure cannot be provided. Maybe the formation of domains is avoided by K atoms fluctuating between the two T_4 sites on a timescale faster than typical STM measurements. Unfortunately a measurement at high positive bias voltage where the K atoms can be imaged directly [186] was not successful due to the strong interaction of the surface with the tip.

As a next step a region where the honeycomb and uniform phase are coexisting will be investigated in order to get a deeper insight into the two structures. The measurement in

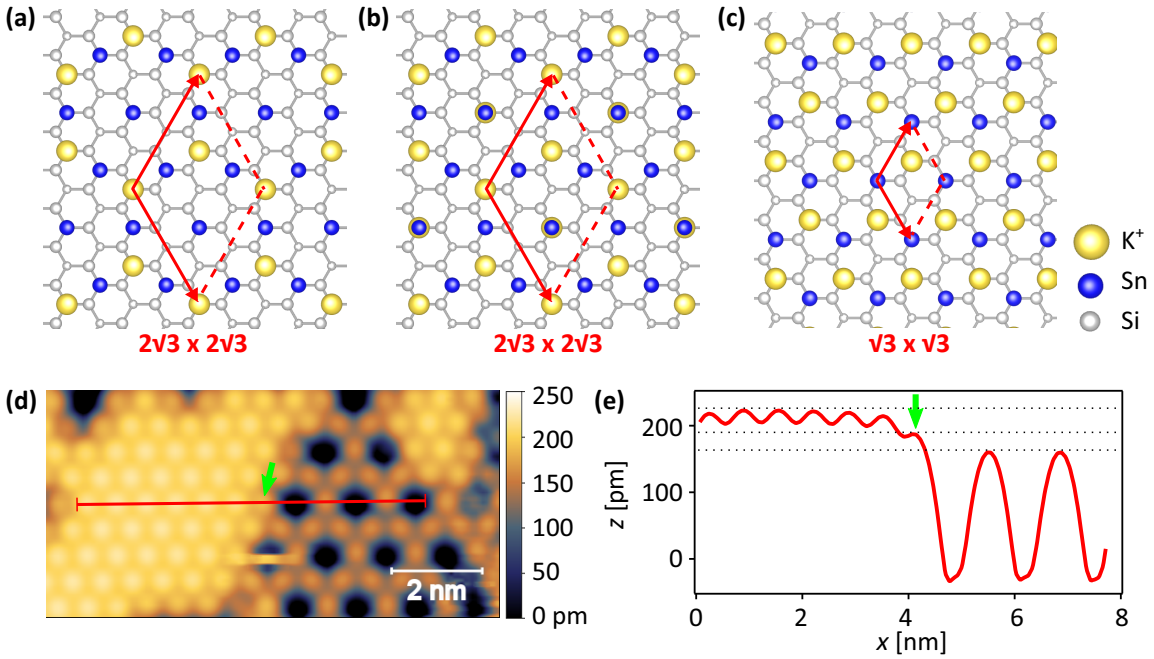

Fig. 7.6.: **(a)** Structure model of the honeycomb phase of K-Sn/Si(111). This configuration is the natural result of the two empirical rules found from studying STM images with low K coverage: K atoms are adsorbed on empty T_4 positions and have to be at least $2a_{\mathrm{Si}}$ apart. This structure model has a $2\sqrt{3} \times 2\sqrt{3}R30°$ in agreement with STM. **(b)** Possible structure model of the uniform phase of K-Sn/Si(111) with a K/Sn ratio of 0.75. If another K atom is adsorbed in the center of the honeycombs sketched in Panel (a), one ends up in a possible uniform phase. Here, K atoms already situated on the surface can remain in their position. The additional K atoms are drawn below the Sn atoms and are only visible as thin yellow circles in the structure model. **(c)** Alternative structure model for the uniform phase. This model has a K/Sn ratio of 1 and features the $\sqrt{3} \times \sqrt{3}R30°$ observed in experiment. All Sn atoms end up surrounded by three K atoms but the mirror symmetry of the system is broken. A positional reorganization of K atoms is required to turn from the honeycomb to the uniform phase. **(d)** Topographic STM measurement of a region featuring both the honeycomb and the uniform phase of K-Sn/Si(111). Tunneling conditions $V = -2\,\mathrm{V}$, $I = 50\,\mathrm{pA}$, $T = 4.3\,\mathrm{K}$. **(e)** Height profile taken along the red line indicated in the left panel from left to right.

question is shown in Fig. 7.6(d) and a height profile which was taken along the indicated red line is depicted in Panel (e). The height profile starts in the uniform phase on the left side. Firstly, it clearly confirms the claim that all atoms in the uniform phase are identical which favors the model with a K/Sn ratio of one. Secondly, it establishes a hierarchy in the apparent height of the different phases. While the uniform phase appears 65 pm higher than the kagome rings at the chosen experimental conditions, the rings themselves appear 195 pm higher than the Sn atoms in their center. From what is known on this system to date, this hierarchy directly translates to the number of electrons accumulated on the respective Sn atoms. Therefore, a model of a CO state as proposed in Ref. [186] in which the orbitals of the Sn atoms in the honeycomb phase are either completely filled (kagome rings) or empty (center of rings) cannot capture the complete picture since it should result in the kagome rings having the same apparent height as the uniform phase.

It is also worthwhile to take a dedicated look at the transition region between the two phases. The atom right at the boundary, highlighted with a green arrow in Fig. 7.6(d), (e), has an apparent height metered at roughly the average of the value it would have if it solely belonged to one or the other phase. This seamlessly fits into the picture of an electronically governed apparent height. At this atomic site, there are more electrons accumulated than in the honeycomb phase since it is adjacent to the uniform phase, however, a complete filling of the $5p_z$ orbital is not accomplished because the necessary amount of one K atom per Sn site is not reached in the immediate neighborhood.

Even if the whole sample surface is covered with K-Sn/Si(111), additional spots in LEED reflecting a new surface reconstruction have not been observed. For the honeycomb phase this might be related to the sample temperature since the K atoms are known to fluctuate between energetically degenerate positions within the unit cell for $T > 200\,\mathrm{K}$, thereby gradually destroying the $2\sqrt{3} \times 2\sqrt{3}R30°$ symmetry [186]. LEED experiments at LT might resolve this issue in the future. In the uniform phase the missing of additional $2\sqrt{3}\times2\sqrt{3}R30°$ spots is the expected behavior if the structure model developed above is correct. A broken mirror symmetry as described above likely cannot be detected since the measurement is averaged over many rotational domains of K-Sn/Si(111).

Many of the results shown above have similarities with other alkali-decorated surface systems which have been investigated with STM in the past. Oftentimes the K atoms themselves are not visible directly for a wide range of bias voltages but only through their interaction with other adatoms [189, 190]. Therefore, it can be difficult to determine the exact K coverage when the evolution of the surface upon K evaporation is not accurately tracked. On bare Si(111), it was found that small amounts of potassium induce a local charge redistribution in a triangular fashion [191]. Only for higher coverage the K atoms begin to cluster and are thereupon clearly imaged in STM [192]. Furthermore, even small amounts of alkali metals can be easily imaged with STM when they are positioned on top of an adatom system as in the case of Na-Au/Si(111) [193]. The Na atoms are adsorbed above empty T_4 positions, however, the bonding situation on the surface is more complex than in the case of Sn/Si(111).

7.2.3. Independent coverage determination via XPS

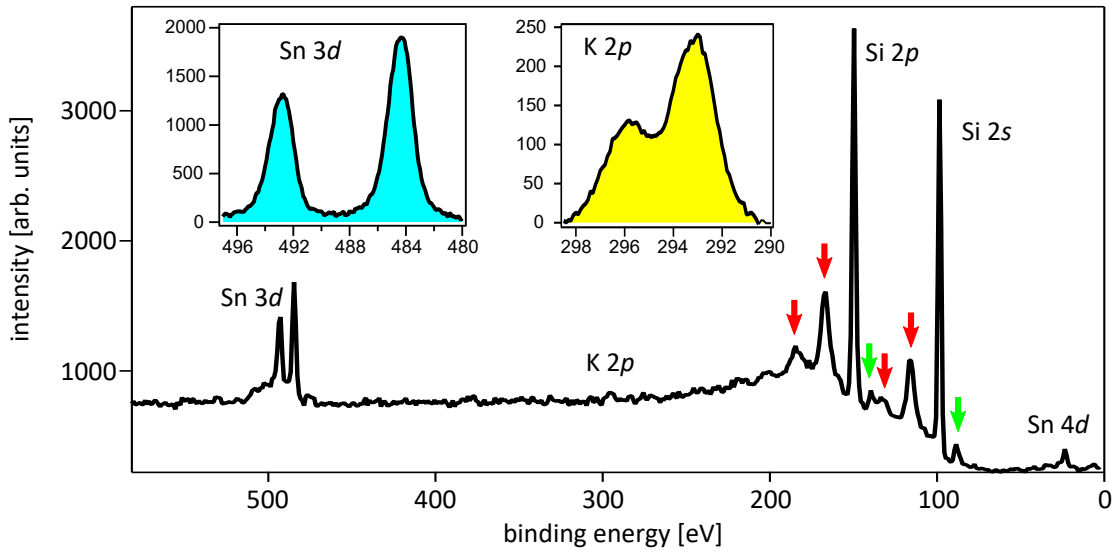

Fig. 7.7.: Overview spectrum of the honeycomb phase of K-Sn/Si(111). The core level lines of Sn and Si are clearly visible while the signal from potassium is very low due to the small cross section of the associated photoionization. The substrate peaks are accompanied by plasmon satellites on the higher (red arrows) and the Al Kα_3 satellite on the lower binding energy side (green arrows). The insets show the Sn 3*d* and the K 2*p* spectra that were used for the determination of the relative K coverage. $h\nu = 1486.6\,\mathrm{eV}$, $T = 300\,\mathrm{K}$.

So far, the structure models of K-Sn/Si(111) established above are only based on input from STM. Thus, we performed XPS to collect independent evidence by measuring the chemical composition of the surface, i.e., the proportion of potassium to tin. To this end, two samples hosting the honeycomb and the uniform phase of K-Sn/Si(111), respectively, have been transferred from the STM chamber to the PES setup maintaining a pressure smaller than 5×10^{-9} mbar at all time by using a vacuum suitcase. Figure 7.7 shows an overview spectrum of a sample with the honeycomb phase. Apart from peaks originating from the Si substrate, the Sn 3*d* and K 2*p* states are most prominent in the spectrum and are therefore chosen for the chemical analysis. There are no traces of contaminants on this surface while the sample with uniform K-Sn/Si(111) showed a contamination with oxygen. The measurement was conducted with Al Kα radiation, which leads to an electron inelastic mean free path of a few nanometers for the two core level lines in question [194]. As we are dealing with a surface system, damping of the photoelectron current due to inelastic scattering is a minuscule effect and will be ignored. To determine the relative weight of the two core level lines, separate measurements of the Sn 3*d* and K 2*p* states, shown in the respective insets in Fig. 7.7, were conducted. After subtraction of a Shirley-type background [95] and under consideration of photoemission cross sections [195] the ratio of potassium

to tin comes out as 35 % for the honeycomb phase and 61 % for the uniform phase. This is smaller than the theoretically expected values of 50 % and 100 %, respectively. However, the determination of an absolute stoichiometry in an unknown system using XPS is difficult since the cross sections have a significant error bar. Furthermore, the analyzer transmission function has to be included as well. An exact determination thereof is, however, laborious because it depends on the exact analyzer setting used for the measurement and is therefore unknown. The general trend for this type of analyzer and the kinetic energies in question is that the analyzer transmission slightly decreases for higher kinetic energies [196], meaning that the K content is underestimated accordingly. In addition, the tin content is slightly overestimated due to sporadic islands of $2\sqrt{3} \times 2\sqrt{3}R30°$ Sn/Si(111). This phase has a coverage of 7/6 ML with respect to the underlying substrate [176] and there is no evidence that potassium is adsorbed on that surface, see Fig. A.3(a). The relative spectral weight supports to a reasonable degree that there is twice as much potassium in the uniform phase compared to the honeycomb phase. Regarding the absolute values, the structure model does not suffer since the isolated features observed in STM, e.g., in Fig. 7.4(a), have to originate from at least one K atom, meaning that the K content cannot be deemed to low. Thus, the chemical analysis via XPS corroborates our interpretation of the STM data.

7.2.4. Evidence for localized doping from STS

With plenty of evidence regarding the structural model of different K-Sn/Si(111) phases, we now turn toward a characterization of their electronic properties. In order to class alterations in STS upon potassium doping correctly, it is again necessary to take a precise look at the corresponding data of pristine $\sqrt{3}_\alpha$-Sn/Si(111), too. There is already a pool of pertinent work available in literature [40, 104, 157, 177], with results consistent with the data measured in the framework of this thesis. As it turns out, the doping level of the substrate has a clear influence on STS experiments, in contrast to the closely related $\sqrt{3}_\alpha$-Pb/Si(111) where no notable influence was found, see Sect. 6.2.6. Figure 7.8 shows tunneling spectra of $\sqrt{3}_\alpha$-Sn/Si(111) grown on substrates with different doping level. The characteristic signature related to doping is a peak slightly above the Fermi level at $V \approx 0.1\,\mathrm{V}$ which was taken as a QPP that emerges due to hole-doping of the 2DES via a heavily doped substrate [40]. It is very pronounced for samples grown on a substrate with high p-doping. For lower p-doping and n-doping the spectra do not show this feature. Although a clear hierarchy as in Ref. [40] could not be established here, the existence of an additional peak for Sn/Si(111) grown on highly p-doped substrates is clearly confirmed. The interpretation leaves room for discussion as a QPP in a hole-doped Mott insulator is expected to form right above the LHB, see Sect. 3.1. Furthermore, it has not been observed using another technique such as (inverse) PES although it should be partly occupied. Thus, we will refer to this feature as a SIP in the following.

Interestingly, the intensity of this feature increases continuously from substrates with high n-doping to those with high p-doping, i.e., the SIP can only be induced with holes.

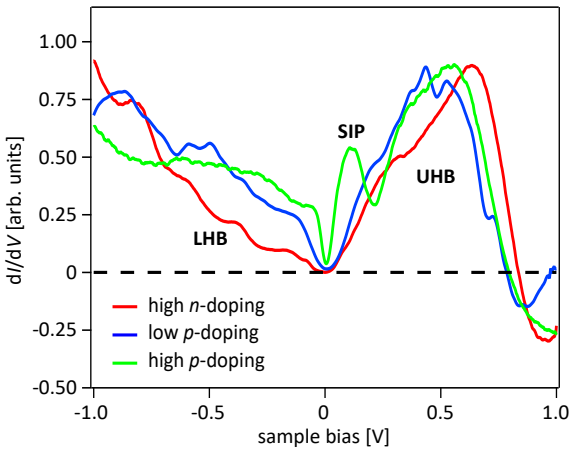

Fig. 7.8: Tunneling spectra of pristine $\sqrt{3}_\alpha$-Sn/Si(111) samples grown on substrates with varying doping level. Highly p-doped substrates induce an additional peak slightly above the Fermi level. The intensity of this feature is also linked to the spectral weight at the Fermi level. All three spectra share a broad peak in the unoccupied states, the UHB, which was used for mutual scaling to increase comparability. The blue spectrum was measured at 77.5 K, the others at 4.3 K. Setpoints were $V = -1\,\mathrm{V}$, $I = 150\,\mathrm{pA}$ (high n-doping), $V = -2\,\mathrm{V}$, $I = 100\,\mathrm{pA}$ (low p-doping), $V = -1\,\mathrm{V}$, $I = 100\,\mathrm{pA}$ (high p-doping).

The reason is that the substrate layer close to the surface of Si(111) gets enriched with p-dopants during preparation, see Sect. 2.1 and Refs. [42–44]. Therefore, the doping hierarchy relevant for an adatom system ranges from n-type substrates that have an almost undoped surface layer to lowly and highly p-doped substrates where the hole doping in the immediate subsurface is increased compared to the supplier specifications. This can also explain small differences between the results from various groups because the spectral weight of the SIP consequently not only depends on the intrinsic doping of the wafer but also on the annealing history of the substrate and contamination of the respective UHV chambers with potential hole dopants.

The rest of the spectrum consists of the UHB and LHB whereas the latter one only manifests in a broad increase of spectral weight. The nature of the LHB in STS is not very well understood since the agreement with PES experiments is limited. On a smaller energy scale it was already observed that features measured in STS can be heavily distorted when electronic correlations play a significant role [103]. Furthermore, a contribution of inelastic tunneling has been suspected to be responsible for the observed differences between STS and PES [105]. For high bias voltages $V \gtrsim 0.8\,\mathrm{V}$, a negative differential resistance which is already familiar from $\sqrt{3}_\alpha$-Pb/Si(111), see Fig. 6.4, is observed. It is therefore not specific to either of the systems but a more general property. The possible explanation given in Sect. 6.2.2 based on a lack of states within the silicon band gap thus still holds.

STS of K-Sn/Si(111) at low K coverage

Having elaborated on the electronic properties of pristine Sn/Si(111), we can now investigate changes in the spectra when potassium is present on the sample. This is firstly studied at low K coverage to develop an understanding in a similar way as for the topographic images. Fig. 7.9(a) shows a K-Sn/Si(111) sample with K/Sn ratio of 14 %. At this coverage, there are both regions where several K atoms are clustered and areas where the next K atom is

several atomic sites away. Tunneling spectra were taken in a narrow grid over the whole surface. As discussed above, the K-induced changes in the topographic image are locally confined to the immediate neighbors. Thus, spectra were selected depending on the distance of the examined adatom to the next K-induced feature. They can be categorized into three types which are depicted in Fig. 7.9(b) and color-coded according to the respective sites exemplarily shown by arrows in Panel (a). If the tip is placed far away from any K atom (green arrow), an intrinsic spectrum of $\sqrt{3}_\alpha$-Sn/Si(111), as also seen in Fig. 7.8, is produced.[8] When measuring adjacent to one of the protrusions (blue arrow), the LDOS changes notably and a third type of spectrum is found on Sn atoms directly adjacent to K atoms, i.e., on the K-induced protrusions themselves (red arrow).

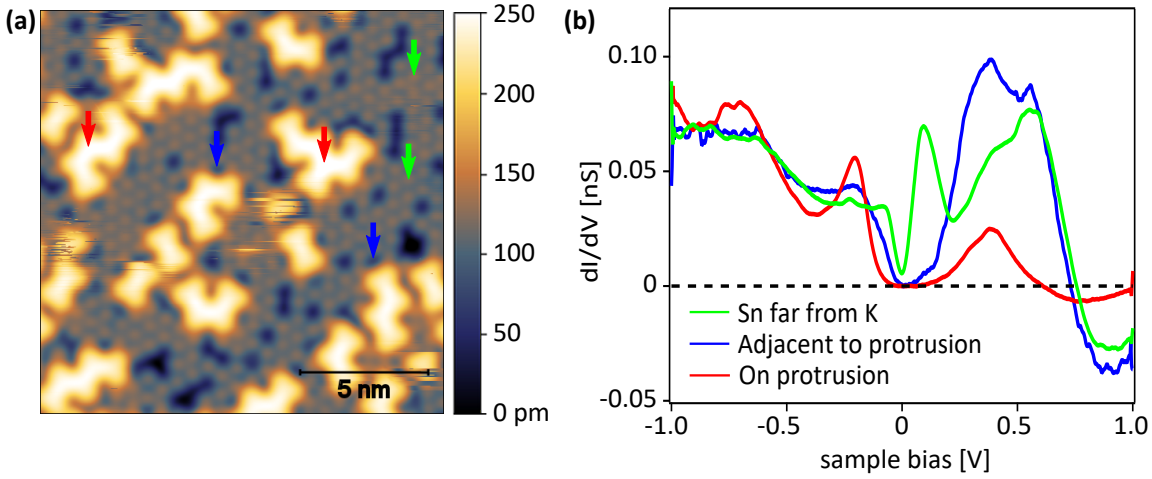

Fig. 7.9.: **(a)** Topographic image of K-Sn/Si(111) with a K coverage of 14 %. In this exact frame CITS was performed to investigate the influence of K adsorption on the local electronic structure. Tunneling conditions $V = -1\,\mathrm{V}$, $I = 50\,\mathrm{pA}$, $T = 4.3\,\mathrm{K}$. **(b)** Tunneling spectra depending on the distance from nearby protrusions originating from K atoms. The spectra are averaged over several sites, of which some are exemplarily marked with arrows of matching color in Panel (a).

In this case, the substrate is highly p-doped and a pronounced SIP is induced for Sn atoms that are not near any K atom. If the SIP emerges due to charge transfer from the substrate, any electron transfer from potassium should therefore work in a balancing way, suppressing the formation of a SIP. This is exactly what is observed in the transition region between the K-induced protrusions and the bare Sn lattice. Sn atoms directly adjacent to the protrusion still receive a small fraction of the electron donated by potassium. The SIP is almost completely suppressed and only a small shoulder remains in the corresponding spectrum, i.e., the blue curve in Fig. 7.9(b). Furthermore, the insulating character of the intrinsic $\sqrt{3}_\alpha$-Sn/Si(111) system is locally restored.

[8] The differences between the two spectra are within the expected range of variations due to tip modifications or the actual doping in the substrate surface region. Fig. A.3(b) shows an example with more even spectra.

Spectra taken directly on the K-induced protrusions do not show any remnants of a SIP at all and the gap between the band onsets gets larger as well. The two peaks that were originally identified as the LHB and UHB become more narrow, indicating a change in the many-body interactions. As STS is not well-suited to address this kind of problem, a detailed inspection of that matter will be provided in Sect. 7.2.5 using ARPES. In the unoccupied states one mainly notices a strong decrease of the spectral weight upon K doping. Since it was already argued that the K-induced protrusions in the topographic images are caused by an increased LDOS, the described behavior can be attributed to a twofold effect. Firstly, the p_z states are filled up with electrons which reduces the amount of unoccupied states. Secondly, STS was performed with the same setpoint voltage as the topographic image in Fig. 7.9(a), viz. $V = -1\,\mathrm{V}$. Spectra measured on the protrusions will thus be taken at a higher distance between sample and tip which in turn results in a lower signal for states at higher energies.

These results corroborate the findings of the STM measurements. The influence of K atoms is locally restricted and this conclusion is now extended to the electronic structure of the whole sample. Although some Sn atoms already have two K atoms in their immediate neighborhood in the low-coverage regime – this is the same number as is found in the honeycomb phase for the Sn atoms constituting the Kagome lattice – they do not form a periodic lattice yet. In the following, we will thus also study the electronic properties of the two phases with long-range order, namely the honeycomb phase and the uniform phase.

STS of the honeycomb and uniform phase of K-Sn/Si(111)

For this investigation, STS is performed on a sample where both phases are coexisting as seen in Fig. 7.10(a) since this obviously guarantees the best comparability of spectra among each other. We will focus on the three different sites associated with these two phases: Sn atoms within the uniform phase, Sn atoms forming the kagome lattice in the honeycomb phase, and Sn atoms in the center of the kagome ring. The respective spectra are depicted in Fig. 7.10(b).

In the uniform phase there is a large gap of roughly 1.25 eV. Any unoccupied K-derived states are apparently located at higher energies and merge with the Si bulk states which cause the steep increase at around 1.1 eV. There are also no remnants of the UHB which supports the previously set-up model that the Sn $5p_z$ are completely filled by dopant electrons. In contrast, the two types of atoms in the honeycomb phase both show a state at $V = 0.65\,\mathrm{V}$. In accordance with their supposed electron occupation – the atoms on the kagome ring are directly adjacent to a K atom and therefore receive a bigger share of its valence electron – STS on the center atoms yields the bigger spectral weight than on the atoms on the kagome ring. This characteristics are also correctly predicted in a DFT simulation of the projected DOS [186]. The energy position of the state has shifted from 0.4 V in Fig. 7.9(b) to 0.65 V in the measurements here. This is presumably related to the different doping concentration in the underlying substrates as will be shown below.

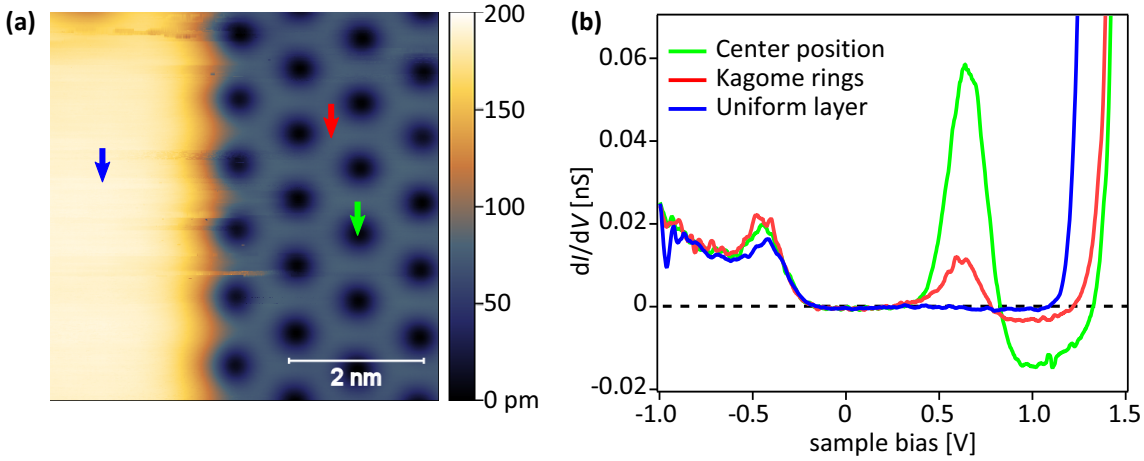

Fig. 7.10.: **(a)** Topographic map of a K-Sn/Si(111) sample with the honeycomb phase on the right side and the uniform phase on the left side. The three characteristic spots on the surface, i.e., Sn atoms on a kagome ring (red arrow), in the center of the ring (green arrow) and in the uniform phase (blue arrow) are marked exemplarily. Tunneling conditions $V = -2.5\,\mathrm{V}$, $I = 50\,\mathrm{pA}$, $T = 77.5\,\mathrm{K}$. **(b)** STS of the honeycomb and uniform phase averaged over several sites as exemplarily marked in Panel (a) with the respective colors. A p-type substrate with low doping was used here. Spectroscopy setpoint $V = -2\,\mathrm{V}$, $I = 50\,\mathrm{pA}$.

In the occupied states all three curves have a very similar appearance and the peak at $V = -0.45\,\mathrm{V}$ is attributed to the Sn $5p_z$ state. The relative weight of all curves is certainly affected by the setpoint chosen globally for all curves – just as in Fig. 7.9(b) – and should therefore not be taken at face value. Note that measurements at constant height would not resolve this problem since a change in filling is predicted to be accompanied by an adjusted bonding distance [186].

Since there is already a strong dependence of substrate doping for pristine $\sqrt{3}_\alpha$-Sn/Si(111), it is necessary to check for that influence in the K-decorated system as well. The results are shown in Fig. 7.11(a) for the three types of substrates already investigated in Fig. 7.8. The measurements were performed on the honeycomb phase of K-Sn/Si(111) which allows comparison with the data published in Ref. [186]. The spectra clearly show that substrate doping is of great importance for STS results on K-Sn/Si(111) as well. However, it is believed that this is rather an effect of the STM measurement. As already pointed out at the beginning of this section, during the preparation of the substrate, p-dopants are incorporated into its surface region, creating an almost undoped layer for n-doped silicon. If the amount of free carriers is low, the electric field generated by the tip cannot be screened efficiently, leading to tip-induced band bending. Figure 7.11(b) displays a sketch illustrating the consequences for the measured gap in STS. Furthermore, it is possible that a part of the applied voltage does not drop within the tunneling barrier which would lead to a similar effect. Only highly p-doped substrates are believed to yield reliable results at LT in

this matter [41, 197]. A comparison with the work of Smith et al. [186] is in line with the trend found here. They measure the gap in terms of a HOMO-LUMO splitting which is the distance between the two peaks closest to the Fermi level. Using substrates with a moderate p-doping they find a HOMO-LUMO gap of 0.85 eV which is between the numbers found in Fig. 7.11(a), namely 0.6 eV (high p-doping, green curve) and 1.25 eV (low p-doping, blue curve). A clear evidence that the STS measurement is the driving force for the variable gap size will also be seen in Sect. 7.2.5, where the system is investigated by ARPES and the band positions are not correlated to the substrate doping. If this issue ever becomes critical for understanding the general properties of K-Sn/Si(111), an extensive study regarding the band bending for the different phases on substrates of various doping measured at different temperatures is suggested.

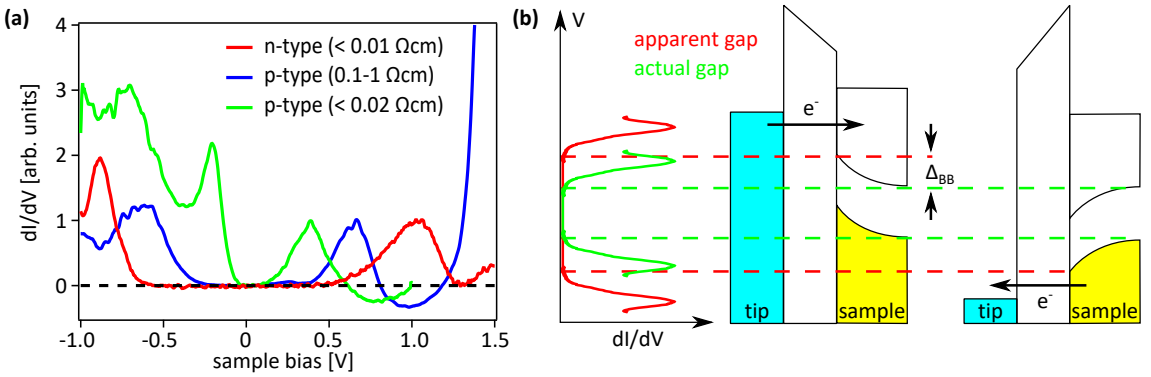

Fig. 7.11.: **(a)** Tunneling spectra of K-Sn/Si(111) measured on the honeycomb phase for substrates with different doping. All spectra show insulating behavior, however, the size of the gap clearly depends on the substrate doping. Setpoint $V = -2.5\,\mathrm{V}$, $I = 100\,\mathrm{pA}$, $T = 4.3\,\mathrm{K}$ (green, red) or $V = -2\,\mathrm{V}$, $I = 50\,\mathrm{pA}$, $T = 77.5\,\mathrm{K}$ (blue). **(b)** Qualitative sketch of how tip-induced band bending affects the gap measured in STS. The electrical field generated by the tip penetrates into the surface of a non-metallic system and causes the band onset to shift by Δ_{BB}. Image adapted from Ref. [198].

In summary, it is not possible to realize a doped Mott insulator, i.e., a correlated metallic system featuring a QPP, by evaporating potassium on $\sqrt{3}_\alpha$-Sn/Si(111). Instead, the K atoms act as electron donors for the Sn $5p_z$ orbitals in their immediate vicinity. Since the adsorption happens on T_4 high-symmetry sites, an increasing K coverage leads to long-range ordered systems of K-Sn/Si(111). At a K/Sn ratio of 0.5, K atoms form a honeycomb lattice with a $2\sqrt{3} \times 2\sqrt{3}R30°$ reconstruction. After this phase is completed, further addition of potassium produces the uniform phase which features a $\sqrt{3} \times \sqrt{3}R30°$ reconstruction and is believed to consist of Sn and K atoms in equal share. The characteristics observed via XPS of the Sn 4d core level upon doping, viz. a transfer of spectral weight that saturates after the deposition of 1/3 ML of potassium [179], fits well into the picture of an ordered alloy of K-Sn/Si(111) that is completed at the same coverage. The whole system remains insulating at all K coverages but a transformation of the LHB towards a more narrow feature close to

the K atoms demands a more detailed examination since it hints towards a modification of the effective electron-electron interactions. Although STM is a great tool to investigate the local properties of a system, it is not optimal to investigate many-body physics which are enclosed in the spectral function. In the following section the analysis of this system will therefore be pursued using ARPES which grants direct access to the k-resolved spectral function.

7.2.5. Evolution of the spectral function upon K adsorption

Starting from pristine $\sqrt{3}_\alpha$-Sn/Si(111), the evolution of the band structure upon a gradually increasing K content in K-Sn/Si(111) will be studied using ARPES. A spectrum around the Γ-point is measured after each step of K evaporation which consists of heating the dispenser with $I_{\text{evap}} = 6.5\,\text{A}$ for 1 min at a time.[9] There will be a special focus on the p_z-like surface state that forms the LHB and thus contains information about electronic correlation effects. Fig. 7.12(a) shows a spectrum of pristine $\sqrt{3}_\alpha$-Sn/Si(111) which marks the starting point of the K deposition series. Since this data is taken at RT, it features marginal spectral weight at the Fermi level in agreement with Ref. [104]. Data taken at LT which was already shown in Fig. 6.16(a) in the context of a comparison with XVCA calculations is, however, indubitably insulating. The distribution of spectral weight in the LHB is tied to the uncorrelated band structure, i.e., there is little spectral weight for wave vectors between Γ and $K_{2\sqrt{3}}$ where the uncorrelated band would be unoccupied [10]. At LT the shadow band induced by the row-wise antiferromagnetic state can be observed in this part of the BZ [10]. The position of the most pronounced Si bulk band without any potassium on the surface is marked with a horizontal line about 1.8 eV below the Fermi level because it will be instructive to track the evolution of band positions and correlate them with the K content on the sample. The stepwise addition of potassium firstly triggers three effects which can be seen in Figs. 7.12(b)-(d):

- The LHB drastically changes its shape. It becomes sharper while the total bandwidth is increased simultaneously. Concomitantly, a more even distribution of spectral weight along the $\overline{\Gamma K}$ high-symmetry direction develops, i.e., the state gains more intensity especially around the Γ point.

- The Si bulk bands undergo an incremental energy shift towards the Fermi level. The Sn surface state does not follow this shift in an equal manner, thereby reducing the energy distance between both states.

- The $p_{x,y}$ states which form the backbonds to the Si substrate (well visible at the $K_{\sqrt{3}}$ point about 1.3 eV below the Fermi level) gradually lose intensity to the point where they are almost fading into the background.

[9] After 18 steps longer evaporation times were used since spectra did not change drastically anymore.

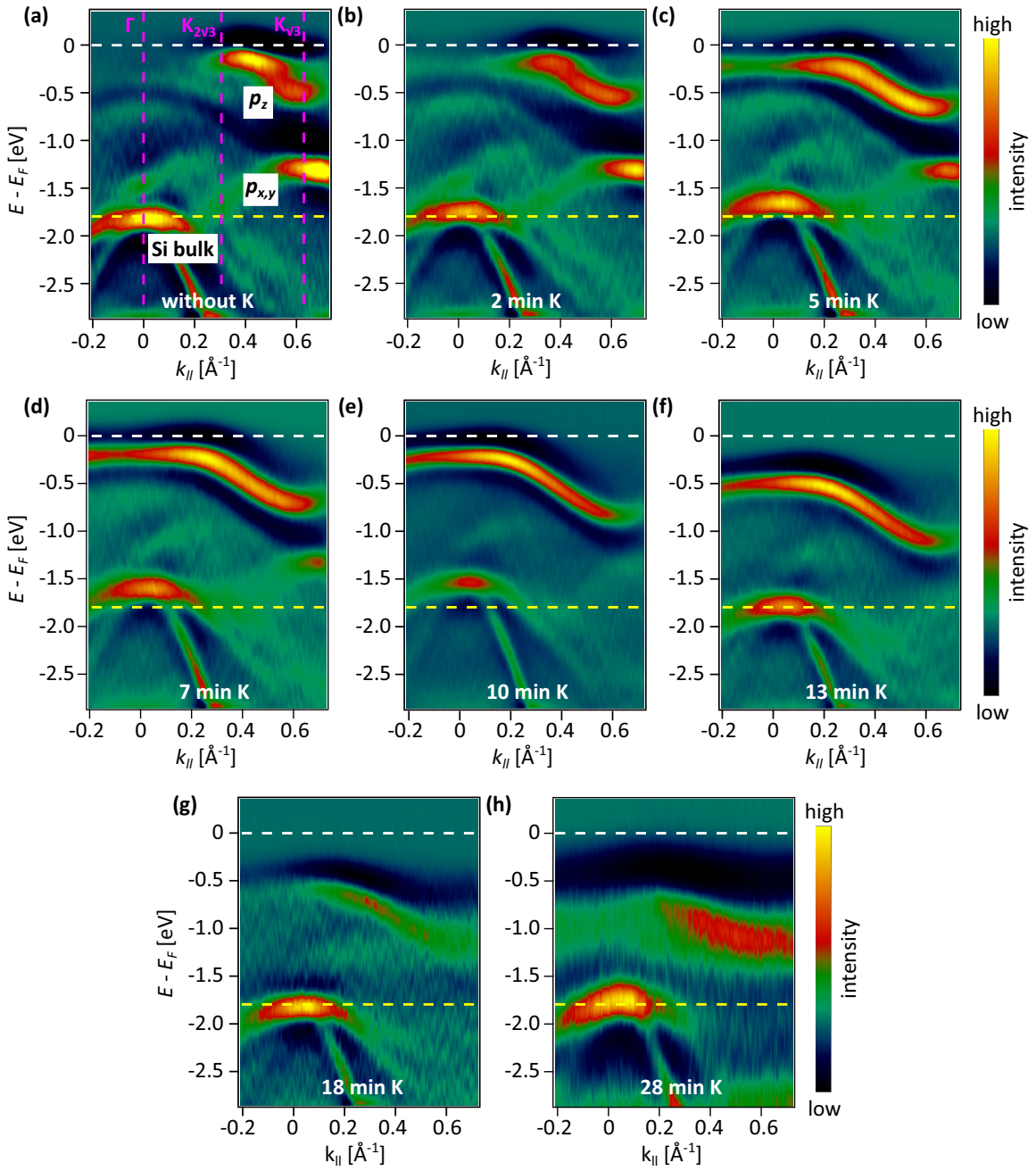

Fig. 7.12.: ARPES series of K-Sn/Si(111) with increasing K content on the surface. The Fermi level is marked with a white dashed line and the position of the band maximum of the most prominent Si bulk band without any potassium on the surface is marked with a yellow dashed line 1.8 eV below the Fermi level. Each panel is labeled with the total K evaporation time. Substrate: lowly p-doped. $T = 300\,\mathrm{K}$, $h\nu = 21.2\,\mathrm{eV}$. The intensity shown here reflects the negative second derivative of the count rate with respect to the energy. The raw data including spectra not shown in this selection can be found in the Appendix in Fig. A.4.

All three effects reach their maximum after 10 min of K evaporation when the p_z-like surface state appears sharpest and the energy shift of the bulk bands amounts to almost 0.3 eV, see Fig. 7.12(e). Now the experiment has reached a *turning point*. Adding more potassium as done for the spectra shown in Figs. 7.12(f)-(h) leads to a rigid down-shift of the whole band structure which simultaneously gets blurred out, indicating disorder on the surface. The band shift eventually levels out and one finds the Si bulk band at approximately the same position as in the case of pristine $\sqrt{3}_\alpha$-Sn/Si(111).

Tracking the energy position of the K-Sn surface state is more ambiguous due to the transformation of its shape. Since the changes around the Γ point are mostly concerning the intensity, it is suitable to track any energetic shifts there. The relative shifts with regard to the pristine sample are plotted in Fig. 7.13(a) for the Si bulk bands and for the Sn p_z band, respectively. To get an insight into possible effects of substrate doping, the experiments were repeated with a sample grown on n-type silicon, resulting in a qualitatively similar curve. At the beginning of the measurements both samples are a bad metal and discrepancies in the absolute energy position of bands are likewise not found. Therefore, the arguments provided in the context of Fig. 7.11 that ascribed the vast energy differences in STS measurements to tip-induced band bending are validated since the spectra are indistinguishable in PES. While the Si bulk band linearly shifts upwards until the turning point at the 10 min mark, the Sn surface state at the Γ point only varies slightly in energy. After the turning point, the position of both tracked feature drops linearly and in a comparable fashion, hallmarking a rigid band shift. However, no additional states are filled up close to the Fermi level. This favors an electrostatic effect as the origin of the observed shift.

The experiment was also repeated at a temperature of 20 K which did not yield a conclusive behavior in terms of energy shifts. It is known that the Fermi level in such an insulating system on a semiconductor platform can depend on the interplay of several factors. Firstly, the band bending can be influenced by the adsorption of electronically active atoms [199]. Furthermore, there could also be an electric field perpendicular to the surface if K and Sn atoms are not situated within the same plane. This field might also change with temperature as the bonding length of the Sn atoms is affected by frequent hopping events of the K atoms observed at temperatures above 77 K [186]. Lastly, the Fermi level could still be pinned by defect states which might vary between samples. All these effects can be enhanced at low temperature when the amount of free carriers in the substrate is reduced. On the other hand, effects of surface photovoltage or charging were excluded by rerunning spectra at different photon fluxes. An extensive study with different substrate types measured at various temperatures might be required to disentangle all these contributions.

During the whole process, the marginal spectral weight at the Fermi level gradually disappears and a true gap opens. In PES, this can be captured by tracking the onset of spectral weight at low energies as done in Fig. 7.13(b), (c). Panel (b) shows angle-integrated spectra of K-Sn/Si(111) for different K coverages as red lines. The spectral onset of each curve is plotted in Panel (c). It is determined as the point of intersection between a linear fit of the spectral edge at low energy and a horizontal line at zero intensity. An example for

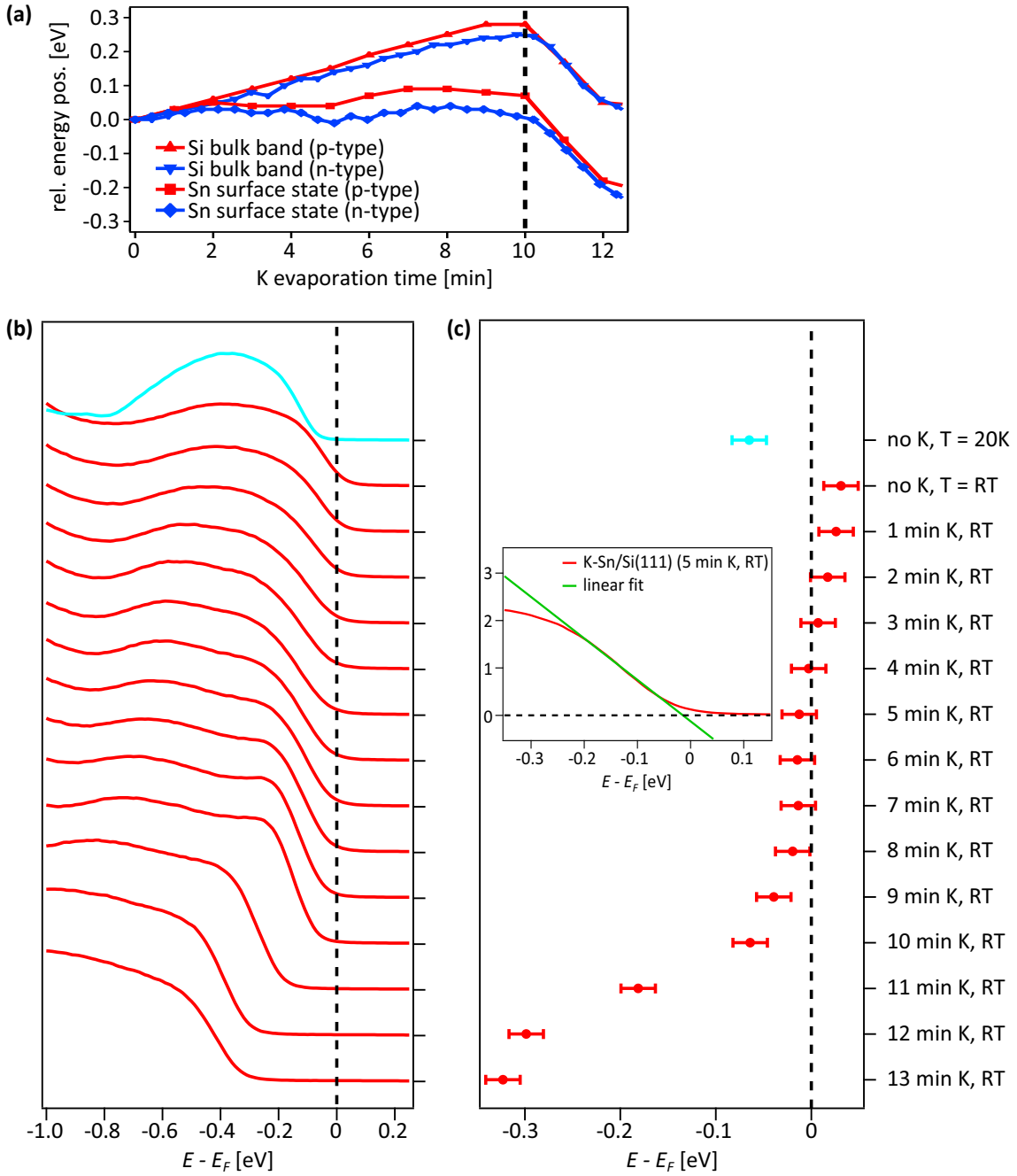

Fig. 7.13.: **(a)** Evolution of the relative energy positions of the Si bulk band and the Sn $5p_z$ surface state with increasing K concentration on the surface (indicated as total evaporation time). Data from K-Sn/Si(111) grown on substrates with high p/n doping is depicted in red/blue color and shows only marginal differences in the relative band positions. The red lines include data from the spectra shown in Fig. 7.12. **(b)** Angle-integrated (between Γ and K) photoemission spectra of K-Sn/Si(111) for different K coverages at RT (red). In addition, a spectrum of pristine $\sqrt{3}_\alpha$-Sn/Si(111) measured at $T = 20\,\mathrm{K}$ (teal) is shown. Spectra are offset vertically for clarity. $h\nu = 21.2\,\mathrm{eV}$. The associated angle-resolved data is compiled in Fig. A.4. **(c)** Spectral onset of the data shown in Panel (b) based on the point of intersection between a linear fit of the spectral edge at low energy and a horizontal line at zero intensity. An example is shown in the inset for the spectrum associated with 5 min of K evaporation. The error bars reflect the uncertainty of the Fermi level and variations due to the choice of the fitting interval. The data provides evidence for a metal-insulator transition both with temperature and K coverage.

this procedure is shown in the inset of Panel (b) for the spectrum with 5 min of potassium evaporated onto the surface. In addition, the metal-insulator transition of pristine $\sqrt{3}_\alpha$-Sn/Si(111) is shown for comparison, too, with the LT spectrum and the corresponding spectral onset plotted in teal. This transition from a bad metal with a pseudo-gap-like behavior to a Mott insulator at approximately 40 K is already documented in literature [104, 177]. Figure 7.13(c) shows that the spectral onset remains in very close proximity of the Fermi level until an eventual deviation after 9 min of K evaporation, i.e., close to the turning point described above. Due to the limited resolution, the exact point of the metal-insulator transition cannot be determined. However, it is clear that the system is in an insulating state at the turning point after 10 min of K evaporation. In an attempt to realize a metallic K overlayer on the surface, potassium is evaporated on the sample for a total of 84 min. However, the spectra remain insulating and just become increasingly featureless making an assignment of band positions questionable.

It is obvious that the turning point found in the ARPES measurements above is a pivotal feature in this study. Therefore, we take a dedicated look at a sample where the K evaporation was stopped at or slightly before the turning point is reached. Fig. 7.14(a), (b) shows a comparison of ARPES data along a high-symmetry direction of the $\sqrt{3} \times \sqrt{3}R30°$ BZ for pristine and K-doped Sn/Si(111). The drastic change of the p_z surface state can be clearly identified. The broad LHB has developed into a much sharper band that spans the whole BZ. Both the distribution of spectral weight and the energetic bandwidth have been modified by the presence of the K atoms. A detailed analysis thereof will be presented below. For illustrative purposes, we also take a look at constant energy surfaces measured on such a K-doped sample. Here the K evaporation was stopped slightly before the turning point, i.e., a direct comparison with Panel (a) is unfortunately not possible. 200 meV below the Fermi level, see Fig. 7.14(c), the appearance is dominated by the p_z surface state that is dispersing downwards when approaching the edge of the BZ. The energy maximum of the p_z surface state is located away from the Γ point which is the reason for the reduced intensity observed in the center of the BZ. For pristine $\sqrt{3}_\alpha$-Sn/Si(111), the maximum is marked by the $2\sqrt{3} \times 2\sqrt{3}$ zone boundary where the backfolding of the spectral function occurs at LT. With increasing K content, the maximum is shifts closer to the Γ point. At $E - E_F = -700$ meV, as in Fig. 7.14(d), one sees the top of the Si bulk bands in the center as well as the minima of the p_z surface state at the K points of the BZ.

Identifying the coverage at the turning point

Now that this characteristic turning point in the K doping series is found in ARPES measurements, it is important to assign an exact K coverage. Therefore, the results from Sect. 7.2.3 will be extended in the following to link the ARPES results to the discoveries made in STM. The two samples that were already investigated with XPS which featured the pure honeycomb and uniform phase, respectively, were also investigated with ARPES. For the latter one the surface was already too contaminated to allow for a identification

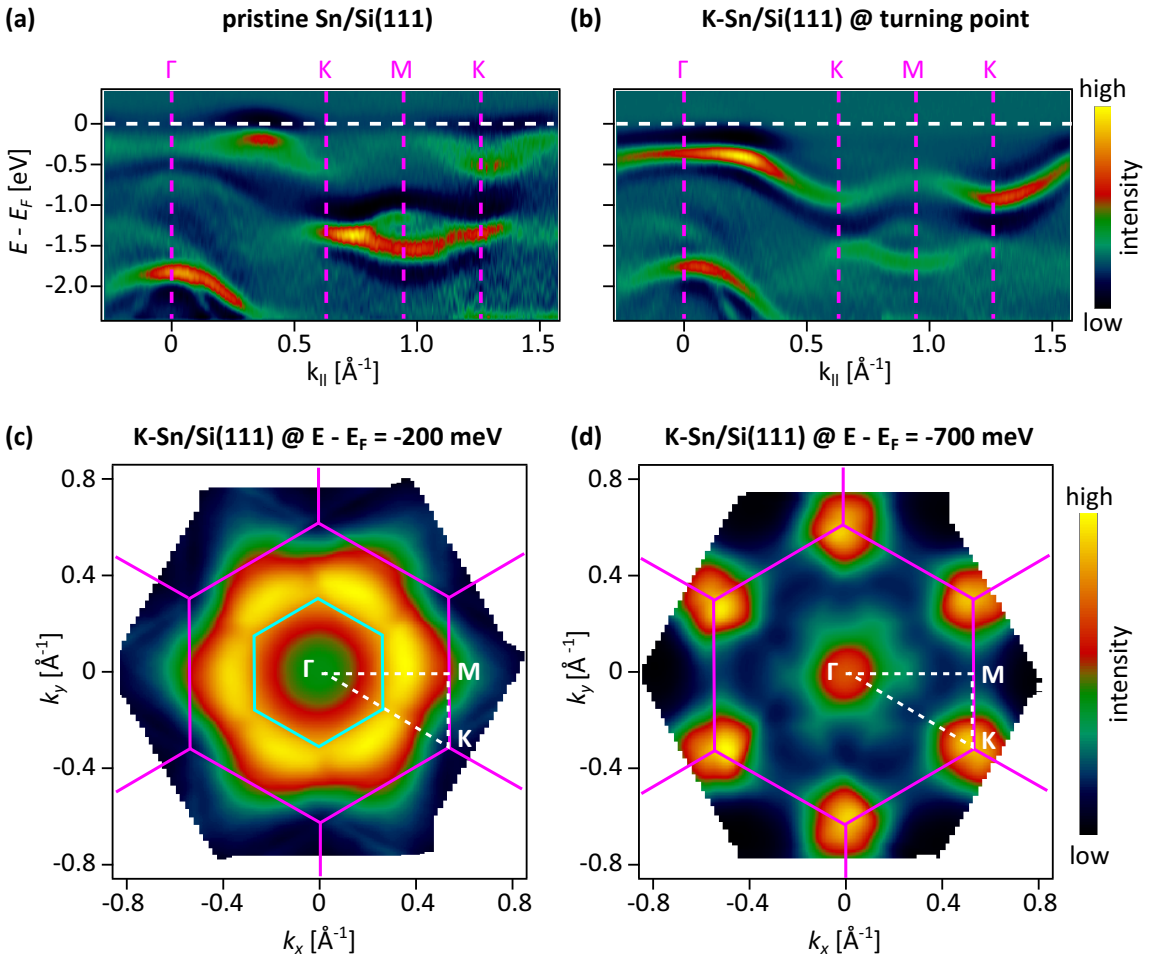

Fig. 7.14.: Second derivative of ARPES data of **(a)** pristine and **(b)** K-doped $\sqrt{3}_{\alpha}$-Sn/Si(111) along high-symmetry directions of the $\sqrt{3} \times \sqrt{3}R30°$ BZ. K evaporation was stopped at the previously described turning point. In addition to the p_z surface state, the $p_{x,y}$ states (between the two K points at $E - E_F = -1.4\,\mathrm{eV}$) and the Si bulk bands are visible as well. Raw data can be found in the Appendix in Fig. A.5. $h\nu = 21.2\,\mathrm{eV}$, $T = 300\,\mathrm{K}$. **(c)** Constant energy surface of K-Sn/Si(111) at $E - E_F = -200\,\mathrm{meV}$. The K doping was stopped slightly before the turning point was reached. The data was integrated in a window of $\pm 15\,\mathrm{meV}$ around the respective energy and symmetrized in a 6-fold manner. $h\nu = 21.2\,\mathrm{eV}$, $T = 300\,\mathrm{K}$. Purple lines indicate the boundaries of the $\sqrt{3} \times \sqrt{3}R30°$ BZs, teal lines do the same for the central $2\sqrt{3} \times 2\sqrt{3}R30°$ BZ. **(d)** Constant energy surface of K-Sn/Si(111) at $E - E_F = -700\,\mathrm{meV}$. Data processing and experimental conditions identical to Panel (c).

of surface bands and therefore only the information already gathered in Sect. 7.2.3, viz. that the ratio of K/Sn measured in XPS being 61 %, is available. For the sample with the honeycomb structure, the band structure shown in Fig. 7.15(a), (b) was measured. Although the spectrum is slightly blurred due to the transfer in the UHV suitcase, it is clear that we are dealing with the same kind of electronic structure as seen in Fig. 7.12. Identifying the exact K coverage from an ARPES measurement, however, is not error-proof. A possible variable to quantitatively estimate the doping progress on the surface is the energy distance between the Si bulk band and the p_z surface state at the Γ point. In the transferred sample this amounts to 1.37 eV which corresponds to the distance measured after seven steps in the series presented in Fig. 7.12. However, this graph also shows that there is some variation between different samples and, furthermore, it is not known if adsorbants on the surface affect these positions as well, e.g., by donating electrons or holes to the K-Sn/Si(111) system. Thus, the ARPES measurements cannot be used to reduce the error bar set by the XPS experiment but only act as a proof that the same kind of system is investigated in the two UHV setups with their complementary experimental techniques.

As a next step the experiment was done in reverse order, i.e., a sample fabricated within the PES setup was transferred to the STM chamber using the UHV suitcase. Before the transfer the ratio of K and Sn was determined to be 28 % with XPS. Fig. 7.15(c) shows a STM image taken on this surface. As already expected from the previous experiment the surface gets heavily contaminated during the transfer which for STM is maybe even more crucial than for ARPES. Although the estimation of a global K coverage is strongly limited by adsorbants on the surface, the free areas resemble the appearance of Fig. 7.5(b) which had a K content of 35 % with respect to tin. This is in line with the results from XPS which was found to underestimate the actual effective ratio, see Sect. 7.2.3. Finally, the K coverage of a sample doped to the turning point as monitored by ARPES was determined via XPS which resulted in K/Sn = 0.72. This value is far from the measures gained from the sample of the honeycomb phase and reasonably close to the one with the uniform phase. As stated before, disregarding the general uncertainty of the actual PES cross sections, higher-coverage Sn phases on the sample are the main source of error for this kind of assessment.

In summary, it was observed that the surface gets disordered when adding potassium after the uniform phase is completed. We also saw that ARPES spectra get increasingly blurred when adding potassium after the turning point is reached. It is well known that disorder on a surface has exactly this effect on spectra. As mentioned earlier, synchrotron studies of the Sn 4*d* core level revealed that the transfer of spectral weight in the substructure of the peak is completed after 1/3 ML of potassium [179]. We therefore conclude that this characteristic point which was observed with three different techniques corresponds to the same state of K-Sn/Si(111), namely the uniform phase described in Sect. 7.2.2 and depicted in Fig. 7.6(c). Any K-doping beyond this point does not lead to a change in the electronic properties but will instead create disorder on the surface. This means that 1 min of K evaporation corresponds to 10 % doping in the ARPES experiments.

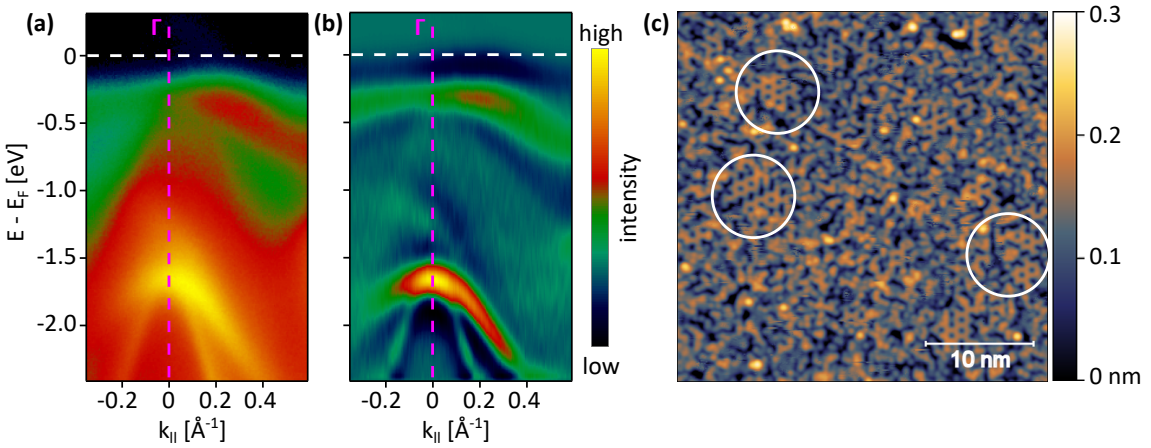

Fig. 7.15.: **(a)** Band structure of the honeycomb phase of K-Sn/Si(111) along the $\overline{\Gamma K}$ direction. The sample was first characterized by STM and transferred to the PES setup thereafter. According to XPS it has a K coverage of 35 %. $h\nu = 21.2\,\mathrm{eV}$, $T = 300\,\mathrm{K}$. **(b)** Second derivative of the same data for comparison with Fig. 7.12. **(c)** Topographic STM image of a sample that was grown in the PES setup and transferred to the STM chamber thereafter. From XPS its K coverage was measured to be 28 %. The sample is mostly covered with adsorbants but some free areas feature a not fully completed honeycomb phase (white circles) – in agreement with expectations from XPS. Tunneling conditions $V = -2.5\,\mathrm{V}$, $I = 50\,\mathrm{pA}$ and $T = 4.3\,\mathrm{K}$.

Analysis of the continuous evolution of the p_z surface state upon K deposition

In Sect. 7.2.4 we have seen that tunneling spectra on K-doped Sn/Si(111) are only affected locally by the presence of K atoms. Therefore, we will now also take a detailed look on the evolution of the spectral function upon increasing K concentration via ARPES to get a complementary insight. Figure 7.16(a) gives an overview of different properties that will be tracked starting from a pristine sample up to a coverage slightly above the turning point which is reached after 10 min of K evaporation. The ARPES data in the background is a measurement after 5 min of K evaporation and just acts as an example to graphically illustrate the meaning of variables extracted from the data set which is the one already presented in Fig. 7.12. The evolution of the $5p$ surface state is captured in the following four variables:

- The sharpness of the p_z surface state. It is measured as the full width at half maximum of a gaussian curve fitted to an EDC at the K point. This location is chosen as it offers good intensity as well as separation from other bands over the whole coverage series. Furthermore, the spectral function disperses perpendicular to the energy axis in this region which yields the most meaningful value for this quantity. The exemplary EDC and the corresponding gaussian fit are depicted in Fig. 7.16(b) while the results for the whole series are compiled in Fig. 7.16(c) in matching teal color. The EDCs for all K coverages can be found in the Appendix in Fig. A.6(a). Over the course of the experiment

the gaussian width of the former LHB decreases by about 1/3 until the turning point. Afterwards the width increases again which is in line with the observed blurring of the whole spectrum.

- The total band width of the p_z surface state. This is measured as the distance between the maximum of the gaussian peak described in the previous bullet point and an equivalent analysis performed at the maximum of the spectral function close to the Γ point. The results are summarized in the green curve in Fig. 7.16(c). The change in bandwidth is a striking feature of the K adsorption as the measured value is doubled with completion of the uniform phase. Afterwards the value remains constant.

- The spectral weight of the surface state at the Γ point. Since the corresponding peak in the EDCs can also be modeled with a gaussian function, see Fig. 7.16(d), the integral of the gaussian directly measures the spectral weight. The results are depicted in Fig. 7.16(e) as the blue curve. The EDCs for all K coverages can be found in the Appendix in Fig. A.6(b). The weak intensity between the Γ and $K_{2\sqrt{3}}$ point is gradually turned into a continuous part of the surface state with the intensity at the Γ point rising by a factor of 12. After the turning point, it drops again which is in line with disordered K atoms on the surface acting as scatterers. During these measurements, the intensity of the Si bulk band varied slightly on the order of 5 %, likely related to pressure changes of the Helium gas in the light source. To compensate for this influence, all intensities are normalized with the weight of the Si bulk band. However, this does not change any result qualitatively.

- The spectral weight of the $p_{x,y}$ state which is represented by the hatched area in Fig. 7.16(b). Here, fitting with an analytic function was not successful for most spectra of the data set. Instead, the area is calculated by numeric integration after substraction of a linear background (dotted line). The results are also found in Fig. 7.16(e) as the red curve. After decreasing monotonically in intensity up to the turning point, the $p_{x,y}$ state almost fades into the background of Si bulk states for high K coverages.

As can be seen in Figs. 7.16(c), (e), the turning point is not only relevant for the band shifts documented in Fig. 7.13(a) but also for the evolution of several other key features of the spectra. These results corroborate the finding that the turning point is associated to the uniform phase since the observed behavior, i.e., an increased width of EDCs and a decreasing spectral weight, can be perfectly explained with disordered K atoms on the surface. This is exactly what was found in STM measurements when potassium was added to the surface after completion of the uniform phase, see Figs. 7.5(e), (f).

Finally, the evolution of the dispersion will be discussed. The STM coverage series in Fig. 7.5 showed that the evolution of the surface morphology can be divided into two parts. In the first part small structures consisting of a few K atoms are formed. They are not connected with each other why a dispersive state due to long-range order is not expected. With more

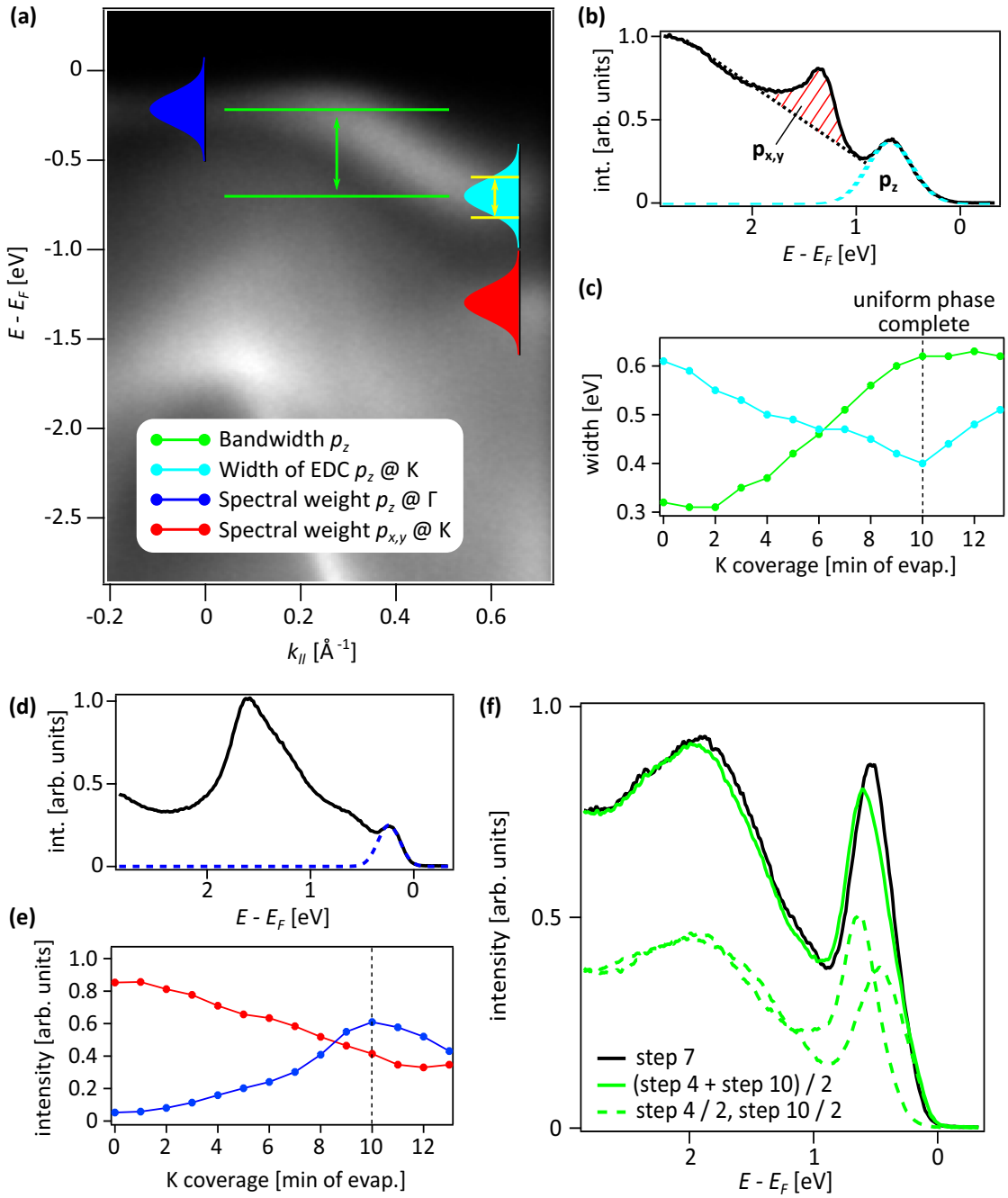

Fig. 7.16.: **(a)** Overview sketch to illustrate the meaning of the curves presented in the following. The ARPES data in the background was already shown as a second derivative in Fig. 7.12(c). **(b)** EDC at the K point of the data shown in Panel (a). While the gaussian fit (teal) measures the spectral weight of the p_z state, the hatched area provides the same for $p_{x,y}$. The whole set of EDCs can be found in Fig. A.6(a). **(c)** Total bandwidth of the p_z surface state (green) as well as the width of an EDC at the K point (teal) upon K deposition. **(d)** EDC at the Γ point of the data shown in Panel (a). The spectral weight of the p_z surface state corresponds to the integral of the Gaussian fit (blue). The whole set of EDCs can be found in Fig. A.6(b). **(e)** Spectral weight of the p_z surface state at the Γ point (blue) and of the $p_{x,y}$ state at the K point (red) upon K deposition. **(f)** Comparison of EDCs taken at $k_{||} = 0.45\,\text{Å}^{-1}$ from data after 7 steps of K evaporation (black) and a mixed data set (50 % after 4 steps and 50 % after 10 steps, solid green). The dashed green line shows the two individual components. All EDCs shown here were integrated over an angular width of $0.035\,\text{Å}^{-1}$.

potassium on the surface the patches are gradually forming the honeycomb phase which is completed at K/Sn = 0.5. In the second part a clear separation of phases is observed. With increasing K coverage, the uniform phase grows at the expense of the honeycomb phase whereas each forms patches of several nanometers in diameter. However, in ARPES measurements the evolution of the spectral function is continuous in every examined aspect as we have seen in Fig. 7.16(a)-(e). The completion of the honeycomb phase is not associated with any outstanding features in the spectral function. One might, e.g., expect to find a backfolding induced by the $2\sqrt{3} \times 2\sqrt{3}R30°$ superstructure. Furthermore, there is also no evidence that there is a separation of phases for $0.5 < \mathrm{K/Sn} < 1$, see Fig. 7.16(f). One might expect that the spectrum of an intermediate coverage like K/Sn = 0.7 could be generated by combining weighted spectra of higher and lower coverage. This is not the case which is also clear from other results such as the evolution of the bandwidth of the p_z surface state shown in Fig. 7.16(c).

In order to resolve these discrepancies, an extensive study to link results from STM and ARPES in more detail is required. This especially concerns measurements at different temperatures. So far, the system was only investigated at cryogenic temperatures in STM. Since there are already indications that the K atoms in the honeycomb phase are very mobile at RT [186], this might also be true for the uniform phase. It is also unclear if the separation of phases observed in Fig. 7.5(d) prevails at RT which calls for pertinent STM experiments. Furthermore, it is not clear if the distribution of potassium is as homogeneous as observed here when evaporated onto a sample held at 20 K which is the temperature of LT PES experiments. Evaporating potassium inside the cryostat of the STM setup could give the necessary insights. In addition, a $2\sqrt{3} \times 2\sqrt{3}R30°$ of the honeycomb phase has not been observed in ARPES or LEED so far. While the expected backfolding might be too weak to be detected in ARPES, the surface reconstruction should be well visible in LEED suggesting pertinent measurements at LT. Concerning the inconclusive behavior of band shifts at low temperature, an extensive PES measurement series that is tailored to identify the effects of substrate doping, measurement and evaporation temperature as well as K coverage might resolve this issue. Last but not least, theoretical calculations of the spectral function of the honeycomb and uniform phase, respectively, could also provide an integral part in an improved understanding of the experimental data.

Comparison of the band structure of uniform K-Sn/Si(111) with DFT calculations

Due to a lack of availability of dedicated calculations for this system, the experimental data is compared to DFT band structure calculations of pristine $\sqrt{3}_\alpha$-Sn/Si(111). However, the peculiar similarities might be perfectly suited to expose the nature of uniform K-Sn/Si(111). Figure 7.17(a) shows LDA calculations of Sn/Si(111) performed by A. Fleszar. In agreement with the available electrons, the Fermi level is set to produce a half-filled surface state for this case. To accomplish an agreement with ARPES data such as in Fig. 7.14(b), the bands have to be shifted. The result is presented in Fig. 7.17(b) where a spectrum measured at

the turning point is overlayed with the bands from LDA calculations in white color. In order to achieve this excellent agreement, the Sn p_z state from DFT has to be shifted down by 0.60 eV while the remaining bands are shifted by only 0.33 eV, thereby compensating the relative shift between the two states that was already documented in Fig. 7.13(a). Accordingly, uniform K-Sn/Si(111) can be well described within a simple DFT framework without the need of dedicated many-body techniques. This is expected if the K atoms just donate there valence electron to the Sn $5p_z$ state without any other significant interference because it results in a completely filled band. This agreement also supports our preference for the structure model in Fig. 7.6(c) where tin and potassium occur in equal quantities, leaving no partially filled orbitals on the surface. The calculations also reflect the fact that the energetic maximum of the surface state is not exactly at the Γ point.

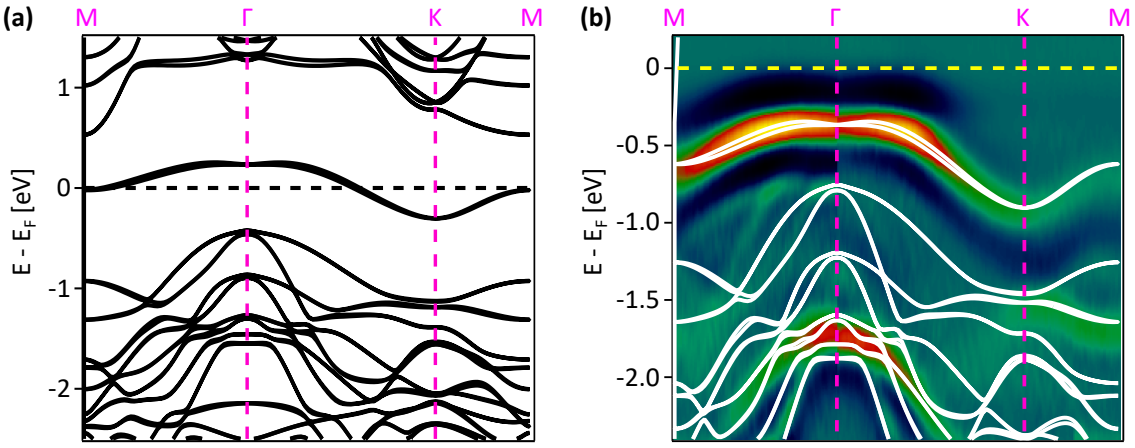

Fig. 7.17.: **(a)** LDA-DFT band structure of pristine $\sqrt{3}_\alpha$-Sn/Si(111) along the high-symmetry directions of the $\sqrt{3} \times \sqrt{3}R30°$ BZ. The Fermi level is set to result in half filling of the p_z surface band. Calculation by A. Fleszar. **(b)** Overlay of the calculated band structure from Panel (a) with the second derivative of an ARPES spectrum of uniform K-Sn/Si(111). The necessary energy shifts are specified in the main text. $h\nu = 21.2\,\text{eV}$, $T = 300\,\text{K}$.

In summary, the approach using adsorbed K atoms as dopants was only partly successful. The original goal of forming a doped Mott insulator featuring a QPP in a triangular geometry which might host an exotic ground state was not achieved. Instead, the system remains insulating for any K coverage. During the stepwise doping, a metallization might be prevented by the localization of the additional electrons in the immediate vicinity of their respective associated K cation. This was also suspected during conductivity measurements in Na-Sn/Si(111) at low dopant coverage [184]. Alternatively, the formation of insulating magnetic phases has been predicted for a doped triangular 2DES [19]. For higher K coverage the formation of an ordered honeycomb phase which was found to be insulating in STS was observed. Although it has a partly filled surface state, the emergence of CO might prevent a

metallic state [186]. Further adding of potassium produces a uniform phase which consists of Sn and K atoms in equal parts. The close resemblance of its band structure with DFT calculations of pristine Sn/Si(111) suggests that it is a simple band insulator. In order to resolve the discrepancy between the continuous evolution of the spectral function observed in ARPES and the phase separation observed in STM an extensive measurement series of K-Sn/Si(111) for different temperatures and K contents is suggested. Nevertheless, this system remains an interesting platform to study electronic correlations since a continuous evolution of a system from a Mott-Hubbard state to a trivial band insulator can be rarely observed in actual materials.

8. Summary and Outlook

In this thesis it was shown that group IV triangular lattices provide a rich playground for the examination of correlated electrons in a frustrated geometry. Although these systems have already been studied for decades, the combined application of high-resolution measurements, novel preparation and doping techniques, as well as state-of-the-art many-body calculations is still able to address current questions in solid-state research. On the basis of three selected substrate-adatom combinations, namely Sn/SiC(0001), Pb/Si(111), and Sn/Si(111), fascinating insights into the diverse behavior of correlated electrons in 2DESs were given.

Substrate-boosted correlations in $\sqrt{3}_\alpha$-Sn/SiC(0001)

For $\sqrt{3}_\alpha$-Sn/SiC(0001), the available STM data was complemented by a measurement of the k-resolved spectral function. As already inferred from the angle-integrated data presented in Ref. [A6], it features a substantial band gap despite the half-filled surface state. Using DFT, the SiC substrate was found to boost the effective correlation strength. Due to its wide band gap, the Coulomb repulsion between electrons cannot be screened effectively. Furthermore, the partly ionic character of the Si-C bond weakens the hybridization with the adatom lattice which reduces substrate-mediated hopping. Both effects drive the system deep into the Mott-insulating regime.

Since the spectral function only reflects the symmetry of the lattice, namely a $\sqrt{3} \times \sqrt{3}R30^\circ$ reconstruction, the mutual alignment of the uncompensated spins on each site remains an open question. It would be interesting to test the hypothesis of a skyrmion state with spin-resolved STM in a magnetic field at ultra-low temperature. Besides this, SiC(0001)-based group IV triangular lattices are still scarcely investigated in general. Since the inter-site hopping is small, the spin-orbit splitting can be relatively big compared to the total band width. Thus, Pb/SiC(0001), a system not synthesized so far, is potentially the ultimate candidate material for future studies of the interplay of electronic correlations and SOC in a group IV triangular lattice.

Correlation driven CO in $\sqrt{3}_\alpha$-Pb/Si(111)

By investigating the ground state of $\sqrt{3}_\alpha$-Pb/Si(111), it was identified that the well-known 3×3 reconstruction forming below 86 K is linked to the emergence of a charge-ordered state. Using anchor points obtained from QPI measurements in which the dispersion of the 2DES was traced at small energies, the spectral function of $\sqrt{3}_\alpha$-Pb/Si(111) was reconstructed

with the XVCA. This revealed that the CO observed in $\sqrt{3}_\alpha$-Pb/Si(111) is driven by electronic correlations. Furthermore, the topographic buckling of adatoms that emerges concomitantly with the charge-ordered state was resolved to be 2-up/1-down – a result DFT-based calculations have struggled to predict, possibly because many-body interactions are not included correctly.

Although $\sqrt{3}_\alpha$-Pb/Si(111) is now well-explored in terms of STM and STS, the system provides many possibilities for future studies. Using the doping approach from Chap. 7 or Ref. [40] might be promising since the effect of doping on a group IV triangular lattice with correlation-driven CO has not been explored so far. Furthermore, the nano-ARPES endstation at the MAESTRO beamline is planned to reach a spot size of 50 nm in the future [200]. This coincides with the biggest domains found for $\sqrt{3}_\alpha$-Pb/Si(111) and therefore has the potential to resolve many open questions regarding this system, especially concerning the k-resolved spectral function.

As a second Pb-based system, the mosaic $\sqrt{3}_\gamma$-Pb/Si(111) was examined where Pb and Si adatoms are distributed in a pseudo-random fashion. In agreement with literature it was found that the LDOS of Pb adatoms is extremely sensitive to the immediate chemical environment. For Si adatoms this could not be confirmed in a similar manner as spectra showed a wide range of appearances despite an identical chemical environment for the nearest neighbors. However, all measured spectra were insulating which points towards electronic correlations being essential for the description of $\sqrt{3}_\gamma$-Pb/Si(111), too. This was also confirmed by ARPES which revealed an insulating spectral function with a $\sqrt{3} \times \sqrt{3}R30°$ symmetry. To get a deeper understanding for the physics in such a chemically disordered system, many-body calculations of both local and k-resolved electronic properties would be helpful.

K doping of $\sqrt{3}_\alpha$-Sn/Si(111)

Finally, the effect of K doping on $\sqrt{3}_\alpha$-Sn/Si(111) was examined. Using STM, it was found that K atoms are adsorbed on empty T_4 sites of the underlying substrate thereby forming an ordered lattice with a honeycomb structure and a K coverage of 1/6 ML with respect to the substrate. Once this honeycomb structure is complete, a second ordered phase develops upon further potassium deposition. This phase has a K coverage of 1/3 ML with respect to the substrate and a uniform appearance in STM. After it is completed, additional potassium evaporated on the surface is adsorbed in a disordered fashion. Electronically, the anticipated IMT did not occur. At low coverage, it was found that the influence of K atoms on the LDOS is locally confined, indicating that the additional charges cannot move freely. The two ordered phases, viz. the honeycomb and uniform phase, either did not show metallic behavior. The former supposedly forms a charge-ordered state [186] while the latter is a simple band insulator. This was also confirmed in ARPES experiments where the evolution of the spectral function of K-Sn/Si(111) was tracked in detail for a K coverage between 0 and 1/3 ML. For the uniform phase the spectral function agrees well with DFT calculations

of pristine $\sqrt{3}_{\alpha}$-Sn/Si(111) that are shifted to account for the complete band filling. This indicates that potassium does not interfere with the electronic structure besides donating its valence electron.

Nevertheless, the investigations of this system are not yet completed. While the spectral function features a smooth transformation with increasing K coverage in ARPES, a phase separation is observed in STM. Additional experiments including RT STM and LT K evaporation should be carried out to fathom the origin of this seeming discrepancy. Furthermore, dedicated calculations of the band structure and LDOS for various K coverages would certainly improve the understanding of this interesting system. Moreover, the examination of K-doped group IV triangular lattices with STM and ARPES should be extended to other systems, e.g., Ge(111)- or SiC(0001)-based adatom lattices.

In conclusion, correlated electrons in a frustrated geometry set the framework for the interesting phenomena that are observed in all three investigated systems. A further exploration of the phase diagram of group IV triangular lattices in terms of band filling and electronic correlation strength is therefore a promising route towards the realization of exotic physics in an accessible and tunable environment. As demonstrated in this thesis, doping approaches or the realization of new adatom lattices can be suitable measures to make the next big step in this direction.

A. Appendix

A.1. Additional data referred to in the main text

This section provides additional information, raw data and full measurement series that were not accommodated in the main text.

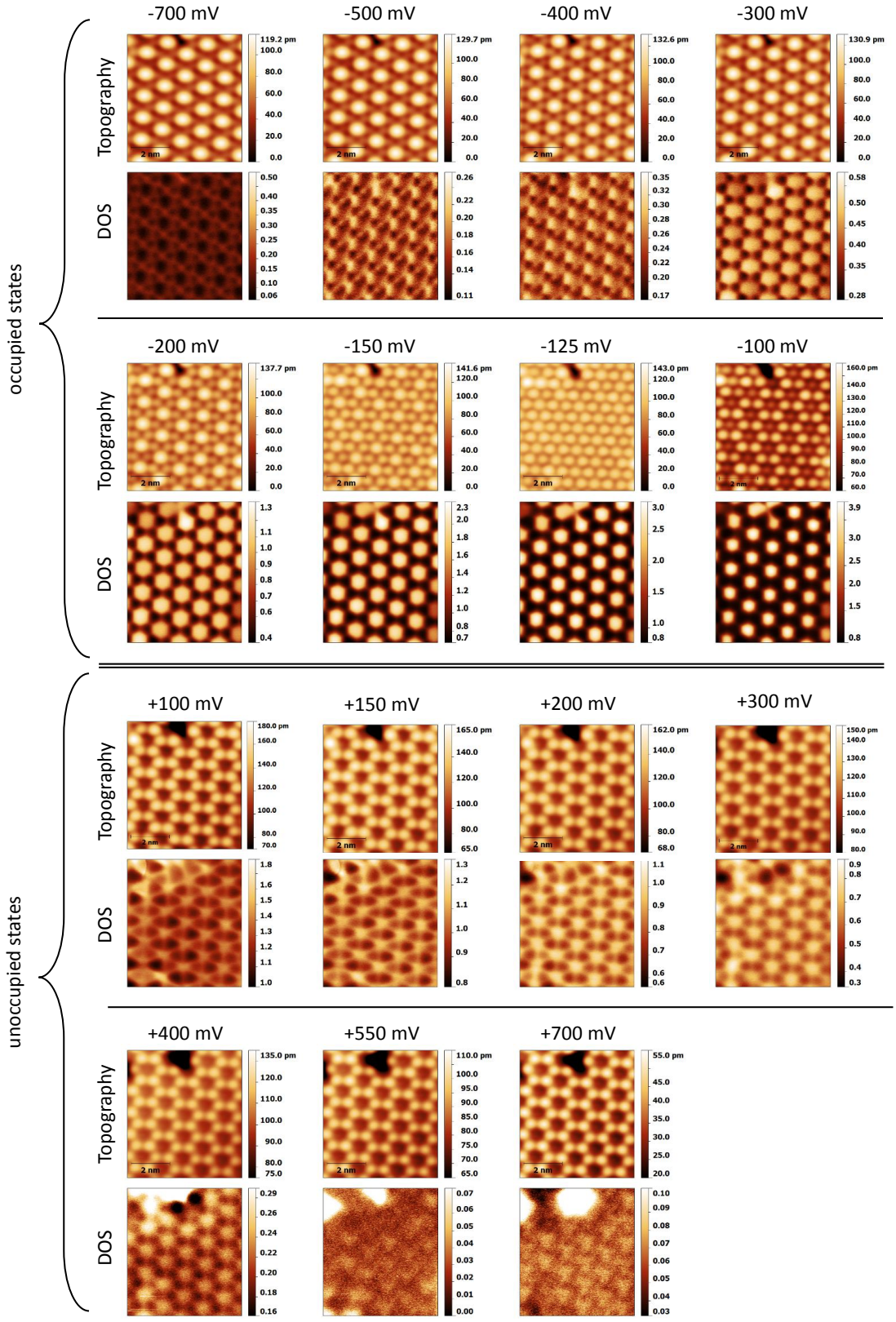

Fig. A.1.: Full series of the STM/STS measurements of $\sqrt{3}_{\alpha}$-Pb/Si(111) to determine the topographic buckling. The bias voltage is given for each scan. $I = 200\,\mathrm{pA}$ and $T = 4.3\,\mathrm{K}$ for all measurements. From Ref. [A1].

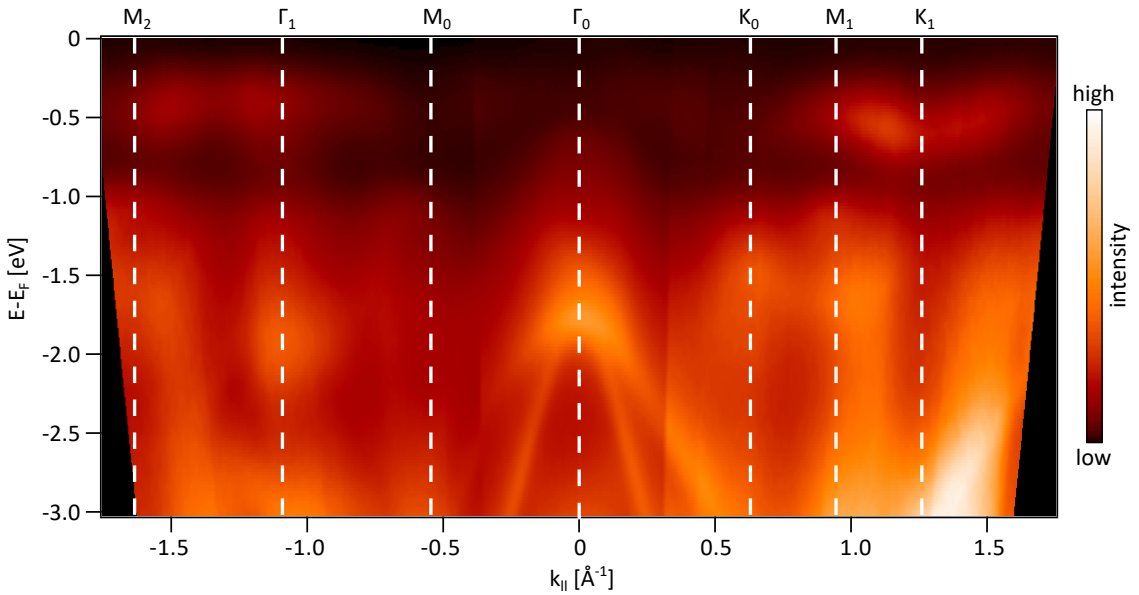

Fig. A.2.: Raw ARPES data of $\sqrt{3}_\gamma$-Pb/Si(111) as shown in Fig. 6.23(a).

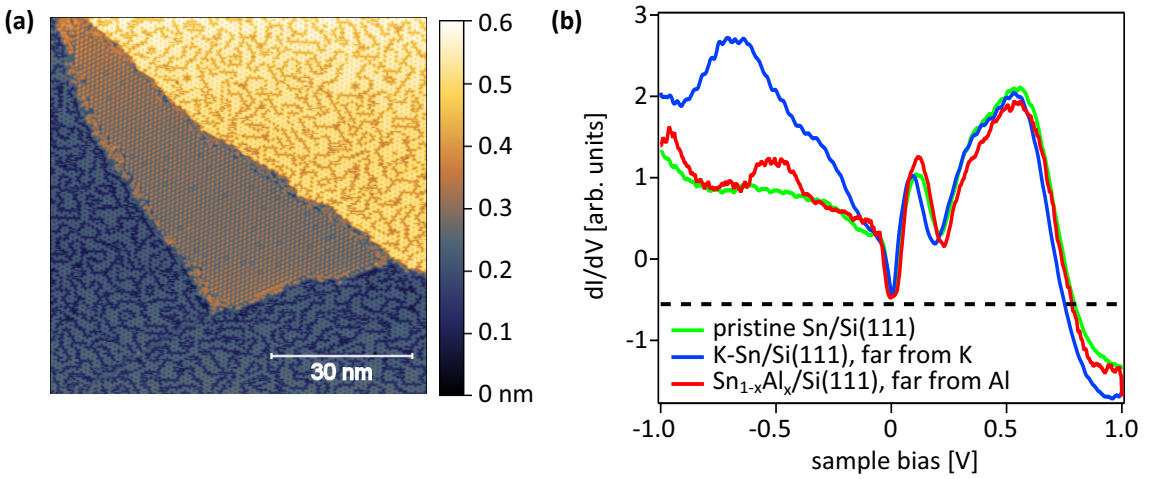

Fig. A.3.: **(a)** STM of K-Sn/Si(111) with an almost completed honeycomb phase. The $2\sqrt{3} \times 2\sqrt{3}R30°$ Sn/Si(111) domain in the center of the scan frame does not adsorb any K atoms. Some atoms have a slightly different apparent height which can also be seen in images without any potassium present [176]. **(b)** STS from Sn/Si(111) samples grown on substrates with high p-doping. Spectra are taken on a sample without any additional dopants, a sample with sporadic K doping and a sample with sporadic Al doping. $V = -1\,\mathrm{V}$ and $T = 4.3\,\mathrm{K}$ for all spectra. $I = 100\,\mathrm{pA}$ (AlSnSi), $I = 150\,\mathrm{pA}$ (KSnSi), $I = 100\,\mathrm{pA}$ (SnSi).

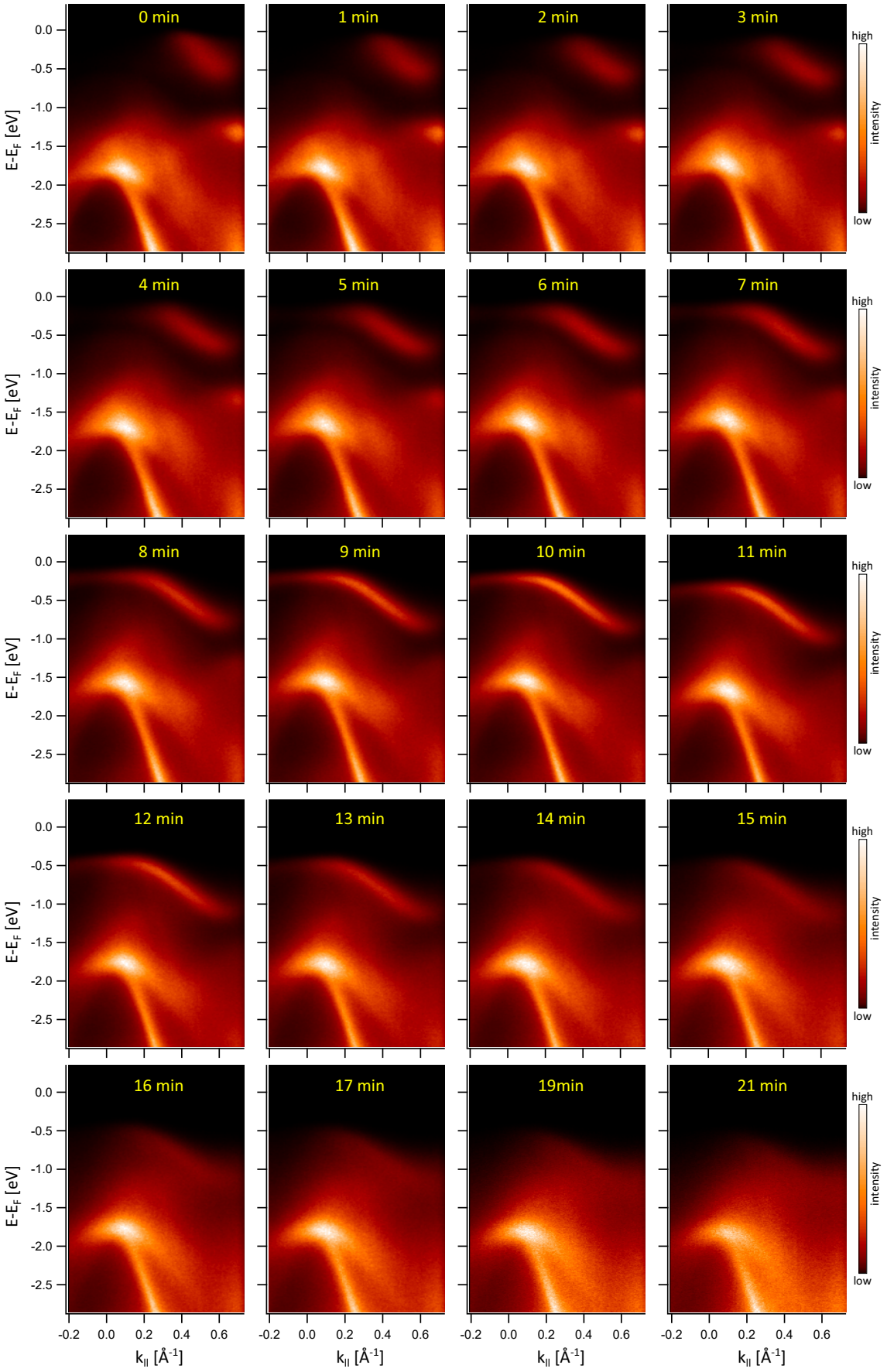

Fig. A.4.: Full series/raw data of Fig. 7.12. K deposition time marked in each panel. $T = 300\,\mathrm{K}$, $h\nu = 21.2\,\mathrm{eV}$.

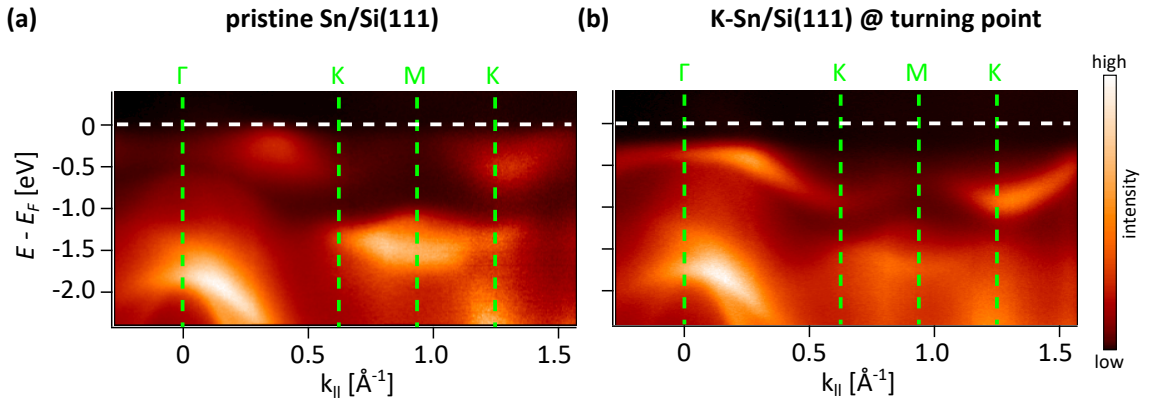

Fig. A.5.: Raw data of Fig. 7.14(a), (b).

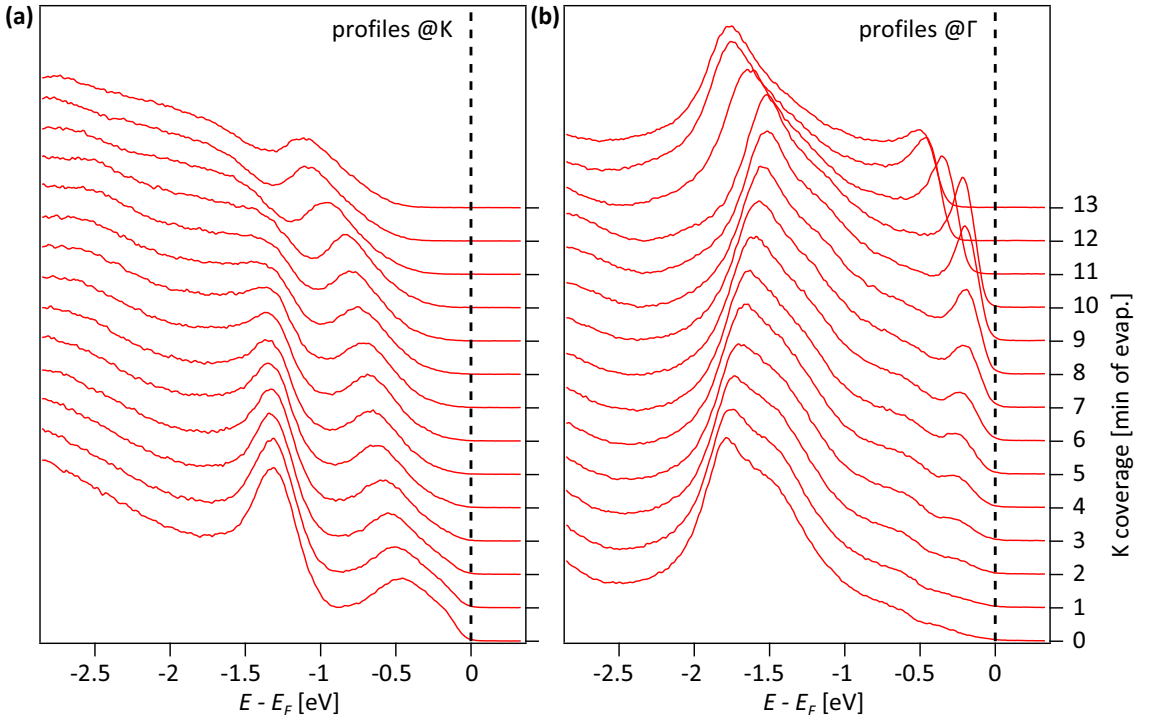

Fig. A.6.: **(a)** EDCs at the Γ point from the evaluation in Fig. 7.16. **(b)** EDCs at the K point from the evaluation in Fig. 7.16.

A.2. Investigation of doping in $\sqrt{3}_\alpha$-Sn/Si(111) via aluminum substitution

In this section, preliminary results for the substitutional doping of $\sqrt{3}_\alpha$-Sn/Si(111) with aluminum are summarized. Especially the preparation recipe has been well-established and can be used as a starting point if this system is reinvestigated in the future.

As argued in Sect. 7.1, there are alternative ways of possibly realizing a doped Mott insulator. As a next step, a substitutional approach where a fraction of the Sn atoms is replaced by atoms from a neighboring main group in the periodic table will be tested. In this case, aluminum was used which offers three valence electrons and can therefore in principle serve as a hole donor for the $\sqrt{3}_\alpha$-Sn/Si(111) system. Preliminary experiments on this matter are scarce but the work from Hirahara et al. [184] can provide a helpful point of contact. The authors report metallic conductivity characteristics of $Sn_{1-x}In_x$/Si(111) in micro-four-point probe measurements down to 260 K. For lower temperatures the system turns insulating which is attributed to carrier localization due to the dopants themselves. Although the elemental composition is not the same as in this thesis, it is at least isovalent.

A.2.1. Preparation of $Sn_{1-x}Al_x$/Si(111)

The preparation of $Sn_{1-x}Al_x$/Si(111) was found to be facilitated by a two-step process. In the first step an Al/Si(7 × 7) system with a low Al coverage is produced by evaporating Al onto a freshly flashed Si(7×7) substrate held at RT and subsequential annealing at 800°C for 10 s. This preparation step already sets the Al content x in the eventual $Sn_{1-x}Al_x$/Si(111) system. A topographic STM image at this level is shown in Fig. A.7(a). The Al atoms can be easily identified as bright protrusions on top of the characteristic (7 × 7) pattern of the Si substrate. Here, the Al atoms are located on isolated sites or in small clusters with only a few constituents.

Despite the overall low Al coverage, patches of $\sqrt{3}_\alpha$-Al/Si(111) can be found on the sample as well, see Fig. A.7(b). This is in clear contrast to the K-Sn/Si(111) system where similar accumulations of K atoms were never observed at low coverage. As one might expect, $\sqrt{3}_\alpha$-Al/Si(111) is structurally identical to group IV triangular lattices but has empty $5p_z$ orbitals making it a simple band insulator [38, 201, 202]. Therefore, the maximum Al concentration of $Sn_{1-x}Al_x$/Si(111) without any phase separation is limited. For $x \approx 0.15$ there is already a weak $\sqrt{3} \times \sqrt{3}R30°$ contribution in LEED images of Al/Si(7 × 7), documented in the inset of Fig. A.7(b). These reflexes can only originate from sporadic clusters of $\sqrt{3}_\alpha$-Al/Si(111).

After Al/Si(7 × 7) has been successfully prepared tin can be added to the system. This is done using the recipe already described in Sect. 7.2.1. It makes sense to slightly reduce the evaporation time because some of the designated adsorption sites are already occupied by Al atoms. After annealing at 650°C for 5 min, the STM image in Fig. A.7(c) gives a good impression of the sample surface. At bias voltages $1.2\,\mathrm{V} \leq V \leq 1.7\,\mathrm{V}$ the Al atoms appear

as bright protrusions. For higher voltages it becomes increasingly hard to distinguish them from the surrounding Sn atoms. At lower bias voltage they appear as depressions and are easily mixed up with other defects such as the vacancies also present in said STM scan. This is especially true when investigating occupied states. Simple atom counting identifies the phase in Fig. A.7(c) locally as $Sn_{0.84}Al_{0.16}$/Si(111). The actual total ratio of Sn/Al on the sample, however, might be different because of sporadic domains of $\sqrt{3}_\alpha$-Al/Si(111) and $2\sqrt{3} \times 2\sqrt{3}R30°$ Sn/Si(111).

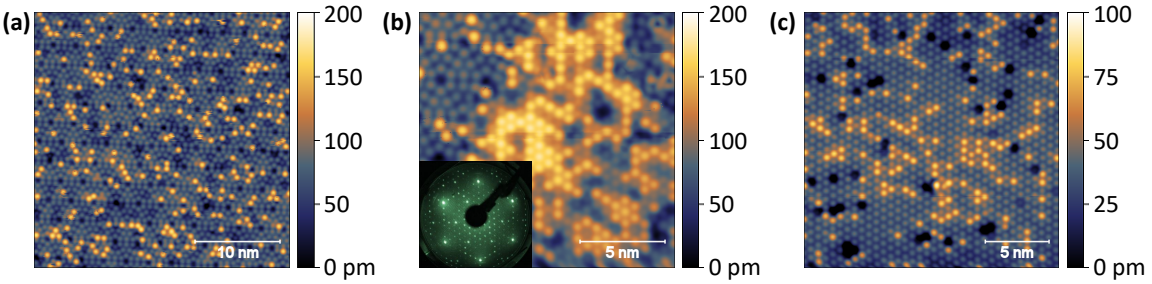

Fig. A.7.: **(a)** Topographic STM image of Al/Si(7 × 7) after annealing at 800°C for 10 s. $V = 1.6\,\mathrm{V}$ and $I = 50\,\mathrm{pA}$. **(b)** Topographic image of another location of the same sample as shown in Panel (a). Even at low coverage Al atoms tend to form clusters of $\sqrt{3}_\alpha$-Al/Si(111). $V = 1.6\,\mathrm{V}$ and $I = 50\,\mathrm{pA}$. **(c)** Topographic STM image of $Sn_{1-x}Al_x$/Si(111) with $x = 0.16$. At this bias voltage Al atoms appear as bright protrusions. The sample also has adatom vacancies which appear as dark depressions. $V = 1.4\,\mathrm{V}$ and $I = 50\,\mathrm{pA}$. All measurements were made at $T = 4.3\,\mathrm{K}$.

The success of the two-step preparation process described above is certainly connected to the different annealing temperatures necessary to move and lock the two respective adatom species to T_4 position on the Si(111) substrate. For other combinations the inverse order, i.e., adding the dopant after the group IV element, or a co-deposition as the authors of Ref. [184] seem to have used for the realization of $Sn_{1-x}In_x$/Si(111) might be a more promising approach.

A.2.2. Investigation of $Sn_{1-x}Al_x$/Si(111) with STS

As the two adatom species Sn and Al can be reliably discriminated, we will now investigate the influence of aluminum on the LDOS of nearby Sn atoms. Figure A.8(a) shows a topographic image of a suitable region. All the depressions in this scan frame were verified to originate from Al atoms through preceding measurements at different bias voltages.

Spectra taken in this area can be assigned to five categories and are compiled in Fig. A.8(b): Isolated Al atoms, Al atoms within an agglomeration, Sn atoms not adjacent to an Al atom, Sn atoms adjacent to an isolated Al atom and Sn atoms adjacent to an Al agglomeration. Besides being already identifiable from topographic images, there is also a characteristic state that is exclusive to the Al atoms which is located at $V > 0.9\,\mathrm{V}$. It has been observed by inverse PES in the isostructural $\sqrt{3}_\alpha$-In/Si(111) system as well and is

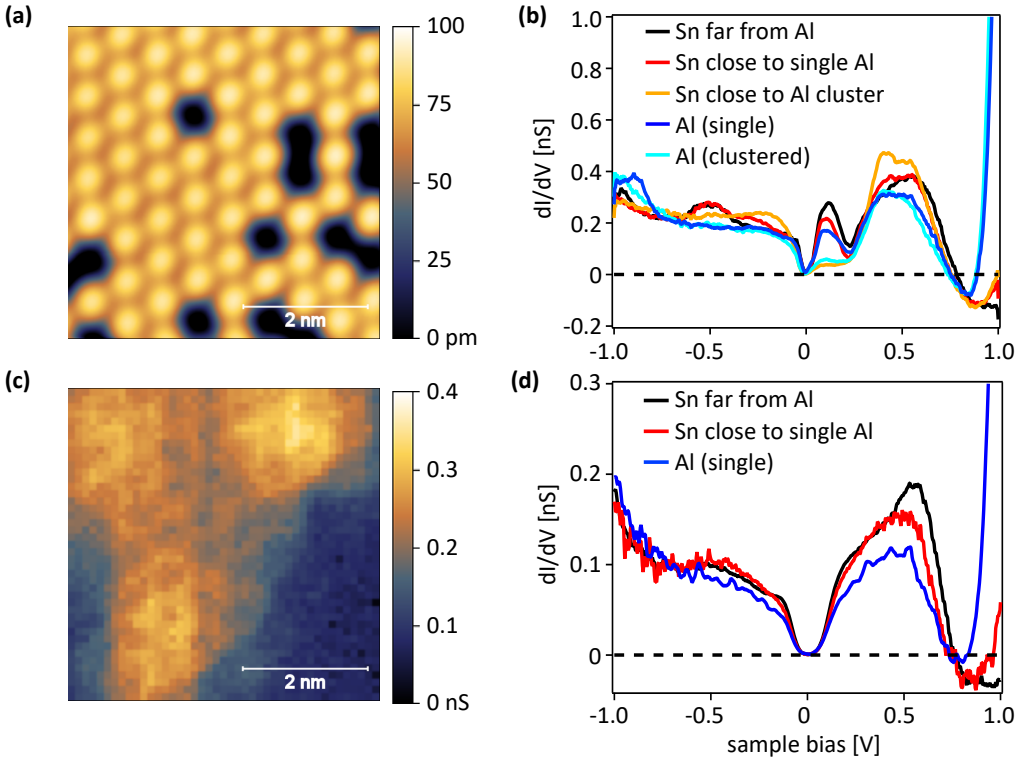

Fig. A.8.: **(a)** Topographic STM image of a region chosen for STS measurments. At a bias voltage of $V = -1.1\,\mathrm{V}$ Al adatoms appear as depressions. By scanning the same region with positive bias voltage it was verified that all depressions in this frame are indeed Al adatoms. $I = 250\,\mathrm{pA}$. **(b)** Tunneling spectra of $Sn_{1-x}Al_x/Si(111)$ fabricated on a highly p-doped substrate. Significant differences are limited to the spectral weight of the QPP and the Al-induced state at $V = 1\,\mathrm{V}$. Setpoint $V = -1.1\,\mathrm{V}$, $I = 250\,\mathrm{pA}$ and $T = 4.3\,\mathrm{K}$. **(c)** LDOS map of the investigated region taken at $V = 100\,\mathrm{mV}$, i.e., it reflects the intensity of the QPP. In contrast to other LDOS maps shown in this thesis, the one here is taken from a corresponding CITS measurement. It shows that an aggregation of Al atoms can suppress the QPP almost completely, both for the Sn and Al atoms present in that microscopic region. The energy integration window is set by the modulation voltage $V_{mod} = 10\,\mathrm{mV}$. **(d)** Tunneling spectra of $Sn_{1-x}Al_x/Si(111)$ fabricated on a lowly p-doped substrate. Setpoint $V = -1.1\,\mathrm{V}$, $I = 110\,\mathrm{pA}$ and $T = 77.4\,\mathrm{K}$.

attributed to the empty $3p_z$ states [203]. Apart from that, the spectra are similar to the ones measured on Sn atoms. If the respective Al atom is found within an agglomeration of Al atoms, the weight of the SIP is clearly suppressed.

This is also the criterion for categorizing the three kinds of Sn atoms. Just like in the case of K-Sn/Si(111) Sn atoms which are not in immediate vicinity of a possible dopant atom are not influenced by its presence and have the same LDOS as in intrinsic $\sqrt{3}_\alpha$-Sn/Si(111). In the case of $Sn_{1-x}Al_x$/Si(111) direct adjacency reduces the weight of their SIP slightly while being adjacent to an agglomeration of Al atoms almost suppresses it totally. To illustrate this more clearly the differential conductivity of the SIP at $V = 100\,\mathrm{mV}$ for the selected region is plotted in Fig. A.8(c). In the bottom right area where an agglomeration of Al atoms is found, the SIP for all atoms is clearly suppressed. It also shows that the described behavior has to be understood as a general trend among the atoms and the assignment of a spectrum to one category or another can be ambiguous due to a smooth transition.

Since the *p*-doping on the highly doped substrates also translates to the 2DES, it might be more difficult to detect contributions from the Al atoms. Therefore, pertinent experiments were also conducted for $Sn_{1-x}Al_x$/Si(111) fabricated on lowly *p*-doped substrates. The resulting tunneling spectra are depicted in Fig. A.8(d). Again, the spectra from Al atoms can be easily identified by the Al induced state at $V > 0.9\,\mathrm{V}$ and look similar to the spectra taken on Sn sites otherwise. For those, the shape of the UHB slightly changes if they are taken in immediate vicinity of an Al atom. Aside from that the spectra have an almost identical appearance, especially in the occupied states. The reduction of the SIP apparently was already the most prominent effect of Al atoms onto the Sn lattice.

These results raise the question of the actual role of aluminum in this system. Although it comes with one less electron than tin in its outer shell, the shape of the tunneling spectrum is not very different except the characteristic state at $V > 0.9\,\mathrm{V}$. This would point to the fact that the charge is distributed equally among all atoms and that aluminum is an efficient dopant. On the other hand, tunneling spectra taken a few sites away from any Al atom cannot be distinguished from spectra of pristine Sn/Si(111) indicating that aluminum does not act as a dopant at all. Another concern is the effect of Al atoms on the SIP. If aluminum would act as a local dopant in a similar way as potassium does in K-Sn/Si(111), one would expect an increased SIP if Al atoms are nearby because it is thought to emerge from *p*-doping mediated by the substrate [40]. Since the SIP rather shrinks in the vicinity of Al atoms, their role as possible *p*-dopants must be discarded. Instead, it seems that Al atoms are just distorting the local electronic landscape leading to slight changes in the LDOS. This might be most detrimental for coherent excitations like the quasiparticle. Therefore, we conclude that substitutional doping of $\sqrt{3}_\alpha$-Sn/Si(111) with Al does not result in the desired insulator-to-metal transition through formation of a quasiparticle. Since higher doping levels were shown to result in coexisting phases, this route was also not proceeded any further. Nevertheless, it became clear that the spectra measured on this system with STS are not yet well understood to date.

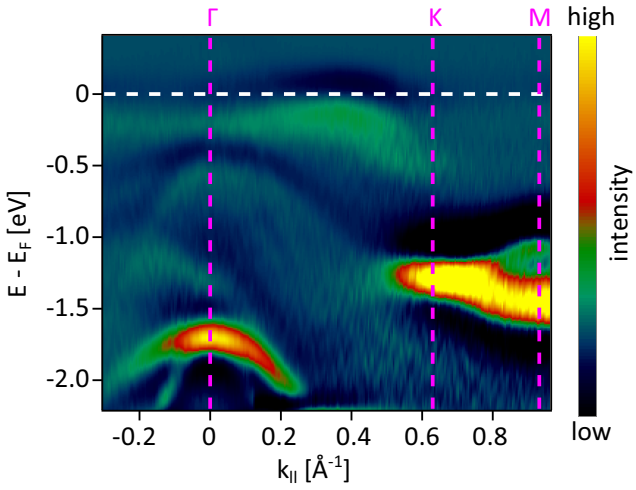

Fig. A.9: ARPES measurement of $Sn_{1-x}Al_x$/Si(111) with $x \lesssim 0.15$. Similar to K-Sn/Si(111) the spectral weight of the p_z surface state at the Γ point is increased. In addition, the $p_{x,y}$ states have a stronger spectral weight than in the pristine system. $T = 300\,\mathrm{K}$, $h\nu = 21.2\,\mathrm{eV}$, strongly p-doped substrate. Data shown as negative second derivative with respect to the energy.

A.2.3. Investigation of $Sn_{1-x}Al_x$/Si(111) with ARPES

As a complementary technique, the system is also investigated with ARPES. These are preliminary results that have not been reproduced so far. The Al content is estimated to be $x \lesssim 15$ %. The spectrum is shown in Fig. A.9. Similar to the K-doped samples it features a slightly increased spectral weight around the Γ point. However, it is not clear that this additional spectral weight would also develop into a dispersing band if it was possible to increase the Al content without the formation of Al/Si(111) clusters. After all, the adsorption of aluminum does not lead to an ordered lattice as in the case of K-Sn/Si(111) but towards randomly scattered Al atoms or – for higher Al coverage – a separation of phases. Furthermore, the $p_{x,y}$ states have a clearly increased spectral weight. Here aluminum indeed acts oppositional to potassium which lowered the intensity of these states. It is therefore likely that the hybridization with the Si substrate is changed when other elements are present on the Sn/Si(111) surface. Aside from this, the spectrum is not very different than the one of pristine Sn/Si(111). Given that the STS results also showed no big differences in the occupied states, this is not surprising. In addition, the evolution of the spectral function in K-Sn/Si(111) happened in a range where Sn and dopant atoms reached equal numbers. Here, there is less than one Al atom for five Sn atoms which is a second reason why striking differences are not expected. Since the desired emergence of a SIP was not achieved at low Al coverage and domains of Al/Si(111) prevented the formation of a highly doped $Sn_{1-x}Al_x$/Si(111) system, the experiments with this class of substitutionally doped triangular lattices were not pursued any further.

Bibliography

[1] K. Takada, H. Sakurai, E. Takayama-Muromachi, F. Izumi, R. A. Dilanian, and T. Sasaki, Nature **422**, 53 (2003).

[2] L. Balents, Nature **464**, 199 (2010).

[3] S. T. Bramwell, S. R. Giblin, S. Calder, R. Aldus, D. Prabhakaran, and T. Fennell, Nature **461**, 956 (2009).

[4] J. M. Carpinelli, H. H. Weitering, E. W. Plummer, and R. Stumpf, Nature **381**, 398 (1996).

[5] J. M. Carpinelli, H. H. Weitering, M. Bartkowiak, R. Stumpf, and E. W. Plummer, Phys. Rev. Lett. **79**, 2859 (1997).

[6] G. Profeta and E. Tosatti, Phys. Rev. Lett. **98**, 086401 (2007).

[7] P. Hansmann, T. Ayral, L. Vaugier, P. Werner, and S. Biermann, Phys. Rev. Lett. **110**, 166401 (2013).

[8] K. Misumi, T. Kaneko, and Y. Ohta, Phys. Rev. B **95**, 075124 (2017).

[9] G. Li, M. Laubach, A. Fleszar, and W. Hanke, Phys. Rev. B **83**, 041104 (2011).

[10] G. Li, P. Höpfner, J. Schäfer, C. Blumenstein, S. Meyer, A. Bostwick, E. Rotenberg, R. Claessen, and W. Hanke, Nat. Comm. **4**, 1620 (2013).

[11] G. Santoro, S. Scandolo, and E. Tosatti, Phys. Rev. B **59**, 1891 (1999).

[12] R. Coldea, D. A. Tennant, A. M. Tsvelik, and Z. Tylczynski, Phys. Rev. Lett. **86**, 1335 (2001).

[13] Y. Shimizu, K. Miyagawa, K. Kanoda, M. Maesato, and G. Saito, Phys. Rev. Lett. **91**, 107001 (2003).

[14] J. A. Paddison, M. Daum, Z. Dun, G. Ehlers, Y. Liu, M. Stone, H. Zhou, and M. Mourigal, Nat. Phys. **13**, 117 (2017).

[15] W. Witczak-Krempa, G. Chen, Y. B. Kim, and L. Balents, Ann. Rev. Cond. Mat. Phys. **5**, 57 (2014).

[16] M. Jäger, C. Brand, A. P. Weber, M. Fanciulli, J. H. Dil, H. Pfnür, and C. Tegenkamp, Phys. Rev. B **98**, 165422 (2018).

[17] D. I. Badrtdinov, S. A. Nikolaev, M. I. Katsnelson, and V. V. Mazurenko, Phys. Rev. B **94**, 224418 (2016).

[18] D. I. Badrtdinov, S. A. Nikolaev, A. N. Rudenko, M. I. Katsnelson, and V. V. Mazurenko, Phys. Rev. B **98**, 184425 (2018).

[19] G. Li, A. E. Antipov, A. N. Rubtsov, S. Kirchner, and W. Hanke, Phys. Rev. B **89**, 161118 (2014).

[20] Z.-X. Li, M. L. Cohen, and D.-H. Lee, Phys. Rev. B **100**, 245105 (2019).

[21] M. L. Kiesel, C. Platt, W. Hanke, and R. Thomale, Phys. Rev. Lett. **111**, 097001 (2013).

[22] C. Weber, A. Läuchli, F. Mila, and T. Giamarchi, Phys. Rev. B **73**, 014519 (2006).

[23] C. Kallin and J. Berlinsky, Rep. Prog. Phys. **79**, 054502 (2016).

[24] R. E. Schaak, T. Klimczuk, M. L. Foo, and R. J. Cava, Nature **424**, 527 (2003).

[25] M. Vojta and E. Dagotto, Phys. Rev. B **59**, R713 (1999).

[26] S. Rachel, unpublished.

[27] X. Wu, F. Ming, T. S. Smith, G. Liu, F. Ye, K. Wang, S. Johnston, and H. H. Weitering, Phys. Rev. Lett. **125**, 117001 (2020).

[28] R. C. Dynes, V. Narayanamurti, and J. P. Garno, Phys. Rev. Lett. **41**, 1509 (1978).

[29] X. Cao, T. Ayral, Z. Zhong, O. Parcollet, D. Manske, and P. Hansmann, Phys. Rev. B **97**, 155145 (2018).

[30] S. Wolf, D. Di Sante, T. Schwemmer, R. Thomale, and S. Rachel, unpublished (2020).

[31] P. J. Estrup and J. Morrison, Surf. Sci. **2**, 465 (1964).

[32] G. Le Lay, G. Quentel, J. P. Faurie, and A. Masson, Thin Solid Films **35**, 273 (1976).

[33] T. Ichikawa and S. Ino, Surf. Sci. **136**, 267 (1984).

[34] W. Bludau, A. Onton, and W. Heinke, J. Appl. Phys. **45**, 1846 (1974).

[35] K. C. Pandey, Phys. Rev. Lett. **47**, 1913 (1981).

[36] J. E. Northrup and M. L. Cohen, Phys. Rev. Lett. **49**, 1349 (1982).

[37] K. Takayanagi, Y. Tanishiro, S. Takahashi, and M. Takahashi, Surf. Sci. **164**, 367 (1985).

[38] J. E. Northrup, Phys. Rev. Lett. **53**, 683 (1984).

[39] K. Momma and F. Izumi, J. Appl. Cryst. **44**, 1272 (2001).

[40] F. Ming, S. Johnston, D. Mulugeta, T. S. Smith, P. Vilmercati, G. Lee, T. A. Maier, P. C. Snijders, and H. H. Weitering, Phys. Rev. Lett. **119**, 266802 (2017).

[41] J. Settelein, *Rastertunnelspektroskopie am korrelierten Elektronensystem Sn/Si(111)*, Masterarbeit, Unversität Würzburg (2012).

[42] M. Liehr, M. Renier, R. A. Wachnik, and G. S. Scilla, J. Appl. Phys. **61**, 4619 (1987).

[43] S. Bensalah, J.-P. Lacharme, and C. A. Sébenne, Phys. Rev. B **43**, 14441 (1991).

[44] J. D. Mottram, A. Thanailakis, and D. C. Northrop, J. Phys. D **8**, 1316 (1975).

[45] G. Masetti, M. Severi, and S. Solmi, IEEE Trans. on Elec. Dev. **30**, 764 (1983).

[46] W. F. Hosford, *Materials Science* (Cambridge University Press, 2006).

[47] C. Haberstroh, R. Helbig, and R. A. Stein, J. Appl. Phys. **76**, 509 (1994).

[48] A. Ferreira da Silva, J. Pernot, S. Contreras, B. E. Sernelius, C. Persson, and J. Camassel, Phys. Rev. B **74**, 245201 (2006).

[49] S. Glass, *Wachstum und Struktur von hexagonalen Sn- und Bi-Lagen auf SiC(0001)*, Masterarbeit, Unversität Würzburg (2014).

[50] L. I. Johansson, F. Owman, and P. Mårtensson, Phys. Rev. B **53**, 13793 (1996).

[51] N. Sieber, T. Seyller, L. Ley, D. James, J. D. Riley, R. C. G. Leckey, and M. Polcik, Phys. Rev. B **67**, 205304 (2003).

[52] V. Ramachandran and R. M. Feenstra, Phys. Rev. Lett. **82**, 1000 (1999).

[53] R. Ostendorf, K. Wulff, C. Benesch, H. Merz, and H. Zacharias, Phys. Rev. B **70**, 205325 (2004).

[54] Private communication with Raúl Stühler.

[55] T.-L. Chan, C. Z. Wang, M. Hupalo, M. C. Tringides, Z.-Y. Lu, and K. M. Ho, Phys. Rev. B **68**, 045410 (2003).

[56] C. Tresca, C. Brun, T. Bilgeri, G. Menard, V. Cherkez, R. Federicci, D. Longo, F. Debontridder, M. D'angelo, D. Roditchev, G. Profeta, M. Calandra, and T. Cren, Phys. Rev. Lett. **120**, 196402 (2018).

[57] A. A. Escuadro, D. M. Goodner, J. S. Okasinski, and M. J. Bedzyk, Phys. Rev. B **70**, 235416 (2004).

[58] K. Conway, J. Macdonald, C. Norris, E. Vlieg, and J. van der Veen, Surf. Sci. **215**, 555 (1989).

[59] J. S. Pedersen, R. Feidenhans'l, M. Nielsen, K. Kjær, F. Grey, and R. L. Johnson, Surf. Sci. **189-190**, 1047 (1987).

[60] M. Sabisch, P. Krüger, and J. Pollmann, Phys. Rev. B **55**, 10561 (1997).

[61] S. Schuwalow, D. Grieger, and F. Lechermann, Phys. Rev. B **82**, 035116 (2010).

[62] J. H. de Boer and E. J. W. Verwey, Proc. Phys. Soc. **49**, 59 (1937).

[63] N. F. Mott and R. Peierls, Proc. Phys. Soc. **49**, 72 (1937).

[64] N. F. Mott, Philosophical Magazine **6**, 287 (1961).

[65] J. Hubbard and B. H. Flowers, Proc. R. Soc. London A **276**, 238 (1963).

[66] M. C. Gutzwiller, Phys. Rev. Lett. **10**, 159 (1963).

[67] J. Kanamori, Prog. Theo. Phys. **30**, 275 (1963).

[68] F. Gebhardt, *The Mott Metal-Insulator Transition* (Springer, 1997).

[69] P. Fazekas, *Lecture Notes on Electron Correlation and Magnetism* (World Scientific, 1999).

[70] G. Baym and C. Pethick, *Landau Fermi-Liquid Theory* (Wiley, 2004).

[71] N. W. Ashcroft and N. D. Mermin, *Solid State Physics* (Brooks/Cole, 1976).

[72] W. Metzner and D. Vollhardt, Phys. Rev. Lett. **62**, 324 (1989).

[73] A. Georges and G. Kotliar, Phys. Rev. B **45**, 6479 (1992).

[74] G. Kotliar and D. Vollhardt, Physics Today **57**, 53 (2004).

[75] M. Imada, A. Fujimori, and Y. Tokura, Rev. Mod. Phys. **70**, 1039 (1998).

[76] S. B. Roy, *Mott Insulators: Physics and applications* (IOP Publishing, 2019).

[77] D. Qian, L. Wray, D. Hsieh, D. Wu, J. L. Luo, N. L. Wang, A. Kuprin, A. Fedorov, R. J. Cava, L. Viciu, and M. Z. Hasan, Phys. Rev. Lett. **96**, 046407 (2006).

[78] J. P. F. LeBlanc, A. E. Antipov, F. Becca, I. W. Bulik, G. K.-L. Chan, C.-M. Chung, Y. Deng, M. Ferrero, T. M. Henderson, C. A. Jiménez-Hoyos, E. Kozik, X.-W. Liu, A. J. Millis, N. V. Prokof'ev, M. Qin, G. E. Scuseria, H. Shi, B. V. Svistunov, L. F. Tocchio, I. S. Tupitsyn, S. R. White, S. Zhang, B.-X. Zheng, Z. Zhu, and E. Gull (Simons Collaboration on the Many-Electron Problem), Phys. Rev. X **5**, 041041 (2015).

[79] M. Potthoff, M. Aichhorn, and C. Dahnken, Phys. Rev. Lett. **91**, 206402 (2003).

[80] M. Potthoff, Eur. Phys. J. B **32**, 429 (2003).

[81] K. Misumi, T. Kaneko, and Y. Ohta, Journal of the Physical Society of Japan **85**, 064711 (2016).

[82] S. R. Hassan and D. Sénéchal, Phys. Rev. Lett. **110**, 096402 (2013).

[83] M. Laubach, D. G. Joshi, J. Reuther, R. Thomale, M. Vojta, and S. Rachel, Phys. Rev. B **93**, 041106 (2016).

[84] S. Rachel, M. Laubach, J. Reuther, and R. Thomale, Phys. Rev. Lett. **114**, 167201 (2015).

[85] H. Hertz, Annalen der Physik **267**, 983 (1887).

[86] A. Einstein, Annalen der Physik **14**, 164 (2005).

[87] C. Nordling, E. Sokolowski, and K. Siegbahn, Phys. Rev. **105**, 1676 (1957).

[88] A. Damascelli, Physica Scripta **T109**, 61 (2004).

[89] S. Hüfner, *Photoelectron Spectroscopy - Principles and Applications* (Springer, 2003).

[90] S. Suga and A. Sekiyama, *Photoelectron Spectroscopy - Bulk and Surface Electronic Structures* (Springer, 2014).

[91] T. Miller, W. E. McMahon, and T.-C. Chiang, Phys. Rev. Lett. **77**, 1167 (1996).

[92] E. D. Hansen, T. Miller, and T.-C. Chiang, Phys. Rev. Lett. **78**, 2807 (1997).

[93] L. Hedin and J. Lee, J. Electron Spectrosc. **124**, 289 (2002).

[94] M. P. Seah and W. A. Dench, Surf. Interface Anal. **1**, 2 (1979).

[95] D. A. Shirley, Phys. Rev. B **5**, 4709 (1972).

[96] G. Binnig, H. Rohrer, C. Gerber, and E. Weibel, Phys. Rev. Lett. **49**, 57 (1982).

[97] F. Schwabl, *Quantenmechanik - Eine Einführung* (Springer, 2007).

[98] R. Wiesendanger, *Scanning Probe Microscopy and Spectroscopy* (Cambridge University Press, 2001).

[99] J. Tersoff and D. R. Hamann, Phys. Rev. Lett. **50**, 1998 (1983).

[100] J. Bardeen, Phys. Rev. Lett. **6**, 57 (1961).

[101] J. Tersoff and D. R. Hamann, Phys. Rev. B **31**, 805 (1985).

[102] M. M. Ervasti, F. Schulz, P. Liljeroth, and A. Harju, J. Electron Spectrosc. **219**, 63 (2017).

[103] Y. Xie, B. Lian, B. Jäck, X. Liu, C.-L. Chiu, K. Watanabe, T. Taniguchi, B. A. Bernevig, and A. Yazdani, Nature **572**, 101 (2019).

[104] S. Modesti, L. Petaccia, G. Ceballos, I. Vobornik, G. Panaccione, G. Rossi, L. Ottaviano, R. Larciprete, S. Lizzit, and A. Goldoni, Phys. Rev. Lett. **98**, 126401 (2007).

[105] M. Zahedifar and P. Kratzer, Phys. Rev. B **100**, 125427 (2019).

[106] S. Crampin, H. Jensen, J. Kröger, L. Limot, and R. Berndt, Phys. Rev. B **72**, 035443 (2005).

[107] J. E. Hoffman, K. McElroy, D.-H. Lee, K. M. Lang, H. Eisaki, S. Uchida, and J. C. Davis, Science **297**, 1148 (2002).

[108] M. F. Crommie, C. P. Lutz, and D. M. Eigler, Nature **363**, 524 (1993).

[109] L. Petersen, P. Hofmann, E. W. Plummer, and F. Besenbacher, J. Electron Spectrosc. **109**, 97 (2000).

[110] C. Davisson and L. H. Germer, Phys. Rev. **30**, 705 (1927).

[111] M. A. Van Hove, W. H. Einberg, and C.-M. Chan, *Low-energy electron diffraction - Experiment, Theory and Surface Structure Determination* (Springer, 1986).

[112] L. I. Johansson, F. Owman, and P. Mårtensson, Surf. Sci. **360**, L478 (1996).

[113] F. Owman and P. Mårtensson, Surf. Sci. **330**, L639 (1995).

[114] R. Ostendorf, K. Wulff, C. Benesch, H. Merz, and H. Zacharias, Phys. Rev. B **70**, 205325 (2004).

[115] J. E. Northrup and J. Neugebauer, Phys. Rev. B **57**, R4230 (1998).

[116] J. Furthmüller, F. Bechstedt, H. Hüsken, B. Schröter, and W. Richter, Phys. Rev. B **58**, 13712 (1998).

[117] M. Rohlfing and J. Pollmann, Phys. Rev. Lett. **84**, 135 (2000).

[118] N. Sieber, T. Seyller, L. Ley, D. James, J. D. Riley, R. C. G. Leckey, and M. Polcik, Phys. Rev. B **67**, 205304 (2003).

[119] K. V. Emtsev, T. Seyller, L. Ley, L. Broekman, A. Tadich, J. D. Riley, R. G. C. Leckey, and M. Preuss, Phys. Rev. B **73**, 075412 (2006).

[120] F. Reis, *tbd.*, Dissertation, Unversität Würzburg (2020).

[121] R. I. G. Uhrberg, H. M. Zhang, T. Balasubramanian, S. T. Jemander, N. Lin, and G. V. Hansson, Phys. Rev. B **62**, 8082 (2000).

[122] A. Tejeda, R. Cortés, J. Lobo, E. G. Michel, and A. Mascaraque, J. Phys. Cond. Mat. **19**, 355008 (2007).

[123] J.-H. Lee, X.-Y. Ren, Y. Jia, and J.-H. Cho, Phys. Rev. B **90**, 125439 (2014).

[124] R. Ravichandran, A. X. Wang, and J. F. Wager, Opt. Mat. **60**, 181 (2016).

[125] L. Patrick and W. J. Choyke, Phys. Rev. B **2**, 2255 (1970).

[126] W. C. Dunlap and R. L. Watters, Phys. Rev. **92**, 1396 (1953).

[127] X.-Y. Feng, X. Dong, and J. Dai, Phys. Rev. B **84**, 212406 (2011).

[128] G. Jackeli and G. Khaliullin, Phys. Rev. Lett. **102**, 017205 (2009).

[129] M. Saitoh, K. Oura, K. Asano, F. Shoji, and T. Hanawa, Surf. Sci. **154**, 394 (1984).

[130] G. Le Lay, J. Perettic, and M. Hanbrücken, Surf. Sci. **204**, 57 (1988).

[131] E. Ganz, I.-S. Hwang, F. Xiong, S. K. Theiss, and J. Golovchenko, Surf. Sci. **257**, 259 (1991).

[132] E. Ganz, F. Xiong, I.-S. Hwang, and J. Golovchenko, Phys. Rev. B **43**, 7316 (1991).

[133] I. Brihuega, O. Custance, R. Pérez, and J. M. Gómez-Rodríguez, Phys. Rev. Lett. **94**, 046101 (2005).

[134] M. Švec, V. Cháb, and M. C. Tringides, J. Appl. Phys. **106**, 053501 (2009).

[135] I.-S. Hwang, S.-H. Chang, C.-K. Fang, L.-J. Chen, and T. T. Tsong, Phys. Rev. Lett. **93**, 106101 (2004).

[136] K. Horikoshi, X. Tong, T. Nagao, and S. Hasegawa, Phys. Rev. B **60**, 13287 (1999).

[137] J. Kraft, S. L. Surnev, and F. P. Netzer, Surf. Sci. **340**, 36 (1995).

[138] M. Hupalo, J. Schmalian, and M. C. Tringides, Phys. Rev. Lett. **90**, 216106 (2003).

[139] M. Yakes, V. Yeh, M. Hupalo, and M. C. Tringides, Phys. Rev. B **69**, 224103 (2004).

[140] T. Zhang, P. Cheng, W.-J. Li, Y.-J. Sun, G. Wang, X.-G. Zhu, K. He, L. Wang, X. Ma, X. Chen, Y. Wang, Y. Liu, H.-Q. Lin, J.-F. Jia, and Q.-K. Xue, Nat. Phys. **6**, 104 (2010).

[141] K. Horikoshi, X. Tong, T. Nagao, and S. Hasegawa, Phys. Rev. B **60**, 13287 (1999).

[142] I. Brihuega, O. Custance, M. M. Ugeda, and J. M. Gómez-Rodríguez, Phys. Rev. B **75**, 155411 (2007).

[143] O. Custance, I. Brihuega, J.-Y. Veuillen, J. M. Gómez-Rodríguez, and A. M. Baró, Surf. Sci. **482-485**, 878 (2001).

[144] O. Custance, J. M. Gómez-Rodríguez, A. M. Baró, L. Juré, P. Mallet, and J.-Y. Veuillen, Surf. Sci. **482-485**, 1399 (2001).

[145] T. Mitsui and K. Takayanagi, Phys. Rev. B **62**, R16251 (2000).

[146] R. Pérez, J. Ortega, and F. Flores, Phys. Rev. Lett. **86**, 4891 (2001).

[147] P. J. Timans, J. Appl. Phys. **74**, 6353 (1993).

[148] M. Grobis, A. Wachowiak, R. Yamachika, and M. F. Crommie, Appl. Phys. Lett. **86**, 204102 (2005).

[149] M. Švec, P. Jelínek, P. Shukrynau, C. González, V. Cháb, and V. Drchal, Phys. Rev. B **77**, 125104 (2008).

[150] F. Reis, G. Li, L. Dudy, M. Bauernfeind, S. Glass, W. Hanke, R. Thomale, J. Schäfer, and R. Claessen, Science **357**, 287 (2017).

[151] R. M. Feenstra, J. A. Stroscio, and A. P. Fein, Surf. Sci. **181**, 295 (1987).

[152] P. Cudazzo, G. Profeta, and A. Continenza, Surf. Sci. **602**, 747 (2008).

[153] A. V. Melechko, J. Braun, H. H. Weitering, and E. W. Plummer, Phys. Rev. Lett. **83**, 999 (1999).

[154] A. V. Melechko, J. Braun, H. H. Weitering, and E. W. Plummer, Phys. Rev. B **61**, 2235 (2000).

[155] R. Cortés, A. Tejeda, J. Lobo-Checa, C. Didiot, B. Kierren, D. Malterre, J. Merino, F. Flores, E. G. Michel, and A. Mascaraque, Phys. Rev. B **88**, 125113 (2013).

[156] T. Yoshioka, A. Koga, and N. Kawakami, Phys. Rev. Lett. **103**, 036401 (2009).

[157] F. Ming, T. S. Smith, S. Johnston, P. C. Snijders, and H. H. Weitering, Phys. Rev. B **97**, 075403 (2018).

[158] J. Avila, A. Mascaraque, E. G. Michel, M. C. Asensio, G. LeLay, J. Ortega, R. Pérez, and F. Flores, Phys. Rev. Lett. **82**, 442 (1999).

[159] M. Švec, V. Dudr, M. Vondráček, P. Jelínek, P. Mutombo, V. Cháb, F. Šutara, V. Matolín, and K. C. Prince, Surf. Sci. **603**, 2861 (2009).

[160] J. I. Pascual, G. Bihlmayer, Y. M. Koroteev, H.-P. Rust, G. Ceballos, M. Hansmann, K. Horn, E. V. Chulkov, S. Blügel, P. M. Echenique, and P. Hofmann, Phys. Rev. Lett. **93**, 196802 (2004).

[161] L. El-Kareh, P. Sessi, T. Bathon, and M. Bode, Phys. Rev. Lett. **110**, 176803 (2013).

[162] A. Stróżecka, A. Eiguren, and J. I. Pascual, Phys. Rev. Lett. **107**, 186805 (2011).

[163] P. Sessi, F. Reis, T. Bathon, K. A. Kokh, O. E. Tereshenko, and M. Bode, Nat. Comm. **5**, 5349 (2014).

[164] J. M. Carpinelli, H. H. Weitering, and E. W. Plummer, Surf. Sci. **401**, L457 (1998).

[165] J. A. Kubby, Y. R. Wang, and W. J. Greene, Phys. Rev. Lett. **65**, 2165 (1990).

[166] M. Göthelid, M. Hammar, C. Törnevik, U. O. Karlsson, N. G. Nilsson, and S. A. Flodström, Surf. Sci. **271**, L357 (1992).

[167] V. Dudr, N. Tsud, S. Fabík, M. Vondráček, V. Matolín, V. Cháb, and K. C. Prince, Phys. Rev. B **70**, 155334 (2004).

[168] B. Ressel, J. Slezák, K. C. Prince, and V. Cháb, Phys. Rev. B **66**, 035325 (2002).

[169] C. J. Karlsson, E. Landemark, Y.-C. Chao, and R. I. G. Uhrberg, Phys. Rev. B **45**, 6321 (1992).

[170] J. M. Gómez-Rodríguez, J.-Y. Veuillen, and R. C. Cinti, Surf. Sci. **377-379**, 45 (1997).

[171] J. C. Slater, J. Chem. Phys. **41**, 3199 (1964).

[172] J. A. Carlisle, T. Miller, and T.-C. Chiang, Phys. Rev. B **45**, 3400 (1992).

[173] H. H. Weitering, A. R. H. F. Ettema, and T. Hibma, Phys. Rev. B **45**, 9126 (1992).

[174] V. Dudr, N. Tsud, S. Fabík, B. Ressel, M. Vondráček, K. C. Prince, V. Matolín, and V. Cháb, Surf. Sci. **566-568**, 804 (2004).

[175] A. Tejeda, R. Cortés, J. Lobo, E. G. Michel, and A. Mascaraque, J. Phys.: Condens. Matter **19**, 355008 (2007).

[176] F. Ming, D. Mulugeta, W. Tu, T. S. Smith, P. Vilmercati, G. Lee, Y.-T. Huang, R. D. Diehl, P. C. Snijders, and H. H. Weitering, Nat. Comm **8**, 14721 (2017).

[177] A. B. Odobescu, A. A. Maizlakh, N. I. Fedotov, and S. V. Zaitsev-Zotov, Phys. Rev. B **95**, 195151 (2017).

[178] J. Lobo, A. Tejeda, A. Mugarza, and E. G. Michel, Phys. Rev. B **68**, 235332 (2003).

[179] M. Göthelid, M. Björkqvist, T. M. Grehk, G. Le Lay, and U. O. Karlsson, Phys. Rev. B **52**, R14352 (1995).

[180] M. E. Dávila, J. Avila, M. C. Asensio, and G. Le Lay, Phys. Rev. B **70**, 241308 (2004).

[181] M. E. Dávila, J. Avila, M. C. Asensio, M. Göthelid, U. O. Karlsson, and G. Le Lay, Surf. Sci. **600**, 3154 (2006).

[182] B. Halbig, U. Bass, J. Geurts, and S. Sanna, Phys. Rev. B **100**, 035437 (2019).

[183] P. Hansmann, T. Ayral, A. Tejeda, and S. Biermann, Sci. Rep. **6**, 19728 (2016).

[184] T. Hirahara, T. Komorida, Y. Gu, F. Nakamura, H. Idzuchi, H. Morikawa, and S. Hasegawa, Phys. Rev. B **80**, 235419 (2009).

[185] M. Goshtasbi Rad, M. Göthelid, G. Le Lay, U. O. Karlsson, T. M. Grehk, and A. Sandell, Surf. Sci. **477**, 227 (2001).

[186] T. S. Smith, F. Ming, D. G. Trabada, C. Gonzalez, D. Soler-Polo, F. Flores, J. Ortega, and H. H. Weitering, Phys. Rev. Lett. **124**, 097602 (2020).

[187] S. Jemander, N. Lin, H. Zhang, R. Uhrberg, and G. Hansson, Surf. Sci. **475**, 181 (2001).

[188] L. Cattaneo, C. Maeda, and R. Petersen, AlkaMax Application Note Vol. **1** (2004).

[189] L. Gavioli, M. Padovani, E. Spiller, M. Sancrotti, and M. G. Betti, Surf. Sci. **532-535**, 666 (2003).

[190] C. Tournier-Colletta, L. Chaput, A. Tejeda, L. Cardenas, B. Kierren, D. Malterre, Y. Fagot-Revurat, P. L. Fèvre, F. Bertran, and A. Taleb-Ibrahimi, Appl. Surf. Sci. **267**, 35 (2013).

[191] T. Hashizume, Y. Hasegawa, I. Sumita, and T. Sakurai, Surf. Sci. **246**, 189 (1991).

[192] A. Watanabe, M. Naitoh, and S. Nishigaki, Appl. Surf. Sci. **144-145**, 548 (1999).

[193] L. V. Bondarenko, A. V. Matetskiy, A. A. Yakovlev, A. Y. Tupchaya, D. V. Gruznev, M. V. Ryzhkova, D. A. Tsukanov, E. A. Borisenko, E. N. Chukurov, N. V. Denisov, O. Vilkov, D. V. Vyalikh, A. V. Zotov, and A. A. Saranin, J. Phys. Cond. Mat. **26**, 055009 (2014).

[194] S. Tanuma, C. J. Powell, and D. R. Penn, Surf. Interface Anal. **35**, 268 (2003).

[195] J. J. Yeh and I. Lindau, Atomic Data and Nuclear Data Tables **32**, 1 (1985).

[196] R. C. Wicks and N. J. C. Ingle, Rev. Sci. Inst. **80**, 053108 (2009).

[197] Private communication with Prof. Hanno Weitering.

[198] I. Battisti, V. Fedoseev, K. M. Bastiaans, A. de la Torre, R. S. Perry, F. Baumberger, and M. P. Allan, Phys. Rev. B **95**, 235141 (2017).

[199] Z. Zhang and J. T. Yates, Chemical Reviews **112**, 5520 (2012).

[200] `https://als.lbl.gov/beamlines/7-0-2/`, accessed 09-04-2020.

[201] T. Kinoshita, S. Kono, and T. Sagawa, Phys. Rev. B **32**, 2714 (1985).

[202] H. Huang, S. Y. Tong, W. S. Yang, H. D. Shih, and F. Jona, Phys. Rev. B **42**, 7483 (1990).

[203] J. M. Nicholls, B. Reihl, and J. E. Northrup, Phys. Rev. B **35**, 4137 (1987).

List of own publications

[A1] F. Adler, S. Rachel, M. Laubach, J. Maklar, A. Fleszar, J. Schäfer, and R. Claessen, *Correlation-Driven Charge Order in a Frustrated Two-Dimensional Atom Lattice*, Phys. Rev. Lett. **123**, 086401 (2019).

[A2] V. A. Rogalev, F. Reis, F. Adler, M. Bauernfeind, J. Erhardt, A. Kowalewski, M. R. Scholz, L. Dudy, L. B. Duffy, T. Hesjedal, M. Hoesch, G. Bihlmayer, J. Schäfer, and R. Claessen, *Tailoring the topological surface state in ultrathin α-Sn(111) films*, Phys. Rev. B **100**, 245144 (2019).

[A3] T. Rauch, V. A. Rogalev, M. Bauernfeind, J. Maklar, F. Reis, F. Adler, S. Moser, J. Weis, T.-L. Lee, P. K. Thakur, J. Schäfer, R. Claessen, J. Henk, and I. Mertig, *Nontrivial topological valence bands of common diamond and zinc-blende semiconductors*, Phys. Rev. Mat. **3**, 064203 (2019).

[A4] M. R. Scholz, V. A. Rogalev, L. Dudy, F. Reis, F. Adler, J. Aulbach, L. J. Collins-McIntyre, L. B. Duffy, H. F. Yang, Y. L. Chen, T. Hesjedal, Z. K. Liu, M. Hoesch, S. Muff, J. H. Dil, J. Schäfer, and R. Claessen, *Topological surface state of α-Sn on InSb(001) as studied by photoemission*, Phys. Rev. B **97**, 075101 (2018).

[A5] S. Glass, F. Reis, M. Bauernfeind, J. Aulbach, M. R. Scholz, F. Adler, L. Dudy, G. Li, R. Claessen, and J. Schäfer, *Atomic-Scale Mapping of Layer-by-Layer Hydrogen Etching and Passivation of SiC(0001) Substrates*, J. Phys. Chem. C, **120**, 10361 (2016).

[A6] S. Glass, G. Li, F. Adler, J. Aulbach, A. Fleszar, R. Thomale, W. Hanke, R. Claessen, and J. Schäfer, *Triangular Spin-Orbit-Coupled Lattice with Strong Coulomb Correlations: Sn Atoms on a SiC(0001) Substrate*, Phys. Rev. Lett. **114**, 247602 (2015).

Danksagung

Zum Schluss möchte ich noch die Gelegenheit nutzen, mich bei den vielen Leuten zu bedanken, die zum Gelingen dieser Dissertation und der lehrreichen und schönen Zeit an der EP 4 beigetragen haben. Mein Dank geht an:

- Prof. Dr. Ralph Claessen, der mir nach meiner Diplomarbeit die Gelegenheit gegeben hat, meine Doktorarbeit in der EP 4 anzufertigen. Als Hauptorganisator des erfolgreichen SFB-Antrags hat er für gesorgt, dass meine Arbeit in einem unbeschwerten finanziellen Rahmen stattfinden konnte, so dass Wünsche für Laborequipment oder Reisen zu Konferenzen und Sommerschulen stets bewilligt werden konnten. Durch seine Kompetenz in Sachfragen und seinen Führungsstil hat er maßgeblich zu der gleichsam produktiven und entspannten Atmosphäre am Lehrstuhl beigetragen.

- Prof. Dr. Jörg Schäfer, der immer als erster Ansprechpartner für Diskussionen über aktuelle Messdaten oder die nächste Präsentation zur Verfügung stand. Mit seiner positiven Grundhaltung und seinen vielen Ideen und Anmerkungen hat er dazu beigetragen, dass ich mich motiviert und reflektiert mit meinen Ergebnissen auseinandergesetzt habe.

- Prof. Dr. Stephan Rachel und Dr. Manuel Laubach für die erfolgreiche Kooperation und den lehrreichen Austausch rund um die Ergebnisse, die letztendlich zur Veröffentlichung unseres gemeinsamen Artikels geführt habe. Mein Dank gilt außerdem Dr. Gang Li und Dr. Andrzej Fleszar, die vor allem zu Beginn meiner Doktorarbeit die wichtige Unterstützung von theoretischer Seite geleistet haben.

- Dr. Lenart Dudy, Dr. Victor Rogalev und Dr. Markus Scholz, die als Spezialisten für das ARPES-Labor immer dafür gesorgt haben, dass ich eine bedienfreundliche und funktionierende Anlage vorfinde. Gleiches gilt für Julian Aulbach und Felix Reis, die das STM-Labor während meiner Zeit federführend in Stand gehalten und mir die wichtigsten Handgriffe gezeigt haben.

- Meinen Master-Studenten Julian Maklar sowie meine beiden Bachelor-Studenten Jonas Erhardt und Johannes Jung, die mich bei der Entwicklung der Rezepte für die Probenpräparation, den anschließenden Messungen und der Datenauswertung maßgeblich unterstützt haben.

- Alle Lektoren dieser Arbeit (Raúl, Philipp, Judith, Jonas, Max, Victor, Stef, Michael, Stephan und Jörg), die ihre Zeit und Expertise zur Verfügung gestellt haben, um Fehler und Ungereimtheiten auszumerzen.

- Moni Seifer, die ihren Job weit über ihre Kernaufgaben hinaus ausdehnt und mir somit viele unliebsame Aufgaben abgenommen hat und für jedes nichtwissenschaftliche Problem eine Lösung findet.

- Alle anderen Mitglieder des Lehrstuhls für das kollegiale Miteinander und die immer hilfsbereite Zusammenarbeit im Labor. Insbesondere bedanke ich mich bei den Mitgliedern der mittäglichen Mensa- und Kaffeerunde. Die fast täglichen Gespräche über Physik und die Welt waren definitiv mein Lieblingsritual in der EP 4.